HCl Nanoscience at Copper and Copper/Gold Alloy Surfaces

Hatem Muhmad Altass

Thesis submitted to Cardiff University

in candidature of the degree of Doctor of Philosophy in Chemistry

Department of Chemistry, Cardiff University, Cardiff, Wales, U.K.

April 2013

DECLARATION

This work has not been submitted in substance for any other degree or award at this or any other university or place of learning, nor is being submitted concurrently in candidature for any degree or other award.

Signed ……(***Hatem M Altass***) Date …...**25/04/2013**……

STATEMENT 1

This thesis is being submitted in partial fulfilment of the requirements for the degree of ……**PhD**……

Signed ……(***Hatem M Altass***) Date …...**25/04/2013**……

STATEMENT 2

This thesis is the result of my own independent work/investigation, except where otherwise stated. Other sources are acknowledged by explicit references. The views expressed are my own.

Signed ……(***Hatem M Altass***) Date …...**25/04/2013**……

STATEMENT 3

I hereby give consent for my thesis, if accepted, to be available for photocopying and for inter-library loan, and for the title and summary to be made available to outside organisations.

Signed ……(***Hatem M Altass***) Date …...**25/04/2013**……

This thesis is dedicated to my parents, wife, children, sister, and brothers for their love, endless support and encouragement.

Abstract

The reaction of HCl with clean, Cu(100) and (111), and Au/ Cu(100) surfaces was investigated using x-ray photoelectron spectroscopy (XPS) and scanning tunneling microscopy (STM) under ultra high vacuum (UHV) conditions. Exposure of the Cu(100) and (111) samples to HCl at room temperature leads to the formation of a saturated copper chloride monolayer. In the case of Cu(100), the saturated coverage was half monolayer corresponding to a c(2x2)-Cl reconstruction (half monolayer is $7.25x10^{14}$ cm^{-2}) while for Cu(111) it was one third monolayer consistent with the reconstruction of $(\sqrt{3}x\sqrt{3})R30^{o}$ (one third monolayer $5.9x10^{14}$ cm^{-2}).

The interaction of HCl with preoxidised Cu(100) and (111) showed different behaviour from those of clean copper surface depending on the way of interaction of oxygen with copper surface. Interaction of HCl with peroxidised Cu(111) at saturation oxygen coverage leads to the adsorption of chlorine on top of the copper surface with one third coverage. In contrast, presence of oxygen on Cu(100) surface at saturation coverage or less leads to adsorb chlorine but with an excess in chlorine concentration (more than the expected c(2x2) coverage).

Oxidized Cu(100) and (111) surface at elevated temperature leads to the formation multi oxide layer. The two oxide surfaces (‘’44’’ and ‘’29’’) observed at the Cu(111) depend on the temperature of the substrate at the time of oxidation. The $(\sqrt{2}x2\sqrt{2})R45^{o}$ structure was observed on the Cu(100) surface on heating which is the same structure formed at saturation coverage at room temperature. Interaction of HCl with Cu(100) and (111) surfaces covered by multilayers of oxide lead to adsorption of chlorine on top of the copper surface with a coverage more than more than the saturation coverage.

Interaction of HCl with Au/Cu(100) showed two different behaviour depending on the gold coverage. Au/Cu(100) alloy formed at half monolayer of gold coverage, forming c(2x2) structure. Exposure of the Au/Cu(100) alloy at half monolayer of gold coverage to HCl leads to the formation of c(2x2)-Cl structure with saturation coverage of half monolayer in similar manner of interaction of HCl with the clean cu(100) surface. Interaction of HCl with Au/Cu(100) surface at gold coverage more than half monolayer leads to a dealloying of the gold from the copper surface and forming the Au(111) surface. Cu-Cl formed underneath the Au(111) surface with excess of chlorine concentration.

Acknowledgments

The realization of this work was only possible due to the several people's collaboration, to which desire to express my gratefulness.

To Dr Philip Davies and Dr Albert Carley, my supervisors, I am grateful for the trust deposited in my work and for the motivation demonstrated along this arduous study. Their help was endless, no matter what the issue and time. They give me a lot of knowledge about handling the complicated UHV system. Your guidance was the best guide during the period that I spent with you and I hope this cooperation will continue even after my return to home. I am very grateful to both of them for their supervision and friendship.

I would like to thank from a special way Dr Robert Davies for his help for all the time of my work and when we travel together to attend the scientific conferences. I am very glad to have a friendship with such a man.

I would like to thank Dr David Morgan for his continuous help for solving the UHV system problem, advices and suggestions.

To all my colleagues and researchers in surface science group, for the encouragement, advice suggestions and friendship.

I must also thank all the staff of the School of chemistry for their help and assistance during the time of my work. Special thanks as well for the staff of the mechanical workshop for their help to fix the engineering issues and amazing solutions which they suggested.

I would also to express my appreciation to my friend, Dr Mohammed Baashen and all my friends in Saudi Chemists Group in Cardiff for their enthusiasm, encouragement and fascinating friendship.

Finally, I would like to thank to my family, their love gave me forces to make this work.

Contents

Chapter 1 Introduction

Contents

1.1 Single Crystal of metal surface

To understand the solid state interaction with gas molecules we need to have some insight into the structure of simple crystals. Crystal structures are usually determined by the technique of X-ray back –scattering which is used to determine the requested plane before cutting the crystal by spark erosion. The resulting surface needs to be mechanically polished to get the mirror surface which is a key demand to get good STM and low energy electron diffraction (LEED) images [1, 2].

1.2 Miller indices

Miller indices are used to describe the surface crystal structure derived from three main crystal systems depending on the arrangement of the atom inside the crystal [1]. The first category is face centred cubic (fcc), which has eight corner atoms and six face atoms as shown in Figure 1.1(a). The second category is body centred cubic (bcc), which has eight corner atoms and one centred atom as shown in Figure 1.1(b). The last category is hexagonal close-packed (hcp), which can be described as two hexagonal planes having six atoms in the corners of the hexagon and one centred atom; between these planes is a half hexagon consisting of three atoms as shown in Figure 1.1(c). Three integers (x, y, z) are used to describe the crystal plane for the two crystal (fcc) and (bcc), while four integers (w, x, y, z) describe (hcp). The surface plane produced depends on the direction of cutting the crystal, for example for a simple cubic crystal the three main planes produced are (100), (110), and (111). These numbers are the reciprocal of the fractional intercepts of the distance at which a plane intersects the main axis of the solid as shown in Figure 1.2.

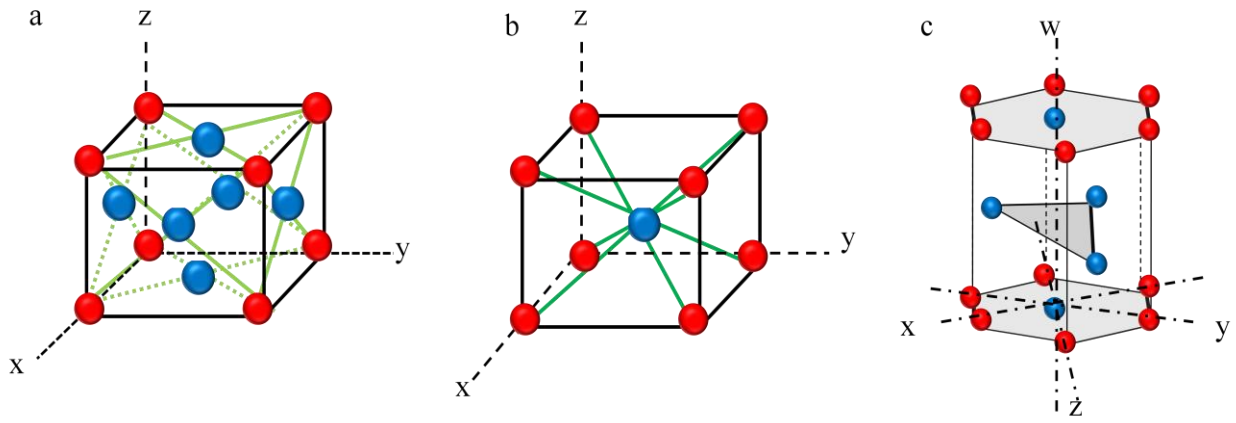

Figure 1.1: Three crystal structures; (a) face centred cubic (fcc), (b) body centred cubic (bcc), and (c) hexagonal close-packed (hcp).

(100) plane: This plan intersects with a, value of x axis, while as it is parallel to the y and z axis as shown in Figure 1.2(a). Therefore this plane has intercepted $\left(\frac{a}{\bar{a}}, \frac{\infty}{\bar{b}}, \frac{\infty}{\bar{c}}\right)$. Which is equal to (1, ∞, ∞). The reciprocal of these values are (100).

(110) Plane: This plan intersects with by a, and y values with both x, and y axis, while as it parallel to z axis as shown in Figure 1.2(b). Therefore this plane has intercept $\left(\frac{a}{\bar{a}}, \frac{b}{\bar{b}}, \frac{\infty}{\bar{c}}\right)$, which is equal to (1, 1, ∞). The corresponding reciprocal of these values are (110).

Plane (111): This plane intersect with x, y, and z axes as shown in Figure 1.2(c). The intercept values of this plane are $\left(\frac{a}{\bar{a}}, \frac{b}{\bar{b}}, \frac{c}{\bar{c}}\right)$. Therefore the corresponding reciprocal of fractional of these values are (111).

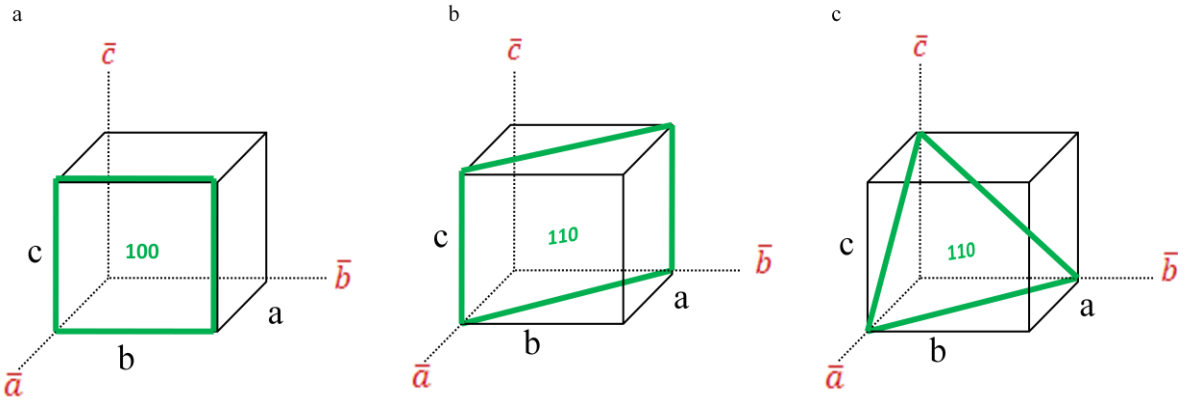

Figure 1.2: Miller indices of some important cubic crystal planes: (*a*) (100), (*b*) (110), and (*c*) (111).

1.3 Surface structures and reactivity

In the case of copper which is a (fcc) crystal, the three simplest surface planes produced are Cu(100), (110), and (111) as shown in Figure 1.3. The reactivity of the surface depends on the coordination number of the surface atoms, since the reaction with a metal surface happens at the top most atomic layer. The reactivity of the surface depends on the surface free energy, in other words, the surface which has highest surface energy will have the highest reactivity. For copper the most open surface is (110) in which the surface atoms have two nearest neighbouring atoms, with four and six nearest neighbouring atoms in case of Cu(100), and (111) respectively.

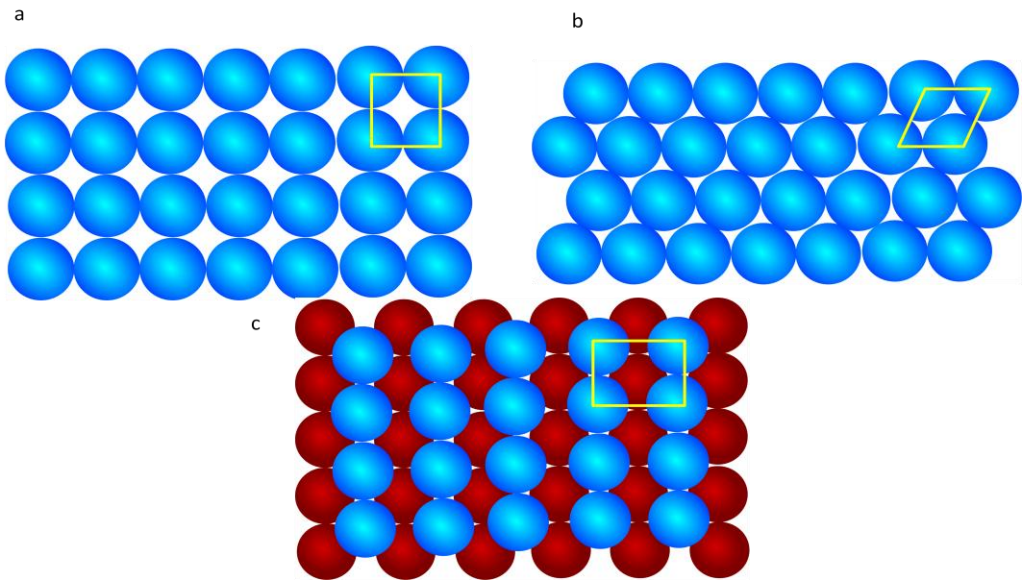

Figure 1.3: Representation of the surface, with the unit cell in yellow for (fcc) crystal lattice planes. From top to bottom, (a) (100) surface, (b) (111) surface, and (c) (110) surface.

The surface structure which is produced after cutting and polishing is not ideally smooth it has a number of surface features (defective structures) as shown in Figure 1.4 [3]. Terraces are the main surface features separated by step edges, while as the step edge itself it could have defects as well such as step kink. Two surface defects that could be found in the terraces are an adatom or missing atom (vacancy). The surface features have different reactivity depending on the free surface energy. So the atoms in the defect site have a lower coordination to the bulks atoms compared with the atoms in the flat terraces, which leads to an increase in the free surface energy for the atoms in the defect site. So the defect site could be the initial reaction site in case of adsorbing a gaseous molecule on the crystal surface.

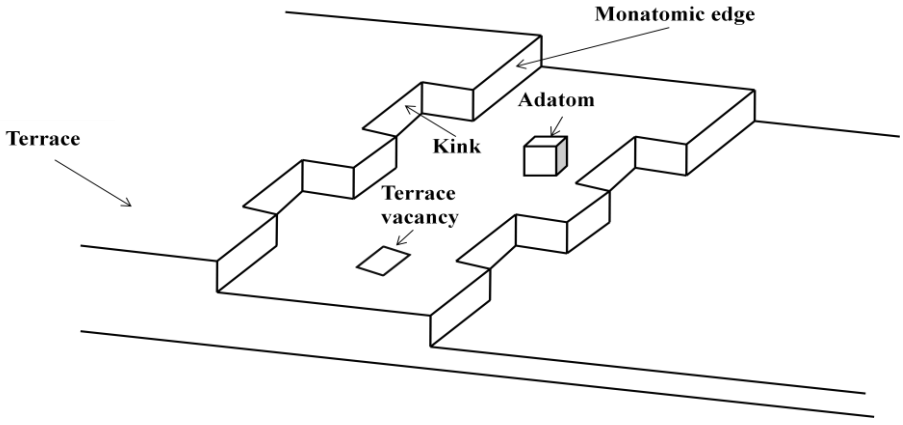

Figure 1.4: Schematic diagram shown the defective structures on the crystal surface after cutting and polishing [3].

1.4 Atomic densities of atoms in the surface plane

In the case of a cube of copper with edges of length 1 cm and (100) surface plane, the area of each unit cell which have square unit cell is given by:

$$a \times a = (a^2) \qquad 1.1$$

Where the copper lattice constant a = 2.55 Å [4]. So the area of Cu(100) unit cell is:

$$(2.55\ Å)^2 = 6.50\ Å^2 = 6.50 \times 10^{-16}\ cm^2 \qquad 1.2$$

Since each unit cell contains one copper atom, so the total number of copper atoms in 1 cm^2 is given by:

$$\frac{1\ cm^2}{6.50 \times 10^{-16} cm^{-2}} = 1.54 \times 10^{15} \qquad 1.3$$

The interlayer spacing in Cu(100) planes is:

$$\frac{2.55}{\sqrt{2}} = 1.80\ Å = 1.80 \times 10^{-8}\ cm \qquad 1.4$$

Therefore the total number of Cu(100) atomic layer in 1 cm^3 is:

$$\frac{1\ cm}{1.28 \times 10^{-8}\ cm} = 5.5 \times 10^{7} \qquad 1.5$$

From equation 1.3 and 1.5, the total number of Cu(100) in 1 cm^3 is:

$$1.54 \times 10^{15} \times 5.5 \times 10^{-7} = 8.56 \times 10^{22} \qquad 1.6$$

The surface atoms in 1 cm^3 are given by:

$$\text{Number of atoms in 1 } cm^2 \text{ x 6} = 1.54 \text{ x } 10^{15} \text{ x 6} = 9.24 \text{x} 10^{15} \qquad 1.7$$

From equation 1.6 and 1.7 the ratio of surface atoms to the bulk atoms is $1:10^8$.

1.5 Adsorption

The adsorption of gaseous molecules on top of the solid surface is classified into two main categories physisorption and chemisorption depending on the nature of bond between the adsorbate and the substrate.

1.5.1 Physisorption

In physisorption, there is a long range weak interaction between adsorbate and substrate due to van der Waals-type forces [5]. The interaction of adsorbate and substrate is reversible due the weak interaction between them leading to equilibrium between the adsorbate layer and the molecule in the gas phase. A multilayer of adsorbate could be formed at low temperature or at high pressure of dosing. The heat of adsorption ΔH_{AD}^{o} is of the order of $\Delta H_{condensation}^{o}$ which is less than 35 kJ mol^{-1}; this small amount of energy could be lost as a thermal motion and a jumping of the molecule across the substrate surface until it is accommodated with the surface [5]. No change in the substrate is observed after physisorption occurred. Increasing the temperature of the substrate will increase the vibration energy of the adsorbate molecule higher than energy of desorption leading it to desorb from the surface. The residence time (τ) is used to measure the strength of interaction between the adsorbate and the substrate depending on the temperature by using the Frenkel equation as given:

$$\tau = \tau_o \, exp^{\left(\frac{\Delta H_{AD}^{o}}{RT}\right)} \qquad 1.8$$

Where:

τ_0 = period of oscillation of the molecule at the surface $\approx 10^{-13}$ s

ΔH_{AD}^{o} = desorption energy (kJ mol^{-1})

k = Boltzmann's constant (1.38×10^{-23} J K^{-1})

T = temperature (K)

1.5.2 Chemisorption

In chemisorption there is a short range of interaction of the gas molecule with substrate associated with strong bonding [5]. The interaction between the adsorbate and the substrate surface is irreversible due to the electron exchange between them. The heat of adsorption ΔH_{AD}^{o} is more than 35 to 1000 kJ mol^{-1}, which strongly depends on the adsorbate's surface coverage due to the internal adsorbate-adsorbate interaction. Dissociation of the adsorbate molecule could happen due to the higher value of ΔH_{AD}^{o}, which forms the basis of most catalytic reactions. The formation of adsorbate layer is limited to a monolayer, which means a further adsorption for the adsorbate after the saturation coverage needs to disturb the

configuration of the adsorbate layer [5]. Since the adsorbate coverage depends on the heat of adsorption ΔH_{AD}^{o}, the increase of substrate temperature leads to increasing the surface coverage. The potential energy vs reaction coordinate diagram for chemisorption shows a potential well for the chemisorbed state much deeper than the one for the physisorption state as shown in Figure 1.5 because the chemisorbed state involves breaking of the adsorbate bond (often leading to dissociation), and rearrangement of the substrate atoms. When the energy barrier between the precursor and the chemisorbed state is below the energy zero reference axis as shown in Figure 1.5(a), non-activated chemisorption occurred, while the activated chemisorption occurred when the energy barrier is above the zero energy axis resulting a slower reaction as shown in Figure 1.5(b).

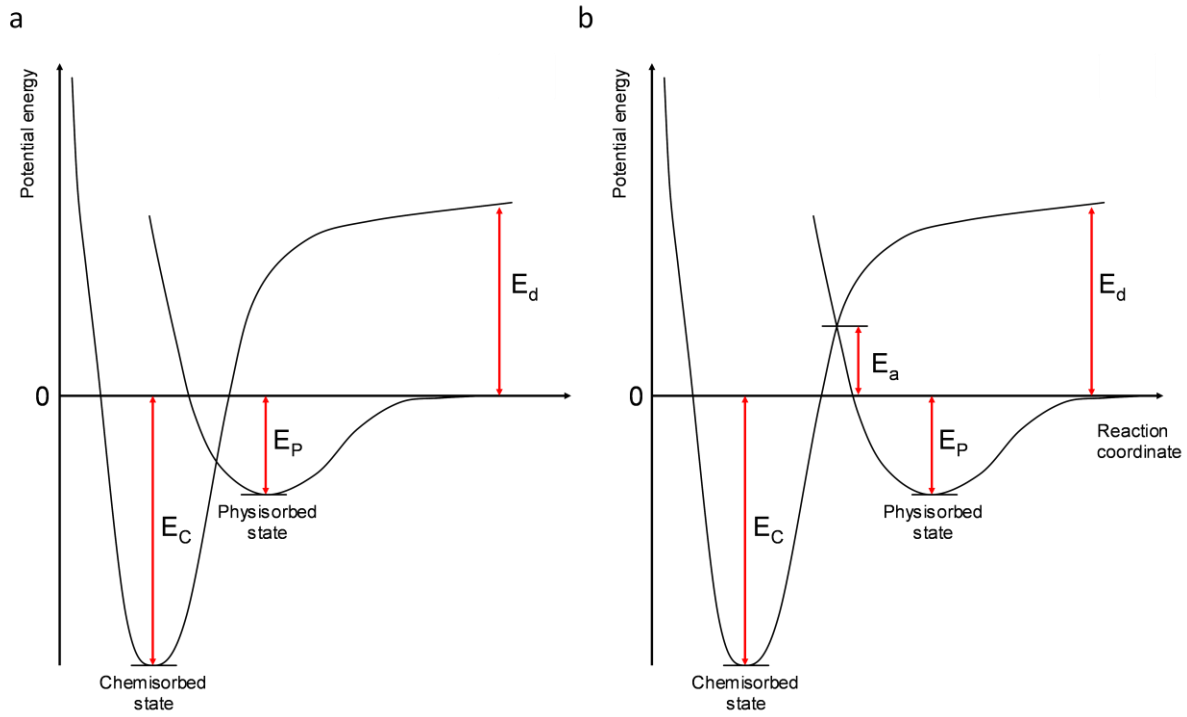

Figure 1.5: Potential energy vs reaction coordinate diagrams for (a) non-activated chemisorption and b) activated chemisorption processes. Where E_d is the dissociation energy, E_p is the physisorption energy, E_c is the chemisorption energy, and E_a is the activation energy.

1.5.3 Adsorption isotherm

Adsorption isotherm is a term used to describe the relationship between the surface coverage of adsorbate and the substrate as a function of pressure at a particular temperature [4, 5]. The Langmuir model is based on several assumptions:

- All the adsorption sites on the surface are equal, so there are no preferred adsorption sites.
- The adsorption of a molecule is not affected by the state of the adjacent site whether it is occupied or not.
- Adsorption is limited to the maximum coverage (a complete monolayer).

For the Langmuir isotherm, the rate of change of surface coverage due to the adsorption process is given by:

$$\left(\frac{d\theta}{dt}\right)_{ads} = k_{ads}\ PN(1-\theta) \qquad 1.9$$

Where:

θ = surface coverage therefore

k_{ads} = rate constant of adsorption

p = pressure of gas (Pa)

N = total number of sites and $N(1-\theta)$ is the number of vacant site

The rate change of coverage θ due to desorption is proportional to the number of adsorbed species (Nθ) and given by:

$$\left(\frac{d\theta}{dt}\right)_{des} = k_{des} N\theta \qquad 1.10$$

Where:

k_{des} = rate constant of desorption

At equilibrium, adsorption and desorption rate must be equal:

$$\left(\frac{d\theta}{dt}\right)_{ads} = \left(\frac{d\theta}{dt}\right)_{des} \qquad 1.11$$

Therefore, resolving for θ, gives the Langmuir isotherm equation:

$$\theta = \frac{Kp}{1+Kp} \qquad 1.12$$

Where:

$$K = \frac{k_{ads}}{k_{des}} \qquad 1.13$$

For the reaction involving several multilayers several isotherm methods have been developed to overcome some of the Langmuir assumptions and present a model more close to reality. For example the Brunauer-Emmett-Teller (BET) model takes into account the possibility that the initial adsorbed monolayer may act as the substrate and allow for further physical adsorption, and the Temkin and Freundlich models account for the non-equivalence of the adsorption sites. The linear form of the BET equation given by:

$$\frac{P}{N_s(P_o - P)} = \frac{1}{NC} + \frac{(C-1)}{NC} \times \frac{P}{P_o} \qquad 1.14$$

Where:

N = total number of surface adsorption sites

N_s = number of surface sites occupied by adsorbate

C = BET constant $\approx e^{\frac{(\Delta H^o des - \Delta H^o vap)}{RT}}$

Useful information about the surface area with specific coverage (θ) can be given from the both of the above isotherm, however no one isotherm can be use to predict the adsorption over all ranges of coverage.

1.6 Surface science and heterogeneous catalysis

We are continually exposed to chemical reactions in most our live whether inside our body (such as food degradation or interaction of drug with our body) or surrounding us such as fabrication of all material used in new technologies (mobile battery memory and huge industrial application). Chemical reactions can be accelerated by using a substance (it is called catalysis) that can be introduced in a chemical process by lowering the activation energy level of the transition state, therefore making it a more favourable process while this substance is regenerated after the end of reaction [6] as shown in Figure 1.6.

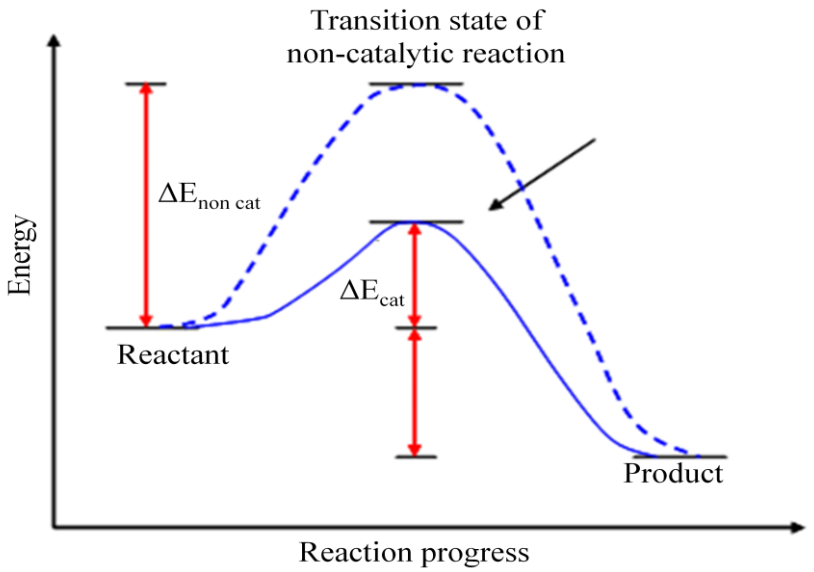

Figure 1.6: The effect of the catalyst on the reaction progress by lowering the activation energy.

Catalysis is classified in the two categories; homogenous and heterogeneous. The later type is more widely used in industrial processes. It called ‘’heterogeneous’’ because the reaction is occurring at the interface between the two, or three, phases present in the system (the reactants are normally in gas or liquid phase), whereas the catalyst is in a solid phase. Solid catalysts are widely used in the pollution reduction such as oxidation of carbon monoxide by using precious metals as catalysts (e.g. platinum, palladium or both) [7-9]. Grain or pellet is the typical form of the industrial catalysis, the pellet being formed by compression of the powdered catalyst [3]. The surface science is important in heterogeneous catalysis, since the catalytic reaction is done over the solid surface. The reactivity of the catalyst depends on the physical properties of the surface and chemical composition [3, 4, 6]. Metal single crystals are used as models of catalysts which provide a uniform surface (making the follow up of the interaction of the reactant with solid surface easier than for polycrystalline metal) to get information of the catalysis reaction at the atomic scale [2, 4, 6, 10]. However applying the knowledge from surface science to the industrial process is a problematic because of the difference between the environments. The surface science study is carried out normally in an ultra high vacuum system (UHV), whereas the industrial process is carried out at high temperatures, with a mixture of crystallites, and high pressures. The requirement of the control of the temperature is provided in most UHV systems. The presence of a mixture of crystallites has an effect on the physical properties of the surface by providing a variety of

morphologies of the surface. Nevertheless, studying the surface chemical and physical properties by surface characterisation techniques is key to understanding the nature of the catalytic reactions [2, 11].

1.7 Copper and gold as a catalyst

Copper has been recognised as a superior catalyst for many years involved in many industrial processes [12]. Copper oxide (CuO_x) is used in many industrial processes such as, oxidation of carbon monoxide [13-15], and alcohol synthesis [16]. Copper chlorides have been shown to play an important role in surface-catalyzed chlorination reactions. Polychlorinated dibenzo-p-dioxins (PCDD), and polychlorinated dibenzo-furans (PCDF) are produced over copper particle surfaces on carbon fly ash particles [17-19]. Oxychlorination of ethylene is a catalytic process performed over a copper based heterogeneous catalyst as it typically contains cupric chloride ($CuCl_2$) as the primary active ingredient [20]. Since the oxychlorination reaction is a highly exothermic reaction, the high volatility of active species is the main problem in this reaction because the rise in temperature leads to deactivation of the catalyst [21]. Deactivation of catalyst and production of unwanted chlorinated products have a high impact on the economy of the process. Production of vinyl chloride by oxychlorination of ethylene is a three step process. First is direct addition of chlorine to ethylene. Second is producing vinyl chloride and HCl by cracking the dichloroethane which formed in the direct addition step. Final step is the oxychlorination reaction in which the HCl from step of cracking the dichloroethane react with oxygen and ethylene over $CuCl_2$ catalyst to produce more of dichloroethane as shown in the following equations [12]:

$$C_2H_4 + Cl_2 \rightarrow CH_2Cl\text{-}CH_2Cl \quad \text{(Direct addition)}$$

$$CH_2Cl\text{-}CH_2Cl \rightarrow CH_2{=}CHCl + HCl \quad \text{(Thermal reaction and HCl recycle)}$$

$$CH_2{=}CH_2 + 1/2O_2 + 2HCl \rightarrow CH_2Cl\text{-}CH_2Cl + H_2O \quad (CuCl_2 \text{ catalyst})$$

The catalyst in the final step is related to the Deacon reaction, which was introduced 1874 by Henry Deacon[22], HCl is oxidized in the presence of $CuCl_2$ to molecular chlorine Cl_2 as shown in the following equation [23]:

$$4HCl + O_2 \rightleftharpoons 2Cl_2 + 2H_2O$$

This catalyst suffers from low stability due to formation of volatile $CuCl_2$ species and too low activity so that the required reaction temperature is above 400 °C.

Gold was recognised as a non-reactive metal, but this assumption about gold has been changed [24]. Catalysis by gold (in nanometre size) has become an interesting area of research, since the important findings of Hutchings for the hydrochlorination of acetylene [25] and Haruta [26] for the oxidation of CO at low temperature.

Oxidation of CO is very important for air purification systems for industrial processes and car exhaust pollution For example, at start up of a car's engine, the catalyst placed in the exhaust takes a little time to become effective due to the time required for heating the catalyst. Hence the idea of finding a catalyst working at low temperature has emerged. Haruta et al. have shown that the oxidation of CO at very low temperatures and in particular at temperatures less than 0 ^{o}C is effectively catalysed by composite of gold and first row transition metals (Fe, Co, and Ni). Later he discovered that gold nanoparticles (2 to 4 nm diameter) supported different oxides (Fe, Co, and Ni) are the active species [27]. This work enhanced the enthusiasm of researchers to predict the identity of the active site. Bollinger et al. observed that the highest activity is for the Au particles (2 to 3 nm diameter) supported on TiO_2 [28]. Goodman et al. have shown that gold clusters (1 to 6 nm diameter) prepared on single crystalline surfaces of Ti were strongly related to the structure sensitivity of the CO oxidation using STM and STS [29].

The oxidation of alcohols and diols to acids and carboxylates, which chemical intermediates, represents a demanding target for many application. Platinum and palladium supported nanoparticles are effective catalysts for such reactions. However poor selectivity is the disadvantage of these catalysts. Rossi et al. have shown that gold nanoparticles can be very effective catalysts for the oxidation of alcohols, including diols, as shown in Figure 1.7 and the gold catalyst showed best stability in recycling tests [30, 31].

Using gold as a catalyst for hydrochlorination of acetylene over gold/carbon catalysts provides a higher activity compared with other metals as shown in ,Figure 1.8 [32]. The interaction of Au/C catalyst with acetylene leads to deactivation, whereas enhancement of the initial activity of the catalyst is observed after the pre-treatment by HCl. Au^{3+} is supposed to be the active species, while as the active site it could be gold cations located either on the surface of gold nanoparticles or in the interface of gold nanoparticles with carbon support [33].

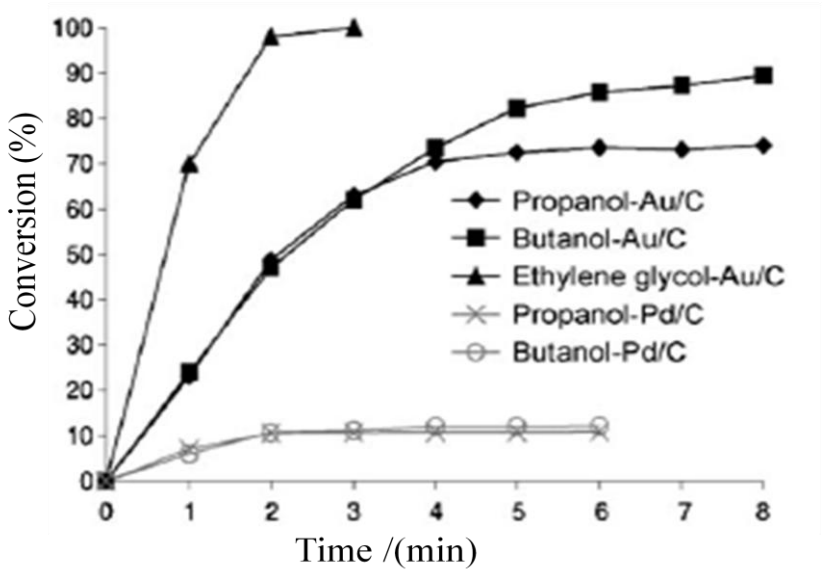

Figure 1.7: Oxidation of alcohols by different supported metal. At [alcohol] = 0.35 M, 3 atm, and T=343 K [30]

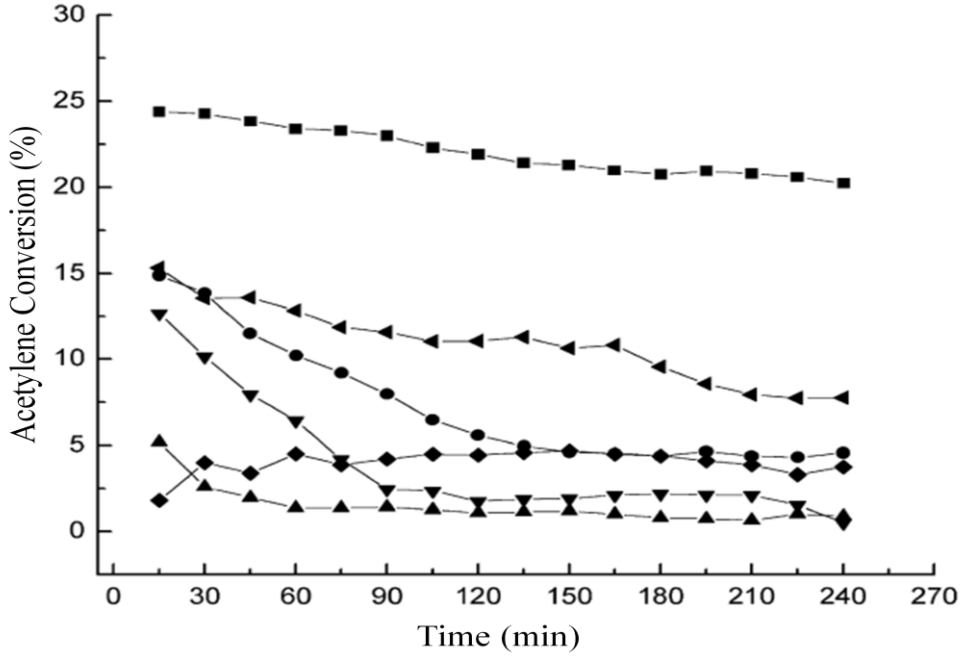

Figure 1.8: Acetylene conversion using metal chlorinated salts of (■) Au, (▾) Pd, (♦) Pt, (▴) Rh, (●) Ir, and (◂) Ru on carbon as catalyst under standard reaction conditions (C_2H_2 and HCl 1:1 ratio; total flow rate 10 mL min^{-1}; catalyst (200 mg); 180 °C).

On the other hand catalysis by metal alloy has attracted considerable attention recently [34]. AuCu alloys supported on TiO_2 have shown a higher catalytic activity toward oxidation of CO compared with monometallics supported on TiO_2 as shown in Figure 1.8 [35]. The catalyst formed by 1% of Au and 8% of Cu/TiO_2 has shown considerable activity compared with the catalyst of 1% of Au/ TiO_2, and more active than the catalyst of 8% of Cu/TiO_2.

For CO oxidation at low temperature a series of catalysts containing Au precipitated on metal hydroxides have been used [36]. The catalytic activity of an $Au(PPh_3)(NO_3)/Cu(OH)_2$ catalyst has been compared with the catalytic activity of $Au(PPh_3)(NO_3)/Mn(OH)_2$. The higher activity was for the latter one as it shows a 50% conversion at a temperature less than -70 ^oC and 100% conversion at 0 ^oC, whereas the $Au(PPh_3)(NO_3)/Cu(OH)_2$ catalyst achieved 50% conversion at 61 ^oC and 100% conversion at 170 ^oC. However, the $Au(PPh_3)(NO_3)/Cu(OH)_2$ catalyst showed a higher activity compared with similar catalysts based on hydroxides of V, Al or Cr.

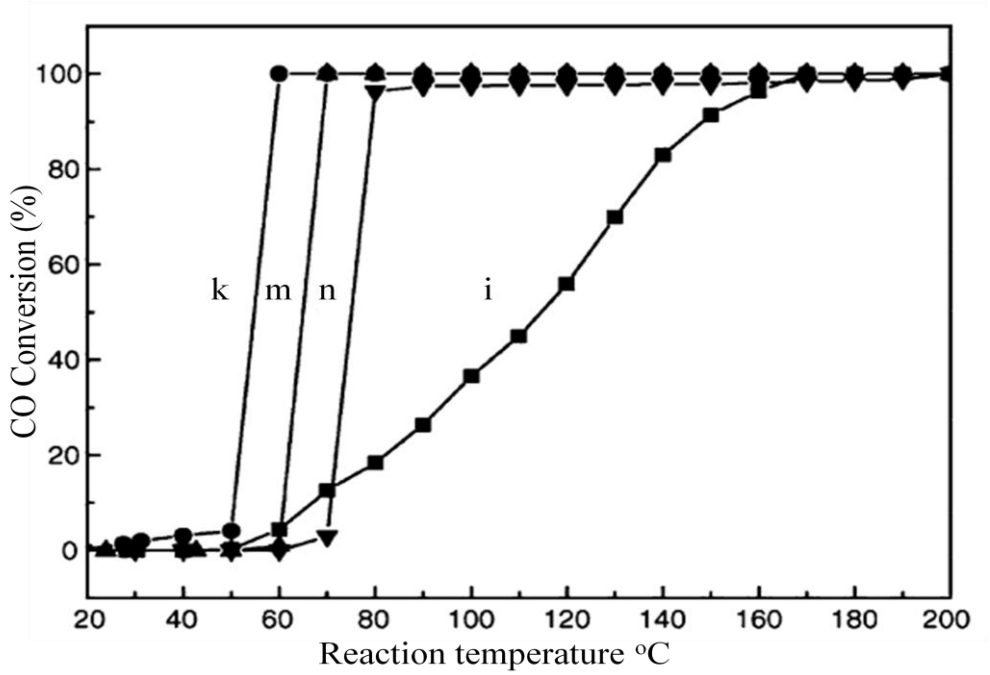

Figure 1.8: CO oxidation activity of (k) 0.5% Au/TiO_2, (i) 0.1% Au/TiO_2 (m) 0.1% Au–8% Cu/TiO_2 and (n) 8% Cu/TiO_2 [35].

1.8 References

1. Borchardtott, W., *Crystallography*. 2012, London: SpringerVerlag Berlin Heidelberg. 356.
2. J. M. Walls, R.S., *Surface Science Techniques*. 1994 Amsterdam: Elsevier Science & Technology. 188.
3. Bowker, M.K., *The Basis and Applications of Heterogeneous Catalysis*. 1998, Oxford: Oxford University Press. 96.
4. Meirion Wynn Roberts, C.S.M., *Chemistry of the metal-gas interface*. 1987, Oxford: Clarendon Press. 594.
5. Attard, G. and C. Barnes, *Surface*. 1998, Oxford: Oxford University Press. 97.
6. Somorjai, G.A. and Y. Li, *Introduction to Surface Chemistry and Catalysis*. 2nd ed. 2010, Chicester: John Wiley and Sons Ltd. 784.
7. Shishu, R.C. and L.S. Kowalczyk, *The Oxidation of Carbon Monoxide on Supported Platinum.* Platinum Metals Rev. 1974. **18**(2): p. 58-64.
8. Conrad, H., et al., *Adsorption of CO on Pd single crystal surfaces.* Surface Science, 1974. **43**(2): p. 462-480.
9. Yatsimirskii, V.K., O.Y. Boldyreva, and L.P. Oleksenko, *Characteristics of the Oxidation of Carbon Monoxide on Platinum and Palladium Acetylacetonates Immobilized on a Silica Surface.* Theoretical and Experimental Chemistry, 2001. **37**(6): p. 360-365.
10. Vickerman, J.C. and I. Gilmore, *Surface Analysis The Principal and Techniques*. 2nd ed. 2009, Chichester: Wiley. 686.
11. Brune, D., et al., *Surface Characterization*. 2008, Weinhemi: John Wiley & Sons 715.
12. Lloyd, L., *Handbook of Industrial Catalysts*. 2011, U.S.: Springer Science+Business Media. 490.
13. Szanyi, J. and D.W. Goodman, *CO oxidation on a model Cu/Rh(100) catalyst.* Catalysis Letters, 1992. **14**(1): p. 27-35.
14. Szanyi, J. and D.W. Goodman, *Surface Science and Kinetic Studies on Model Cu/Rh(100) Catalysts*, in *Studies in Surface Science and Catalysis*, F.S. L. Guczi and T. P, Editors. 1993, Elsevier. p. 1599-1602.
15. Szanyi, J. and D. Wayne Goodman, *CO oxidation on a Cu(100) catalyst.* Catalysis Letters, 1993. **21**(1-2): p. 165-174.
16. Klier, K., *Methanol Synthesis*, in *Advances in Catalysis*, H.P. D.D. Eley and B.W. Paul, Editors. 1982, Academic Press. p. 243-313.

17. Addink, R. and K. Olie, *Mechanisms of Formation and Destruction of Polychlorinated Dibenzo-p-dioxins and Dibenzofurans in Heterogeneous Systems.* Environmental Science & Technology, 1995. **29**(6): p. 1425-1435.
18. Froese, K.L. and O. Hutzinger, *Polychlorinated Benzene, Phenol, Dibenzo-p-dioxin, and Dibenzofuran in Heterogeneous Combustion Reactions of Acetylene.* Environmental Science & Technology, 1996. **30**(3): p. 998-1008.
19. Froese, K.L. and O. Hutzinger, *Polychlorinated Benzene and Polychlorinated Phenol in Heterogeneous Combustion Reactions of Ethylene and Ethane.* Environmental Science & Technology, 1996. **30**(3): p. 1009-1013.
20. Wilkes, C.E., et al., *PVC Handbook*. 2005, U.S.: Hanser Gardner Publications. 723.
21. Over, H. and R. Schomaecker, *What makes a good catalyst for the Deacon Process?* ACS Catalysis, 2013.
22. Deacon, H., *manufacture of chlorine*, U.S. Patent, Editor. 1875. p. 6802.
23. Hisham, M.W.M. and S.W. Benson, *Thermochemistry of the Deacon Process.* The Journal of Physical Chemistry, 1995. **99**(16): p. 6194-6198.
24. Bond, G.C., C. Loui, and D.T. Thompson, *Catalysis by Gold*. 2006, London Imperial College Press.
25. Hutchings, G.J., *Vapor phase hydrochlorination of acetylene: Correlation of catalytic activity of supported metal chloride catalysts.* Journal of Catalysis, 1985. **96**(1): p. 292-295.
26. Haruta, M., et al., *Novel Gold Catalysts for the Oxidation of Carbon Monoxide at a Temperature far Below 0 ^{o}C.* Chemistry Letters, 1987. **16**(2): p. 405-408.
27. Haruta, M., et al., *Gold catalysts prepared by coprecipitation for low-temperature oxidation of hydrogen and of carbon monoxide.* Journal of Catalysis, 1989. **115**(2): p. 301-309.
28. Bollinger, M.A. and M.A. Vannice, *A kinetic and DRIFTS study of low-temperature carbon monoxide oxidation over Au—TiO2 catalysts.* Applied Catalysis B: Environmental, 1996. **8**(4): p. 417-443.
29. Valden, M., X. Lai, and D.W. Goodman, *Onset of Catalytic Activity of Gold Clusters on Titania with the Appearance of Nonmetallic Properties.* Science, 1998. **281**(5383): p. 1647-1650.
30. Prati, L. and M. Rossi, *Gold on Carbon as a New Catalyst for Selective Liquid Phase Oxidation of Diols.* Journal of Catalysis, 1998. **176**(2): p. 552-560.

31. Porta, F., et al., *Metal sols as a useful tool for heterogeneous gold catalyst preparation: reinvestigation of a liquid phase oxidation.* Catalysis Today, 2000. **61**(1–4): p. 165-172.
32. Conte, M., et al., *Hydrochlorination of acetylene using supported bimetallic Au-based catalysts.* Journal of Catalysis, 2008. **257**(1): p. 190-198.
33. Conte, M., et al., *Hydrochlorination of acetylene using a supported gold catalyst: A study of the reaction mechanism.* Journal of Catalysis, 2007. **250**(2): p. 231-239.
34. Ferrando, R., J. Jellinek, and R.L. Johnston, *Nanoalloys: From Theory to Applications of Alloy Clusters and Nanoparticles.* Chemical Reviews, 2008. **108**(3): p. 845-910.
35. Zhu, B., et al., *Characterization and catalytic performance of TiO2 nanotubes-supported gold and copper particles.* Journal of Molecular Catalysis A: Chemical, 2006. **249**(1–2): p. 211-217.
36. Yuan, Y., et al., *Supported Au Catalysts Prepared from Au Phosphine Complexes and As-Precipitated Metal Hydroxides: Characterization and Low-Temperature CO Oxidation.* Journal of Catalysis, 1997. **170**(1): p. 191-199.

Chapter 2 XPS

Contents

2.1 Introduction

X-ray photoelectron spectroscopy (XPS) is a powerful technique providing qualitative and quantitative information in surface science analysis. It depends on the interaction between radiation and matter [1]. When a surface is irradiated by X-ray radiation, electrons are ejected from the core shell depending on the radiation energy (Figure 2.1); this ejected electron is referred to as a photoelectron. Other electrons are also ejected in a sequence of steps that results from the creation of the excited state; these are independent of the radiation energy, and called Auger electrons (AES). XPS and AES processes are schematically represented in Figure 2.2. The X-ray photon transfers its energy to a core-level electron leading to photoemission from the *n*-electron initial state (a). The atom, now in an $(n-1)$-electron state, can reorganize by transferring an electron from a higher energy level to the vacant core hole (b). Since the electron in (b) come down to the lower energy state, the atom can reduce its excess energy by ejecting an electron from a higher energy level; this ejected electron is referred to as an Auger electron (c) [2].

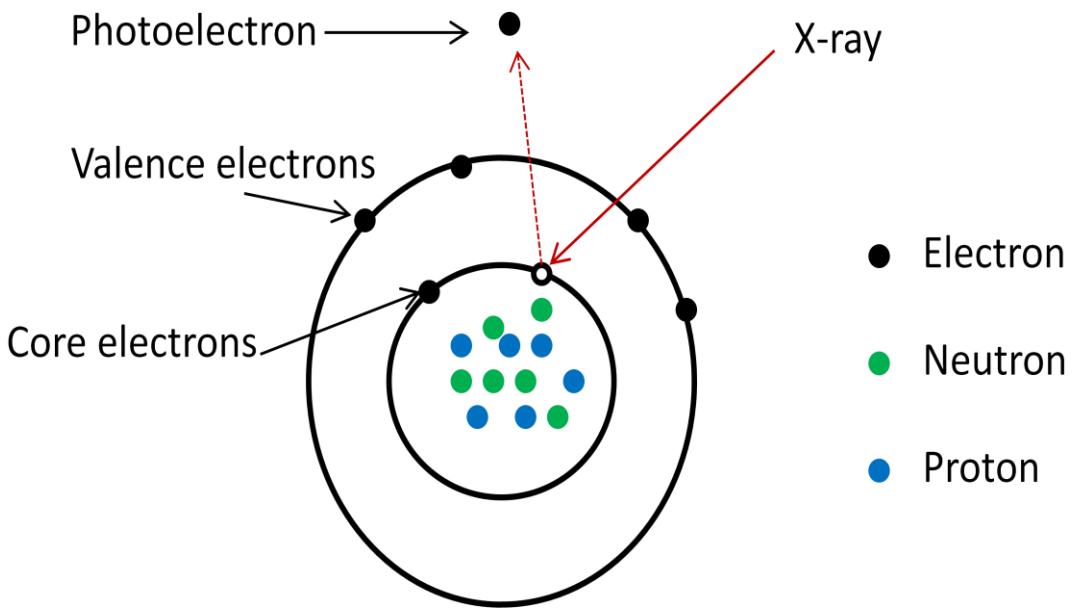

Figure 2.1: Schematic diagram illustrating the interaction of X-ray radiation with surface.

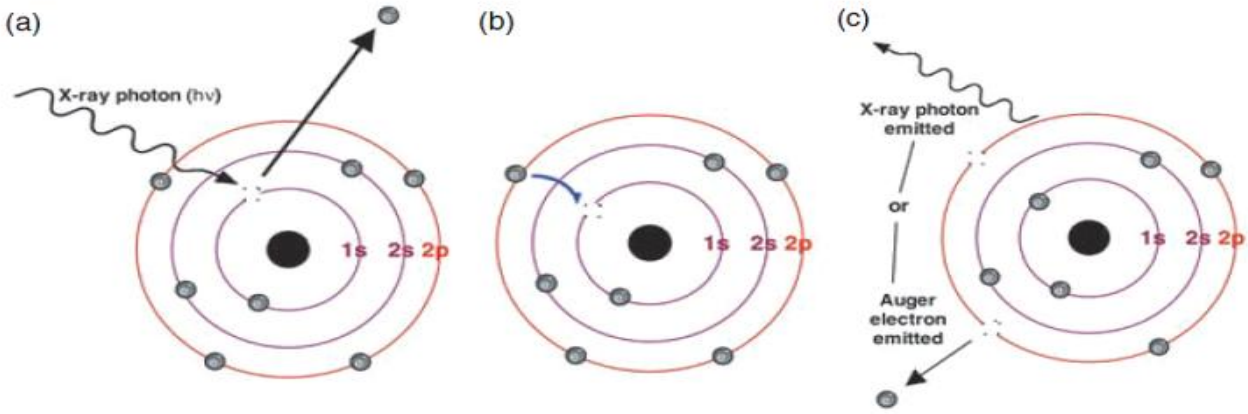

Figure 2.2: schematic diagram represent two processes of ejected of electron from the core level by X-ray radiation. (a) Ejection of a photoelectron by X-ray radiation. (b), and (c) Relaxation of the core-hole by filling with another electron and the ejection of an Auger electron or an X-ray photon (XRF) [2].

2.2 Binding energy

In XPS the kinetic energy (E_k) of the ejected electron is measured. This depends on the energy of radiation (hν) Figure 2.3 (a and b) and the characteristic parameter for the electron, its "binding energy". The relation between these parameters is given by equation 2.1.

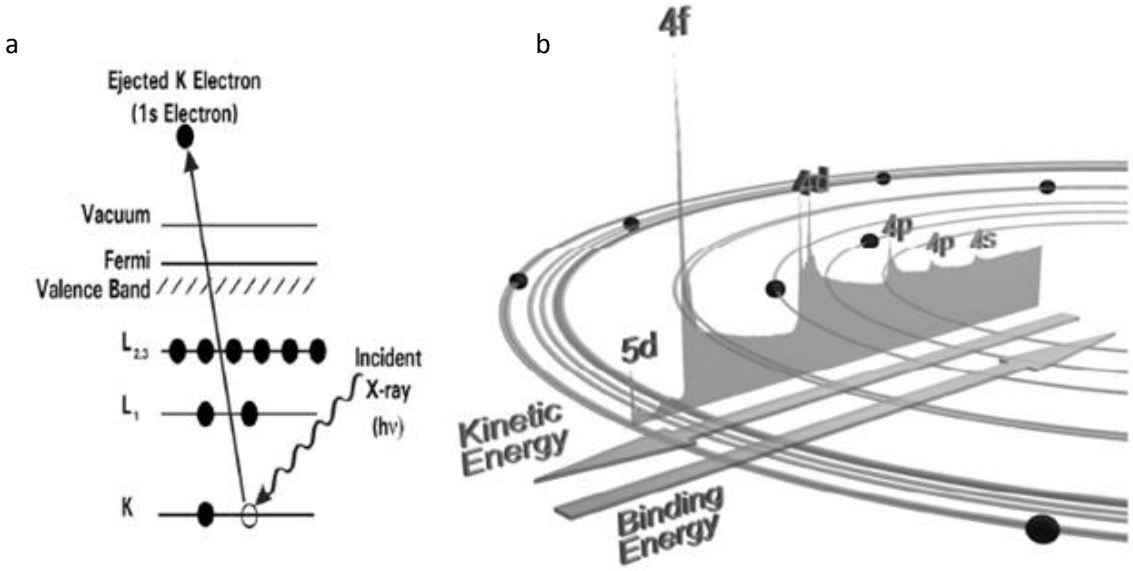

Figure 2.3: (a) interaction of X-ray radiation with core shell electron. (b) The relationship between kinetic energy and binding energy [1].

$$E_B = h\nu - E_K - W \qquad (2.1)$$

Where:

E_B: binding energy.

E_K: kinetic energy.

$h\nu$: radiation energy.

W: work function.

As all three quantities on the right-hand side of the equation 2.1, are known or measurable, it is a simple matter to calculate the binding energy of the electron [1].

2.3 Koopmans' Theorem

The E_B of an electron is describe simply as the difference between an initial state (atom with n electrons) and final state (atom with n-1 electrons) equation 2.2 [3].

$$E_B = E_{final}(n-1) - E_{initial}(n) \qquad (2.2)$$

As Koopmans' Theorem assumes no rearrangement of the electrons in the atom from which the electron was ejected or from the neighbour atoms then the E_B is equal to the negative orbital energy, $-\varepsilon k$ for the ejected photoelectron equation 2.3.

$$E_B \approx -\varepsilon_k \qquad (2.3)$$

The $-\varepsilon_k$ value can be calculated by using Hartree-Fock calculation, but this value has a margin of error about 10-30eV from the real E_B value as seen in Figure 2.4.

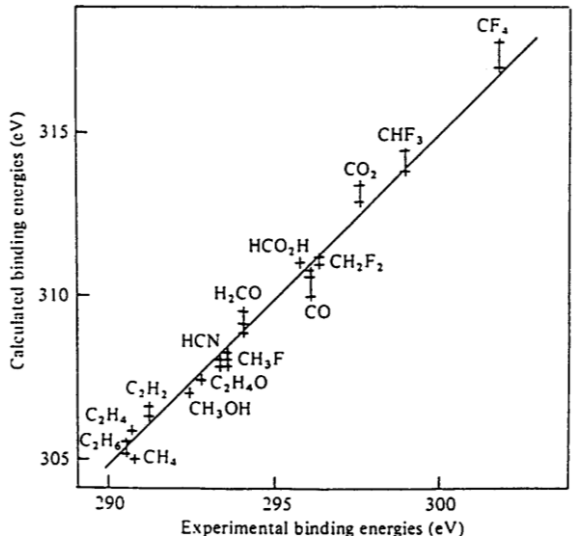

Figure 2.4: Comparison of experimental and calculated C 1s binding energies shows there is difference in about 15 eV between the two values [3].

This discrepancy between the experimental and calculated values is due to relaxation processes in which electrons in the atom which have a core hole and the surrounding atoms adjust to the core-hole and minimise the overall energy. This is a final state effect which Koopmans's Theorem assumes does not take place.

2.4 Initial state effect

The "initial state", is the ground state of the atom. Changing E_B of the atom in the ground state by changing the oxidation state or the chemical environment results in a change in E_B known as "chemical shift". In formal state, E_B increases with increasing oxidation state or by effect of electro negativity of the environment, because it increases the attraction between the positive charge in the atom and electrons [1, 2].

2.5 Final state effects

Relaxation processes in the atom which contains the core hole or in the surrounding atoms causes a lowering of E_B. Relaxation of outer shell electrons has a big effect on the E_B because outer shell electrons have smaller E_B compared with the emitted photoelectron, while the contribution of relaxation of inner shell electrons has a small effect on the E_B because the E_B of inner shell electrons is larger than emitted photoelectrons [1, 2].

2.6 Spectral features

2.6.1 Inelastic background

When a solid sample is exposed to X-ray radiation, three different outcomes for the photoelectron are observed, depending on the distance between the electron and the surface, Figure 2.5. Electrons "near" to the surface can escape from the sample and reach to the analyser without losing energy; these electrons make the main XPS peak. The second possibility is that the electron loses energy but, still reaches the analyser, and these electrons emerge as a background signal. The third possibility is that the electron does not have enough energy to escape from the sample; these do not contribute to the spectrum [1, 2, 4-6].

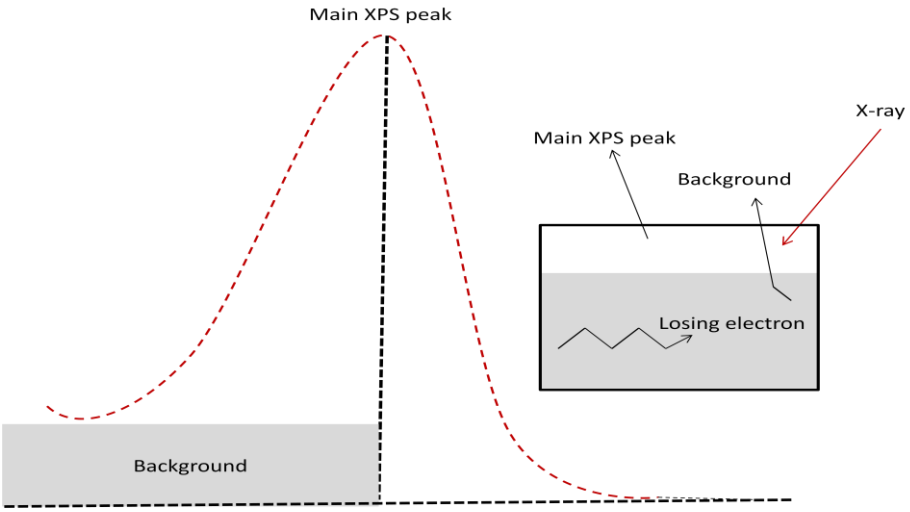

Figure 2.5: Three possibilities of electron behaviour after irradiating the sample X-ray radiation.

2.6.2 Spin-orbit splitting

Due to the spin-orbit coupling between the electron spin and the angular momentum vector of the orbital, peaks p, d, and f appear as doublets whereas the s orbital (orbital angular momentum is zero) appears as a singlet. This interaction between the angular momentum vector (l) and the electron spin (s) can be either parallel or anti-parallel as illustrated in Figure 2.6. In situation of anti-parallel, the interaction is favourable because it has low energy, and it appear at higher E_B, while as in the other type of interaction has high energy and it appear at lower E_B [6].

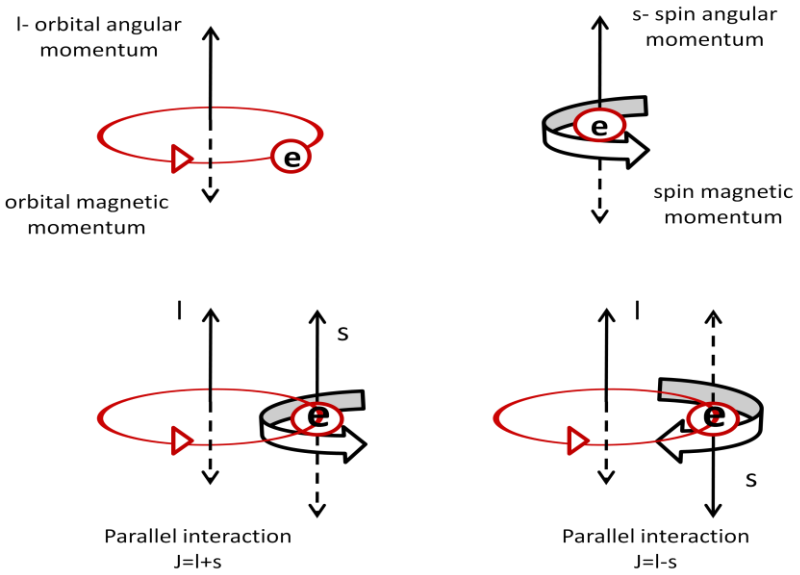

Figure 2.6: Two type of interaction between the angular momentum vector (l) and the electron spin (s).

In the case of Cu2p orbital, the electron spin quantum number (s) = ±½, and the orbital angular momentum quantum number l = 1, so the summation equal the total angular momentum j, which can be either 3/2 (lower E_B) or ½ ((higher E_B) as shown in Figure 2.7. The intensity ratio between the peaks is represented in the degeneracy g which is equal to 2j+1, then the ratio between two peaks 4:2/2 = 2:1 as shown in table 2.1[7].

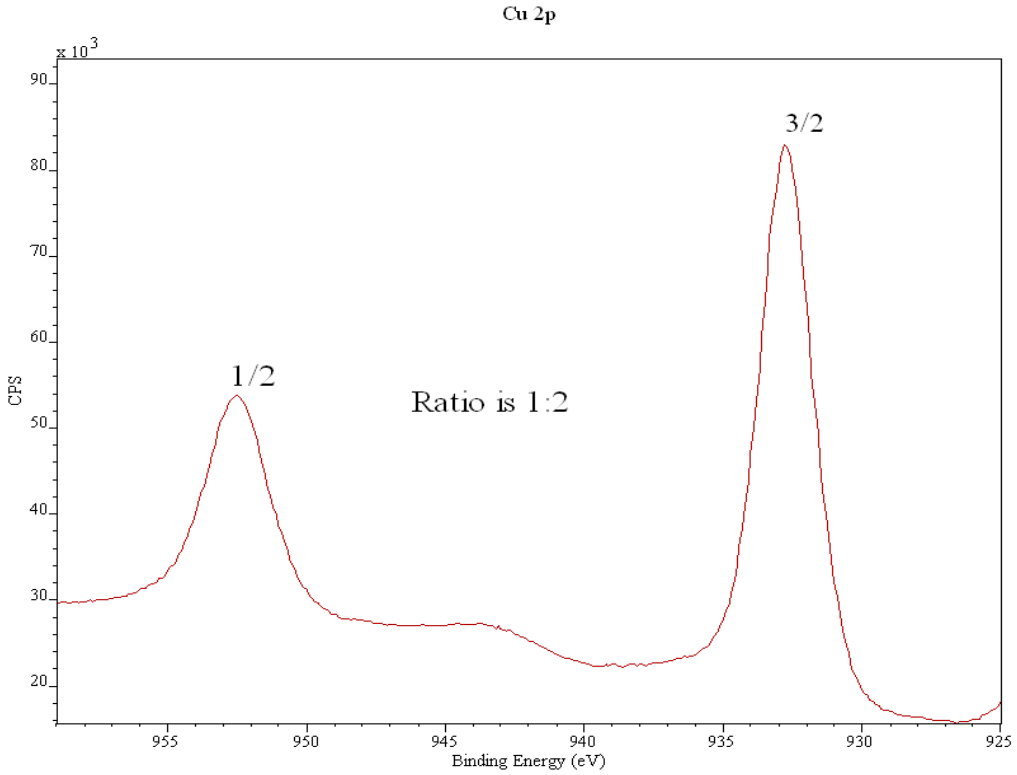

Figure 2.7: XPS spectra of Cu 2p orbital, shows splitting of two peaks 3/2, and ½ with ratio 1:2.

Subshell	Total angular momentum J=(l+s)	Degeneracies g=(2j+1)
S	1/2	
P	1/2, 3/2	1:2
D	3/2,5/2	2:3
f	5/2, 7/2	3:4

Table 2.1: The degeneracy g of different totals angular momentums.

2.6.3 X-ray Satellites

X-ray emission in source depend on x-ray fluorescence process which is producing soft x-rays $K\alpha_{1,2}$ radiation (unresolved doublet) as shown in Figure 2.8. Similar transitions in doubly ionized Mg or Al produce $K\alpha_{3,4}$ lines, So using non-monochromatic source will excite the sample with more than one X-ray line which affected the resolution of XPS spectra by broadening peaks and producing a ghost peak at low E_B. For these reason an aluminium filter is inserted between source and sample to reduce the excess radiation [1, 2].

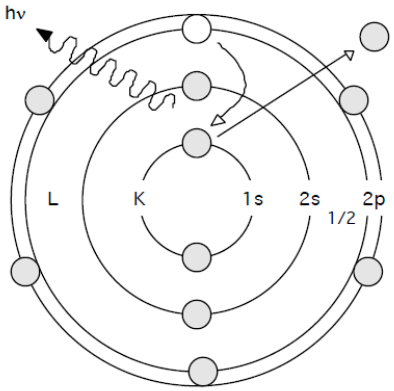

Figure 2.8: Kα1,2 radiation unresolved doublet 2p3/2 to 1s and 2p1/2 to 1s transitions produce soft x-rays.

2.6.4 Auger peaks

Auger peaks are produced in the core-hole relaxation process discussed in section 2.1. We are using the X-ray notation to identify Auger peaks while we use spectroscopic notation to identify XPS peaks. Auger peaks are generally broader and more complex structures than photoemission peaks. The Auger peaks have low energy which is useful for mapping the surface [1].

2.7 Instrument

In XPS we can divide the instrument in two categories; first one is main XPS components (X-ray source, the analyzer, and detector) which form the main structure of the instrument and used in the process of generation of the X-ray radiation and collecting the electrons which are emitted from the sample (Figure 2.9). The second one is requirement environment (Ultra High Vacuum system UHV) and sample processing (such as ion gun, and heating and cooling system). In the present chapter we discusses the main XPS components and leave discussion of the second category to chapter 4.

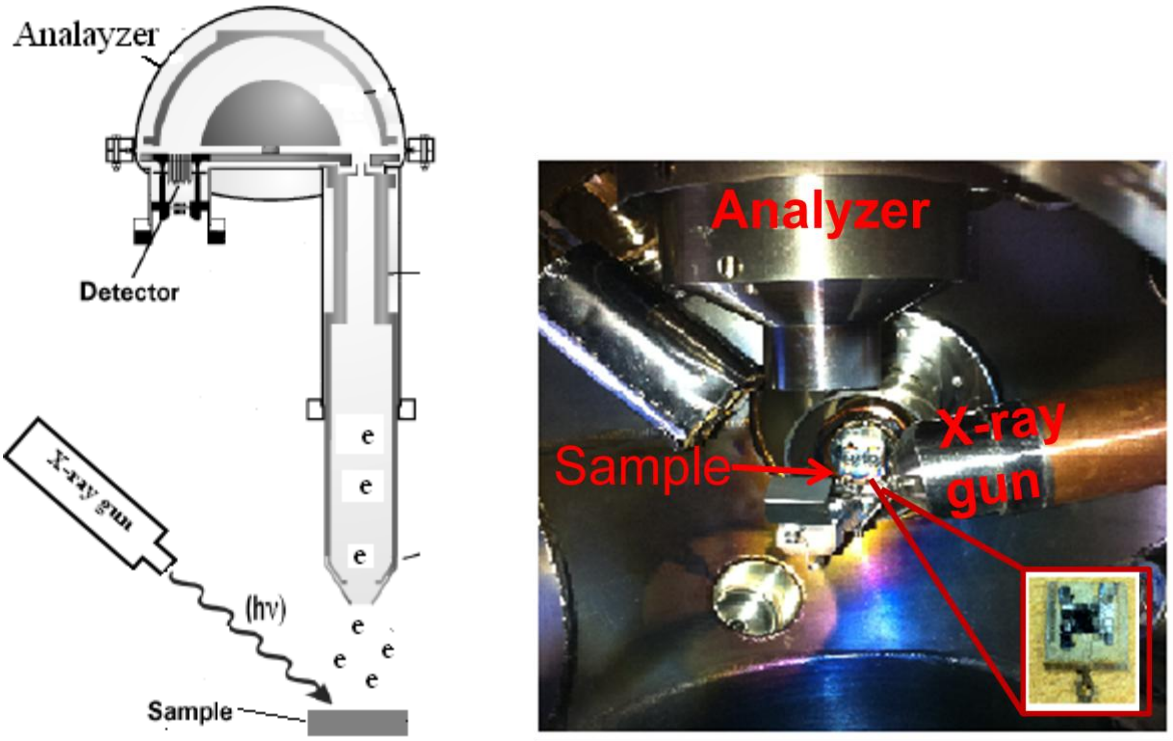

Figure 2.8: Schematic diagram and actual image of the XPS main components (X-ray source, the analyzer, and detector).

2.7.1 X-ray source

The principle of generation of X-ray radiation is by bombarding the anode material by high energy electrons which are emitted from an electrically heated filament (this energy is converted to heat, so the anode usually cooling by water to avoid anode melting or degradation) to create a core hole in the atoms of anode which is following by X-ray fluorescence and emission of electrons. The choice of the anode material depends on the energy of X-ray transition generated, which has to be high enough to eject electrons from the core level of the elements and the natural line width of it has to be narrow to avoid the peak broadening[1, 2, 5]. The most popular anode materials are Al and Mg (both are offered in X-ray dual anode); characteristic emission line of them are listed in table 2.2, this is a specific emission line used because it has high intensity compared with the background emission (Bremsstrahlung) Figure 2.9. Using 2µm thickness Al foil in front of the anode minimizes the effect of the background emission Figure 2.10 [1, 2, 5, 8].

Anode material	Emission line	Energy (eV)	Width (eV)
Mg	Kα	1253.6	0.7
Al	Kα	1486.6	0.85

Table 2.2: Energy, characteristic emission line, and line widths of the Mg, and Al anode materials.

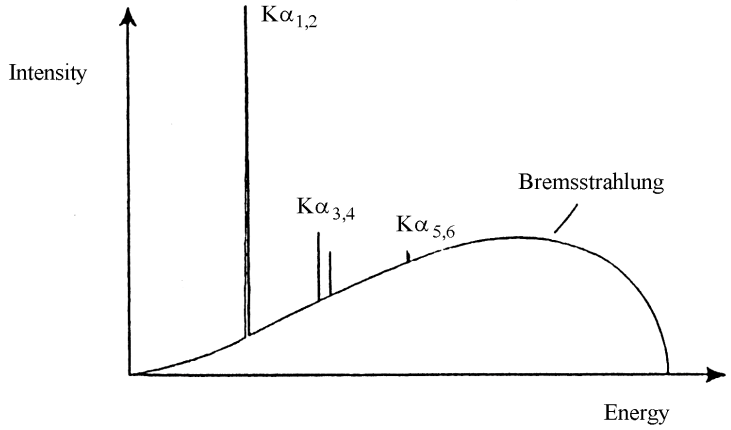

Figure 2.9: X-ray emission spectrum. Main transitions ($K\alpha_i$) are superimposed on the rising Bremsstrahlung background.

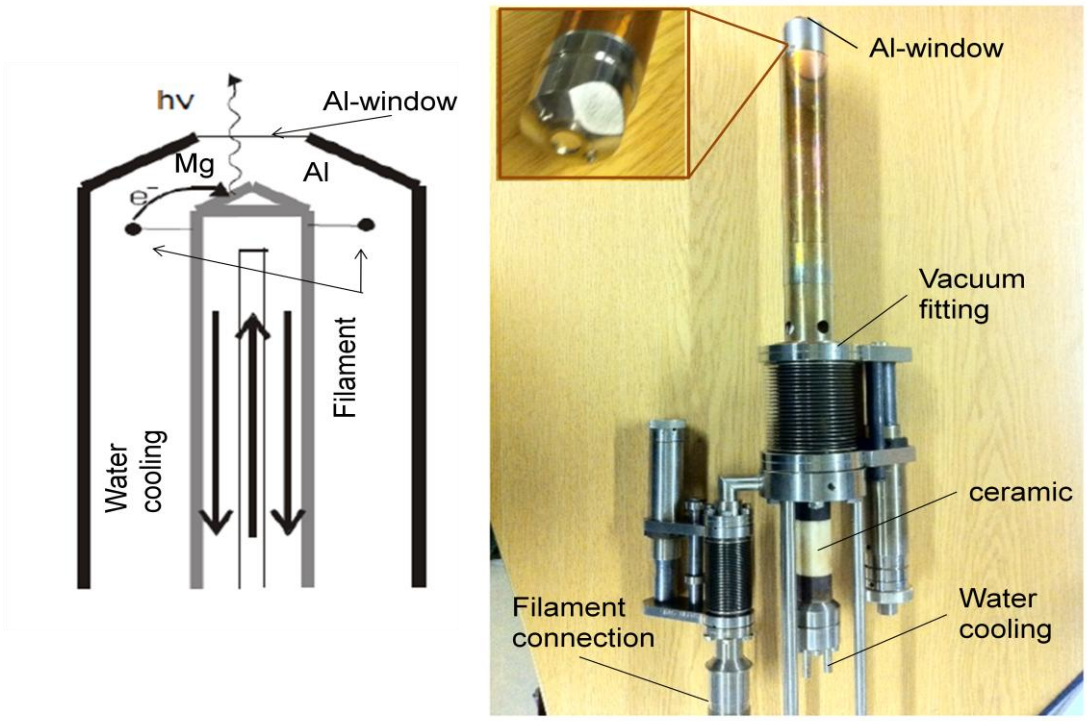

Figure 2.10: schematic diagram and actual image of X-ray source components.

The advantage of using a twin anode is it provides the ability to distinguish between Auger, and XPS peaks, since XPS peaks will move to 233 eV higher in E_K scale when switching between Mg anode to Al anode whereas the Auger peaks remain in the same position because it is not dependent on photon energy.

2.7.2 Analyzer

Three components form the hemispherical analyzer system (collection lenses, the energy analyzer, and the detector) as shown in Figure 2.11. Electrostatic lenses serve a number of purposes such as retarding the electrons which are ejected from the sample to a suitable pass energy of the analyzer, allowing the analyzer to be placed away from the sample to give other instrument components space to access the sample, and maximizing the collecting of photoelectrons from the take off angle of more than 20^o. The energy analyzer consists of two electrodes, the inner side is positive while the outer side is negative, and the space between them is the electron pathway (pass energy) (R_o). The analyzer allows an electron with particular energy to reach the detector as given by equation 2.4; electron with slightly higher or lower energy will not reach the outlet aperture, since the electron with high energy follows the big radius, and the electron with low energy follows the small radius.

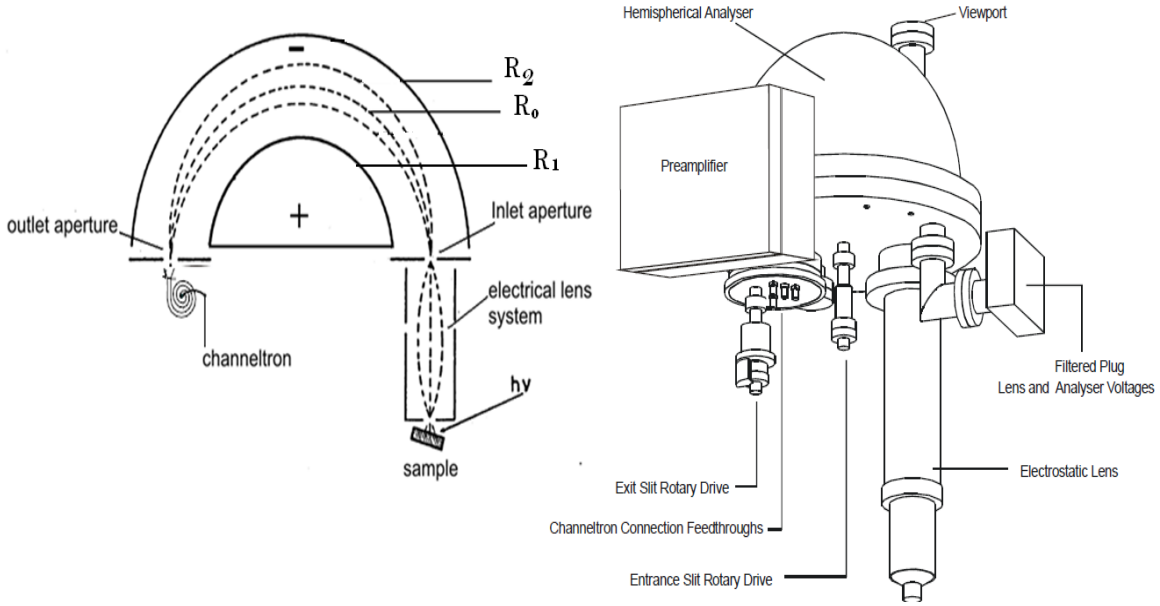

Figure 2.11: schematic diagram of the analyzer system components and the outside view of the analyzer system [9].

$$(E_k) = (e\Delta V)\left(\frac{R_1 R_2}{R_1^2 - R_2^2}\right) \qquad (2.4)$$

Electrons whose energy is too different from the pass energy will hit the outer side of the hemispherical analyzer when it is higher than pass energy and if lower will hit the inner side of the analyzer. Electrons which reach to the outlet aperture are counted by using multichannel electron detector (amplifier), because the number of photoelectrons exiting the analyser is too small to be detected efficiently for spectral analysis. Multichannel electron detector is working by multiplier the electron which is reached to the detector to be suitable to measure as shown in Figure 2.12.

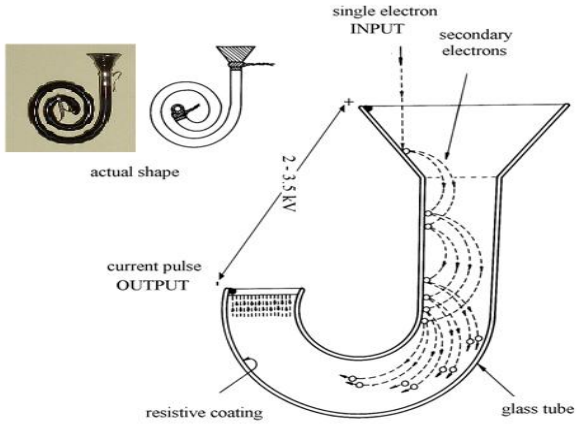

Figure 2.12: schematic diagram of the multichannel electron detector [9].

Secondary electrons are produced inside the multichannel tube due to collision of the single electron arriving from the analyzer with the internal surface coated with a high secondary electron coefficient material (lead oxide), a material that easily produces electrons when excited by photoelectrons. This process is repeated all through the multichannel coil in order to achieve an amplification magnitude of the order 10^8. The resulting signal is recorded by appropriate software as function of kinetic energy.

2.8 Quantification analysis

Quantifying the species present involves the background removal followed by calculating the peak area by using CasaXPS software. The peak area is calculated by integrating the area above the baseline between two chosen points as shown in Figure 2.13. The quantification equation 2.5 which was derived by Madey et al. [9], and modified by Carley and Roberts [10], to include the photoemission cross section (μ), is used to convert the peak area to surface coverage. The equation therefore now takes into account the probability that an

electron is photoemitted from a particular orbital of the particular atom, the value which depends on the size and shape of the orbital and ionising photon energy. The cross section values of both X-ray source Mg Kα, and Al Kα radiation has been tabulated by Schofield [11], relatively to the C1s orbital cross section.

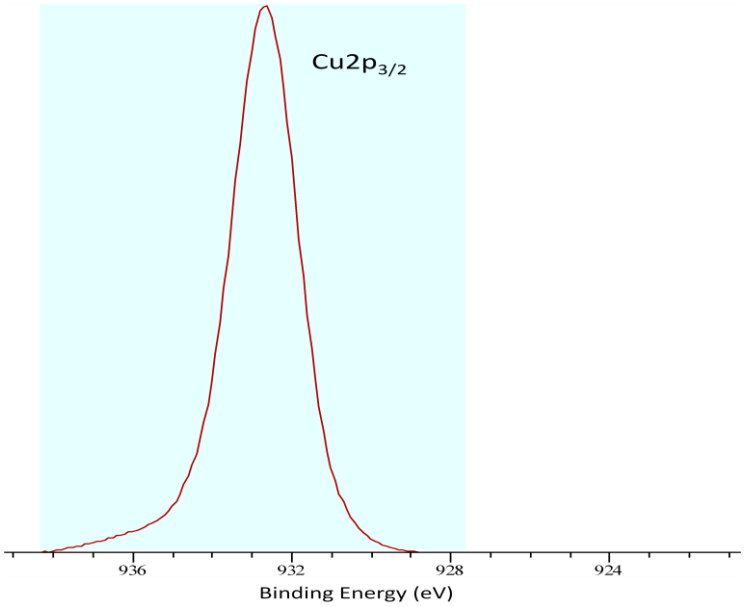

2.13: XP spectra of Cu($2p_{3/2}$) peak showed the way of calculating the peak area by integrating the area under the peak between two chosen points by using CasaXPS software.

$$\sigma_A = \frac{E_{K\,A}}{E_{K\,s}} \times \frac{I_A}{I_S} \times \frac{\mu_A}{\mu_S} \times \frac{N\lambda_S\rho_S cos\emptyset}{M_S} \qquad (2.5)$$

Where:

σ_A= surface coverage or concentration (atoms cm^{-2})

A= adsorbate

S = substrate

E_K = photoelectron kinetic energy

I = intensity of photoelectron peak

μ =photoionisation cross section

N = Avogadro's constant

λ_S = mean free path of photoelectrons within substrate

ρ_S = density of substrate

$\emptyset$ = angle of collection of photoelectrons with respect to the sample normal

M_S = relative atomic mass of substrate

Many of the parameters in the equation 2.5 are constant for particular substrate, and adsorbate, and spectrometer, so the equation 2.5 is simplified to the equation 2.6:

$$\sigma_A = \frac{I_A}{I_S} \times K \qquad (2.6)$$

In most cases the coverage of adsorbate which acquired by XPS is compared to the STM images to obtain a greater understanding of the surface features.

2.9 References

1. Watts, J.F. and J. Wolstenholme, *An Introduction to Surface Analysis by XPS and AES*. 2003: John Wiley & Sons. 212.
2. Vickerman, J.C. and I. Gilmore, *Surface Analysis The Principal and Techniques*. 2nd ed. 2009, Chichester: Wiley. 686.
3. Koopmans, T., *Über die Zuordnung von Wellenfunktionen und Eigenwerten zu den Einzelnen Elektronen Eines Atoms.* Physica, 1934. **1**(1–6): p. 104-113.
4. Walls, J.M., *Methods of Surface Analysis: Techniques and Applications*. 1990, Cambridge/GB: CAMBRIDGE UNIVERSITY PRESS. 352.
5. Heide, P.v.d., *X-ray Photoelectron Spectroscopy: An introduction to Principles and Practices*. 2011 Chichester: John Wiley & Sons. 256.
6. Briggs, D., *Surface Analysis of Polymers by XPS and Static SIMS*, ed. D.R. Clarke, S. Suresh, and I.M. Ward. 1998, Cambridge: CAMBRIDGE UNIVERSITY PRESS. 214.
7. Crist, B.V., *Handbooks of Monochromatic XPS Spectra*. Vol. 1. 1999, California: XPS International, LLC. 511.
8. Hüfner, S., *Photoelectron Spectroscopy: Principles and Applications*. 2nd ed. 1996, Berlin: Springer-Verlag Berlin and Heidelberg GmbH & Co. KG. 530.
9. nanotechnology, O., *EA 125 Energy Analayser*, in *User's Guide*, Omicron, Editor. 2002, Omicron: Taunsstein.
10. Madey, T.E., J.T. Yates Jr, and N.E. Erickson, *ESCA study of fractional monolayer quantities of chemisorbed gases on tungsten.* Chemical Physics Letters, 1973. **19**(4): p. 487-492.
11. Carley, A.F. and M.W. Roberts, *An X-Ray Photoelectron Spectroscopic Study of the Interaction of Oxygen and Nitric Oxide with Aluminium.* Proceedings of the Royal Society of London. A. Mathematical and Physical Sciences, 1978. **363**(1714): p. 403-424.
12. Scofield, J.H., *Hartree-Slater subshell photoionization cross-sections at 1254 and 1487 eV.* Journal of Electron Spectroscopy and Related Phenomena, 1976. **8**(2): p. 129-137.

Chapter 3 STM

Contents

3.1- Introduction

Scanning tunnelling microscopy (STM) is a member of the family of scanning probe microscopy (SPM) techniques. Invented by Binnig and Rohrer in 1982 at IBM laboratories in Zürich, and earning them a Nobel prize in 1986 for the discovery of STM [1, 2]. STM is a powerful technique for studying the surface morphology at the atomic scale [3, 4]. It relies on the concept of quantum tunnelling which is observed when a very sharp conductive tip is brought within a few Ångstroms of a conductive sample and a bias voltage applied between them Figure 3.1.

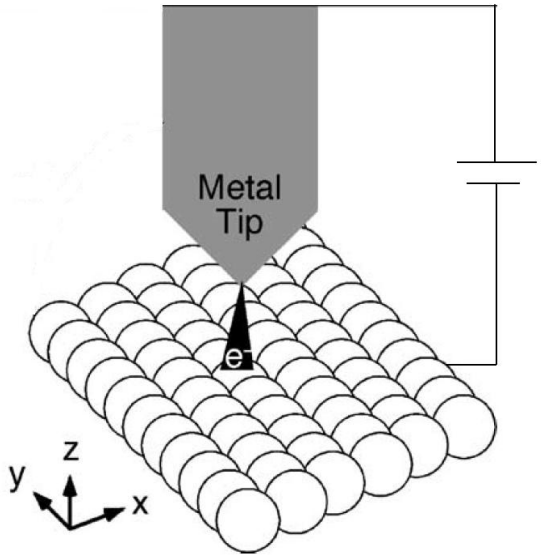

Figure 3.1: Schematic drawing of a scanning tunnelling microscope tip interacting with a surface [5].

3.2 Quantum Tunnelling

Tunnelling is a phenomenon which depends on the wave property of electrons that allows electrons to transfer (tunnel) through the gap between two conductors or semiconductor objects of differing electric potentials when they are brought within a few Ångstroms of each other. Figure 3.2 shows the overlap between the wave function of sample and tip when they are brought to within a certain distance (d) of each other [5]. A measurable current can be achieved by applying a base voltage between tip and sample. The direction of electron flow (tunnel current) depends on the polarity of the electrode; if the tip is negative that means the electrons will flow from the filled energy state of the tip to the empty energy states of the sample. Figure 3-3 shows an energy level diagram of the tip and sample and the direction of electrons where E_F is the highest occupied electron energy level and is called the Fermi level

and φ is the minimum energy required to eject an electron from the Fermi level to vacuum and is called the work function.

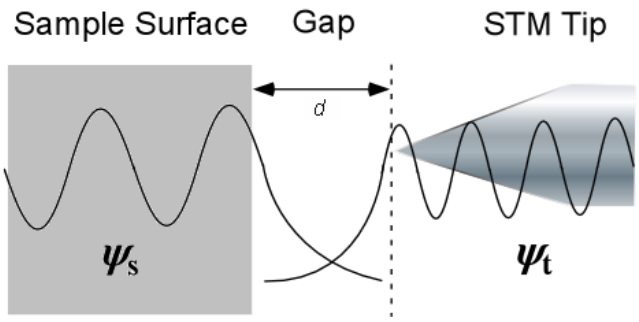

Figure 3.2: Schematic drawing shows the overlapping of electron wave function between tip and sample [5].

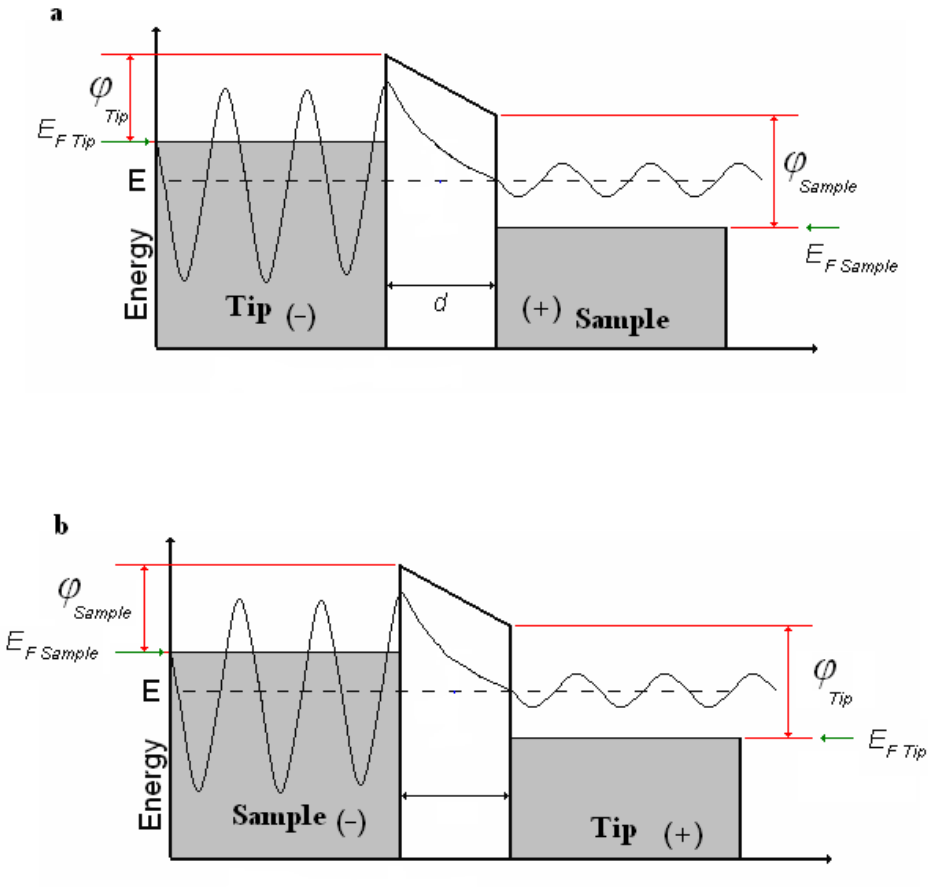

Figure 3.3: Schematic diagrams showing the electron direction flow depending on the base voltage. (a) Electrons flow from the filled energy state of tip to the empty energy state of sample. (b) Electrons flow from the filled energy state of sample to the empty energy state of tip [5].

3.3 Instrumentation

3.3.1 Overview of the Design

The design of the scanning tunnelling microscopy can be divided into three main parts; the first one is the scanner which has a tip, Piezodrive and tunnelling current amplifier. Second is a vibration isolation system. The third part is the data acquisition and processing system. As shown in Figure 3.4.

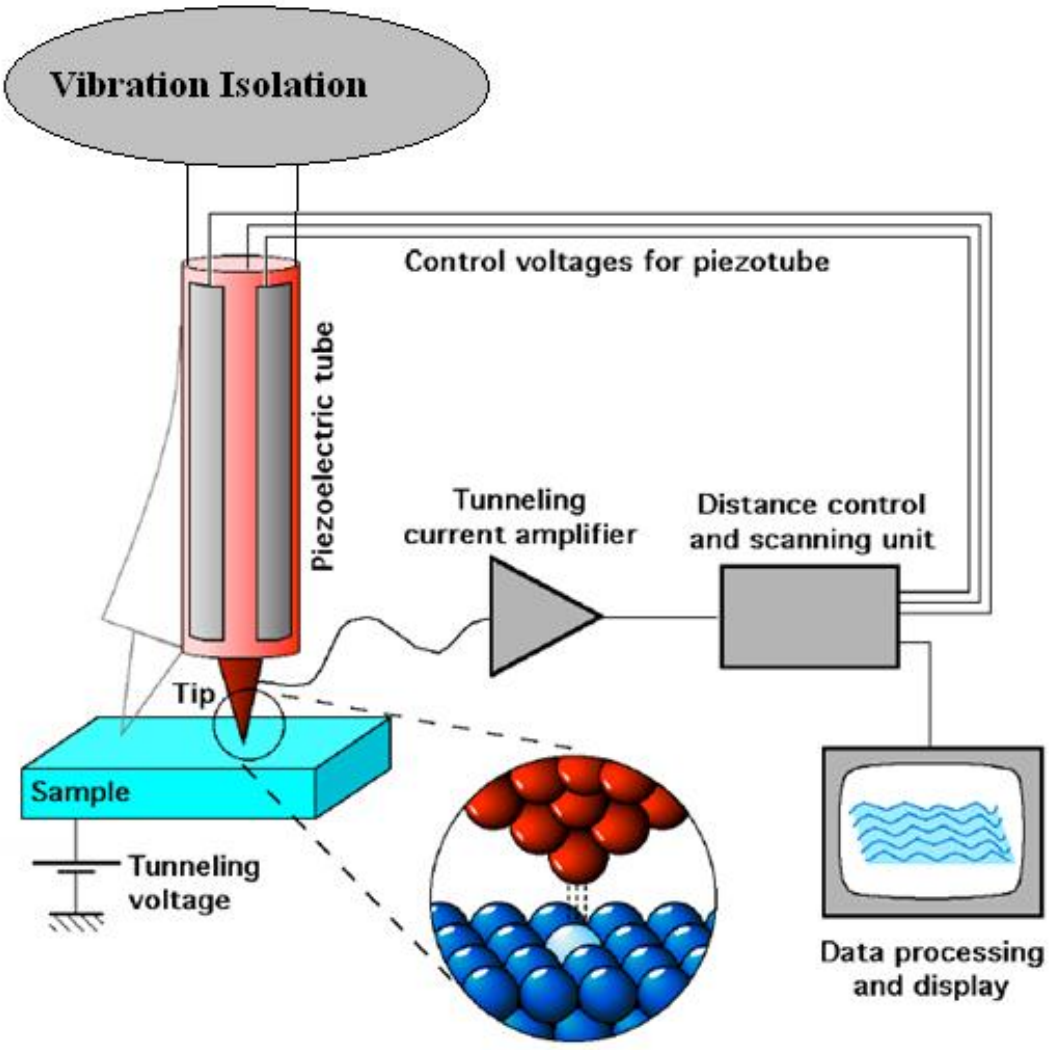

Figure 3.4: Schematic diagram showing the overview design of the STM system [5].

3.3.2 Tip

The main advantage of STM is its ability to image the surface at atomic resolution, and there are different things that can affect the imaging resolution. The most important one is the scanning tip, which should be very sharp (ideally one atom at the top of tip) to achieve such resolution. Electrochemical etching is the most common method of preparation to make such

a tip. Tungsten (W) wire (diameter 0.38mm, and purity 99.9%) supplied by Goodfellow metals. The W wire is surrounded by a tungsten wire ring clamped together by a suitable tip holder the two wires are inserted in 2M NaOH solution and then pulled out to make a bubble within the tungsten ring and around the tungsten wire as shown in figure 3.5. By applying a base voltage between tungsten wire and tungsten rings of about 8.0V it will generate a current through the NaOH(aq) bubble of about 15mA, for 10 – 15min, this current etches the W, and in this way generates two tips at the same time [7].

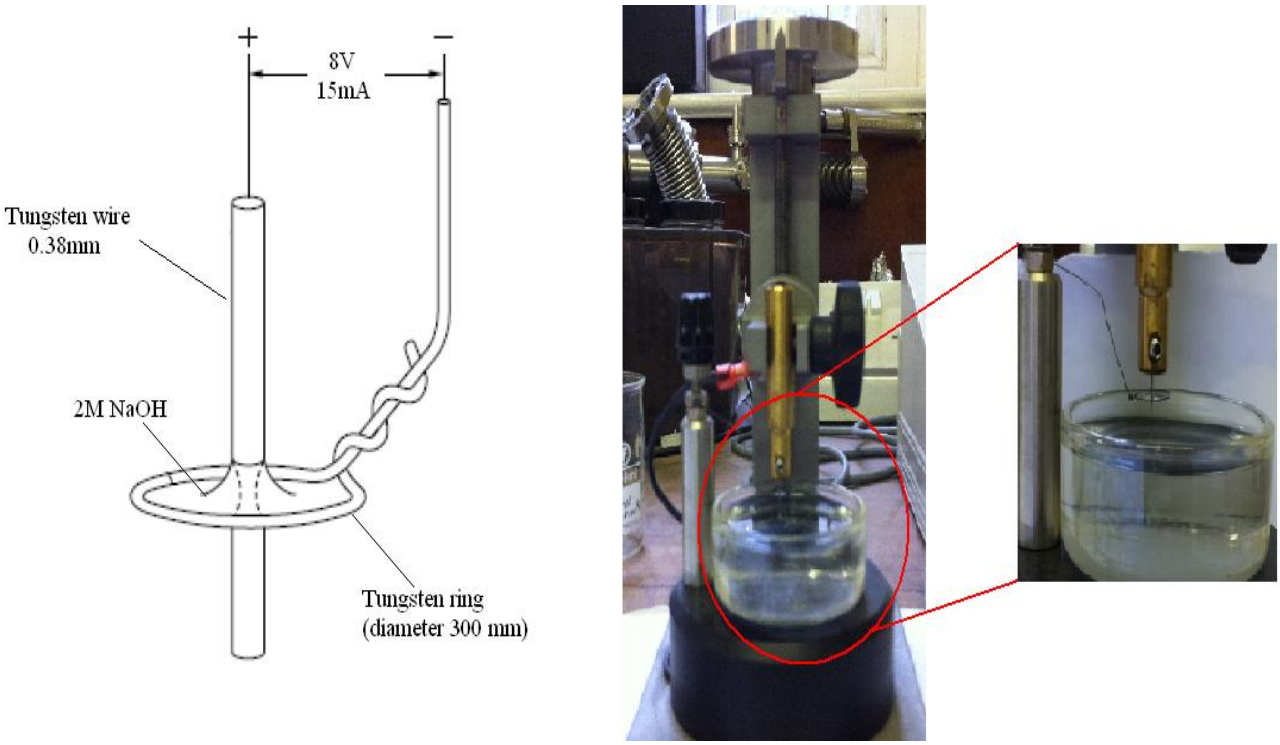

Figure 3.5: Schematic diagram and actual image of the tip etching setup.

The shape of the home made tips was checked using Scanning electron microscopy (SEM) and we found some of the tips are distorted. We think the reason is tip crash when it falls down as shown in Figure 3.6.

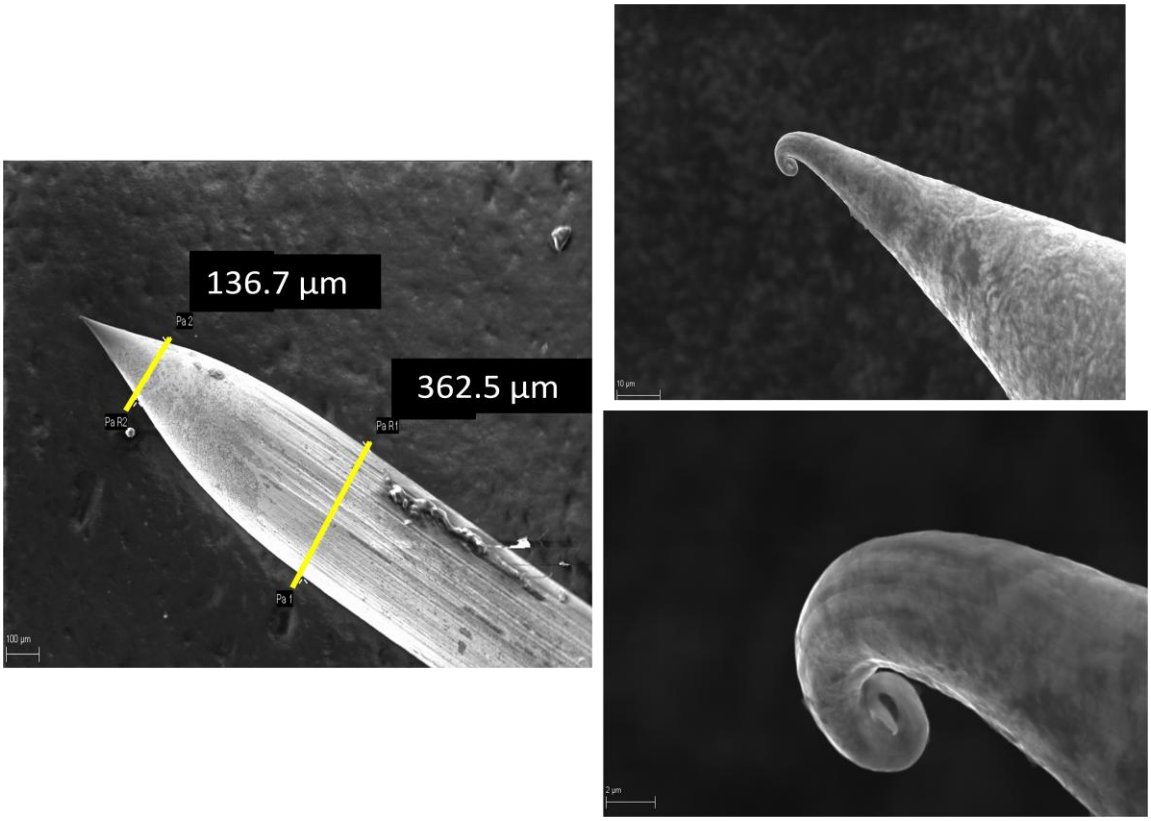

Figure 3.6: SEM image of the crashed tip.

After tip preparation and testing of the tips by (SEM) we made another check inside the spectrometer by trying to get atomic resolution of a standard material like HOPG. The image shown in Figure 3.7 is an example that proves the quality of tips made in this way, and we found the C-C bond length is 1.48Å which agreed with theory distance 1.4 Å [8].

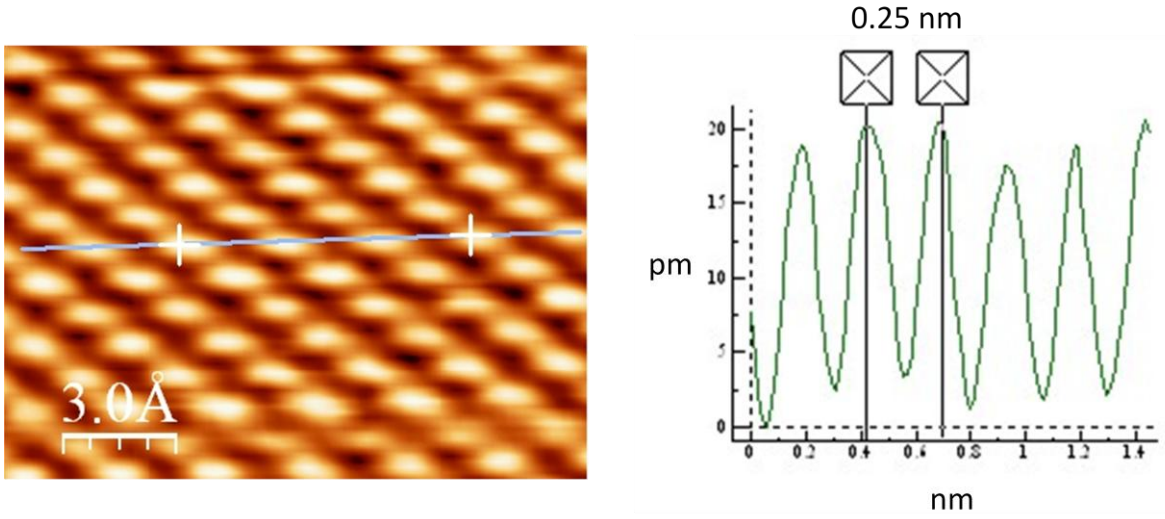

Figure 3.7: The atomic resolution of HOPG at RT, and line profile. C-C-C bond is 2.56 Å.

3.3.3 Piezodrive

The scanner drive is made of a piezoelectric material, which has the ability to change its dimensions when a suitable voltage is applied [9, 10]. The scanner drive tube consists of three independent parts of piezoelectric material (x, y, and z) to give it freedom to move in three directions Figure 3.8.

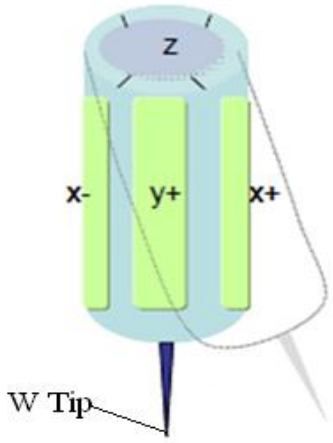

Figure 3.8: Schematic of a tube piezoelectric scanner.

3.3.4 Type of scan

There are classically two ways to scan the STM tip over an area of the surface:

(a) Constant current mode

Constant current mode works by keeping the current constant and changing the gap between the tip and sample surface as shown in figure 3.9. This operation mode is good for imaging a rough surface and gives a nice image for step edges with high accuracy. The disadvantage of this operation mode is in its slow speed [11].

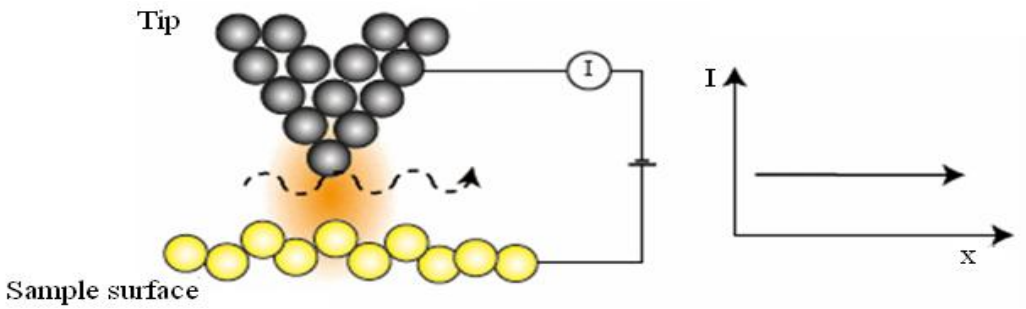

Figure 3.9: Constant current mode [12].

(b) Constant height mode

Constant height mode is faster than the constant current mode because the tip does not have to change position while scanning in the x, and y direction. It is done by keeping the gap between the sample surface and the tip constant and changing the current as shown in figure 3-10. This mode is good for getting good images of atomic resolution but has the limitation of only scanning flat surfaces to avoid tip crash [11].

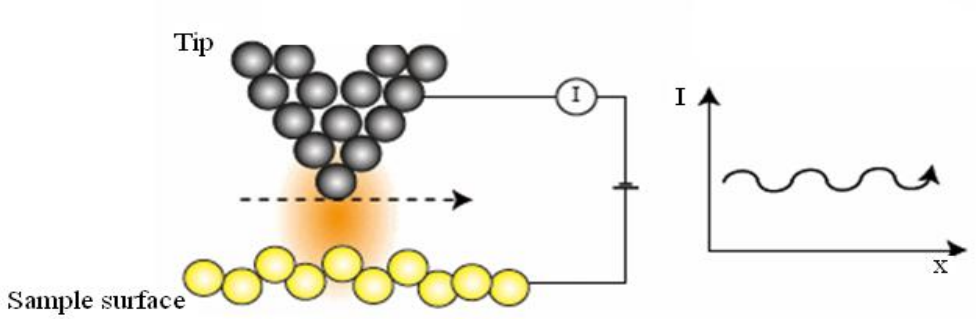

Figure 3.10: Constant height mode [12].

Omicron software has a variable degree of feedback, so the user can change scanning mode depending on the area to be scanned.

3.3.5 Vibration isolation

The Omicron VT STM uses four springs to carry the base platform to isolate the surrounding vibration. This platform is also surrounded by copper fins centred between magnets, to prevent the platform motion using eddy current damping as shown in figure 3-11. The sample surface is pointing to the bottom when it is transferred to the STM sample stage, and the tip approach is from beneath 3.12. The big ‘’coarse approach’’ up to tens of microns is watched by CCD-camera. After that the very ‘’fine approach’’, to find electron tunnelling, choose the scanning area, and choose the voltage and current are done automatically by using Scala software version (4.1) software. Some data were acquired using the updated ‘’Matrix’’ software. The image processing was done using WSxM software [13] to enhance the understanding of the surface or to represent the 3D image-display.

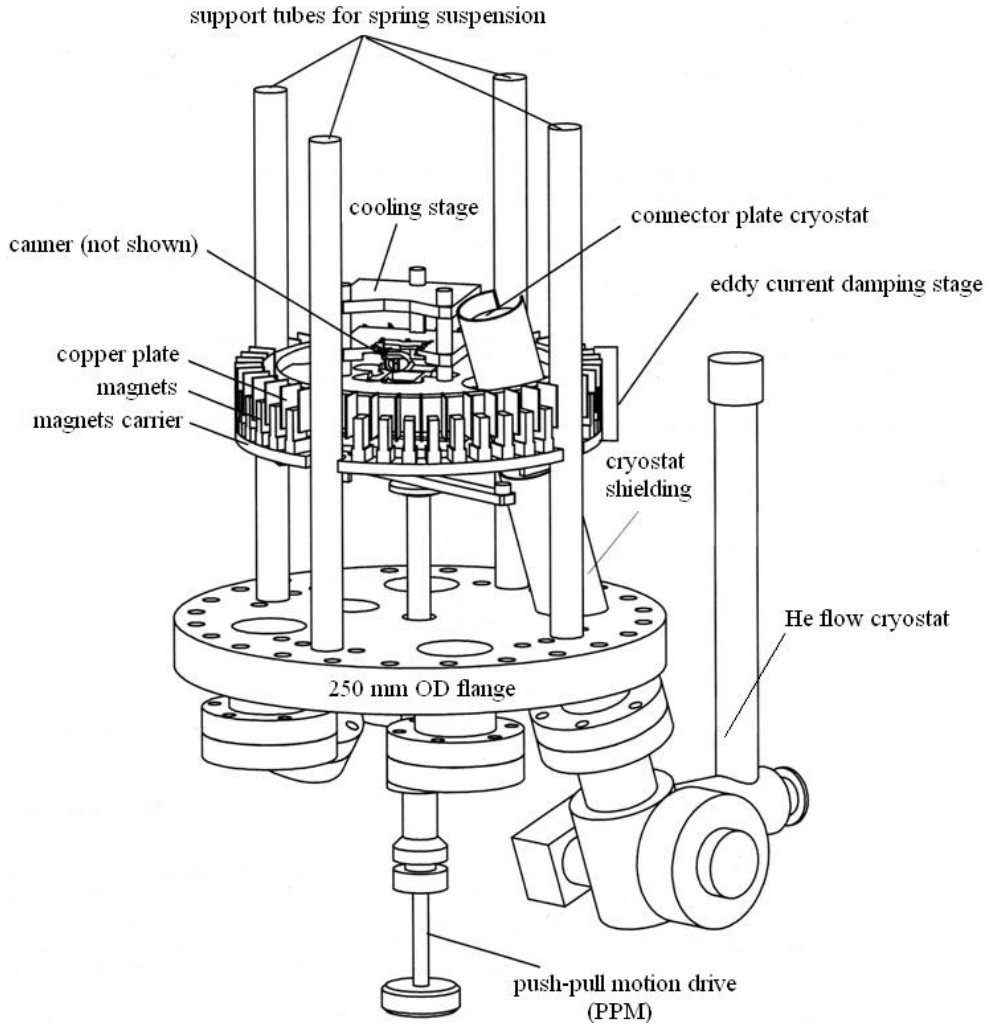

Figure 3.11: Side view of Omicron VT STM [14].

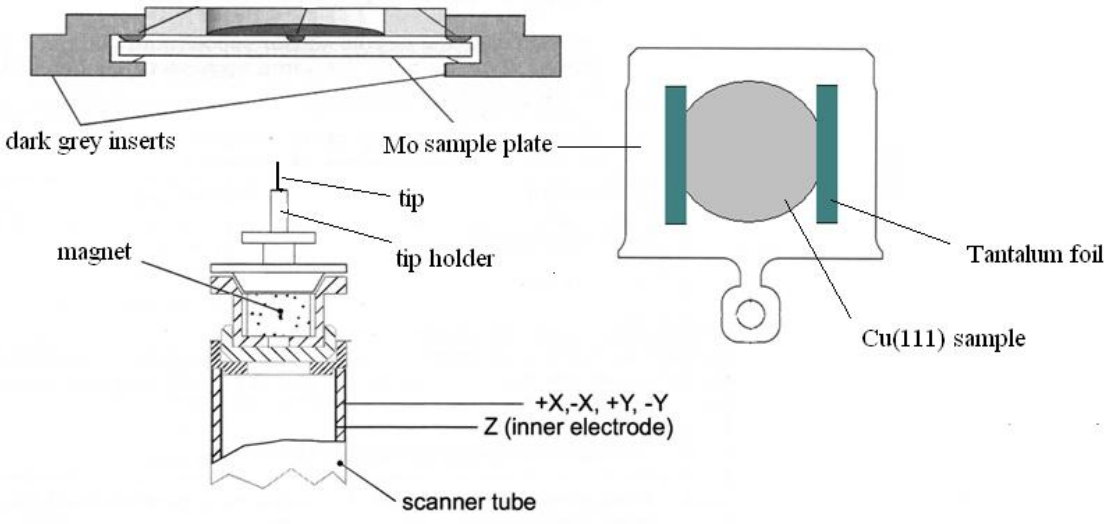

Figure 3.12: Side view of Omicron VT STM scanner and down face of sample plate [14].

3.4 References

1. Binnig, G. and H. Rohrer, *SCANNING TUNNELING MICROSCOPY*. Helvetica Physica Acta, 1982. **55**(6): p. 726-735.
2. Binnig, G. and H. Rohrer, *Scanning tunneling microscopy*. Surface Science, 1985. **152–153, Part 1**(0): p. 17-26.
3. Brune, D., et al., *Surface Characterization*. 2008, Weinhemi: John Wiley & Sons 715.
4. Vickerman, J.C. and I. Gilmore, *Surface Analysis The Principal and Techniques*. 2nd ed. 2009, Chichester: Wiley. 686.
5. British, U.o. *The Scanning Tunneling Microscope*. 2012; Available from: http://www.stm.phas.ubc.ca/Science/Introduction-to-STM.html.
6. J. M. Walls, R.S., *Surface Science Techniques*. 1994 Amsterdam: Elsevier Science & Technology. 188.
7. Tiedje, T., et al., *Tip contamination effects in ambient pressure scanning tunneling microscopy imaging of graphite.* Journal of Vacuum Science & Technology A: Vacuum, Surfaces, and Films, 1988. **6**(2): p. 372-375.
8. Tandon, D., et al., *Surface topography of oxidized HOPG by scanning tunneling microscopy.* Carbon, 1997. **35**(1): p. 35-44.
9. Binnig, G. and D.P.E. Smith, *Single-tube three-dimensional scanner for scanning tunneling microscopy.* Review of Scientific Instruments, 1986. **57**(8): p. 1688-1689.
10. Hammiche, A., et al., *The Surrey STM: Construction, development, and evaluation of a scanning tunneling microscope.* Review of Scientific Instruments, 1991. **62**(12): p. 3010-3021.
11. Bonnell, D.A., *Scanning Tunneling Microscopy and Spectroscopy: Theory, Techniques and Applications*. 2001, New York: John Wiley and Sons Ltd. 436.
12. Horcas, I., et al., *WSXM: A software for scanning probe microscopy and a tool for nanotechnology*. Review of Scientific Instruments, 2007. **78**(1): p. 013705-8.

Chapter 4 UHV

Contents

4.1 The ultra high vacuum system (UHV) systems

4.1.1 Main overview

All of the work described in this thesis has been done in one custom built ultra high vacuum systems (UHV), supplied by Omicron Nanotechnology. The system consists of two main chambers (XPS and STM) as shown in Figure 4.1. The XPS camber contains an ion gun (cold cathode), fast entry lock, gold evaporator, XPS analyzer, ion gauge leak valve, and manipulator for transfer of the sample between two chambers, and rotation of the sample to a suitable angle (for sputtering, XPS, and evaporation), and heating. The XPS chamber is pumped by rotary, turbo, Ion, and TSP pumps. The system is controlled by a main control tower as shown in Figure 4.2.

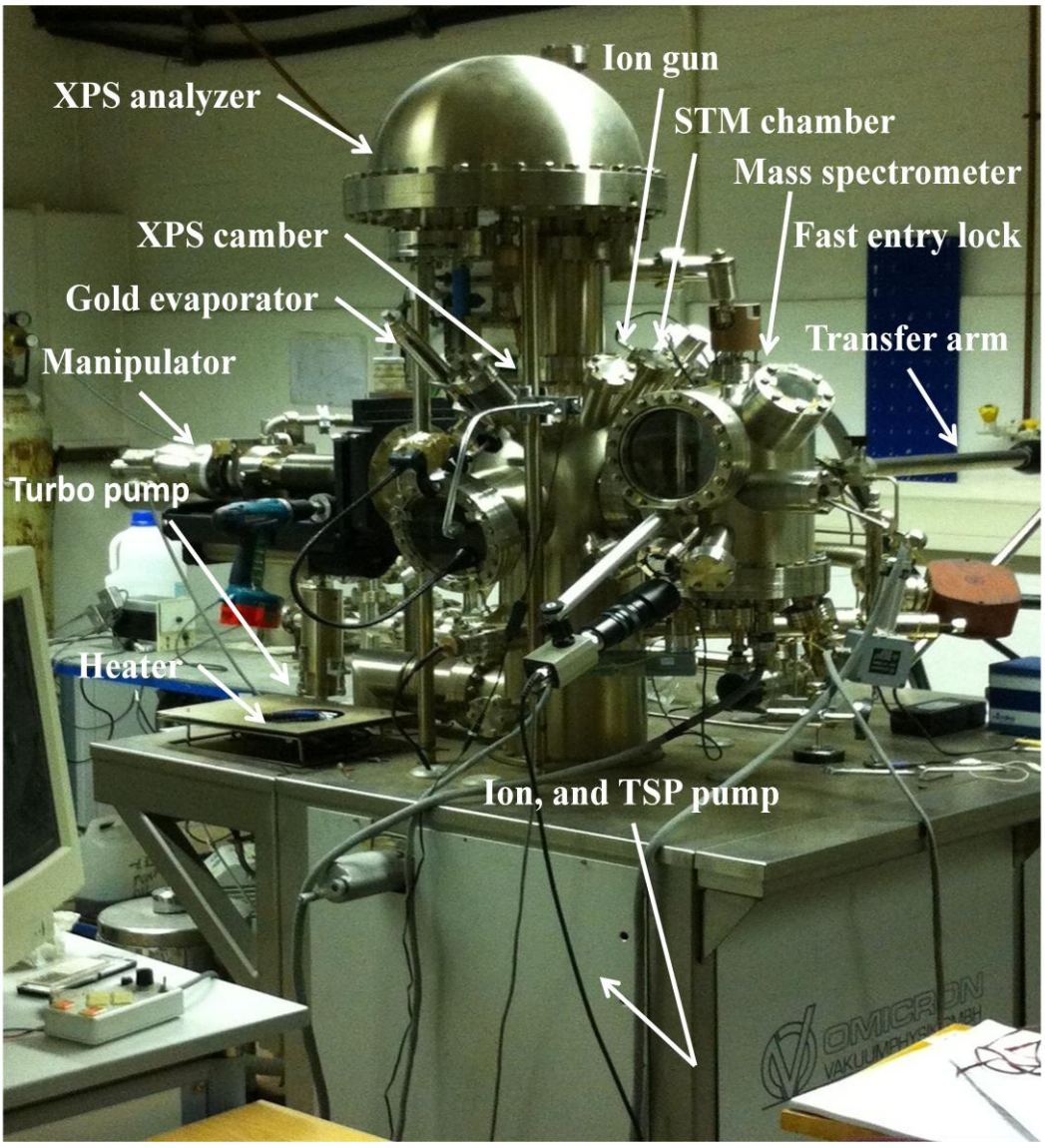

Figure 4.1: Omicron multiprobe UHV system.

Figure 4.2: Control towers of the UHV system

4.1.2 The need for UHV system

A vacuum environment is an essential requirement for most surface science analysis techniques with different requirements of vacuum level [1-3] for three main reasons. First, to increase the mean free path of electrons and ions which are used in surface analysis. By decreasing the pressure of the system, the electrons or ions can travel to the analyzer without collision with gas molecules inside the system. A base pressure of 10^{-6} mbar is enough to give a mean free path of molecular gas of many meters. The mean free path of the gaseous molecule is given by:

$$\lambda = \frac{k\ (m^2 Kg\ s^{-2}K^{-1}) \times T(K)}{\sqrt{2}\pi d^2(m) \times p(Kg\ m^{-1}s^{-2})} \qquad (4.1)$$

Where:

k: Boltzmann constant

T: Temperature in Kelvin

d: Molecular diameter

p: Pressure in Pascal

The second reason for using a vacuum system is to reduce the rate of contamination of the surface during the analysis time. The frequency (Z) of gas molecules colliding with the surface in a time dt is given by:

$$Z = \frac{p(Kg\ m\ s^{-2} cm^{-2})}{\sqrt{2\pi \times M(kg) \times k(Kg\ m^2\ s^2\ K^{-1}) \times T(K)}} \quad cm^{-2}\ s^{-1} \qquad (4.2)$$

Where:

k: Boltzmann constant

k: Pressure

T: Temperature in Kelvin

M: Molecular mass

So at P =1x10^{-6} mbar and T= 300 K, the typical number of molecules colliding with the surface is:

Molecule	M	Z/cm^{-2} s^{-1}
O_2	28	2.91x10^{14}
CO	32	2.71x10^{14}
CO_2	44	2.31x10^{14}

The rate of coverage of certain surface by gas molecules is given by

$$\text{Rate of coverage} = \frac{\text{The frequency } (Z) \text{ of gas molecules colliding with the surface}}{number\ of\ atoms\ in\ the\ unit\ area\ (cm^{-2})\ in\ one\ monolayer} \quad ML^{-1}\ s^{-1} \quad (4.3)$$

For example in case of coverage of the surface (the atomic density of the surface ~10^{15} cm^{-2}) with CO_2 at P =1x10^{-6} mbar, and T= 300 K, assuming all the gas molecules stick on the surface (sticking coefficient = 1), the coverage is:

$$\text{Rate of coverage} = \frac{2.3 \times 10^{14}\ cm^{-2}\ s^{-1}}{10^{15}\ cm^{-2}\ ML^{-1}} = 0.23\ ML\ s^{-1} \quad (3.4)$$

So the time required to cover one monolayer is:

$$\frac{1\ ML}{0.23\ ML\ s^{-1}} = 4.4\ s \qquad (3.5)$$

Which means at 1x10^{-9} mbar, and T= 300 K the surface will be fully covered by CO_2 after 1.2 hours.

The third reason for using a vacuum system in surface science analysis techniques is to avoid the glow discharge in case of using the high voltage equipment.

Different degrees of vacuum have been classified depending on the base pressure used as shown in the following table [3]:

Degree of vacuum	Pressure range
Low Vacuum	atmospheric pressure to 1 mbar
Medium Vacuum	1 mbar to 10^{-3} mbar
High Vacuum (HV)	10^{-3} mbar to 10^{-7} mbar
Ultra High Vacuum (UHV)	10^{-7} mbar to 10^{-10} mbar
Extra High Vacuum (EHV)	Less than 10^{-10} mbar

4.2 Achieving the UHV condition

In order to achieve UHV conditions, the system requires different types of vacuum pumps (mechanical pump, entrapment pump) and thermal treatment (bake the system to degas the vacuum equipment) depending on the degree of vacuum required [4-6].

4.2.1 Mechanical pump

These pumps work by transferring the gas molecule from the system chamber (low pressure area) to the atmospheric side (high pressure area) either by producing the imbalance in the pressure by periodically increasing and decreasing the chamber volume, or by transferring the gas molecules from the high pressure area to the low pressure area while as the chamber volume is constant [3].

4.2.1.1 Rotary pump

The most commonly used pumps for all basic vacuum applications are classified as mechanical pumps [3-6]. It is used for creating a vacuum environment from atmospheric pressure down to 10^{-2} mbar, also used as backing pumps for other high-vacuum gas transfer pumps such as turbo-molecular and diffusion pumps. It works by periodically increasing and decreasing the chamber volume by inserting the gas molecules into the pump chamber from the inlet port and then trapping the gas molecule between the rotary vane and the pump body as shown in Figure 4.3. Then the trapped gas is transferred toward the discharge port due the rotation of the rotary vane while increasing the gas pressure to more than atmospheric

pressure causing the exhaust valve to open and expel the gas molecules. The oil used in the rotary pumps works as a lubricant and sealant. The main problem of the rotary pump is condensation of the pumped material which has gas vapour such as H_2O and other solvents due to the compression process inside the pump. This condensation could lead to the formation of an emulsion by mixing the oil with liquid vapour which decreases the pump efficiency. The vibration of the pump is a secondary disadvantage as well especially when using techniques such as scanning probe microscopy.

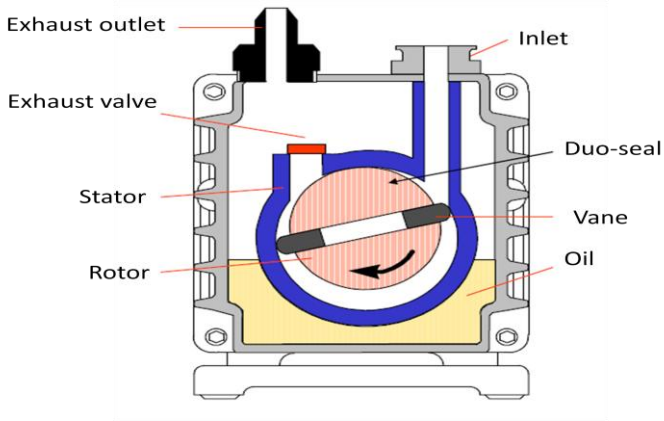

Figure 4.3: Schematic diagram shown the components and the working principle of the rotary pump [3].

4.2.1.2 Turbo molecular pump

One of the most commonly used pumps to create the UHV environment is classified under the mechanical pumps. It works by transferring the gas molecule from the high pressure area to a low pressure area while as the chamber volume is constant, producing the vacuum degree between 10^{-3} to 10^{-9} mbar [3-6]. The pump consists of a many very high-speed rotor vanes, each of these vanes has a multiple blade as shown in Figure 4.4. The blade is designed at an angle shaped to lead the movement of the gas molecules towards the next vane until it leaves the pump body and evacuated by the rotary pump. One of the advantages of the turbo pump, besides creating a good vacuum environment, is that the pump is oil free which means there is no back stream of oil into the vacuum system, in contrast to the rotary, and diffusion pumps. Several disadvantages of the turbo molecular pump can be summarised in the following two points:

1- Expensive purchase and fixing.

2- Vibrations which affect the scanning probe microscopy work.

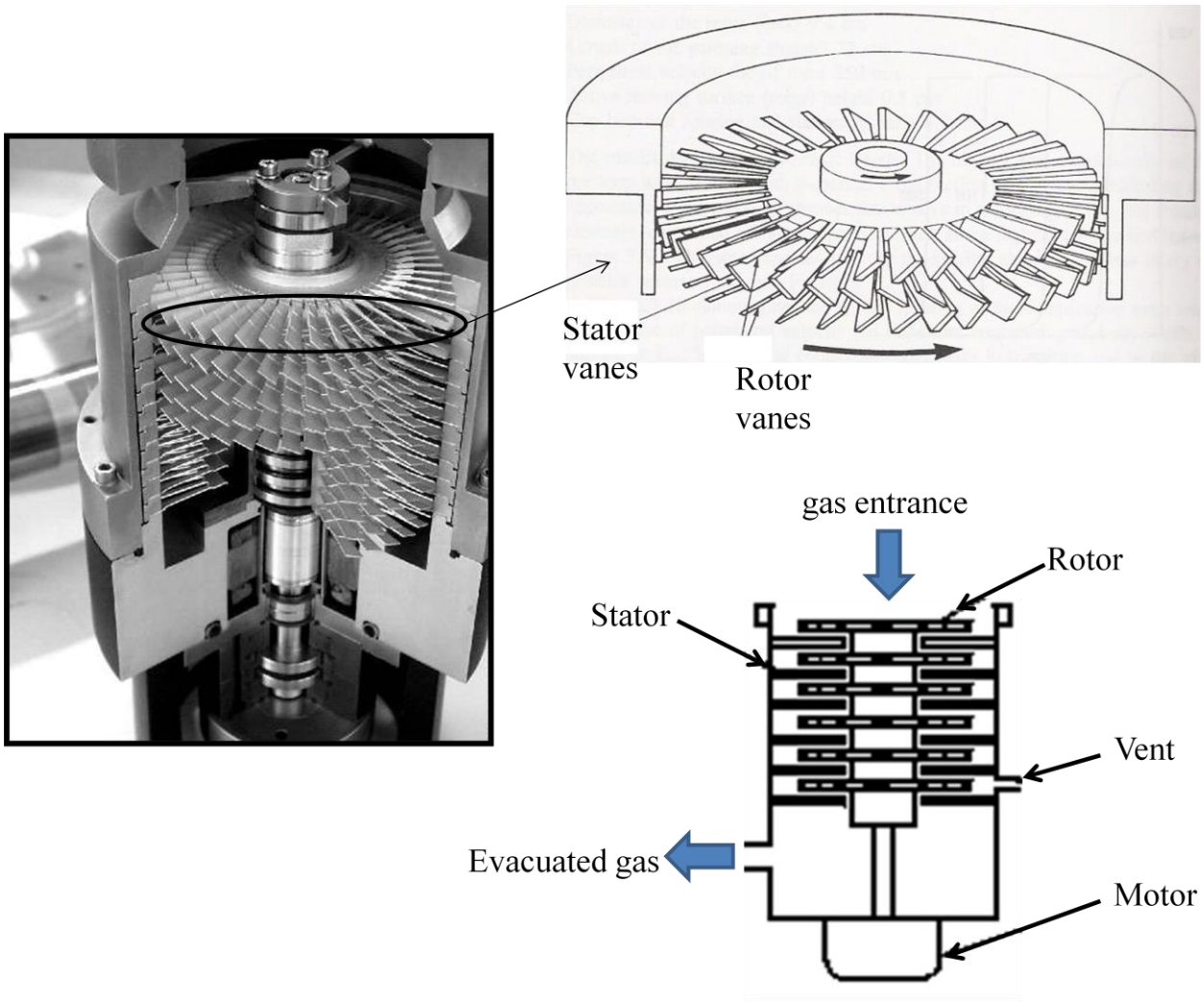

Figure 4.4: Schematic diagram showing the components and the working principle of the turbo molecular pump [4, 6].

4.2.2 Entrapment pump

These pumps work by adsorption or absorption of the gas molecules on the solid surface of the container which is often a part of the pumped system.

4.2.2.1 Ion pump

The ion pump is one of the primary pumps for UHV since it was commercialised by Varian in the late 1950s. It works to create a vacuum degree from 10^{-7} to 10^{-11} mbar by ionisation of the gas molecules by plasma discharge which is produced by applying a high voltage (7 kV) between an anode and cathode [3-6]. The gaseous molecules collide with electrons in the anodic tube leading to the formation of a positive gas molecule which is forced to leave the

anodic tube toward the cathode plate by a high magnetic field as shown in Figure 4.5. Ion pumps are characterised by long lives and, the most important advantage, is a vibration free pump which make it suitable for scanning probe microscopy work. The disadvantages of the ion pump can be summarised in the following two points:

1- It has a memory effect (it can be reduced by baking the system).

2- Does not pump inert gases such as He, and Ar.

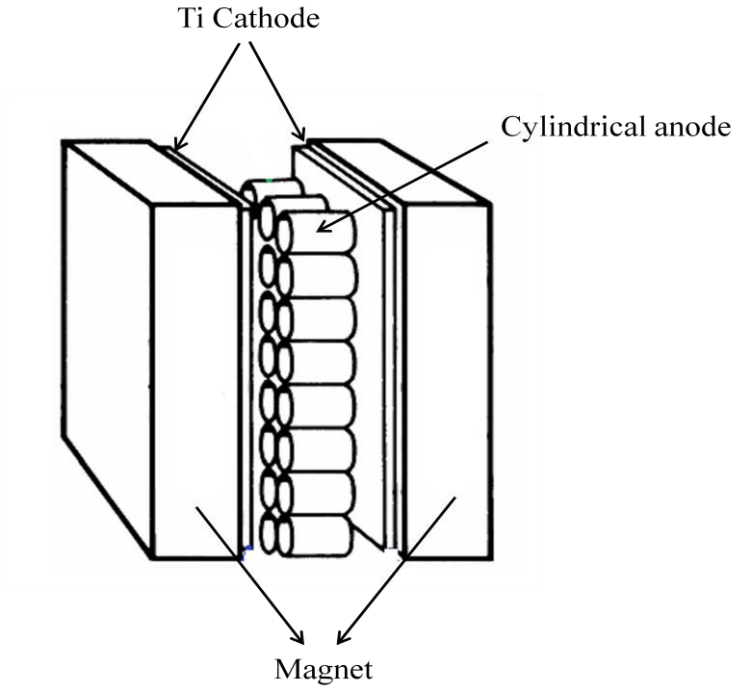

Figure 4.5: Schematic diagram showing the components of the ion pump [3].

4.2.2.2 Titanium sublimation pump TSB

Titanium sublimation pump (TSP) is formed by filament of Ti alloy which sublimes the Ti atoms in the chamber by passing an electrical current through it as shown in Figure 4.6 [3-6]. Active gas molecules such as oxygen and nitrogen hit the Ti film leading to their burial in the film by making a non-volatile compound so it is classified as an entrapment pump. However the TSP is never used as the only type of pump in the UHV system so it is included inside the ion pump to enhance the pumping efficiency from 10^{-10} to 10^{-12} mbar.

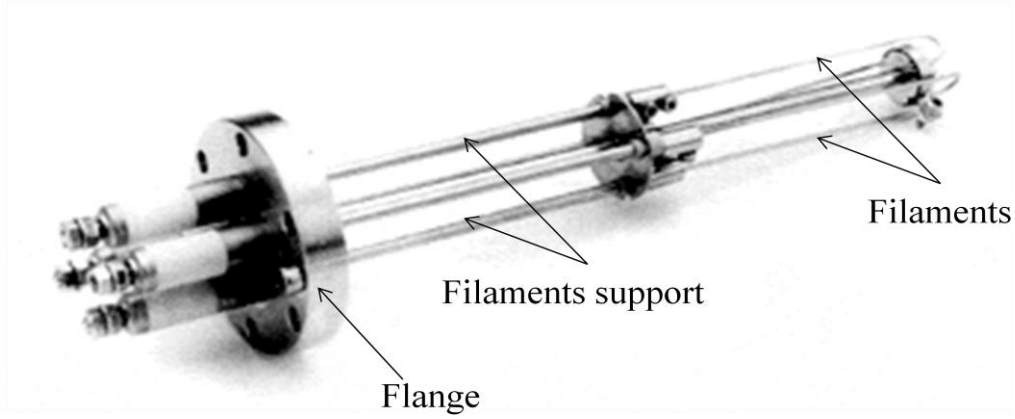

Figure 4.6: Real image showing the components of the TSP.

4.2.3 Bakeout and degas

Bakeout is a necessary step to help the system to reach UHV condition after every time it is opened up to air or after the first installation of the vacuum equipment. The bakeout step is done by heating the system up to 150 ^{o}C for several hours depending on the system condition (in our case 48 hours at least). Degassing the filament (XPS source, ion gauge, and sample heater) is usually preformed after bakeout to improve the pressure and prevent of contamination the sample during analysis.

4.3 Pressure measurements

In order to measuring the pressure, the Omicron multiprobe UHV system which was used in this study contains Pirani gauge, ion gauge, and residual gas analyser depending on the vacuum degree.

4.3.1 Pirani gauge

The Pirani gauge is positioned in the back line of the turbo molecular pump, and it works on the principle of heat transfer [4-6]. The resistance of the W filament inside the vacuum system heated by used the Wheatstone bridge is used to determine the pressure. The temperature of the W filament decreases as a result of collisions with the gas molecules inside the vacuum system leading to a decrease in its resistance whereas the applied voltage through the Wheatstone bridge is constant. So the Pirani gauge actually is measuring the produced electrical current in the Wheatstone bridge as function of changing the pressure inside the vacuum system. The Pirani gauge works in the vacuum degree from atmospheric to 10^{-3} mbar.

4.3.2 Ion gauge

The ion gauge is used to measuring pressures less than 10^{-3} to 10^{-12} mbar and is positioned in the main vacuum chamber. The ion gauge consists of three main parts; the filament (cathode), the grid (anode), and the ion collector as shown in Figure 4.7(a). Heating the filament leads to emission of electrons which are accelerated toward the grid. The gas molecules inside the grid are ionised as a result of collision with accelerated electrons and sequentially collected at the collector as shown in Figure 4.7(b). The produced current at the collector is directly proportional to the pressure of the gas molecules in the chamber. Bakeout and degassing of the ion gauge before use is an important step to reduce of production of H_2, CO, and CO_2 [4-6].

4.3.3 Residual gas analyser

The residual gas analyser is used to measure the pressure inside the UHV system, check on the gas purity, and act as a leak detector. It consists of three main parts; filament (ion source), quadrupole mass filter (two positive, and negative bars) producing a magnetic filed, and ion collector as shown in Figure 4.8 [3]. The gas molecules inside the vacuum system hit the filament which leads to ionisation and then accelerated inside the quadrupole region. Interaction of gas ion with magnetic field works as an ion separation system while the ion collector measuring the producing current depending on the ion mass [4-6].

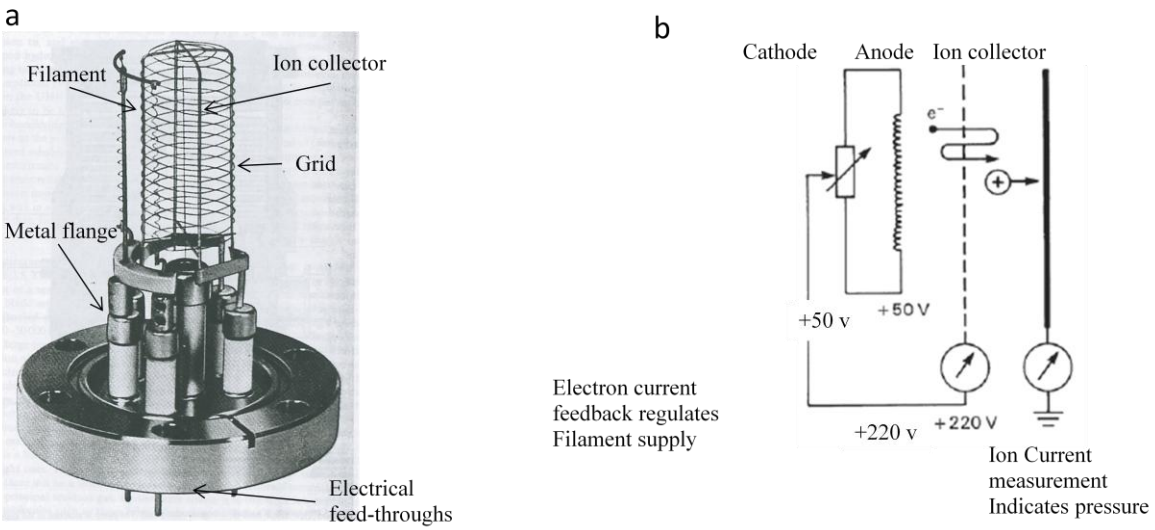

Figure 4.7: (a) Real image of ion gauge, (b) schematic diagram showing the principal of ion gauge [3].

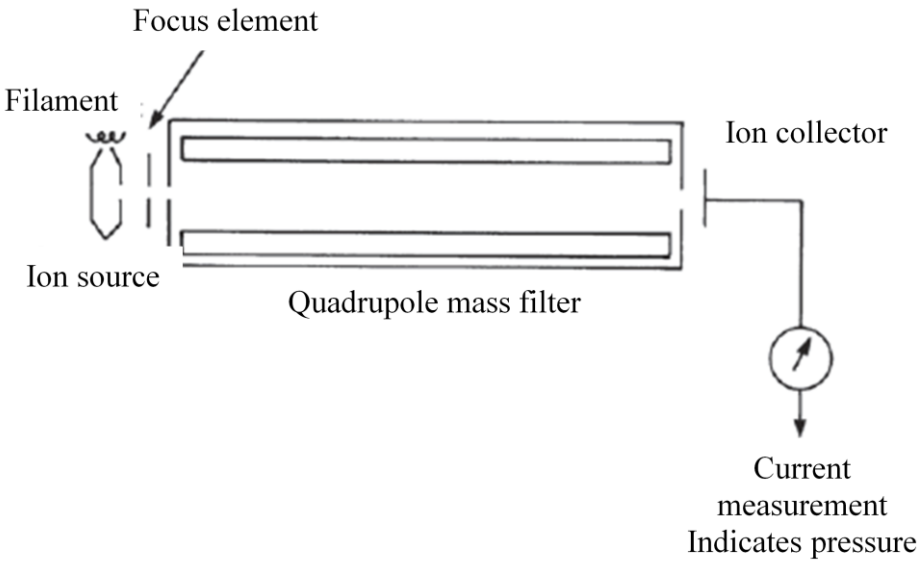

Figure 4.8: Schematic diagram illustrated the residual gases analyser components [3].

4.4 Sample processing

Sample processing includes polishing and mounting, transfer into the UHV system, and cleaning inside the UHV system.

4.4.1 Polishing the sample

The Cu(111), and Cu(100) single-crystals were mechanically polished with diamond spray, with a final grade of 0.25 μm to get a final mirror surface, then the sample was glued on the Mo plate using a conductive adhesive and fixed in place using a Ta foil as shown in Figure 4.9.

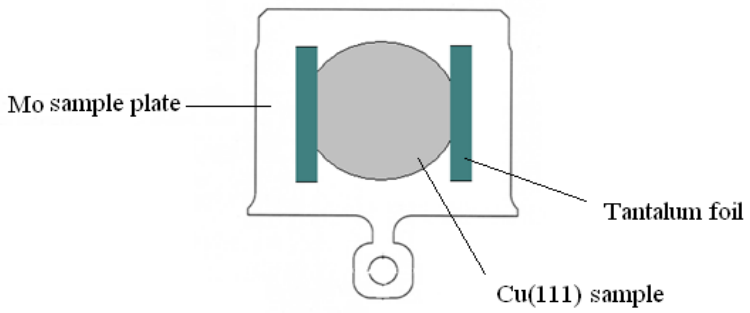

Figure 4.9: Copper sample mounting top of the Mo plate.

4.4.2 Transferring the sample to UHV and in situ cleaning

The copper sample mounted in the Mo plate is deposited in the fast entry lock chamber which is isolated from the main chamber by a valve. Then that fast entry lock chamber is pumped down by turbo molecular pump overnight (8 hour at least) while the main chamber is pumped down by the ion pump. The sample is transferred to the manipulator in the main chamber using the magnetic rod shown in Figure 4.10. Degassing the sample inside the UHV system was the first step of cleaning the sample. Then repeated cycles of sputtering (P_{Ar} = 5x 10^{-5} mbar, 1.0 kV, 5 A sample current) and annealing at 500 ^{o}C were applied at the sample. Sputtering involve bombardment of the sample surface by high energy Ar^{+} to physically remove contaminations of the sample by breaking their bond to the substrate and then pumped in the UHV system. Annealing the sample up to 500 ^{o}C lead segregation of the impurities from the bulk to the surface which made removing them by sputtering easier. The last step after cleaning cycles (from 5 to 7 cycles) is annealing to remove the effect of sputtering (rough surface) and to desorb the Ar atoms which might be embedded in the substrate. For transferring the sample from the manipulator to either storage carousel, or STM stage the wobble stick was used.

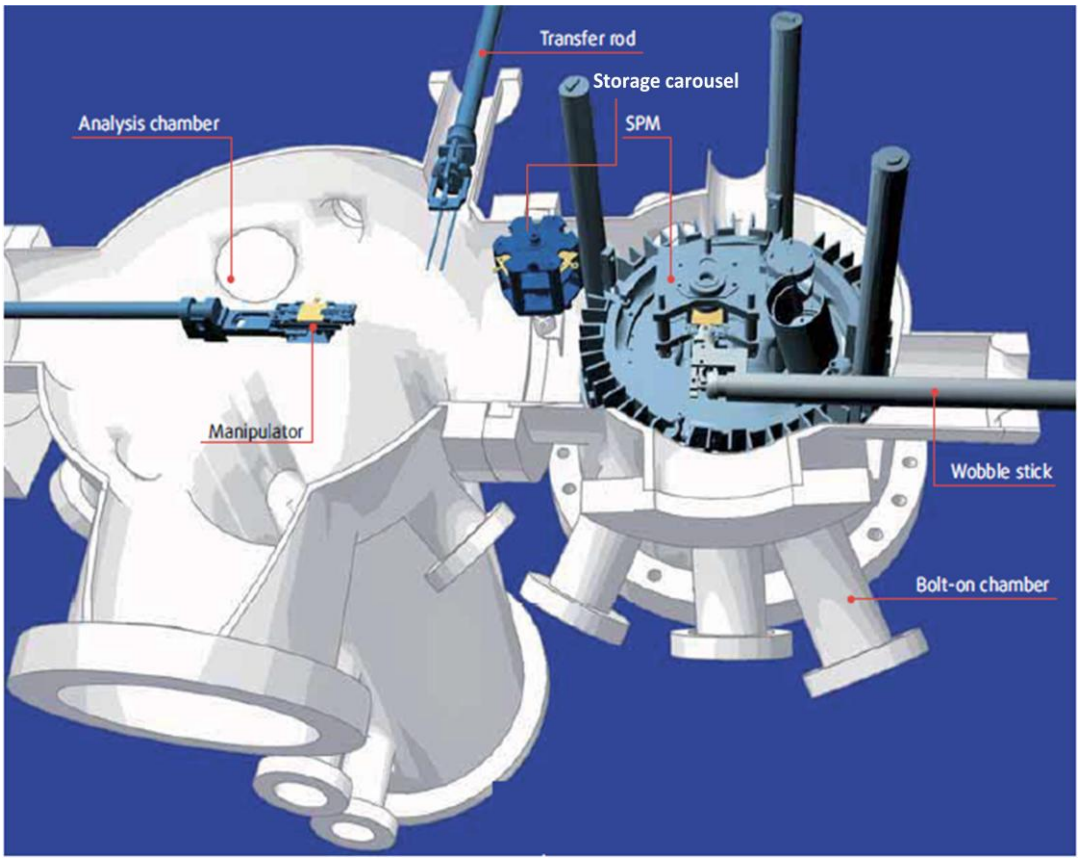

Figure 3.10: 3D model shown the sample transferring inside the UHV system.

4.5 Gold evaporator

A home made gold evaporator consisting of a tungsten filament, pure gold charge attached to the filament, and Ta shield is shown in 4.11. The gold ball is produced by heating the rolled up gold wire around W filament to a pressure about 10^{-6} mbar. Subsequently the gold evaporator is taken off the UHV system and the Ta shield mounted. The shield is added to prevent the gold atoms covering the other vacuum components. The distance between the sample and the evaporator is a few millimetres. After bake out, the gold evaporator is normally degassed at a current more than the usual current used in the experiment to remove all the contamination. The degas procedure is also undertaken every time before using the gold evaporator in experiment.

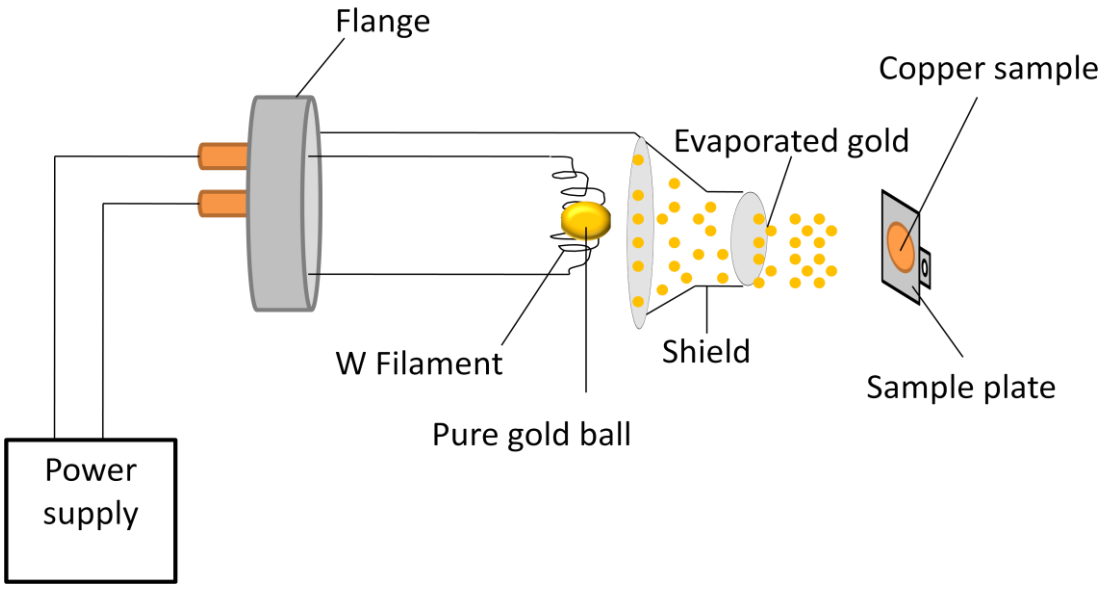

Figure 4.11: Schematic diagram showing the homemade gold evaporator parts.

4.6 Gas line

Normally the gas line is pumped down by using a diffusion pump assisted by a rotary pump. The gas line is usually baked out at 150 ^{o}C overnight to make sure all the gases introduced into the UHV system are pure. The purity of the gas is checked using the residual gas analyser as well. HCl gas and oxygen are introduced into the UHV system through two separate valves to prevent mixing.

4.7 References

1. Brune, D., et al., *Surface Characterization*. 2008, Weinhemi: John Wiley & Sons 715.
2. J. M. Walls, R.S., *Surface Science Techniques*. 1994 Amsterdam: Elsevier Science & Technology. 188.
3. Vickerman, J.C. and I. Gilmore, *Surface Analysis The Principal and Techniques*. 2nd ed. 2009, Chichester: Wiley. 686.
4. Hoffman, D., B. Singh, and J.H. Thomas, *Handbook of Vacuum Science and Technology*. 1997, London: Academic Press Limited. 835.
5. O'Hanlon, J.F., *A User's Guide to Vacuum Technology*. 3rd ed. 2003, New York: John Wiley and Sons Ltd. 536.
6. Jousten, K., *Handbook of Vacuum Technology*. 2008, Weinheim: Wiley-VCH Verlag GmbH. 1040.

Chapter 5 Interaction of HCl with Cu(100) surface

Contents

5.1 Introduction

5.1.1 Interaction of oxygen with Cu(100)

The interaction of oxygen with copper surface is an attractive area of research, because of the large number of industrial applications in which copper is involved as described in Chapter one [1-4]. Oxygen adsorption on the Cu(100) surface has been investigated over 30 years by several spectroscopic and microscopic techniques [5-10]. There is disagreement about what the structure of oxygen on top of the Cu(100) surface is, whether it forms a c(2x2)-O or $(\sqrt{2}x2\sqrt{2})R45^{o}$, the latter being a missing row structure.

At low temperature a LEED, and an AES study of O/Cu(100) shows two arrangements, " four spots" and c(2x2)-O even at full coverage[10], while at high temperature and high exposure the c(2x2)-O is formed, followed by forming the $(\sqrt{2}x2\sqrt{2})R45^{o}$ structure [6, 10]. Malcolm et al used LEED and XPS as well and they found three LEED diffraction patterns; an oblique "four spots" mesh, followed by a c(2x2)-O and finally a $(\sqrt{2}x2\sqrt{2})R45^{o}$ [5].

STM studies suggest the $(\sqrt{2}x2\sqrt{2})R45^{o}$ is formed at half monolayer of oxygen coverage (where one monolayer is defined as the Cu atom density on the (100) plane = $1.5x10^{15}cm^{-2}$) [7-9, 11]. Takaya et al. found the c(2x2)-O is formed in nanometre size domains of oxygen but not large well ordered c(2x2)-O, and the phase boundaries between c(2x2)-O domains made a zigzag structure. They suggested as well the origin of the LEED “four spots" arrangement which is the structure observed before forming the $(\sqrt{2}x2\sqrt{2})R45^{o}$ structure at full coverage. The STM images of the Cu(100) surfaces with different oxygen coverage are shown in Figure 5.1. The dark points observed in the images (a) and (b) are the oxygen atoms adsorbed on the four-fold hollow sites in small c(2x2)-O domains. The surface in image (b) shows the four-spot LEED pattern, and the bright zigzag lines are the phase boundaries of the nanometre size domains of c(2x2)-O. As shown in Figures 5.2(a) and (b), these domain boundaries change their position with time at room temperature, which is illustrated in the figure as a movement of oxygen atoms from a nanometre size c(2x2)-O domain to an adjacent domain with retention of the exact size of the domain. This behaviour give an explanation for appearance of the "four spots" arrangement in LEED as a result of two phase of c(2x2) nanometre size domain which regulated by local strain on the Cu(100) surface as seen in Figure 5.1[12]. The strain increases with increasing coverage of oxygen by increasing the size of c(2x2)-O domains. The way to reduce that stress is by ejecting Cu atoms along the [001] or [010] directions and forming the more stable structure $(\sqrt{2}x2\sqrt{2})R45^{o}$ as seen in Figure 5.1(c) and 5.2(c) [12, 13].

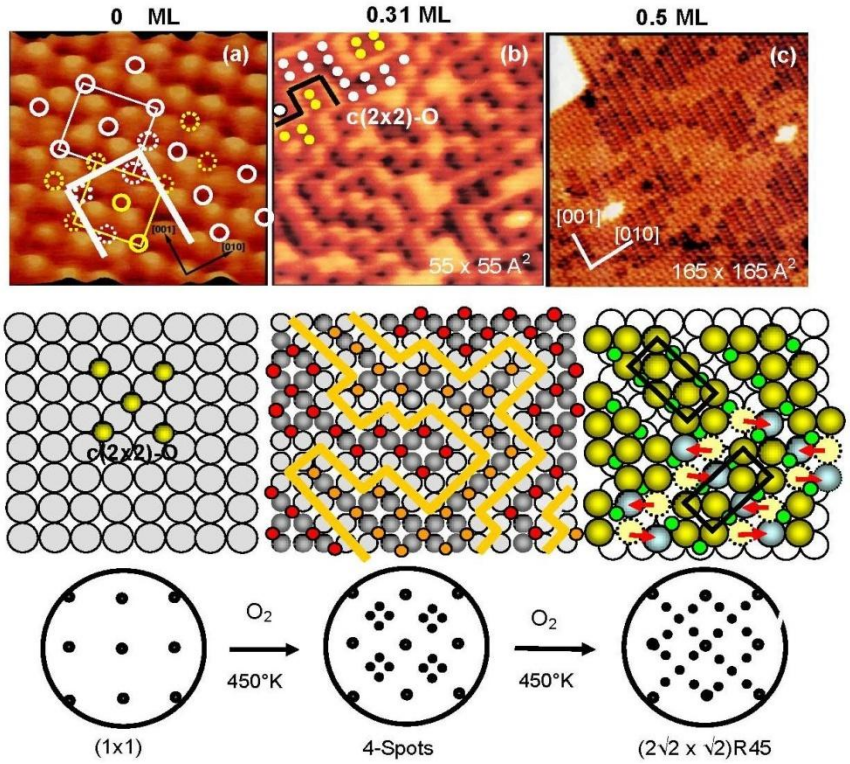

Figure 5.1: STM images of the Cu(100) surface with different oxygen coverage from [8,9], (**a**) Clean Cu(100), (**b**) Four spots surface at 0.31 monolayer oxygen coverage exposed to 8 L of O_2. (10-7 Torr × 80 s) attained at 450 K), and (**c**) (2√2 × √2)R45° surface at 0.5 ML coverage.

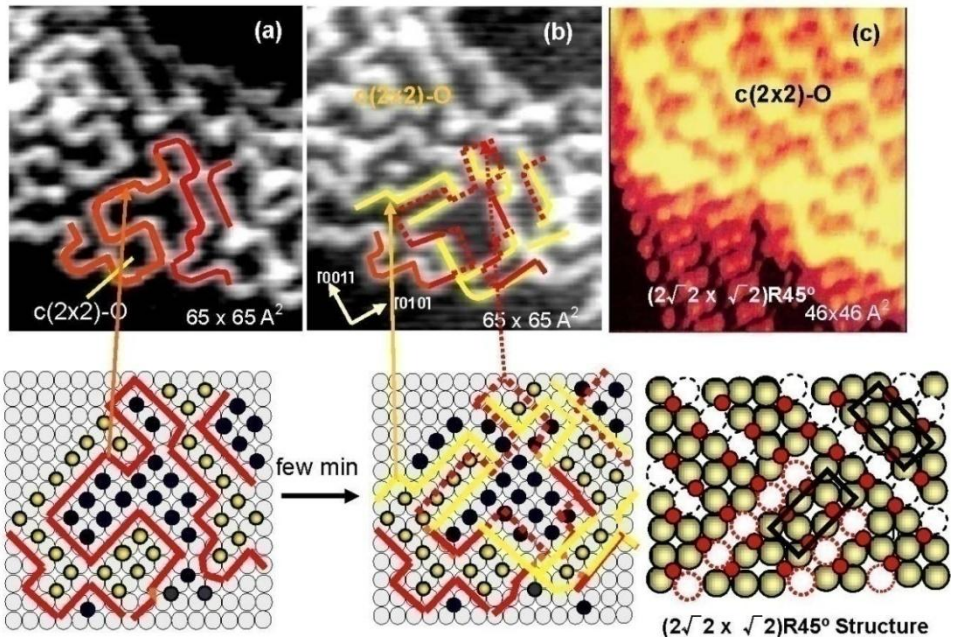

Figure 5.2: (**a**) STM image of a Cu(100) surface with 0.3 ML oxygen coverage, and (**b**) same area after few minutes at room temperature. (**c**) When the surface is relaxed by missing Cu atoms and forming (√2x2√2)R45^{o} structure[12, 13].

On the subject of coverage disagreements appear again; the saturation coverage is kinetically limited to half monolayer but by increasing the rate of impingement of oxygen with Cu(100) surface, a new subsurface is developed at 300 to 400 K [5, 14]. A coverage of 0.75 monolayer is reported by Habraken et al. which they suggested that the interaction of oxygen with Cu(100) happened in two stages. The first stage by formation of $(\sqrt{2}x\sqrt{2})R45^o$ LEED pattern up to 0.5 monolayer, then formation of $(\sqrt{2}x2\sqrt{2})R45^o$ at 0.75 monolayer [15-18].

Recently STM data showing three oxygen reconstructions: (2x1)-O, c(2x2)-O, and $(\sqrt{2}x2\sqrt{2})R45^o$ on top of Cu(100) has been reported depending on the temperature and exposure time [19]. Low exposures of oxygen (about 550 L at 373 K) result in oxygen attack on the terraces, and make them grooved as a result of copper atoms being ejected from the copper terraces and collecting at the step edges. In this grooved area the oxygen atoms create the $(\sqrt{2}x2\sqrt{2})R45^o$ as shown in Figure 5.3. By increasing the exposures time, one layer of ordered island is made via continuous growth in [001], and [010] directions. At the same time a narrow zigzag structure was developed on the wide plan terraces which has been suggested to be a (2x1)-O arrangement in other studies by using a range of surface science techniques such as STM [11], LEED, High resolution electron energy loss spectroscopy (HREELS), and angle-resolved ultra-violet photoelectron spectroscopy (UPS) [20].

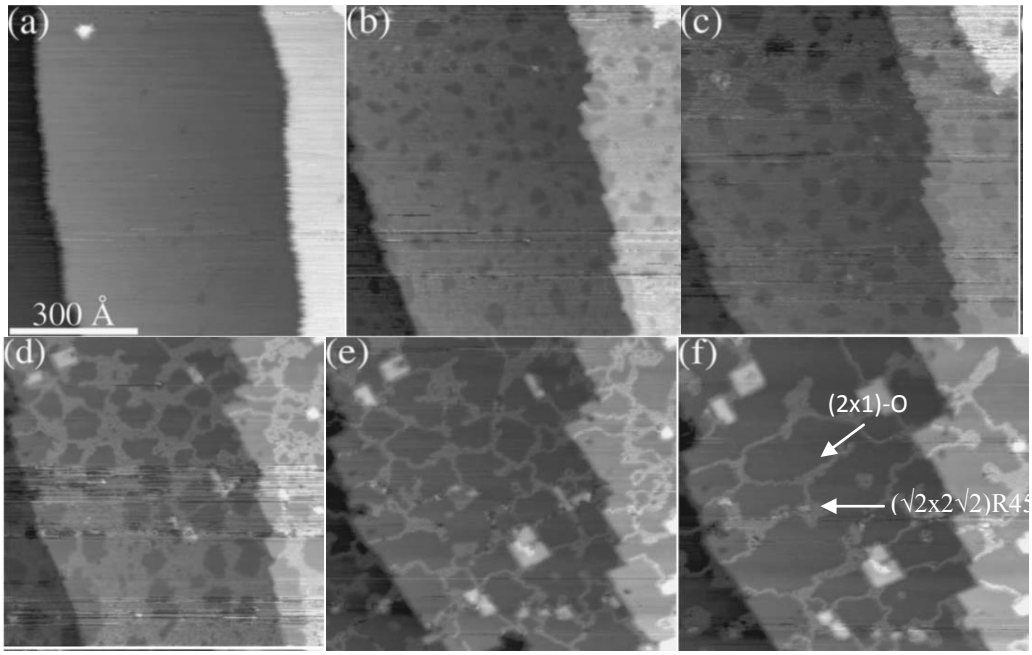

Figure 5.3: STM images (78.3 nm^2) of Cu(100) oxidation at T=373 K and pO_2=7.8x10^{-7} mbar. (a) Clean surface, and oxygen exposures of(b) 550 L, (c) 930 L, (d) 1740 L, (e) 1980 L, (f) 2690 L [21].

5.1.2 Interaction of chlorine with Cu(100)

The copper-chlorine interaction has attracted a great deal of experiments, and has been investigated by several surface science characterisation techniques [22-26]. A strongly bound layer of chemisorbed halogen (Cl, and Br) on Cu(100) has been reported using temperature programmed desorption (TPD) and low energy electron diffraction (LEED) [22, 27-29]. Bond length of interlayer of Cu-Cl is 2.37 Å ± 0.02 Å determined by surface extended x-ray-absorption fine structure (SEXAFS) [30].

At low chlorine coverage no change happened at the step edge but at 90% of saturation (determined by AES) the step edges start to be more sharp and grooved (to make the triangular grooves), and the groove size is increased when heating the sample at 575 K as shown in Figure 5.4[22].

Galeotti et al. created a saturated chlorine monolayer on Cu(100) by dosing Cl_2 at room temperature. They showed that cooling the adlayer to 160 K did not affect the $Cu2p_{3/2}$, and Cl2p signal, but continued exposure after saturation at 160 K formed a thick Cl layer involving about 20 atomic layers confirmed by the decreasing ratio of XPS between $Cu2p_{3/2}$, and Cl2p, and by the disappearance of all the LEED spots[31]. The chloride grows epitaxially to form crystallites of cubic CuC1, with the (111) plane parallel to the substrate surface which was confirmed using X-ray photoelectron diffraction (XPD) [32].
The intensity of the Cu peak in LEIS spectra at 160 K is increased compared to the same peak at room temperature which is related to the different structure of the CuCl(111) topmost layers compared to Cu(100)c(2x2)-Cl which formed at room temperature [22, 31, 32].

LEED and X-ray diffraction (XRD) studies show that the Cl atoms made a c(2x2)-Cl arrangement by adsorbing the Cl atom on the four-fold hollow sites [22, 33]. The atomic resolution of the (2x2)-Cl arrangement can be imaged by STM at 70% of saturation, while it can be detected by LEED at less than 60% of saturation because of the effect of atoms moving on the surface under the STM tip [22, 34]. AES detected the appearance of Cl on the STM tip although the STM chamber was isolated at the time of dosing chlorine and the background pressure of chlorine in the STM chamber was about 5 $x10^{-12}$ Torr. This was explained as a transfer of the Cl atom from copper surface to the STM tip [34]. At full coverage of Cl on the Cu(100) surface the STM atomic resolution shows a square lattice with inter atomic distance 3.5Å ± 0.15Å[34]. To make a CuCl island needs over saturation (about

400 L) of chlorine, because the low sticking properties of chlorine on copper surface at room temperature which is confirmed by AES. STM confirmed that the islands which are under those conditions covered about 6 to 8% of the surface. These islands were removed by heating the sample to 480 K, and STM just showed the atomic resolution of Cu(100)c(2x2)-Cl without any traces of CuCl island while at 820 K the STM just shows the Cu(100)-(1x1) phase[34].

Cu(100)c(2x2)-Cl arrangement formed by the interaction of Cu(100) with 1mM HCl solution has been reported using LEED, AES [35], and confirmed the reconstruction by using STM [36, 37]. Another STM study done after immersion in 10mM HCl reported the $(\sqrt{2}x2\sqrt{2})R45^{o}$ of Cl reconstruction [38], and showed that the preferred reaction sites were step edges at positive potential with moderated dissolution along the Cu(100) [100] direction. Order and disorder transition of Cl adlayers on Cu(100) causes surface reconstruction by a reversible mechanism of grooving and degrooving steps; the ordered c(2x2)-Cl was formed at the defect free step edges while disordered surface were formed at the defected step edges [36, 37].

From the above review it appears that there are disagreements which produce a lot of questions such as;(1) does the oxygen $(\sqrt{2}x2\sqrt{2})R45^{o}$ form directly or does it follow after forming c(2x2)-O?. If it is a following step, at what level of coverage does the transition from c(2x2)-O to $(\sqrt{2}x2\sqrt{2})R45^{o}$ occur? (2) Is the c(2x2)-O stable at less than 0.25 monolayer?

In this chapter we will try to answer the above questions but from the view of the reactivity of the O/Cu(100) (which is poorly understood) toward reaction with HCl (which is fairly well understood).

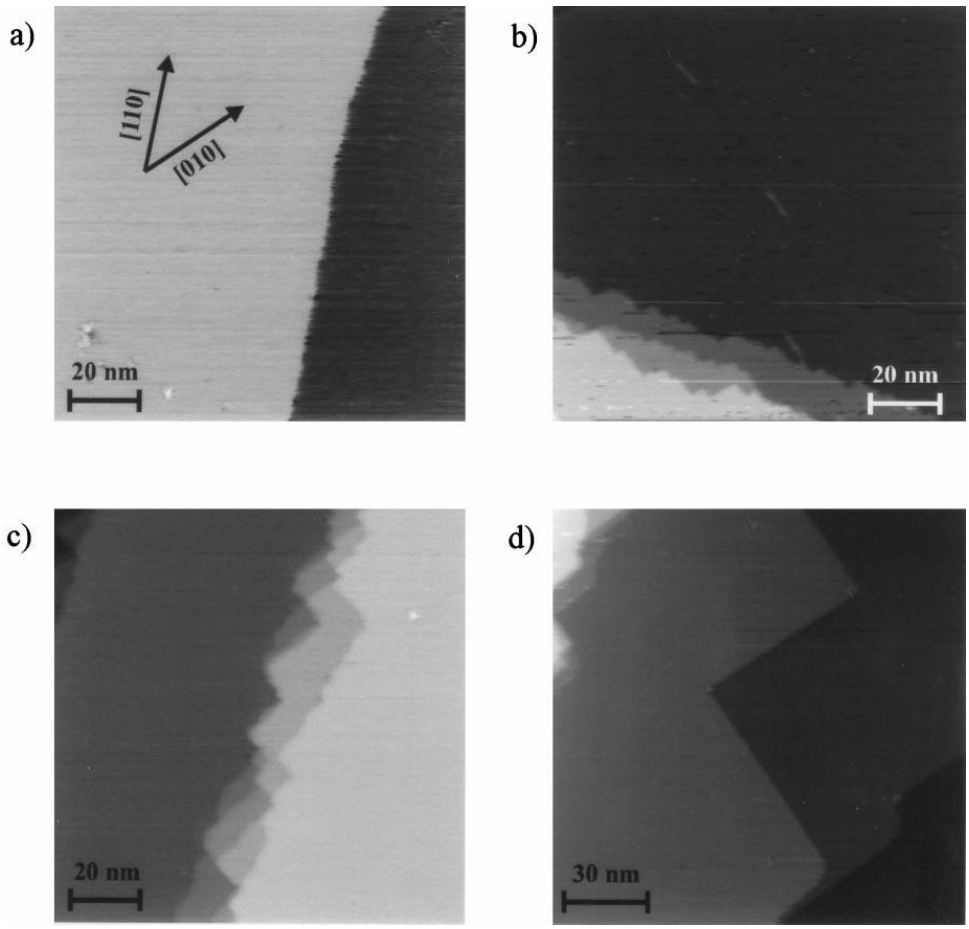

Figure 5.4: large scale STM images describing the change of the step structure among Cl chemisorption at room temperature. (a) Monatomic step below 60% of saturation did not make a different from the clean surface, (b) Image for a Cl coverage of 95% of saturation, shows starting of making the groves in the step edges, (c) Image just below saturation, showing a number of steps are grooved along the [100] directions. (d) Image of the saturated surface after annealing at 575 K [22].

5.2 Experimental

The instrument used in these experiments is described in Chapter 3, together with sample cleaning procedures. Oxygen and HCl gases were purchased from Argo international and the purity was checked using mass spectroscopy.

5.3 Results and discussion

5.3.1 XPS and STM of the clean Cu(100) surface

The wide scan of clean Cu(100) surface excited using an x-ray Al Kα source is shown in Figure 5.5 there are two types of peak in the figure photoemission peaks, { [2s 1069 eV], [$2p_{1/2}$ 952.3 eV], [$2p_{3/2}$ 932.7 eV], [3s 120 eV], and [$3p_{1/2,3/2}$ 74 eV] } and Auger peaks { [LMM d 712.7 eV], [LMM b 649.7 eV], [LMM c 639.7eV], and [LMM a 569.7eV] }. In the following experiment we use the $Cu2p_{3/2}$ at 932.7 eV for calibration of all other elements. The clean sample shows no oxygen, or Cl as shown in Figure 5.6.

STM images of clean Cu(100) revealed terraces having an monatomic height (1.84 Å ±0.04 Å) in agreement with previous study[39] as shown in Figure 5.7.

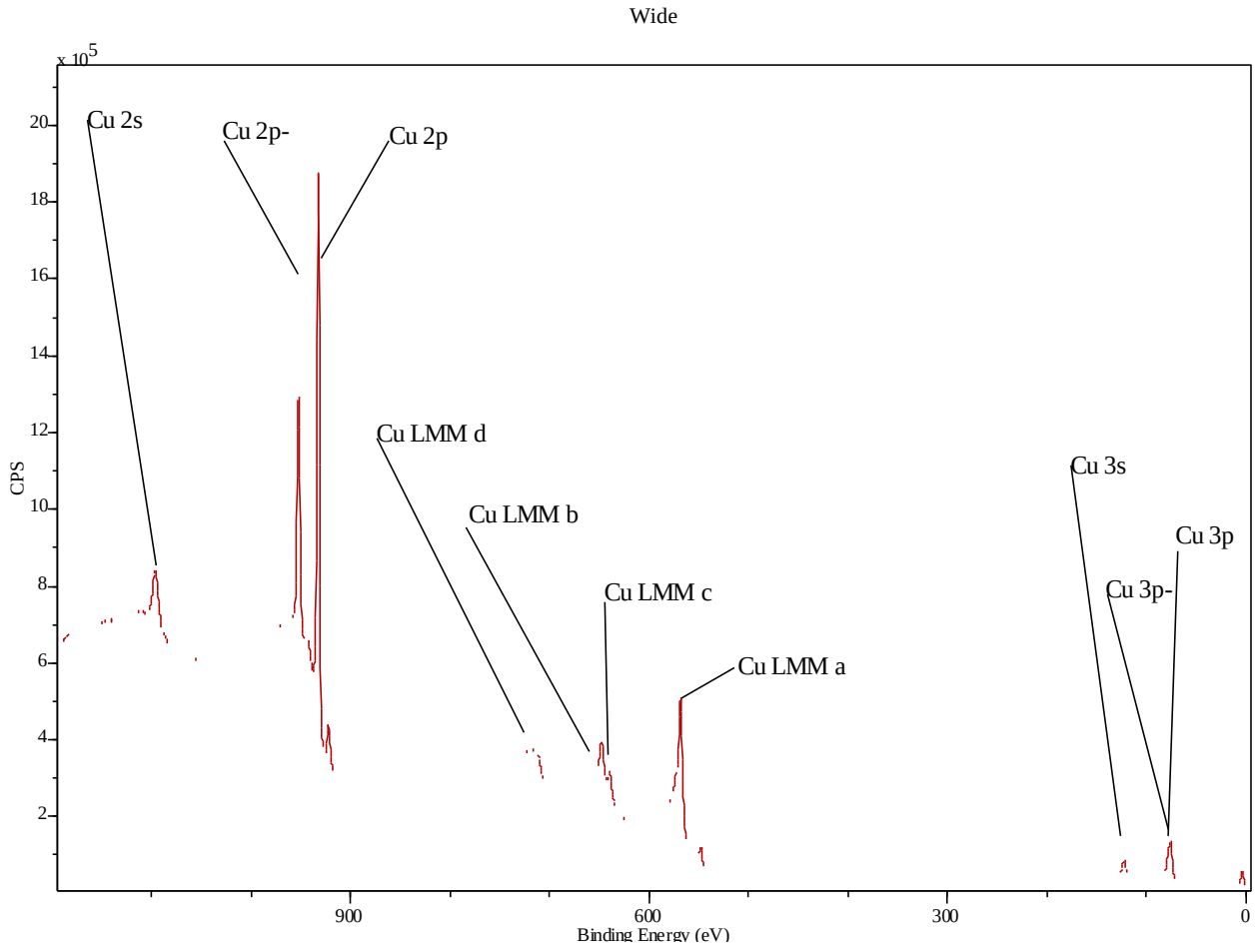

Figure 5.5: XP spectrum of wide scan of clean Cu(100) surface at room temperature excited by Al Kα x-ray source.

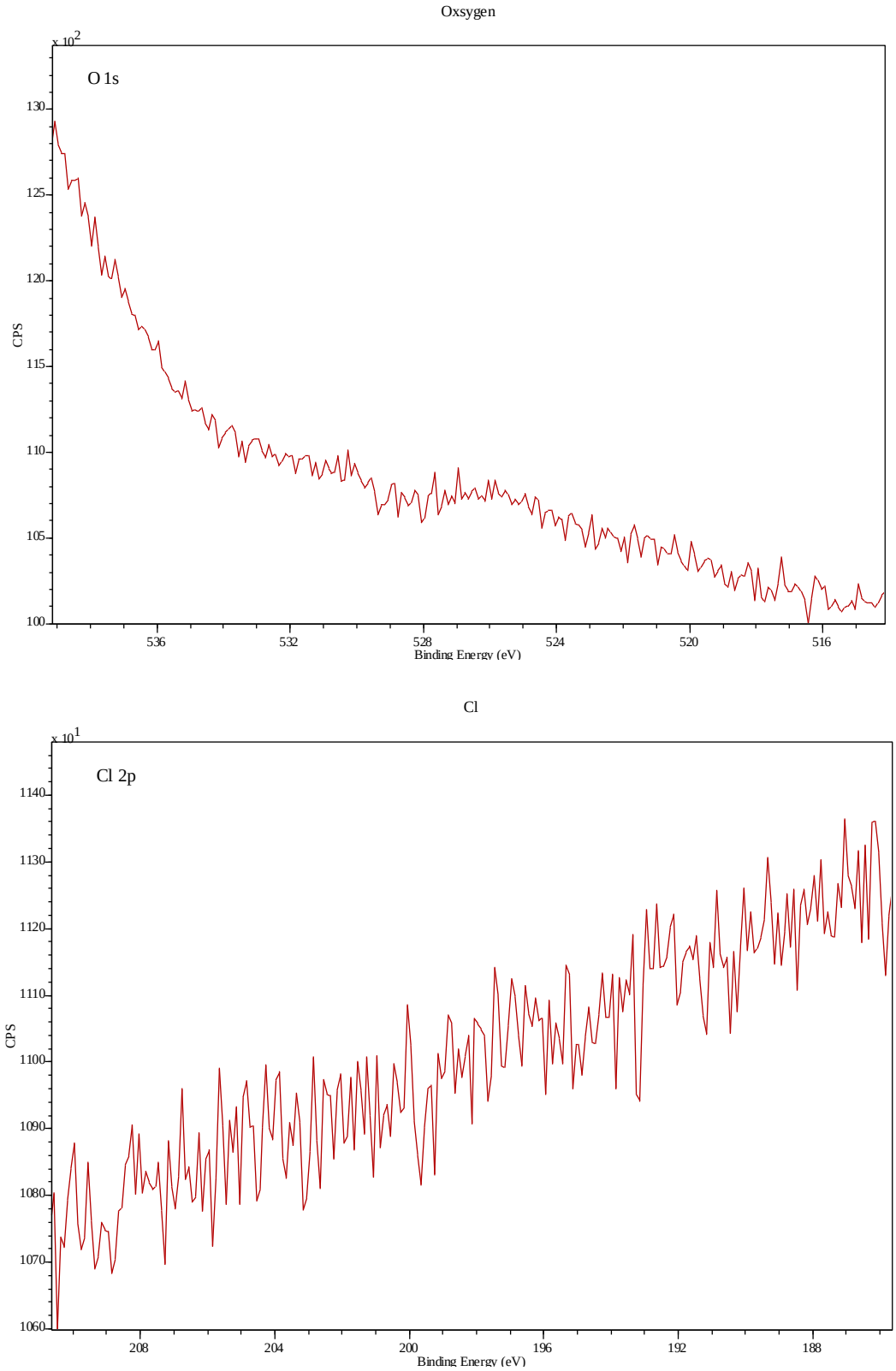

Figure 5.6: XP spectrum of oxygen O1s at 531 eV, and Cl2$p_{1/2,3/2}$ at 200 eV regions of a clean Cu(100) surface at room temperature.

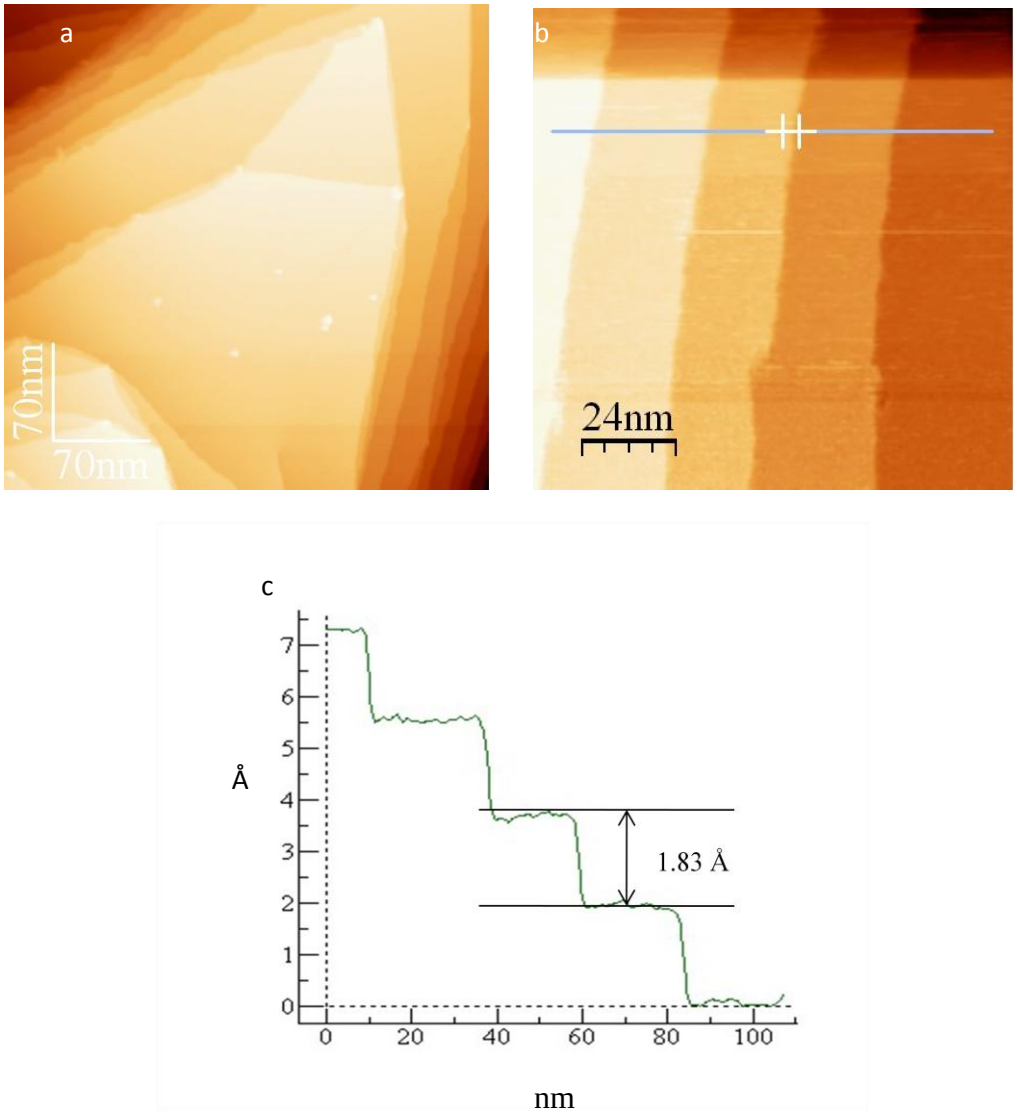

Figure 5.7: STM images of clean Cu(100) surface. a) 350 nm x 350 nm at 1V, and 1nA. b) 120 nm x120 nm at 1V, and 1nA. c) Line profile shows the height of monatomic step is 1.83Å.

5.3.2 Interaction of HCl with clean Cu(100) surface at room temperature

XPS of Cl2p of sequential exposures of the clean Cu(100) surface to HCl at $1x10^{-8}$ mbar are shown in Figure 5.8. The Cu(100) reacts very fast with HCl, and the surface keeps taking Cl until the full coverage at $7x10^{14}$ cm^{-2} corresponding to half monolayer as shown in Figure 5.9.

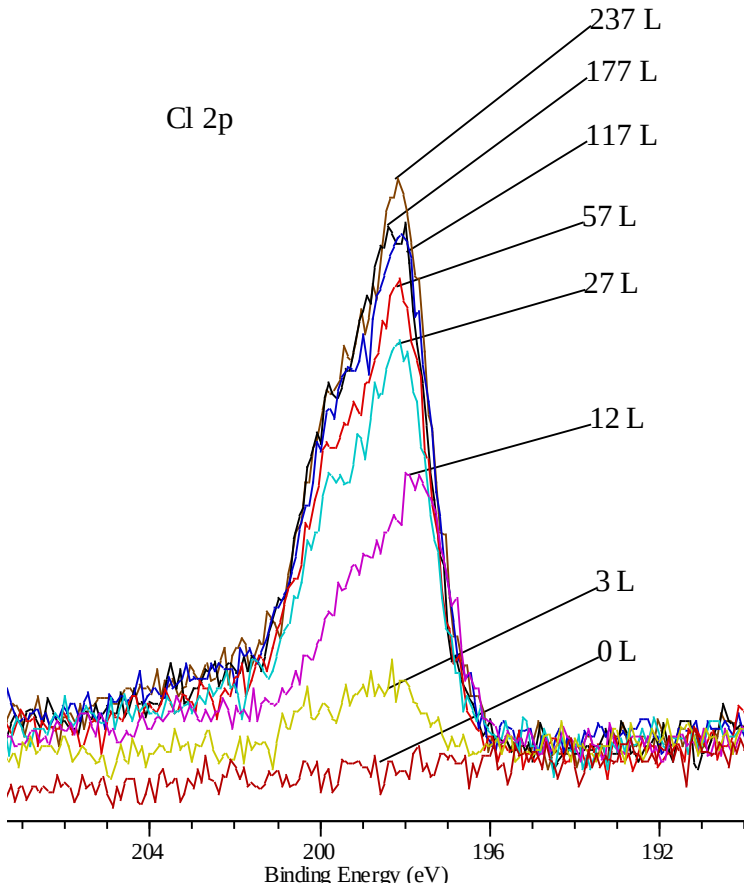

Figure 5.8: XP spectrum of Cl2p showing the increase of Cl concentration with exposure to HCl until the maximum coverage is achieved.

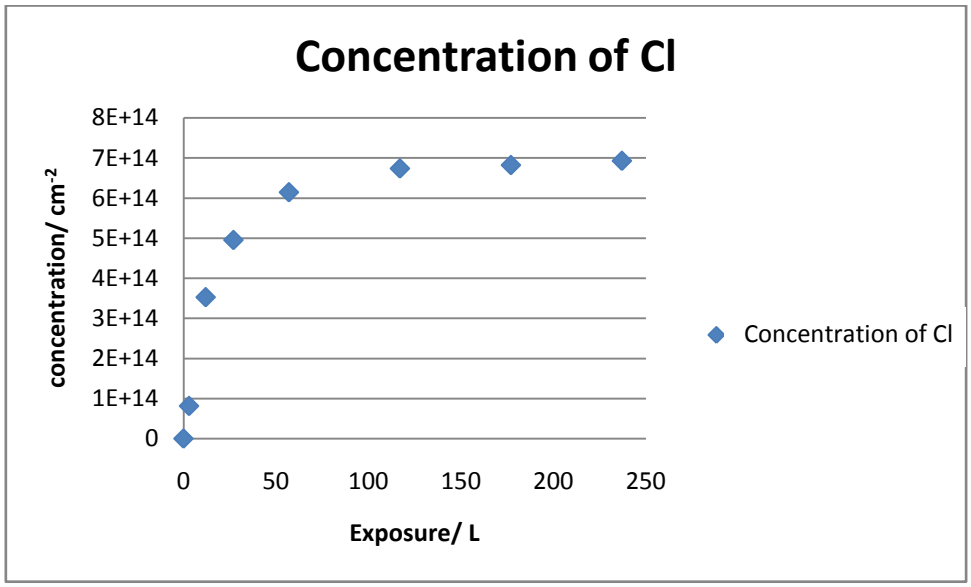

Figure 5.9: Continuous exposure of clean Cu(100) surface to HCl at $1x10^{-8}$ mbar, the concentration of Cl increases until it stabilises at full coverage at $7x10^{14}$ cm^{-2} corresponding to half monolayer.

At about 12-27 L ($3.52x10^{14}$ cm^{-2} to $4.95x10^{14}$ cm^{-2}) the STM images of Cu(100) show a change in the copper steps, losing the sharpness of the step edges in the images which is due to the ejection of Cu atoms from the step edges as shown in Figure 5.10(a, b, c). This agrees with a previous study [22]; the step edge height is 1.8 Å, but there is a lot of noise between the two terraces indicating the atoms movement cross the surface seen in Figure 5.10 (d). Some Cl atomic arrangement has appeared and developed at some area on the surface as shown in Figure 5.10 (b).

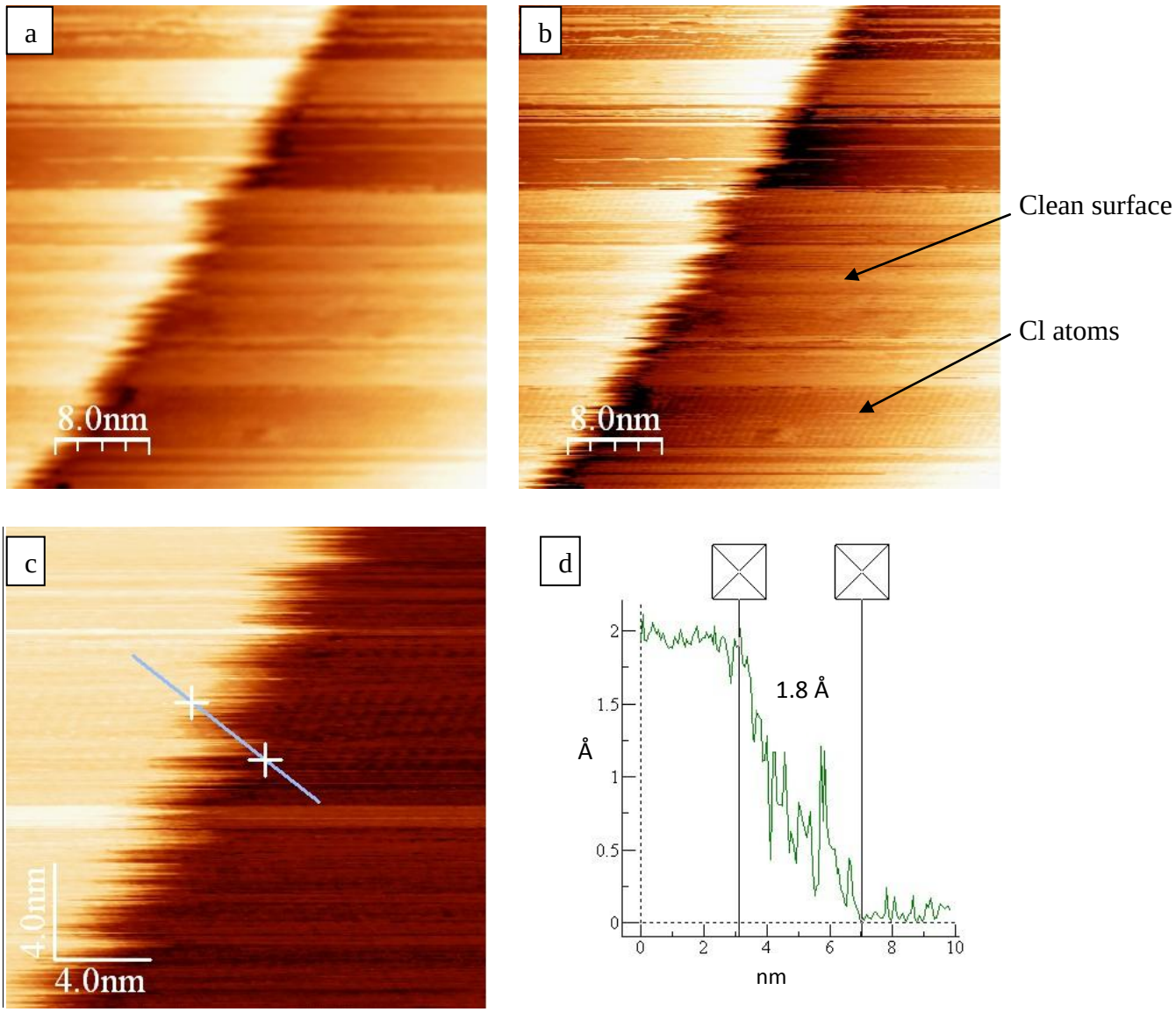

Figure 5.10: STM (0.2 mV, and 1 nA) during the continuous exposure of clean Cu(100) surface to HCl at $1x10^{-8}$ mbar, from 12-27 L (a) Cu(100) after 12 L. (b) Cl atoms appear at some area on the surface. (c) modification of the copper step edge without change the step height. (d) Line profile of image (c) shows the height of the step edge.

At about 117 L ($6.73x10^{14}$ cm^{-2}) atomically resolved Cl atoms are starting to be obvious on all area of the Cu(100) surface as seen in Figure 5.11. No change in the STM images happened after dosing more HCl and that agreed with above XPS result which shows the concentration of Cl on the surface is stable at $6.92x10^{14}$ cm^{-2} even after leaving the sample overnight.

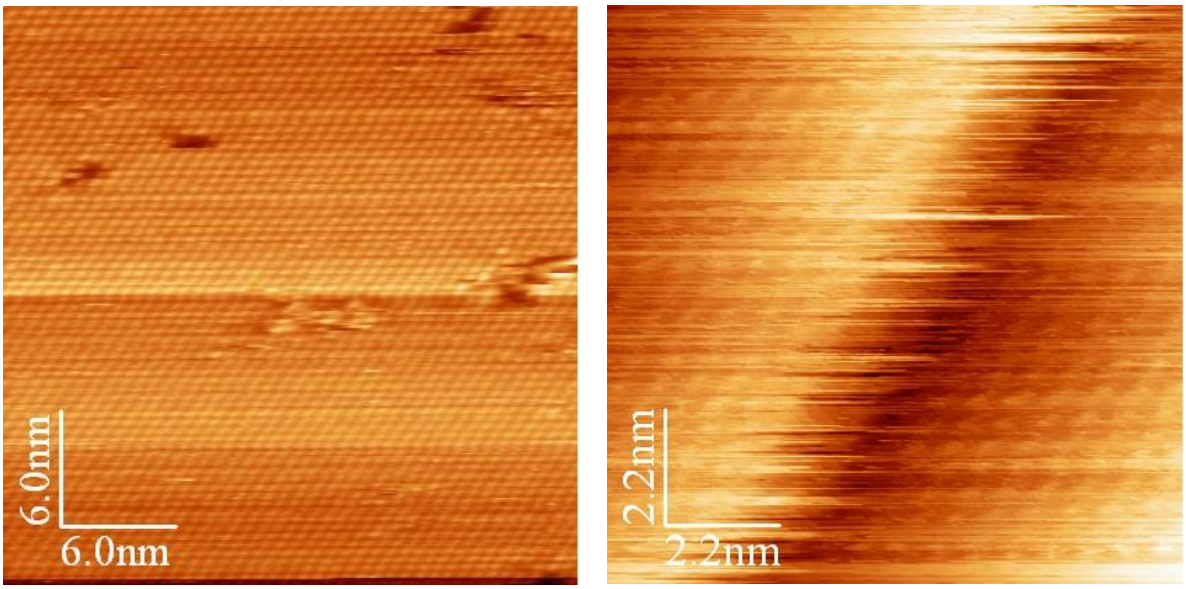

Figure 5.11: atomic resolution of Cl atoms on the Cu(100) surface at $6.73x10^{14}$ cm^{-2}, 1 V, and 0.2 nA.

After saturation no traces of clean Cu(100) were observed in STM and all the surface were covered with c(2x2)-Cl adlyer structure as shown in Figure 5.12. The atomic spacing between Cl atoms is 5.1 Å which is double that between copper atoms 2.55 Å as seen in Figure 5.12.

a

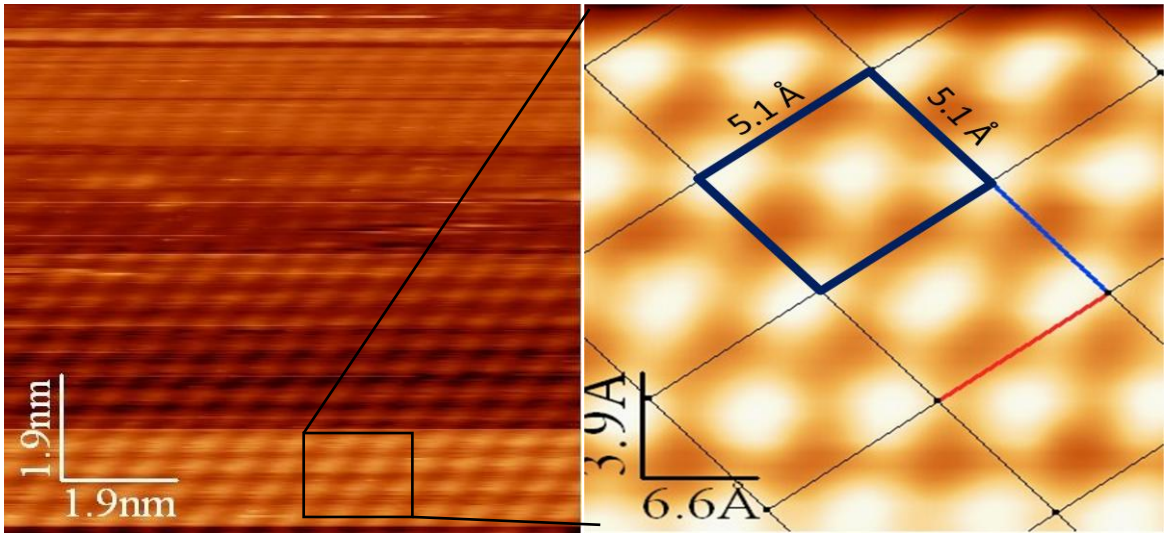

b

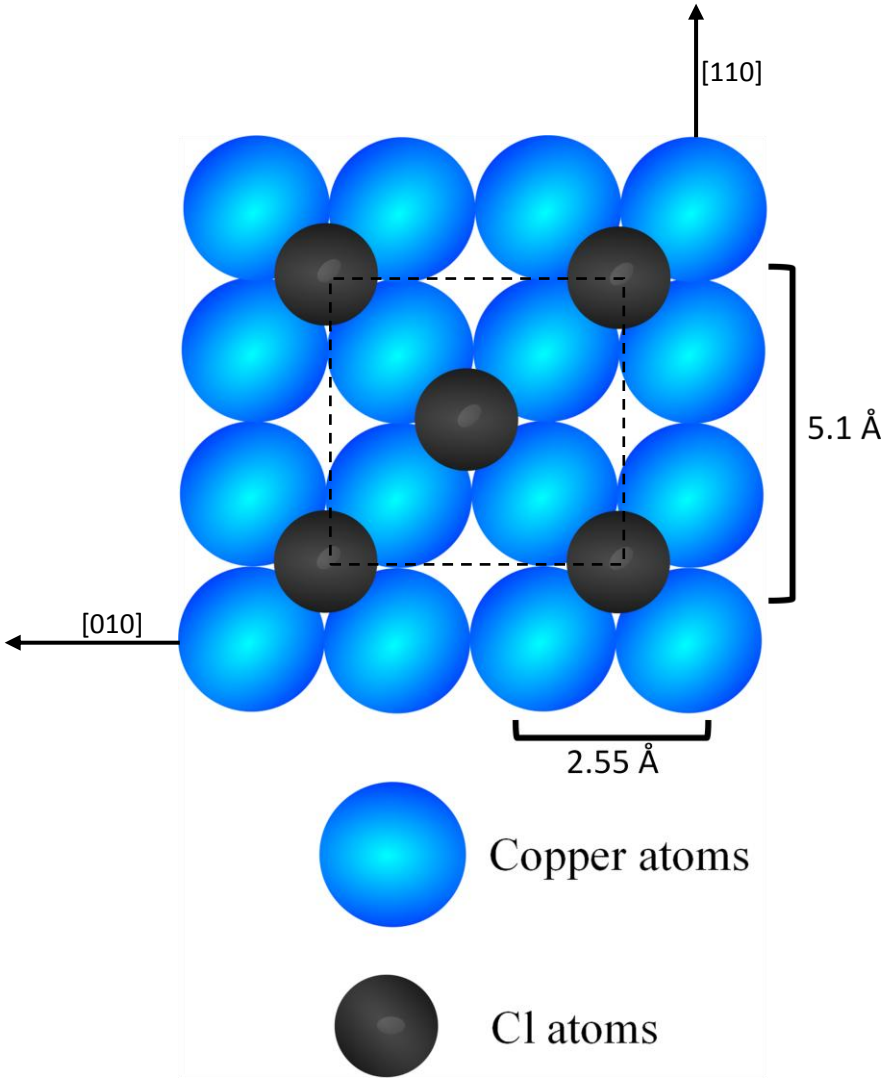

Figure 5.12: (a) atomic resolution of Cl atoms on Cu(100) surface at 6.73x10^{14} cm^{-2}, 1V, and 0.2 nA. (b) Atomic space of c(2x2)-Cl.

5.3.3 Interaction of oxygen with clean Cu(100) surface at room temperature

In this experiment we exposed the Cu(100) surface to oxygen for different length of exposure until we reached saturation indicated by XPS as shown in Figure 5.13.

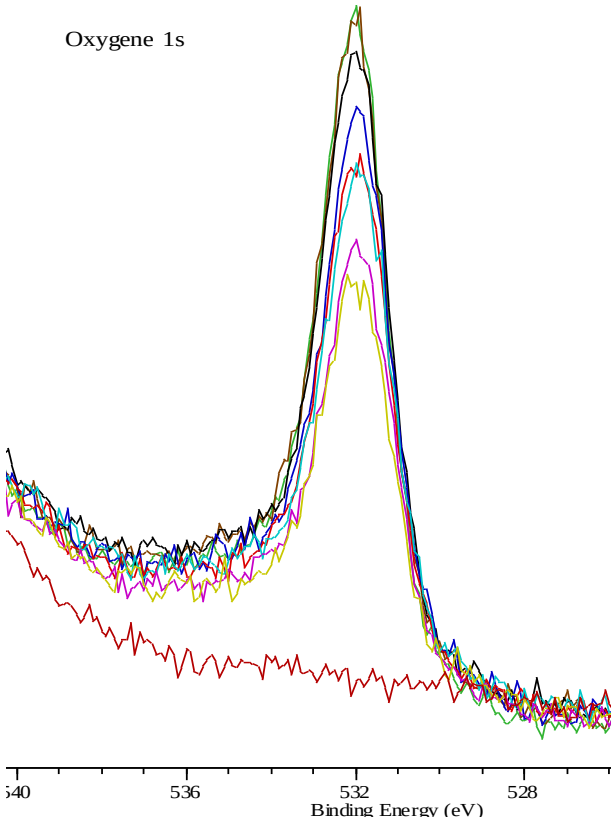

Total exposure/ L	Concentration of Oxygen/ cm^{-2}
30	$4.31x10^{14}$
60	$514x10^{14}$
120	$5.60x10^{14}$
180	$6.01x10^{14}$
300	$6.58x10^{14}$
600	$6.95x10^{14}$
1050	$7.20x10^{14}$
1650	$7.21x10^{14}$

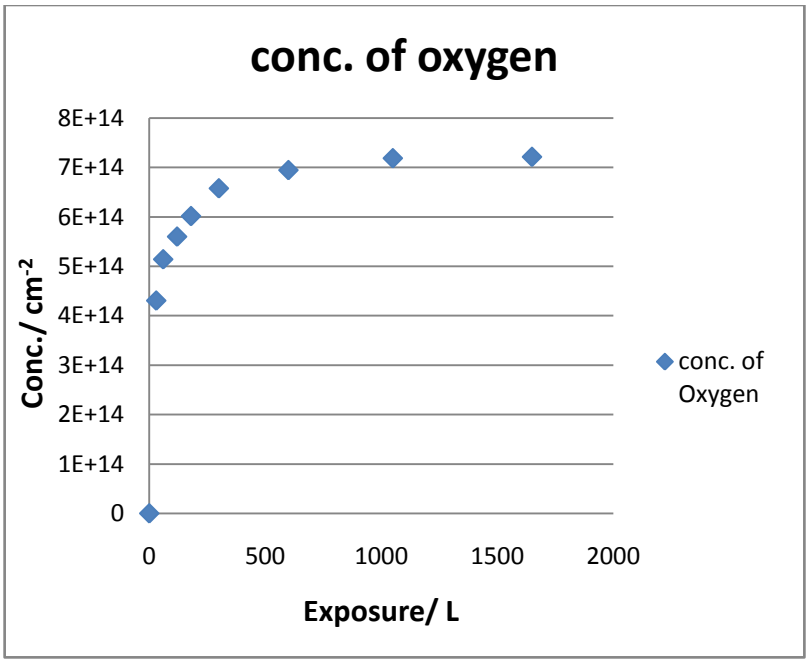

Figure 5.13: Quantified O1s XP spectra shows the increase of oxygen coverage with increasing O_2 exposure until saturated according to value in the table and graph.

Dosing more oxygen at room temperature after saturation doesn't have any effect on the oxygen concentration, which means that all the surface is covered with oxygen, and there are no more sites for occupation on the surface.

STM of sequential exposures of clean Cu(100) to oxygen are shown below in Figure 5.14. At about 10 L we start to see the effect of the oxygen as small holes in the surface, these holes increase to make a grooved surface at about 80 L. At 160 L to 320 the grooves start to disappear, while small islands start to develop on the terraces and step edge. The effect of oxygen on the step edge begins to be clear at 400 L to 800 L when the islands contact together, making a new layer.

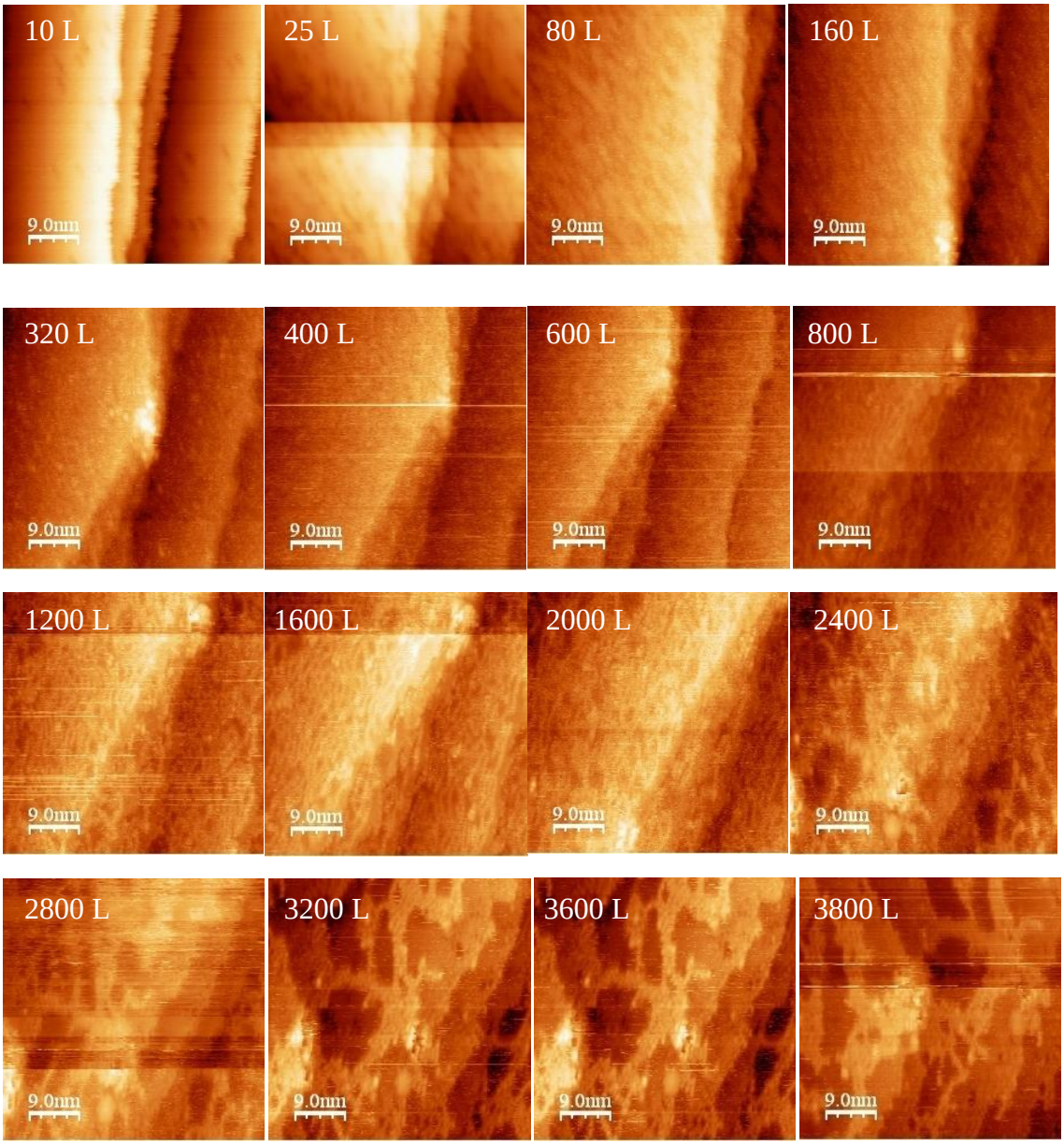

Figure 5.14: STM images of sequential exposure of clean Cu(100) to oxygen at 1.0V, and 0.2 nA.

At 1200 L to 3800 L the step edge starts to disappear while the islands start to grow and join together by making a bridge between them. Large islands start developing on the step edge, and branching and joining to the other island Figure 5.15, while smaller islands develop on the terraces as seen in Figure 5.16.

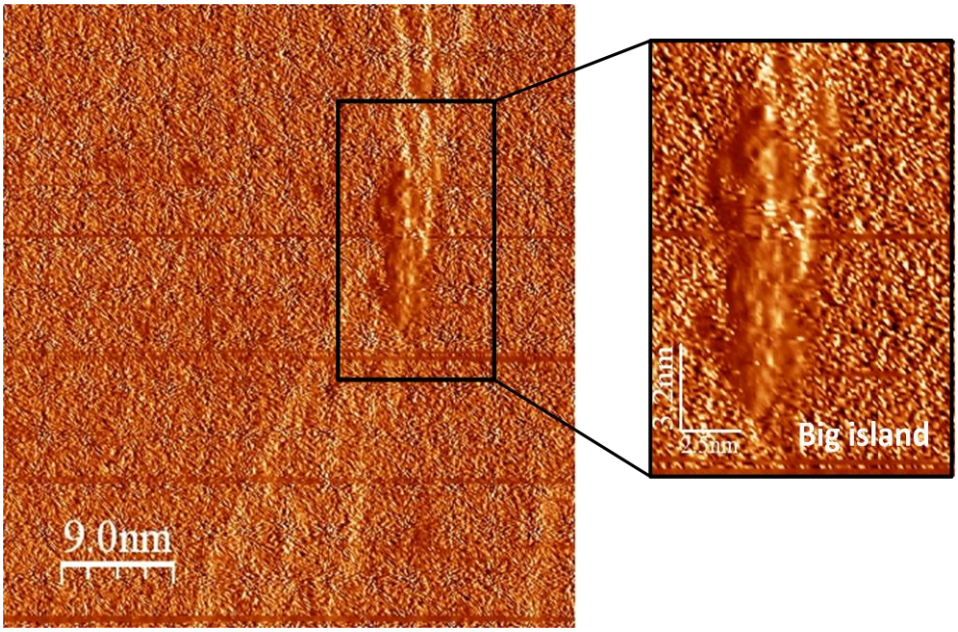

Figure 5.15: large island start to develop at the step edge after exposure to 1200 L of O_2 (1.0V, and 0.2 nA).

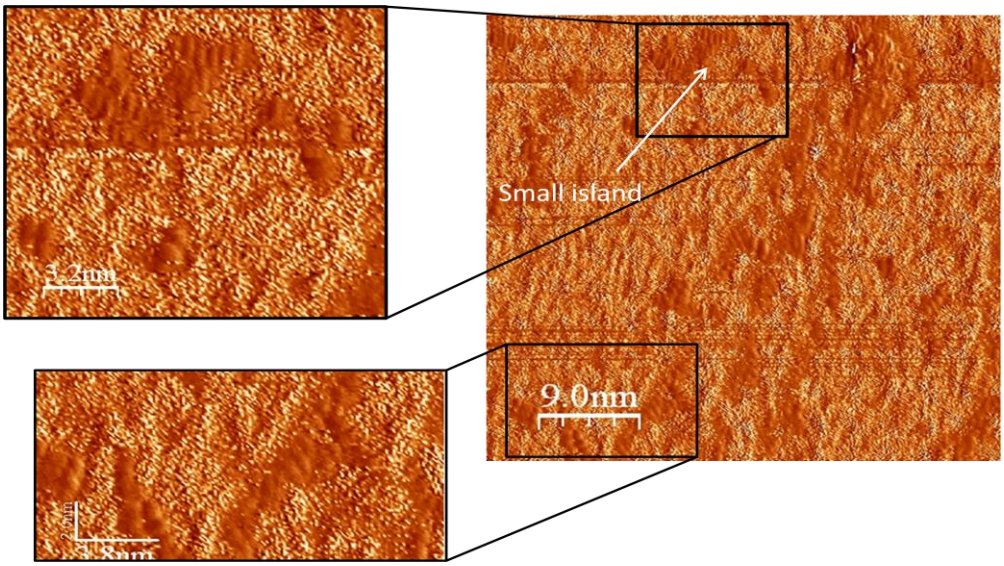

Figure 5.16: small island start to develop on the terraces exposed to 1200 L of O_2 (1.0V, and 0.2 nA).

A low magnification image of Cu(100) after dosing oxygen up to saturation shows the oxygen layer covering all the surface, Figure 5.17.

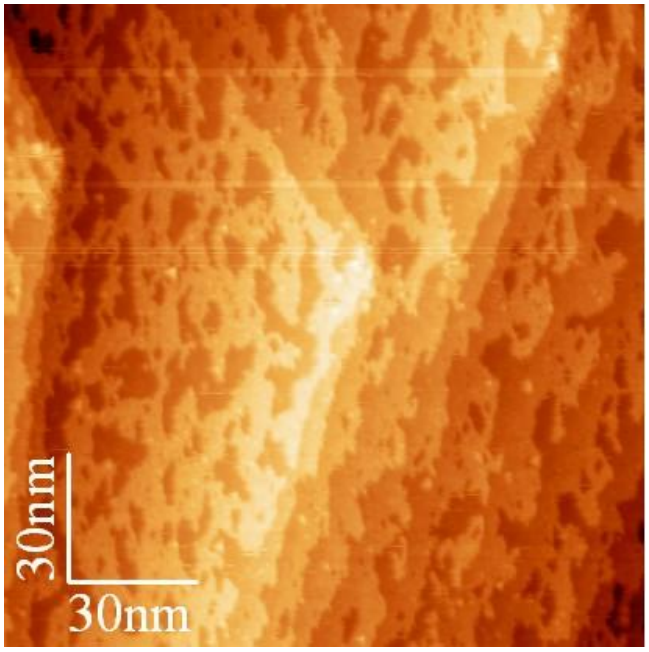

Figure 5.17: Large scale image showing the morphology of the Cu(100) after saturation with oxygen at 1.0V, and 0.2 nA.

We get two types of oxygen structure on Cu(100). First one is c(2x2)-O which appears as a bright zigzag area developed in two directions [001], and [010] as shown in Figure 5.18, while the second type is $(\sqrt{2}x2\sqrt{2})R45^{o}$ which appears as a dark area, and illustrated in the scheme in Figure 5.18. This result is agreement with the results reported by Fujita et al., and Tanaka et al.[12, 40], and again the poor resolution is due to moving of the c(2x2)-O domains.

5.3.4 Interaction of oxygen with clean Cu(100) surface at 100 ^{o}C

By exposing the Cu(100) to 60 L of oxygen at 100 ^{o}C several layers of completed and non-completed oxide layers are created as shown in Figure 5.19 (a). Step edge of two non-completed oxygen layer have sharp triangle shape with a height about 1.8 Å Figure 5.19 (b, and c). The STM images show the atomic resolved $(\sqrt{2}x2\sqrt{2})R45^{o}$ structure at the oxide layer with some disordered structure which may be due none transforming c(2x2)-O as shown in Figure 5.20. The atomic space is 0.78 nm which agrees with the $(\sqrt{2}x2\sqrt{2})R45^{o}$. The ejected copper atom in the processing of making the missing row structure, we think is aggregated at the step edge to make a straight line as shown in the STM image Figure 5.21.

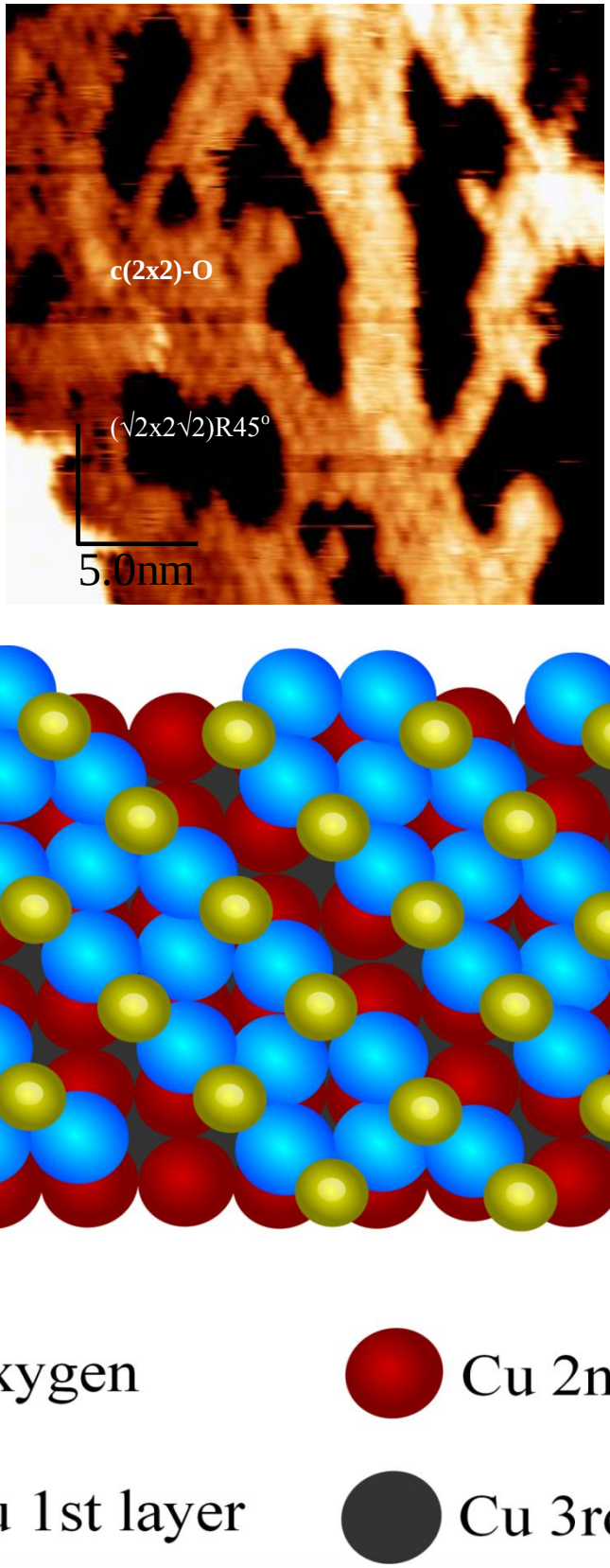

Figure 5.18: STM image shows the two types of oxygen structure on Cu(100) by the end of exposure time at1.0V, and 0.2 nA and scheme represented the missing row structure (√2x2√2)R45°.

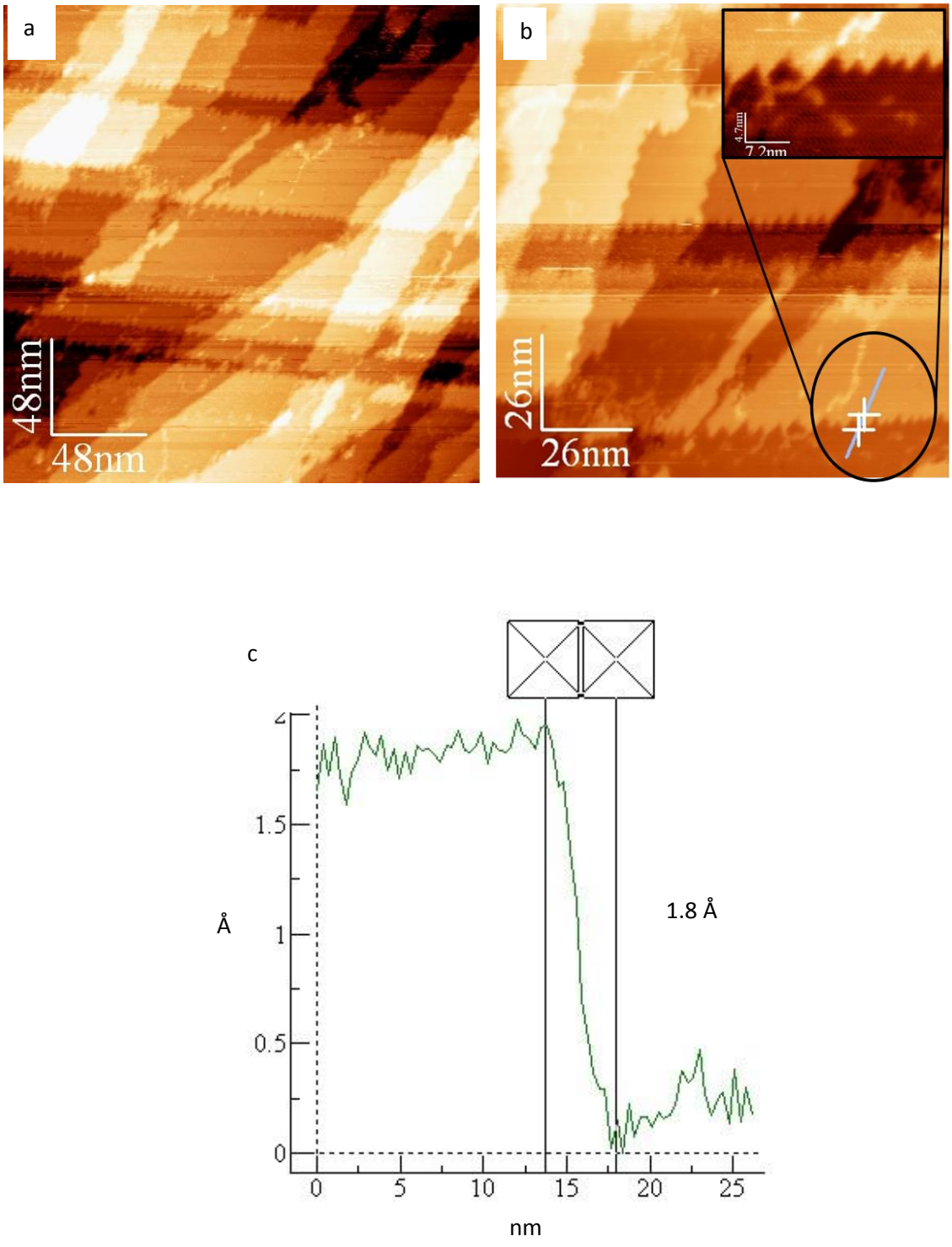

Figure 5.19: (a) STM image of completed and non-completed layer of oxygen after dosing 60 L of oxygen at 100 ^{o}C at Cu(100). (b, and c) the triangle shape of oxide layer and its height 1.8 Å.

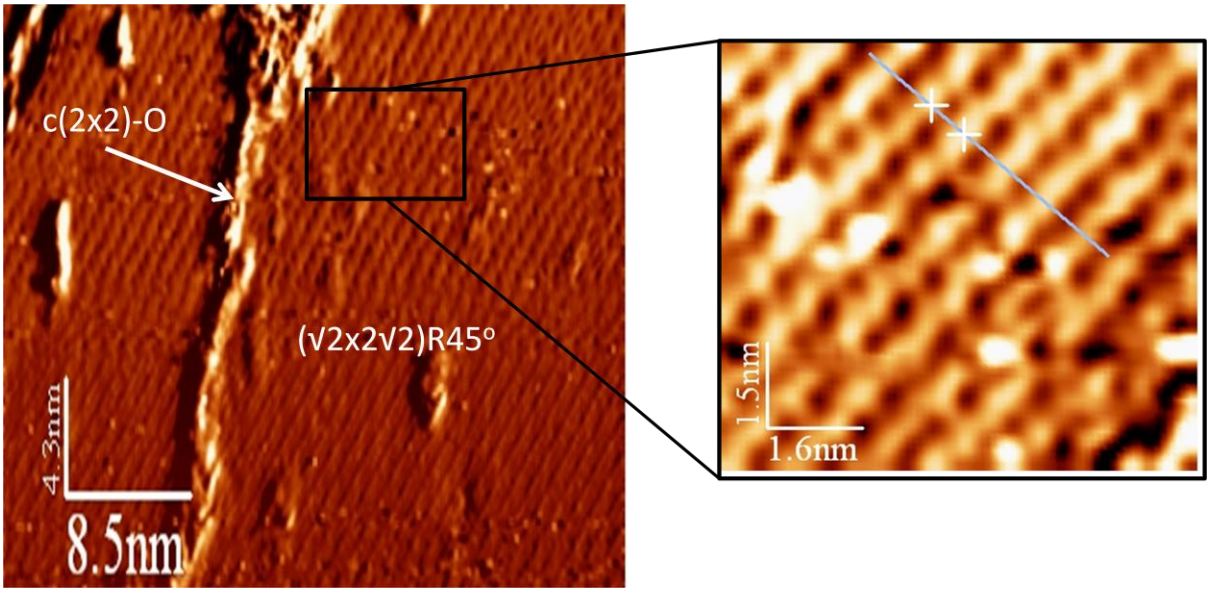

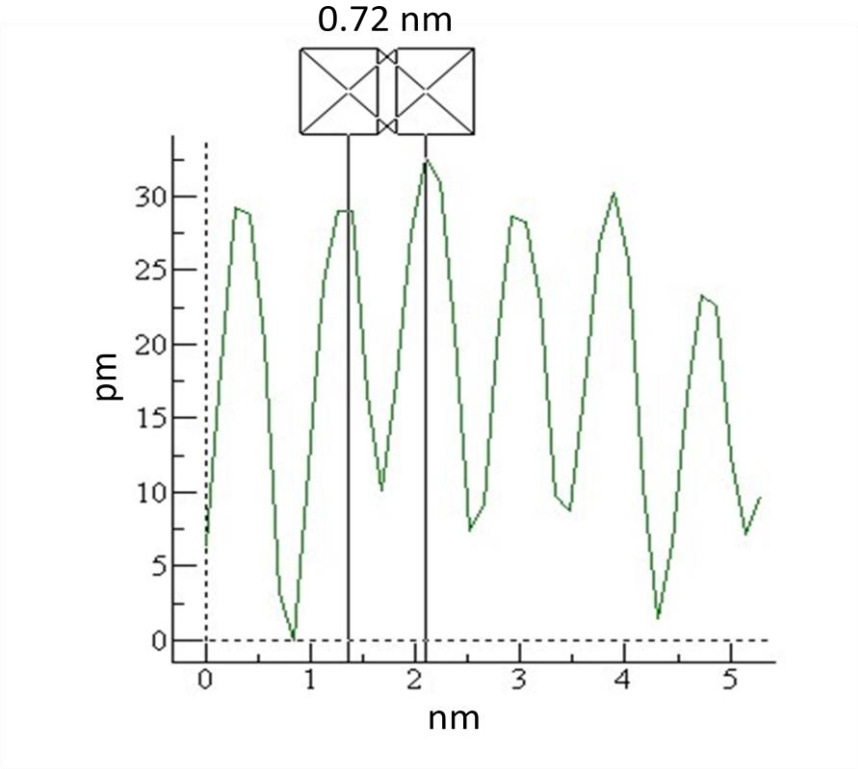

Figure 5.20: STM image showing the atomic resolution of the two types of oxygen (√2x2√2)R45° with atomic space about 0.72 nm, and the c(2x2)-O on Cu(100) after exposed to 60 L of O_2, (1.0 V, and 0.2 nA).

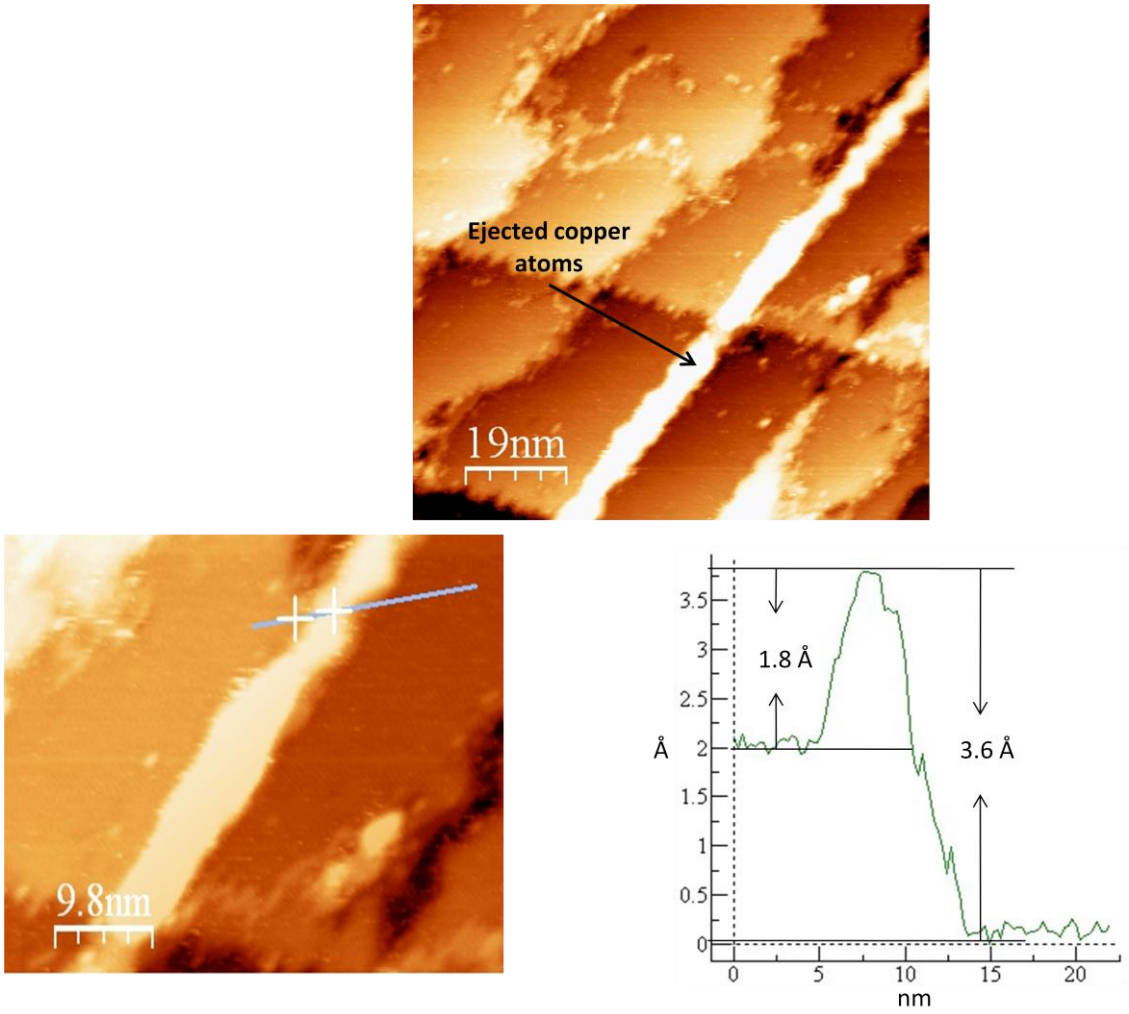

Figure 5.21: STM Image show the ejected copper atoms are aggregate at step edge top of the oxide layer after exposed to 60 L of O_2, (1.0 V, and 0.2 nA).

5.3.5 Interaction of oxygen with clean Cu(100) surface at 250 ^{o}C

Exposure of the Cu(100) sample to 5760 L of oxygen at 250 ^{o}C makes a fully oxidized surface , with oxygen concentration estimated from XPS data (Figure 5.22) to be ($1.4x10^{15}$ cm^{-2}) approximately two monolayers. STM data show several layers with very flat surface of oxygen, and again the end of these layers is sharp triangle at large scale image Figure 5.23. By looking at small scale images of the top of the flat surface we got the atomic resolution of oxygen ($\sqrt{2}x2\sqrt{2}$)R45^{o} clearly, Figure 5.24, and no evidence for c(2x2)-O except may be at some defects on the step edge where copper atoms diffusing during the process of making the missing row structure have been trapped in agreement with the result of Lampimaki et al. [14]. This is shown in the different images in Figure 5.25 where trapped copper aggregates around the ending of oxygen layer (step edge) and phase boundaries between two phase of ($\sqrt{2}x2\sqrt{2}$)R45^{o}. The origin of phase boundaries was not resolved before

[14, 21, 41], but we think the phase boundaries has a relationship between $(\sqrt{2}x2\sqrt{2})R45^{o}$ structure on the upper height terraces and one of two phase at the lower height terraces as shown in Figure 5.26. We assume that one of the $(\sqrt{2}x2\sqrt{2})R45^{o}$ at lower height terraces has the same direction of upper height terraces while the other phase is different because all of the phase boundaries extend from the step edge.

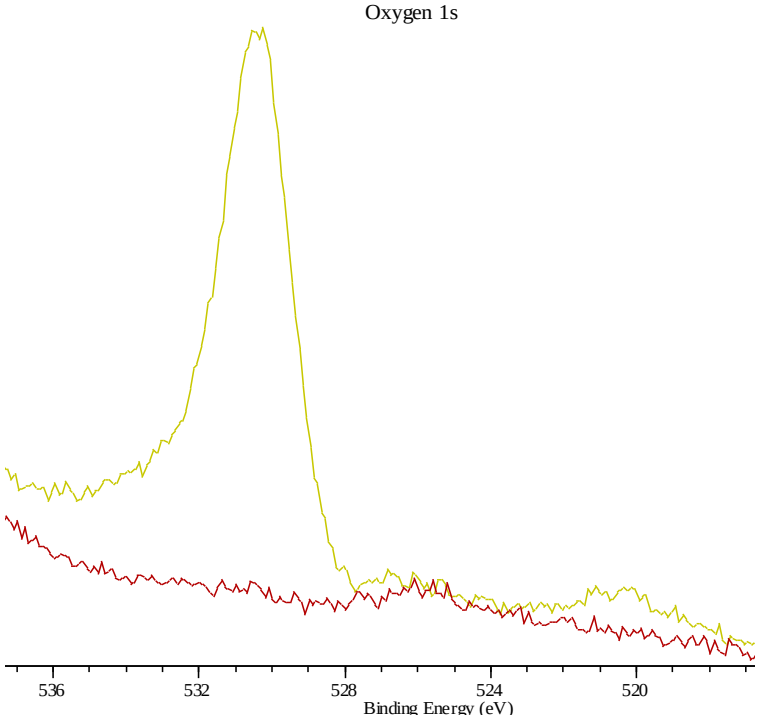

Figure 5.22: XP spectrum of O1s shows the oxygen peak before and after exposure the Cu(100) to 5760 L at 250 ^{o}C.

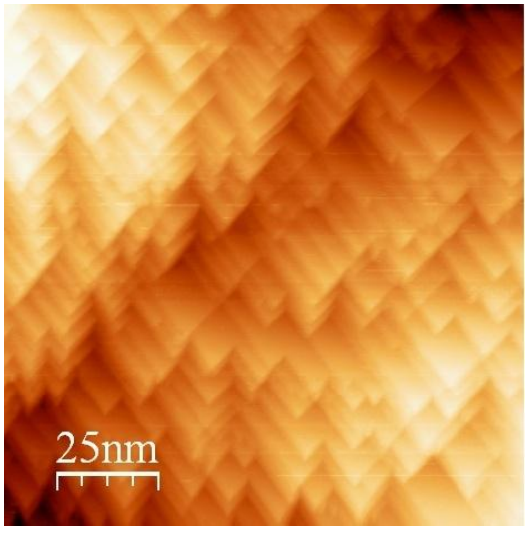

Figure 5.23: large scale STM image shows the multi layer of oxygen by dosing 5760 L of oxygen at 250 ^{o}C on top of Cu(100).

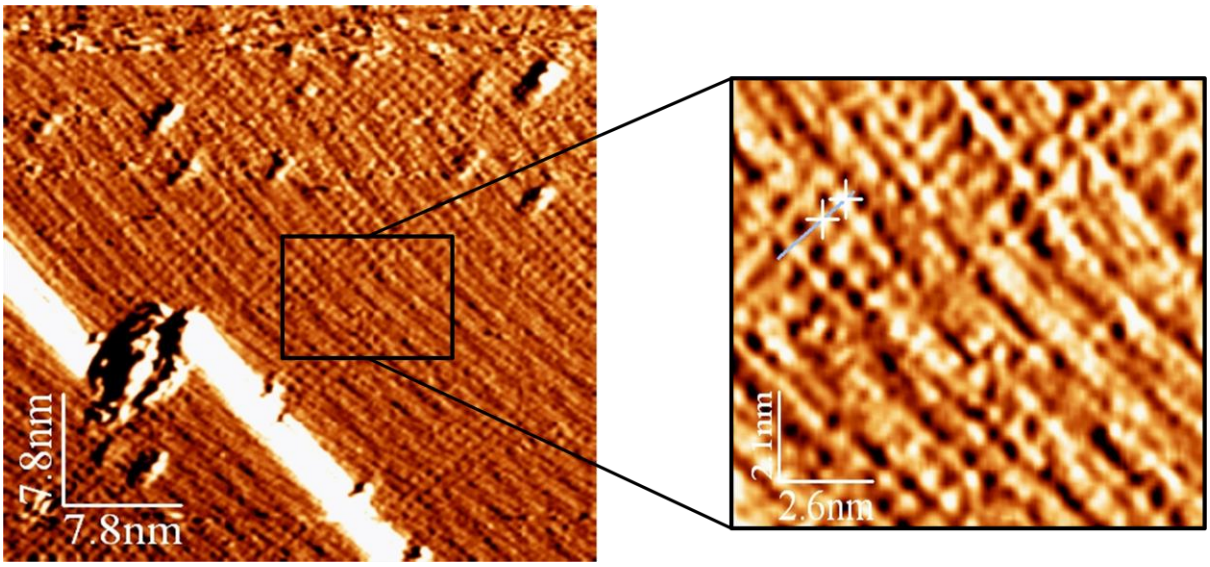

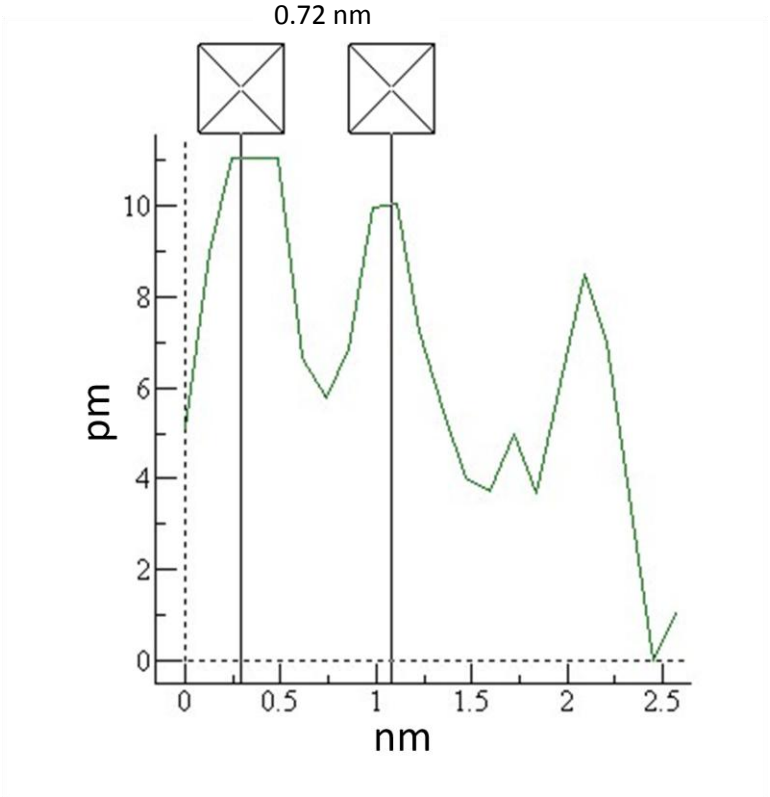

Figure 5.24: STM Images showing the atomic resolution of oxygen ($\sqrt{2}x2\sqrt{2}$)R45^{o} with atomic space about 0.72 nm after exposure of the Cu(100) to 5760 L at 250 ^{o}C (at 1.0 V, and 0.2 nA).

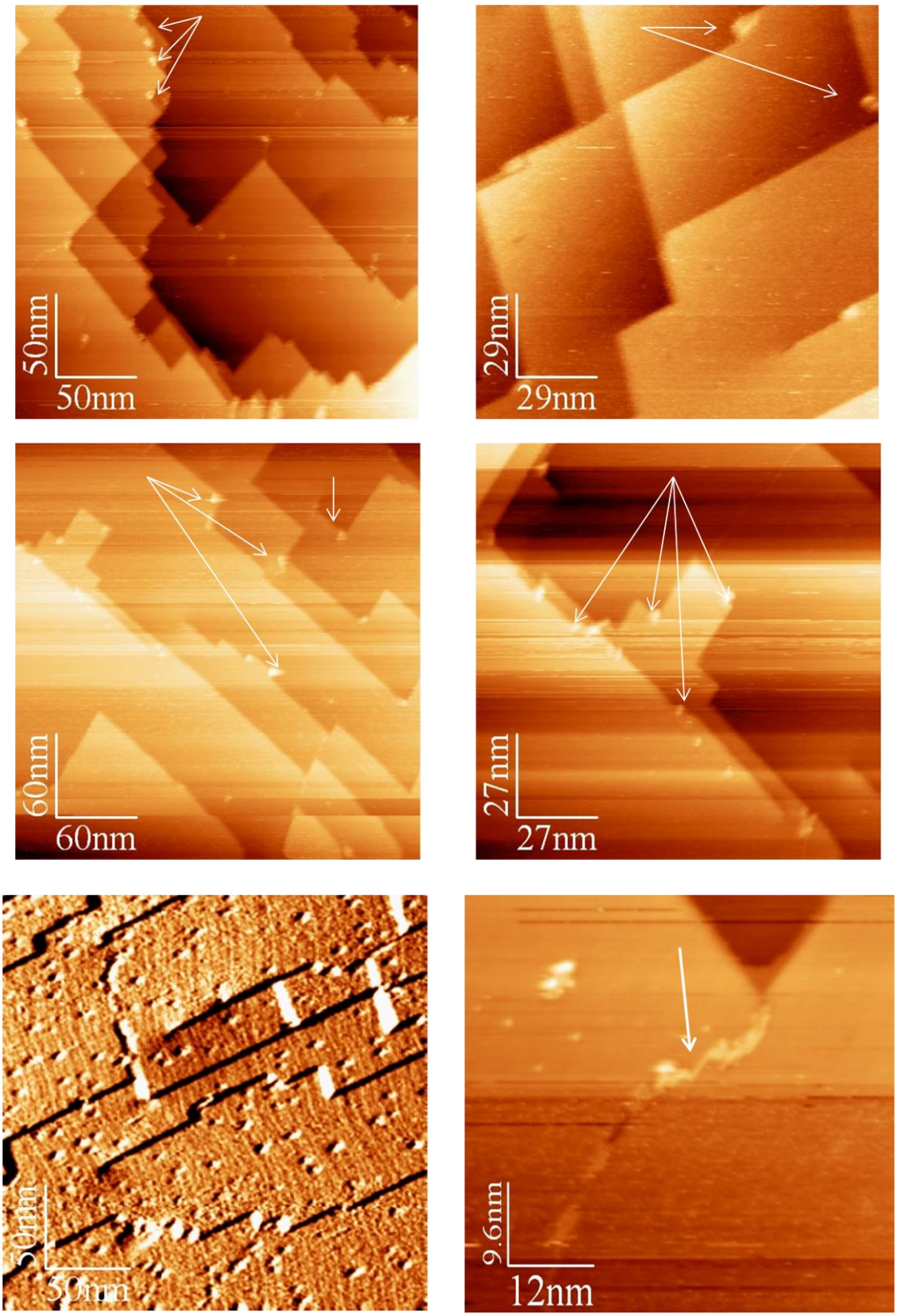

Figure 5.25: STM Images showing the copper atoms aggregating around the end of oxygen layer after exposure the Cu(100) to 5760 L at 250 ^{o}C (at 1.0 V, and 0.2 nA).

.

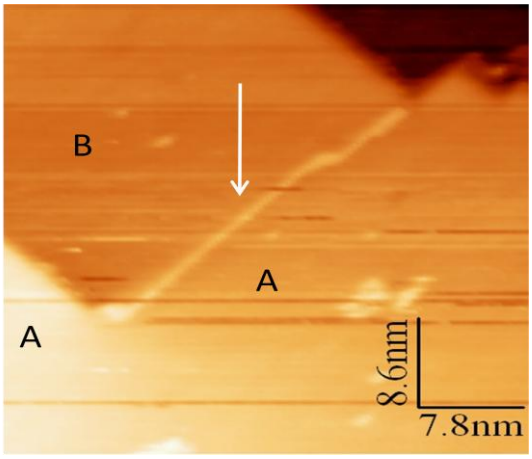

Figure 5.26: STM images show the phase boundaries of two ($\sqrt{2}x2\sqrt{2}$)R45^{o} reconstruction at 1.0 V, and 0.2 nA. Two phases are similar noted with A, while the second reconstruction has a notation B.

5.3.6 Interaction of Cu(100)-O surface with HCl at room temperature

5.3.6.1 Interaction of preoxidised Cu(100) surface at room temperature with HCl.

In this experiment we exposed the Cu(100) sample to oxygen at room temperature for increasing times until a coverage of about one third monolayer of Cu(100) as shown in Figure 5.27, then we exposed the preoxidised surface to HCl at $1x10^{-8}$ mbar for different times at same conditions. Oxygen coverage is decreasing dramatically with a corresponding increase in Cl coverage until about $3.7x10^{14}$ cm^{-2} of oxygen coverage. Subsequently the decreasing of oxygen and increase in Cl is slow and it seem to be the reaction stop as shown in Figure 5.28. Leaving the sample overnight in the background of HCl at a pressure $4.5x10^{-9}$ mbar did not have a big effect, but exposure of the sample to extra 15 L of HCl at $5x10^{-8}$ mbar a large increase in coverage of Cl and the removal of all the oxygen from the surface results. We suppose the interaction of the preoxdised surface to HCl at $1x10^{-8}$ mbar was limited at some point, which expected to be that point shown the small change in the oxygen coverage from $3.73x10^{14}$ cm^{-2} to $3.45x10^{14}$ cm^{-2}. Small changes as well happened to the oxygen coverage even after exposure of the sample to HCl to 114 L, because not enough number of HCl molecule make the transition from "equilibrium state" to the final product, but by increasing the pressure of HCl to $4.5x10^{-9}$ mbar the molecule demand been met and all the oxygen atoms are replaced with Cl, as shown in the following equation

$$2HCl_{(gas)} + O_{(ads)} \rightleftharpoons O\text{-}HCl \xrightarrow{\text{More HCl}} H_2O_{(gas)} + 2Cl_{(ads)}$$

This indicates a pressure dependence of the reaction after the initial process has finished. It can be explain by the need for simultaneous presence of the HCl molecules.

The final Cl coverage is about 8.67×10^{14} cm^{-2} which is more than the saturated coverage (half monolayer) which is illustrated in previous section 5.3.2. As described above, there are two types of oxygen c(2x2)-O, and the missing row structure ($\sqrt{2}x2\sqrt{2}$)R45°; a possible explanation of the reaction kinetics is that one of these structure reacts rapidly with HCl ,while the other reconstruction reacts very slowly.

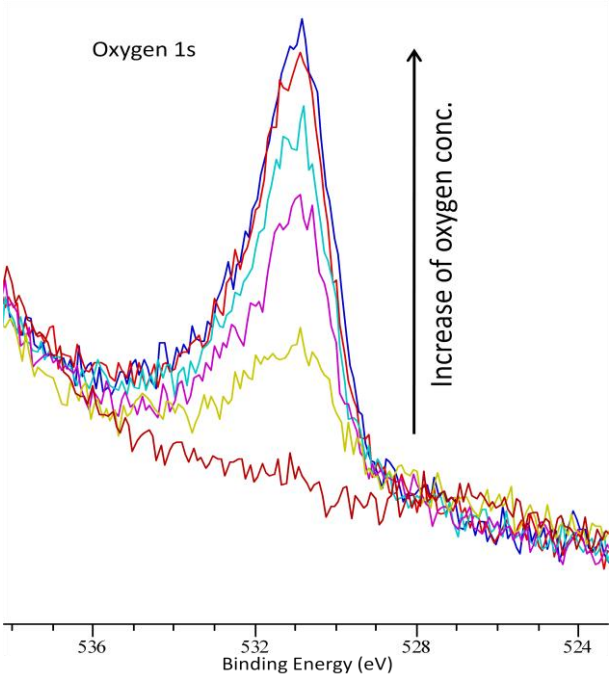

Total exposure/ L	concentration of oxygen/ cm^{-2}
0	0
3	2.01×10^{14}
12	4.10×10^{14}
24	4.63×10^{14}
39	4.99×10^{14}
57	5.58×10^{14}

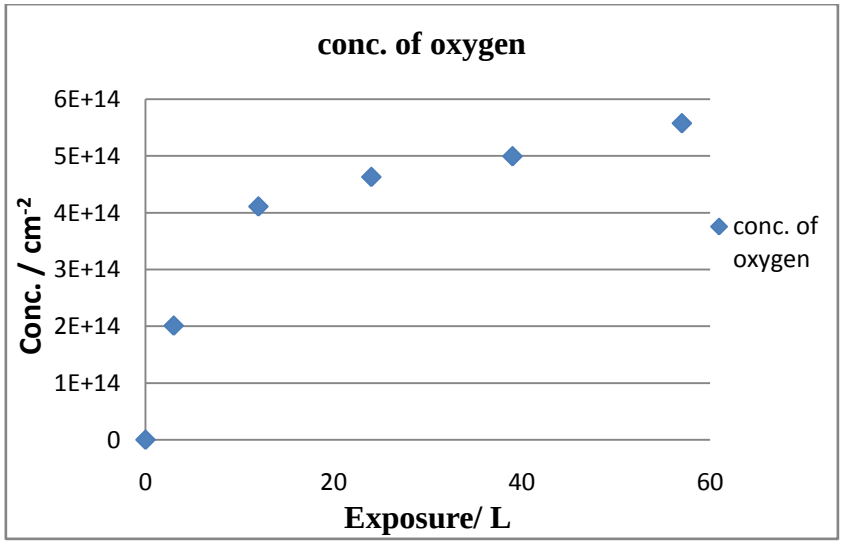

Figure 5.27: XP spectrum of oxygen 1s showing the increase of oxygen with increasing the exposure.

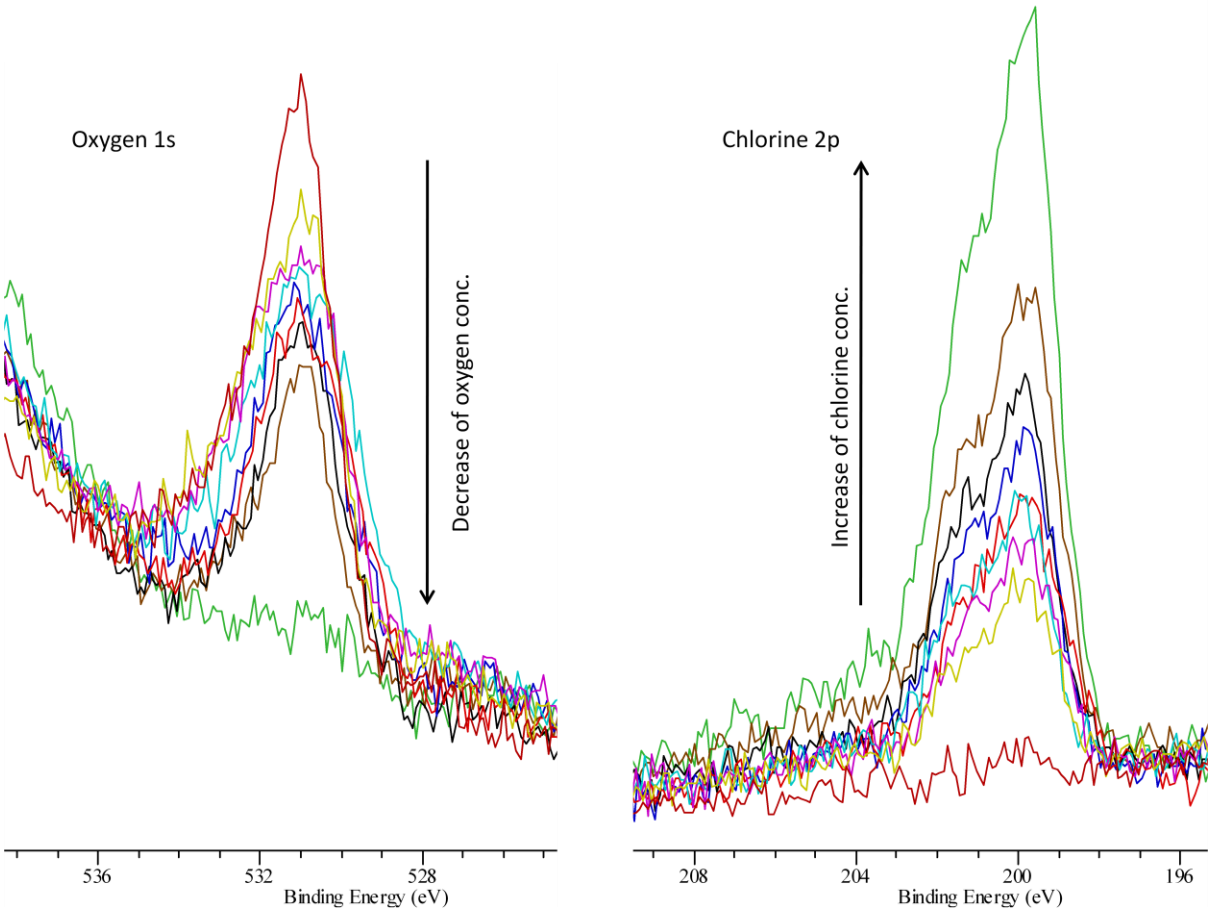

Total exposure to HCl/ L	Conc. of oxygen/ cm^{-2}	Conc. of Cl/ cm^{-2}
0	$5.5x10^{14}$	0
1.5	$5.18x10^{14}$	$2.67x10^{14}$
3	$4.58x10^{14}$	$2.90x10^{14}$
6	$4.48x10^{14}$	$4.10x10^{14}$
12	$4.28x10^{14}$	$5.57x10^{14}$
24	$3.73x10^{14}$	$6.03x10^{14}$
42	$3.45x10^{14}$	$6.57x10^{14}$
OV114	$2.83x10^{14}$	$6.61x10^{14}$
129	0	$8.67x10^{14}$

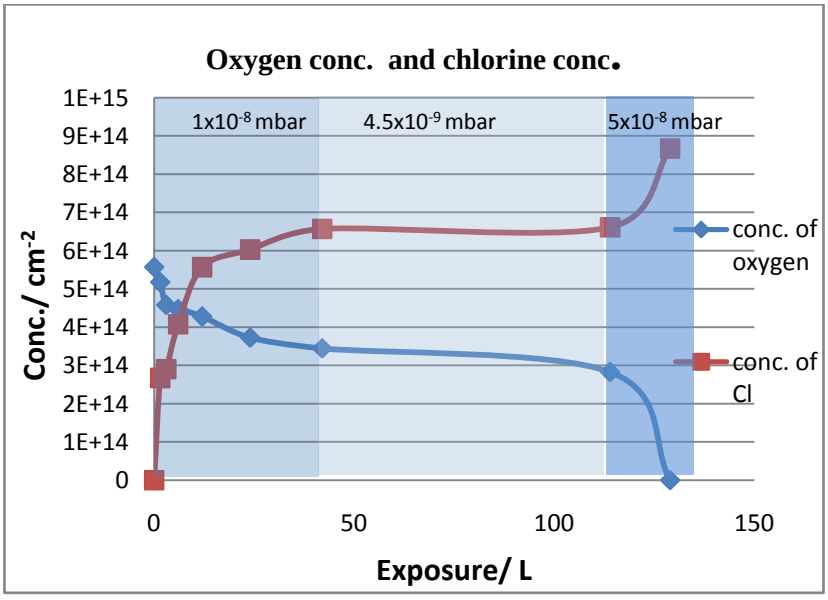

Figure 5.28: XP spectrum of oxygen 1s and Cl 2p showing the decreasing of oxygen concentration and increasing of Cl concentration.

To find out which of the two types of oxygen are more reactive toward HCl we exposed the Cu(100) sample to oxygen, and we stop dosing oxygen before the saturation amount at coverage about $5x10^{14}$ cm^{-2} and as shown in the STM images in Figure 5.29. As described before in section 5.3.3 the interaction of oxygen with Cu(100) surface is started by grooving the surface and then we got two reconstructions of oxygen. The top area is the c(2x2)-O ,while the grooved area is $(\sqrt{2}x2\sqrt{2})R45^{o}$ reconstruction.

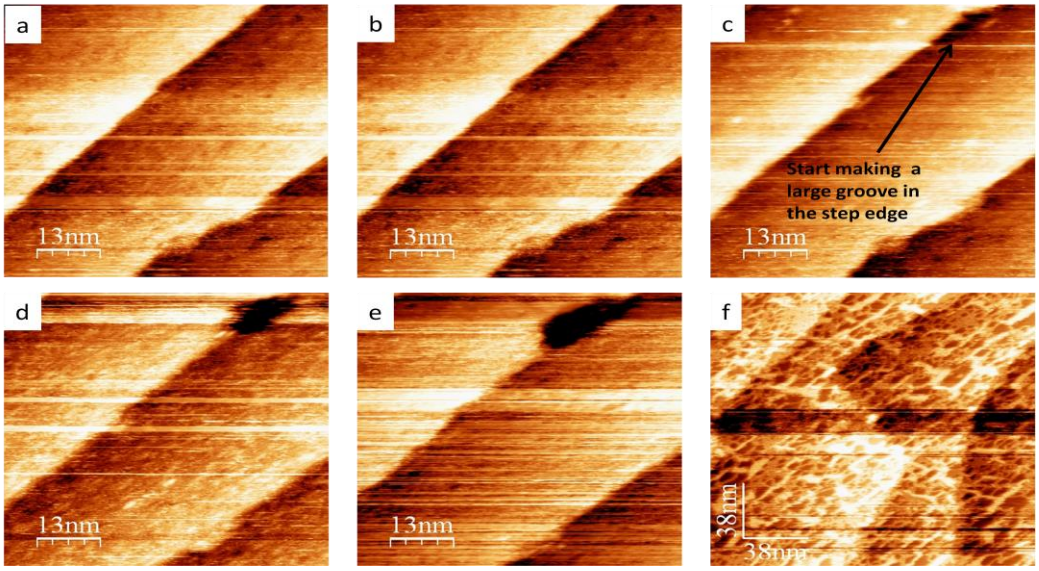

Figure 5.29: (a, b, c, d, and e) STM images of sequential exposure of clean Cu(100) to oxygen. (f) Large scale image show the morphology of the preoxdized surface at coverage about $5x10^{14}$ cm^{-1} at 1.0V, and 0.2 nA.

By exposure of the preoxdized Cu(100) to HCl we found that the change happen very fast on the area which is covered with c(2x2)-O while no change can be detected on the grooved area which is covered by $(\sqrt{2}x2\sqrt{2})R45^{o}$ as shown in Figure 5.30. There are two proposed mechanisms of how HCl is attacking the c(2x2)-O area. First the Cl atoms adsorb between the two neighbours of c(2x2)-O forcing a change in adsorption site as shown in the schematic diagram in Figure 5.30(j) before the complete replacement of oxygen by Cl this would explain the space which is about 7.2 nm as illustrated in the line profile (h) in Figure5.30. This is similar to the proposed mechanism of the interaction of pyridine adsorbed at the preoxidised Cu(110) surface as shown in Figure 5.31[42]. Oxygen adsorbed on Cu(110) made the (2x1)-O reconstruction orientated toward [100] direction. The space between the Cu-O rows was 5.1 Å in the inter-row as shown in schematic diagram in Figure 5.32(a). Exposure of the preoxidised Cu(110) to pyridine at room temperature results in, the inter-row spacing increasing to 7.6 Å as shown in schematic diagram in Figure 5.32(b).

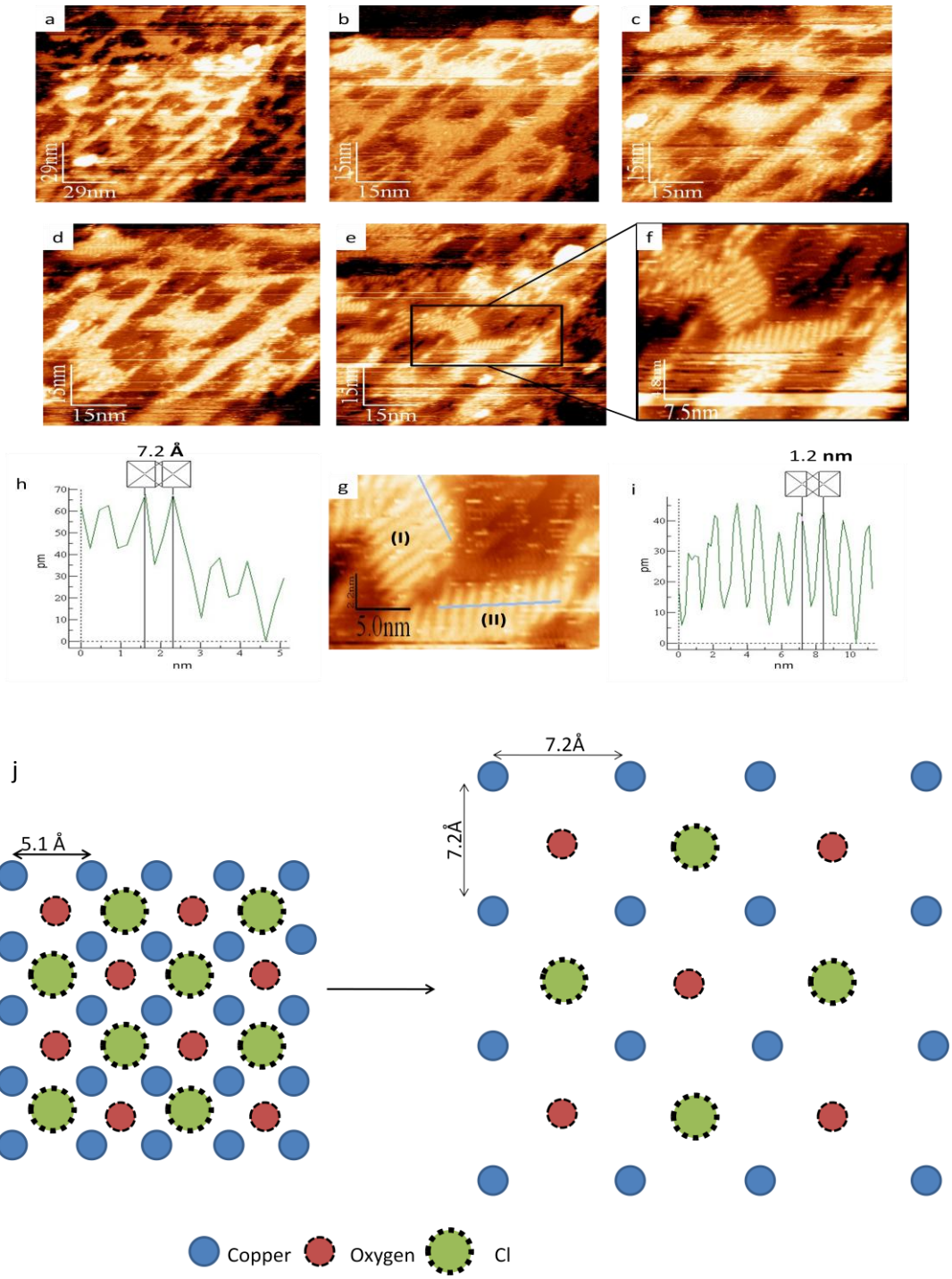

Figure 5.30: (a) STM image of preoxidised Cu(100) surface before dosing HCl. (b, c, d, and e) STM images of sequent exposure of preoxidised Cu(100) surface to HCl. (f, and g) magnificent image showing the effect of dosing HCl on the c(2x2)-O. (h) Line profile show the space in area (I). (i) Line profile show the space in area (II). All images at 1.0V, and 0.2 nA.(j) schematic diagram show the effect of the Cl atoms on the atomic space before the replacement of oxygen atoms.

The XPS result showed the ratio of interaction of pyridine and oxygen on top of preoxdized Cu(110) surface was close to 1:1, suggesting pyridine was adsorbed at the oxygen site on the Cu-O chains while inter-row spacing was a result of laying of pyridine ring which has 5 Å diameter oriented in [110] direction lead to forming the (3x1)-$O_{(ads)}$/pyridine reconstruction because the steric effect of adsorption of pyridine in two adjacent row[42].

The second mechanism which we think is more likely is actually full replacement of c(2x2)-O by Cl and what we see in STM image is two diagonal side of c(2x2)-Cl unit cell, and that explain the 1.2 nm space in line profile (i). The angle between these two sides of diagonal and horizontal is 45^{o} as shown in the schematic diagram 5.33. After dosing more HCl, STM imaging of the surface became more difficult because 0f the significant movement of the surface atoms.

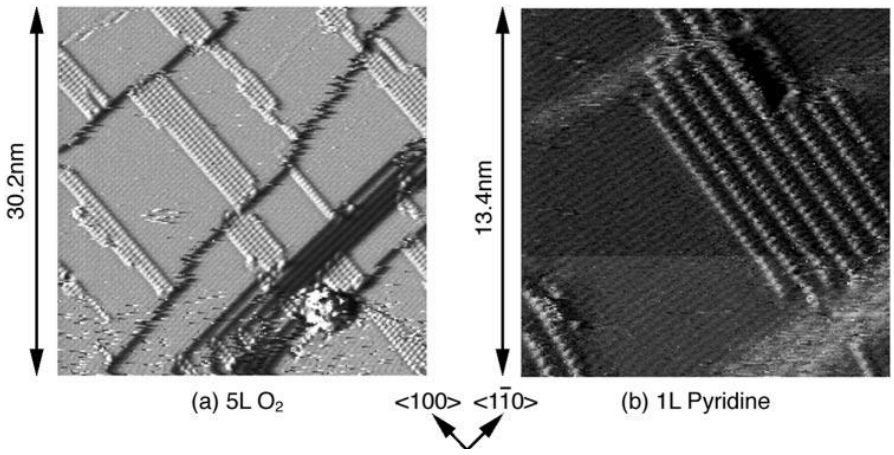

Figure 5.31: The effect of pyridine on preoxdized Cu(110) surface. (a) Cu(110) surface after exposure to 5 L O_2, (b) after exposure to pyridine at room temperature [42].

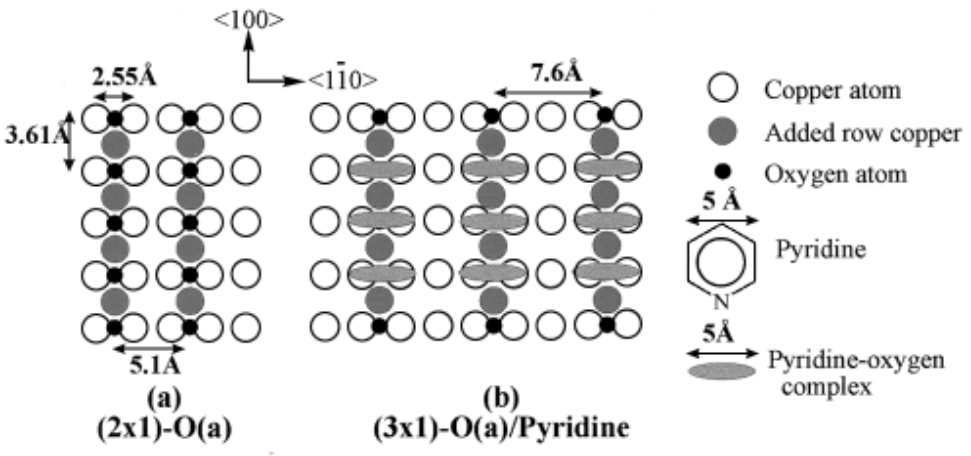

Figure 5.32: (a) Structure of the (2 x1)-O (a) added row reconstruction on Cu(110);(b) proposed structure for pyridine adsorbed at the preoxidised Cu(110) surface[42].

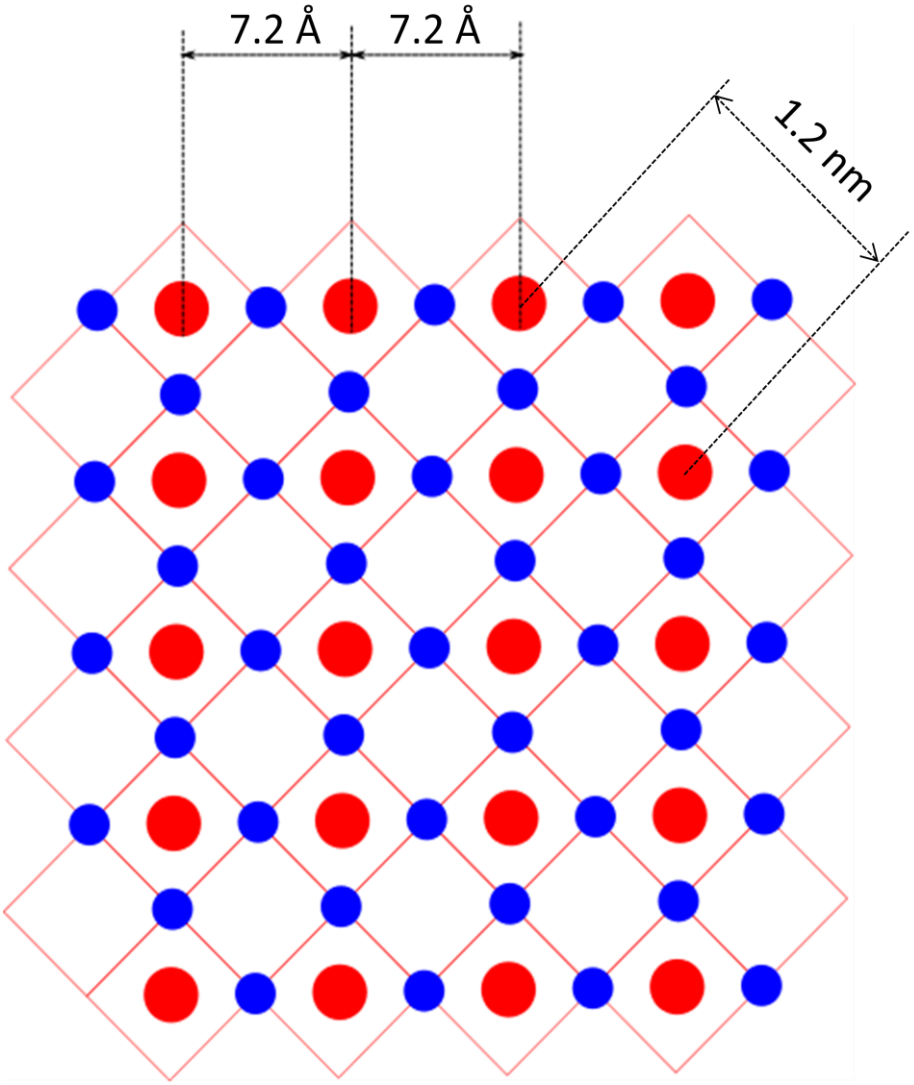

Figure 5.33: schematic diagram showing the two sides of diagonal and horizontal unit cell of c(2x2)-Cl. Oxygen is the red atom, and copper is the blue atom.

5.3.6.2 Interaction of oxygen saturated Cu(100) surface at room temperature with HCl.

In this experiment we exposed the Cu(100) sample to oxygen up to saturation coverage (7.22×10^{14} cm^{-2}) at room temperature confirmed by XPS as shown in Figure 5.34. STM images during exposure were recorded, and it shows the build-up of the oxide layer. Two types of oxygen were found c(2x2)-O, and $(\sqrt{2}x2\sqrt{2})R45^{o}$ as shown in Figure 5.35. The sample picks up some Cl from the background of system about 8.15×10^{13} cm^{-2}, but that doesn't make any change in the STM. Exposure of the oxygen saturated Cu(100) to HCl from 1 to 7 L at room temperature, makes a large decrease in the oxygen coverage and increase of Cl with ratio close to 2:1. Further dose of HCl from 13 to 262 L lead to slight decrease of oxygen coverage and increase of Cl as well but with ratio close to 1:1. The total

of oxygen and Cl coverage is $1.24x10^{15}cm^{-2}$ which is close to one monolayer of Cu(100) ($1.5x10^{15}cm^{-2}$) as described in scheme in Figure 5.37.

STM images of the reaction of HCl with Cu(100) with oxygen present shows poor resolution and is difficult to image. The surface is difficult to image because the huge movement of atoms which happened at the beginning of the reaction, but after leaving the reaction to settle down, three structures were found in the surface as shown in Figure 5.38, two structures in the terraces A, B and one at the step edge C. We think that, structure A is the missing row reconstruction $(\sqrt{2}x2\sqrt{2})R45^{o}$ of oxygen as shown in the Figure 5.39 which did not react yet with HCl. Structure B is assigned to the c(2x2)-Cl which is formed by replacement of c(2x2)-O and confirmed by the measuring the atomic space which is equal 5.2 Å as shown in the Figure 5.40. Structure C is assigned to copper chloride island on top of Cl/Cu surface.

We assume that, at the beginning of reaction of saturated Cu(100) with oxygen, with HCl the Cl atoms replace the oxygen atoms which have c(2x2) reconstruction and make the exact reconstruction as a quick step. Every two HCl molecules replace one atom of oxygen as illustrated in the following equation:

$$O + 2HCl \rightarrow 2Cl + H_2O$$

That agrees very clearly with XPS data of dosing HCl from 1 to 7 L which shows a ratio of increase of Cl coverage vs. decrease of oxygen coverage of 2:1.

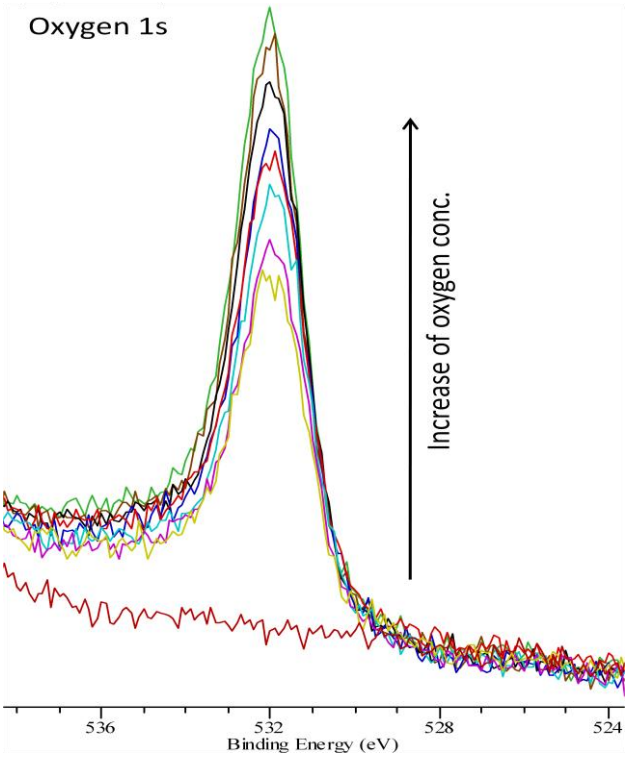

Total exposure/ L	Conc. of oxygen/ cm^{-2}
0	0
30	$4.31x10^{14}$
60	$5.14x10^{14}$
120	$5.60x10^{14}$
180	$6.02 x10^{14}$
300	$6.58 x10^{14}$
600	$6.95 x10^{14}$
1050	$7.19 x10^{14}$
1650	$7.22 x10^{14}$

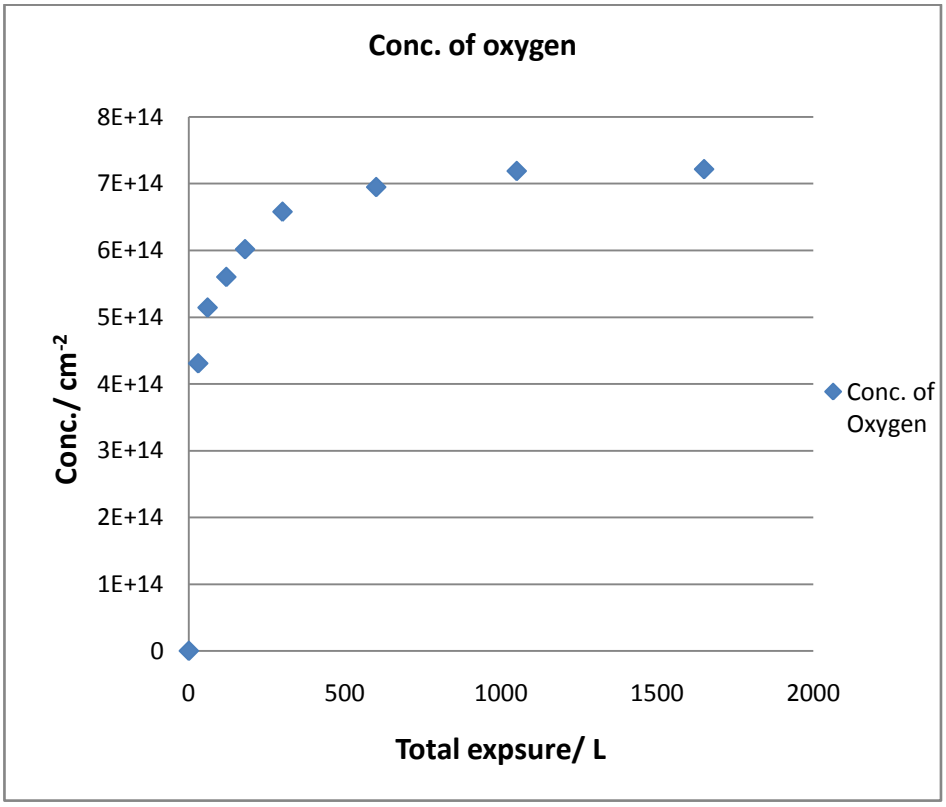

Figure 5.34: XP spectrum of oxygen 1s shows the increase of oxygen coverage with increasing the exposure.

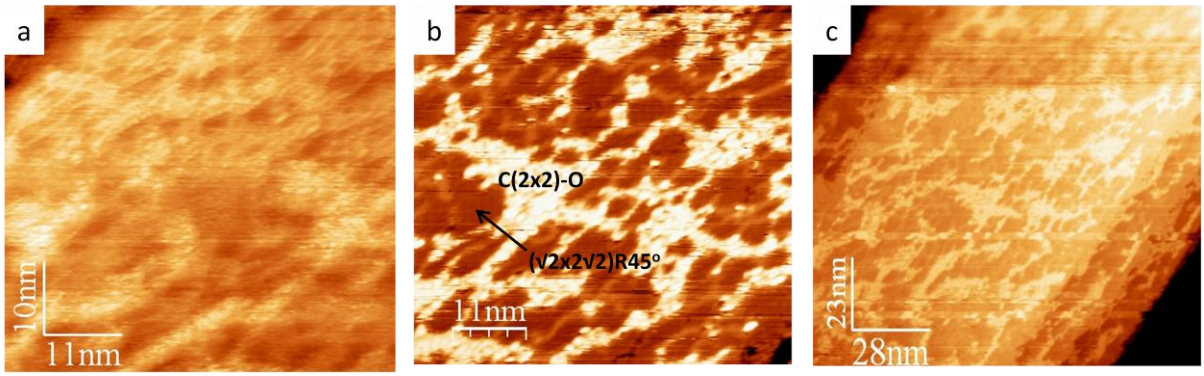

Figure 5.35: STM images of Cu(100) exposure to oxygen up to saturation coverage. (a) STM image of Cu(100) 700 L. (b) STM image at saturation coverage, shown the two types of oxygen reconstruction. (c) Large scale image of saturate Cu(100) surface. All images at 1.0V, and 0.2 nA.

The second reconstruction $(\sqrt{2}x2\sqrt{2})R45^{o}$ of oxygen which is thermodynamically favourable and has a low surface energy reacts with HCl by a different mechanism. By dosing $HCl_{(gas)}$ at $(\sqrt{2}x2\sqrt{2})R45^{o}$ we got $HCl_{(ads)}$, oxygen and OH at the Cu(100) as shown in the following equations.

$$HCl_{(gas)} \rightarrow HCl_{(ads)} \quad (1)$$

$$O_{(ads)} + HCl_{(ads)} \rightarrow Cl_{(ads)} + OH_{(ads)} \quad (2)$$

The product in equation (2) is not stable and by further dose of HCl, the OH molecule produced $H_2O_{(gas)}$ and the oxygen atoms go into the surface and made subsurface oxygen as shown in the following equation:

$$OH_{(ads)} + O_{(ads)} \xrightarrow{HCl} Cl_{(ads)} + H_2O_{(gas)} + O_{(subsurface)} \quad (3)$$

The presence of $O_{(ads)}$, $OH_{(ads)}$, and $H_2O_{(ads)}$ have been reported by Roberts et al. using XPS of interaction of HCl with the preoxidised Cu(111) at low temperature [43]. The overall ratio of interaction of HCl and oxygen in equations 2, and 3 is 2:1, and this agrees with the XPS data which shows a decrease of oxygen coverage during the dose of HCl. These data are similar to the previous study done by Suleiman et al. in 2010 using density functional theory calculations [25]. They found that, the presence of chlorine on the Cu(100) surface leads to subsurface diffusion of oxygen by reducing the energy barrier for diffusion of oxygen into the

lattice and they reported the formation of chlorine mono oxide (ClO), as shown in Figure 5.41. Similar observations were found with Ag(111) [44].

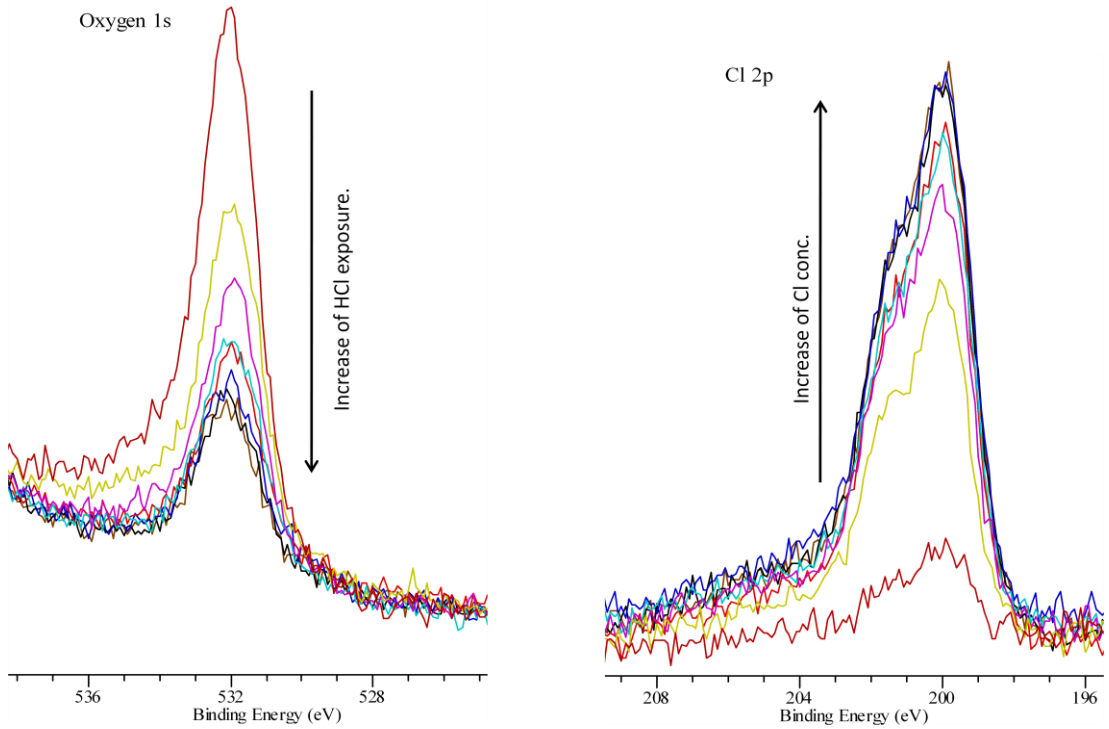

Total exposure/ L	conc. of oxygen/ cm^{-2}	conc. of Cl/ cm^{-2}
0	$7.22x10^{14}$	$8.15x10^{13}$
1	$6.93x10^{14}$	$1.24x10^{14}$
4	$4.49x10^{14}$	$6.14x10^{14}$
7	$3.81x10^{14}$	$8.50x10^{14}$
13	$3.04x10^{14}$	$9.40x10^{14}$
28	$2.73x10^{14}$	$9.74x10^{14}$
88	$2.57x10^{14}$	$9.85x10^{14}$
160	$2.36x10^{14}$	$9.95x10^{14}$
262	$2.35x10^{14}$	$9.95x10^{14}$

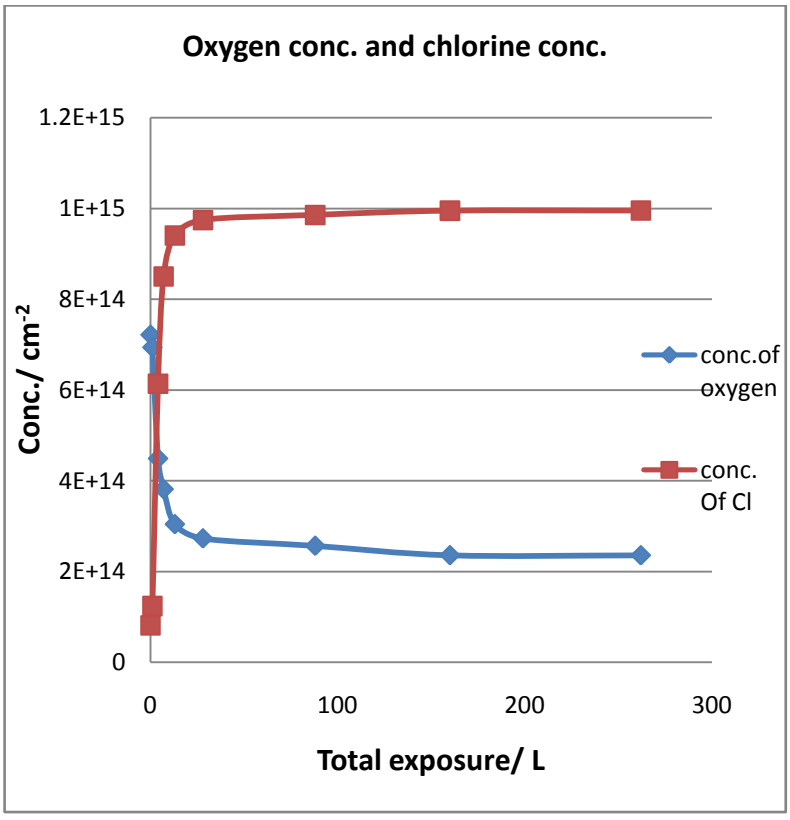

Figure 5.36: XP spectrum of oxygen 1s and Cl 2p shows the decreasing of oxygen concentration and increasing of Cl concentration.

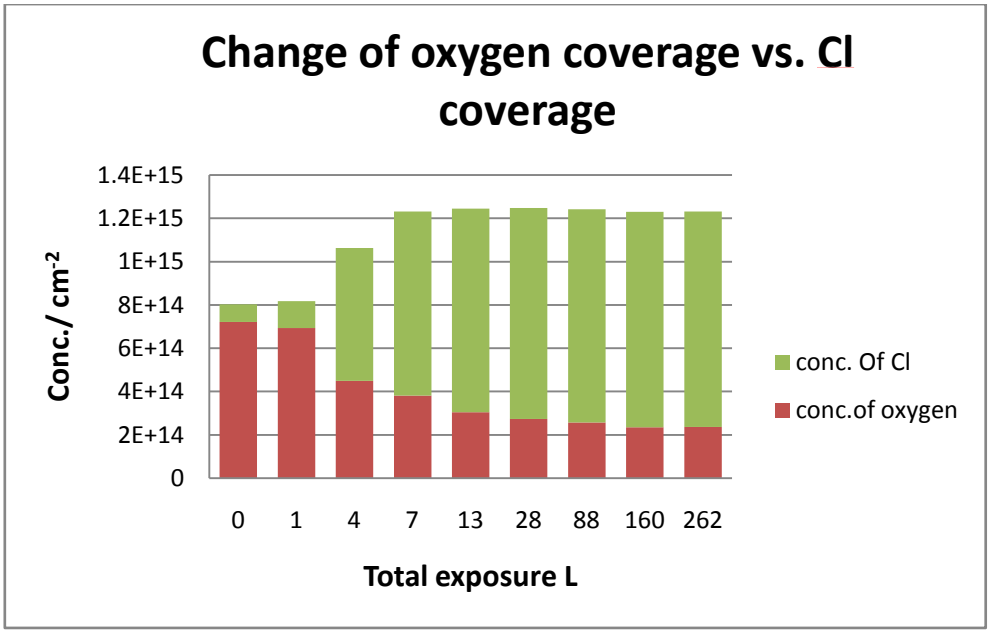

Figure 5.37: schematic diagram show the increase of Cl coverage vs. the oxygen coverage top of saturation Cu(100) with oxygen.

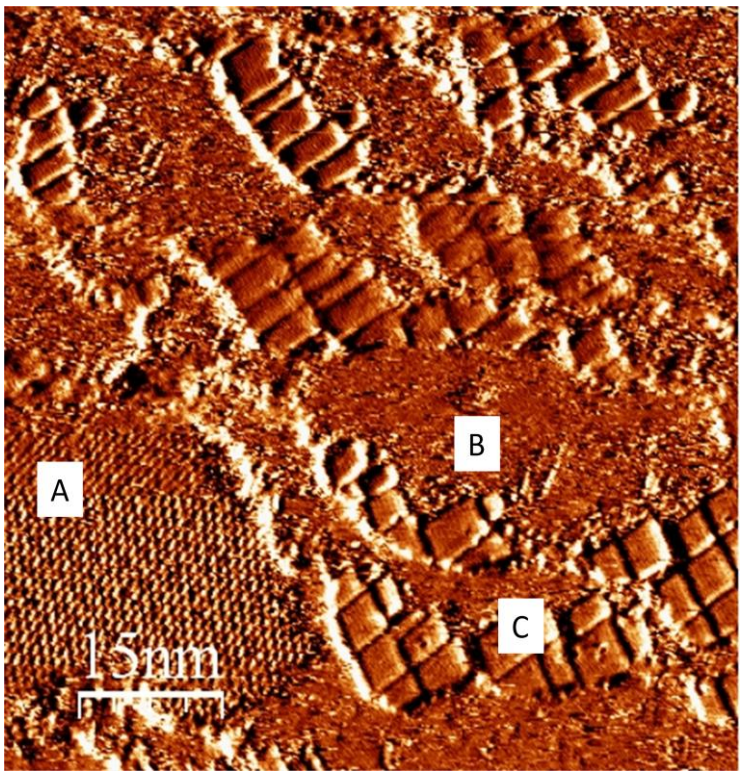

Figure 5.38: STM image of the saturated Cu(100) with oxygen reacted with HCl at room temperature. A represents the missing row reconstruction, B represents the c(2x2)-Cl, and C is copper chloride island top of Cl/Cu surface. Image at 1.0V, and 0.2 nA.

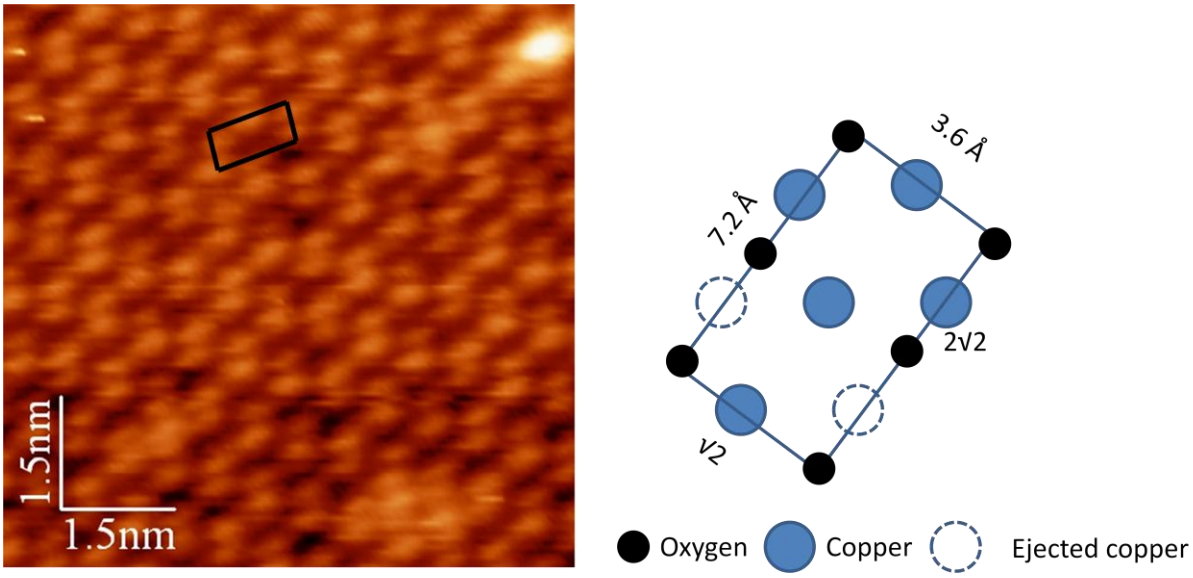

Figure 5.39: STM image of the missing row reconstruction (√2x2√2)R45^{o} at terraces. Image at 1.0V, and 0.2 nA.

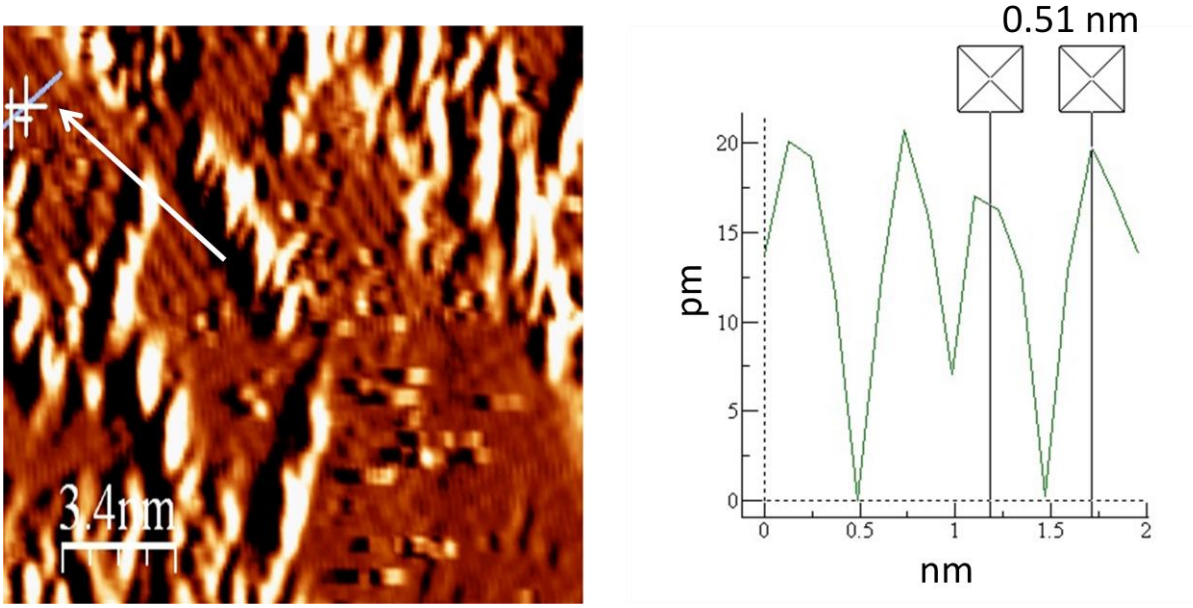

Figure 5.40: STM image of c(2x2)-Cl at terraces. Image at 1.0V, and 0.2 nA.

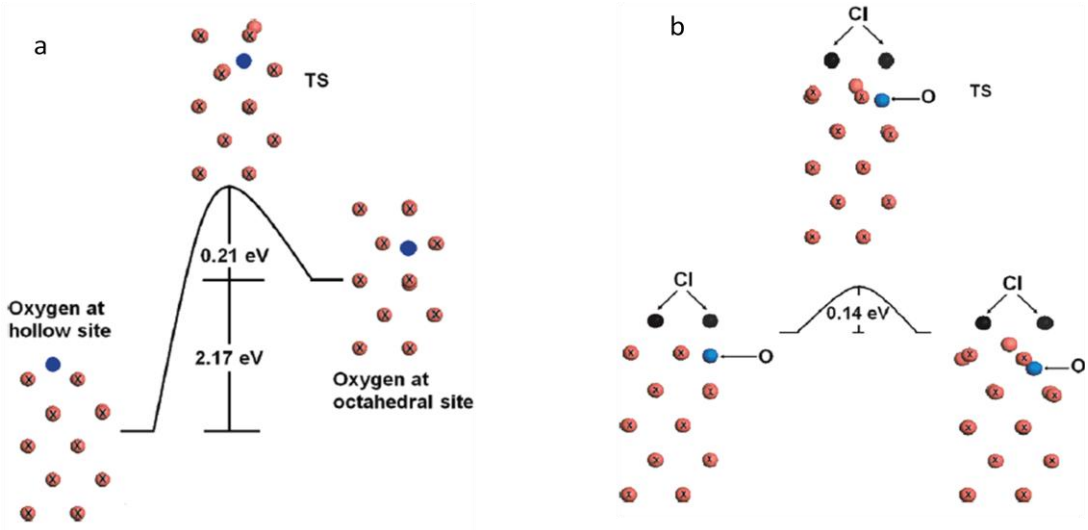

Figure 5.41: Energy diagram of side views for the diffusion of an oxygen atom (shown in blue) (a) on the clean Cu(100) surface, and (b) Cu(100) at presence of chlorine. Red atoms with a symbol X are the front copper atoms while the unmarked red (copper) atoms lie behind, oxygen blue atom, chlorine black atom, and TS denotes the transition state [25].

The STM image in Figure 5.42 may give an explanation of how HCl reacts with the oxygen on top Cu(100), but with $(\sqrt{2}x2\sqrt{2})R45^{o}$ oxygen unlike work of Suleiman et al. [25] who made their calculations on c(2x2)-O. STM image 5.42(a) shows the oxygen $(\sqrt{2}x2\sqrt{2})R45^{o}$ reconstruction when start react with HCl. A black arrow in Figure 5.42(a) assigned to new feature has been observed on the surface before formation of the new surface in Figure 5.42(b). Line profile of the new reconstruction in Figure 5.42(c, and d) shows 1.2 nm spaces. The new reconstruction has two possibilities.

First is the formation of an instantaneous c(4x4) complex of HCl molecules, and oxygen before making the c(2x2)-Cl. A similar model has been suggested by Suleiman et al.[25], and Jia et al.[44] of making a complex p(2x2) reconstruction of oxygen molecules and chlorine atoms. In this case the motivation behind making the instantaneous c(4x4) reconstruction was to reduce the change which happened to the surface energy of $(\sqrt{2}x2\sqrt{2})R45^{o}$ oxygen which have more stability than c(2x2)-O top of Cu(100) [12, 45]. But in our case this suggestion is not acceptable because the formation of c(2x2)-Cl from c(4x4) reconstruction requires a lot of change in the surface energy.

The second is the most likely suggestion since it involves a low amount of energy and is this is that, the reconstruction in Figure 5.42(b) is simply the c(2x2)-Cl, which form after reaction of HCl with $(\sqrt{2}x2\sqrt{2})R45^{o}$ of oxygen reconstruction which lead to adsorbed HCl in the molecular form before removing the oxygen and some of that oxygen being subsurface as shown in the following equation:

$$2HCl + 2O_{(ads)} \rightarrow \{ClH\text{-}O\text{-}HCl\}_{(ads)} + O_{(ads)} \rightarrow H_2O_{(gas)} + O_{(subsurface)}\downarrow + 2Cl_{(ads)}$$

The line profiles in Figure 5.42 (c, and d) represents the diagonal space of the c(2x2)-Cl not the instantaneous c(4x4) in agreement with the previous result in section 5.3.6. The marked features in Figure 5.42(a, and b) have a lot of possibility. They could be one of the following features; HCl, OH, Cu, and H_2O. Presence of OH and H_2O is acceptable at low temperature but is not likely at room temperature according to the previous work [43]. So these features could be HCl adsorbed in the molecular form in agreement with the previous work which suggested the presence of oxygen on the Cu(100) surface leads to adsorbed chlorine in the molecular form [25], alternatively they could be due to Cu atoms moving on the surface which are released from the surface as a result of reduction of the missing row structure of oxygen by HCl.

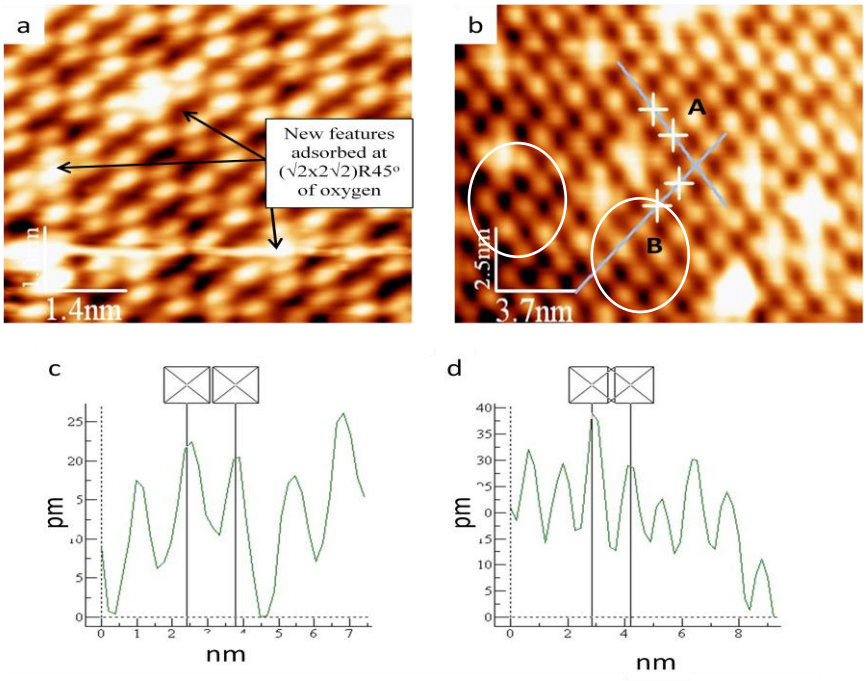

Figure 5.42: (a) STM images show the $(\sqrt{2}x2\sqrt{2})R45^{o}$ of oxygen after exposure to HCl. (b) New surface of chlorine atoms and after remove the oxygen. (c, and d) are the line profile of two directions of atoms A, and B respectively, the space between atoms in two direction are 1.2+0.2 nm.

STM images in Figure 5.43 show the formation of the island of Cu-Cl on top of what we suggest to be a c(2x2)-Cl, surface. These results are in agreement with results of interaction of HCl with oxygen on top of Cu(110) [46, 47] which they show that the presence of oxygen plays an important role in the formation $CuCl_2$ island on Cu(110) surface, but these islands were not stable at room temperature and they disintegrated to c(2x2)Cl, as shown in Figure 5.44. In our case there is no direct evidence in XPS of formation of $CuCl_2$ which would be shown bty the satellite patterns of Cu^{2+}.

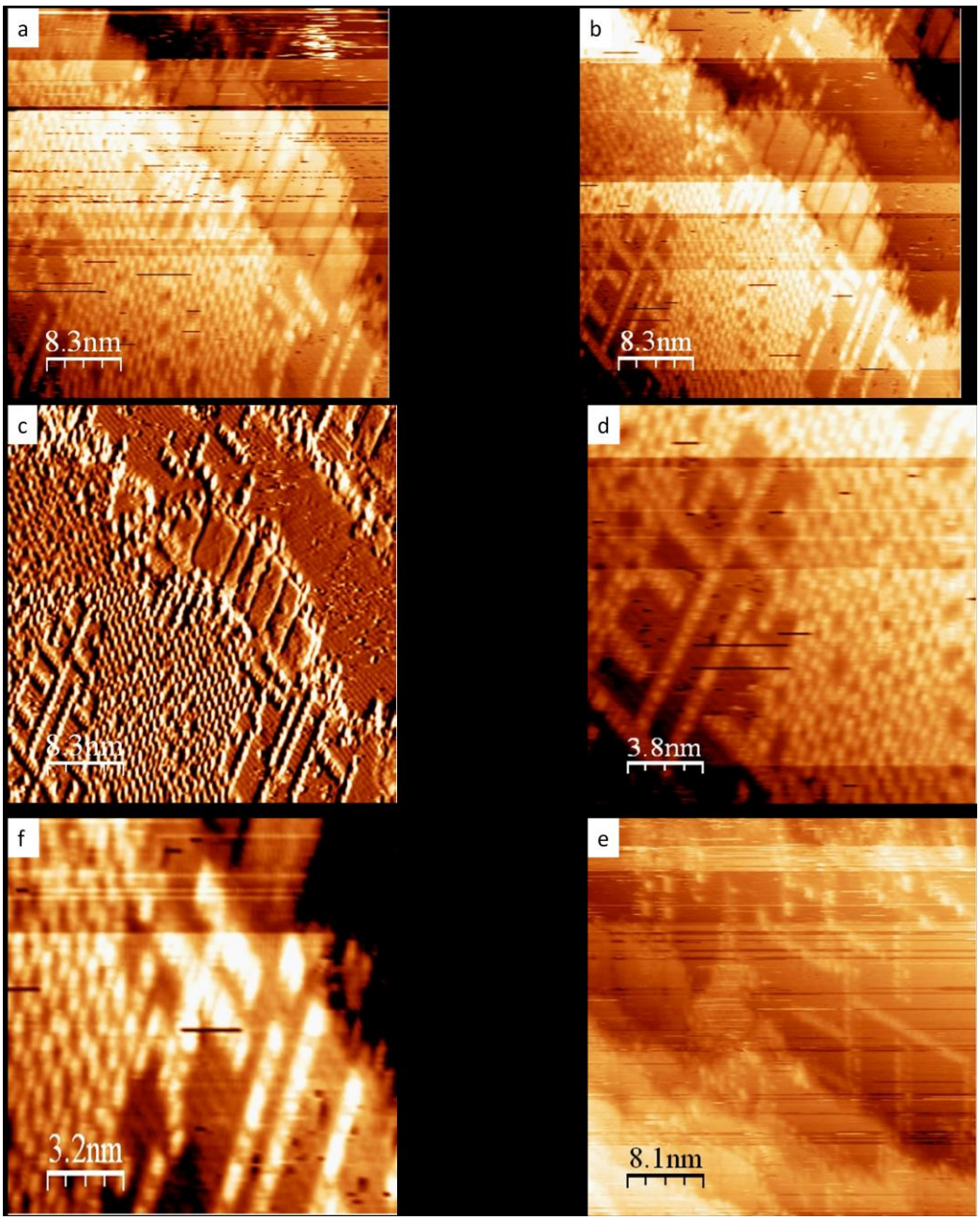

Figure 5.43: (a, b, c, d, and f) STM images show the final stage of chlorine atomic movement on top of Cu(100)/Cl surface. (f) Shows the island border before forming the Cu-Cl islands.

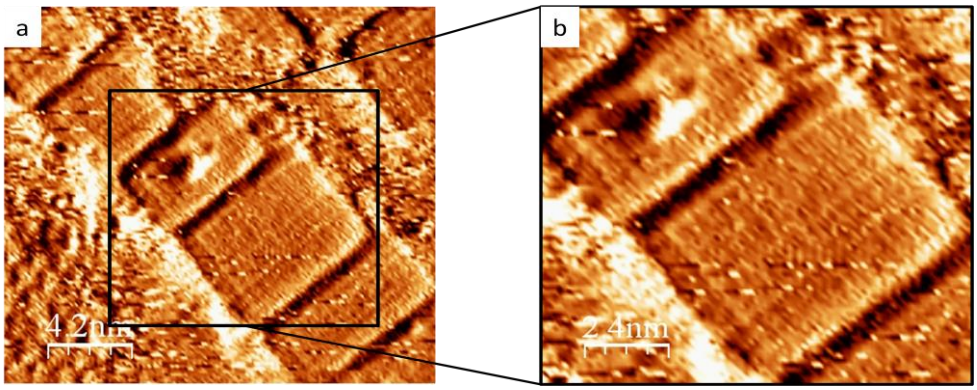

Figure 5.44: (a) STM image of copper chloride formed at step edge. (b) Magnified image shows the boundary between two islands.

5.3.7 Interaction of Cu(100) surface oxidised at 250 ^{o}C, with HCl at room temperature.

In this experiment, the Cu(100) surface was oxidised at 250 ^{o}C (as described above in section 5.3.3) and after cooling down to room temperature was exposed to 270 L HCl. XP spectra show a decrease of oxygen coverage from $1.25x10^{15}$ cm^{-2} to $5.27x10^{14}$ cm^{-2} while increase of Cl coverage to $1.24x10^{15}$ cm^{-2} as shown in Figure 5.45. STM of effect of dosing HCl at room temperature shows the grooves are developed in the oxygen layer. These grooves are attributed to Cl atoms setting in the missing row structure of oxygen as shown in Figure 5.46. Width of these grooves in the surface is 1.4 nm which is equal to double of the space of missing row structure as describe in the line profile in Figure 5.47. By dosing more HCl, the ordered structure of oxygen is destroyed and small islands are developed as shown in Figure 5.48. These islands assigned to Cu-Cl islands forming as a result of interaction HCl with mobile atomic copper produced from ejecting the copper atom when the oxygen missing row structure devolved. These islands are sticking around step edges and on top of terraces of c(2x2)-Cl surface as shown in Figure 5.49. The residual concentration of oxygen which is shown in the XPS data in Figure 5.45 is assigned to the subsurface oxygen. This system can be described in two parts; first part is Cu–Cl surface coming as a result of interaction of HCl atoms with top oxide layer which may not bond as strongly as much as the underneath oxide layer which is bonding directly to the copper surface. We think the top oxide layer is reacting with HCl in 2:1 ratio which agrees with XPS data as illustrated in the following equation:

$$O + 2HCl \rightarrow 2Cl + H_2O$$

Second are small Cu-Cl islands which explain the excess in the Cl concentration as shown in scheme in Figure 5.50.

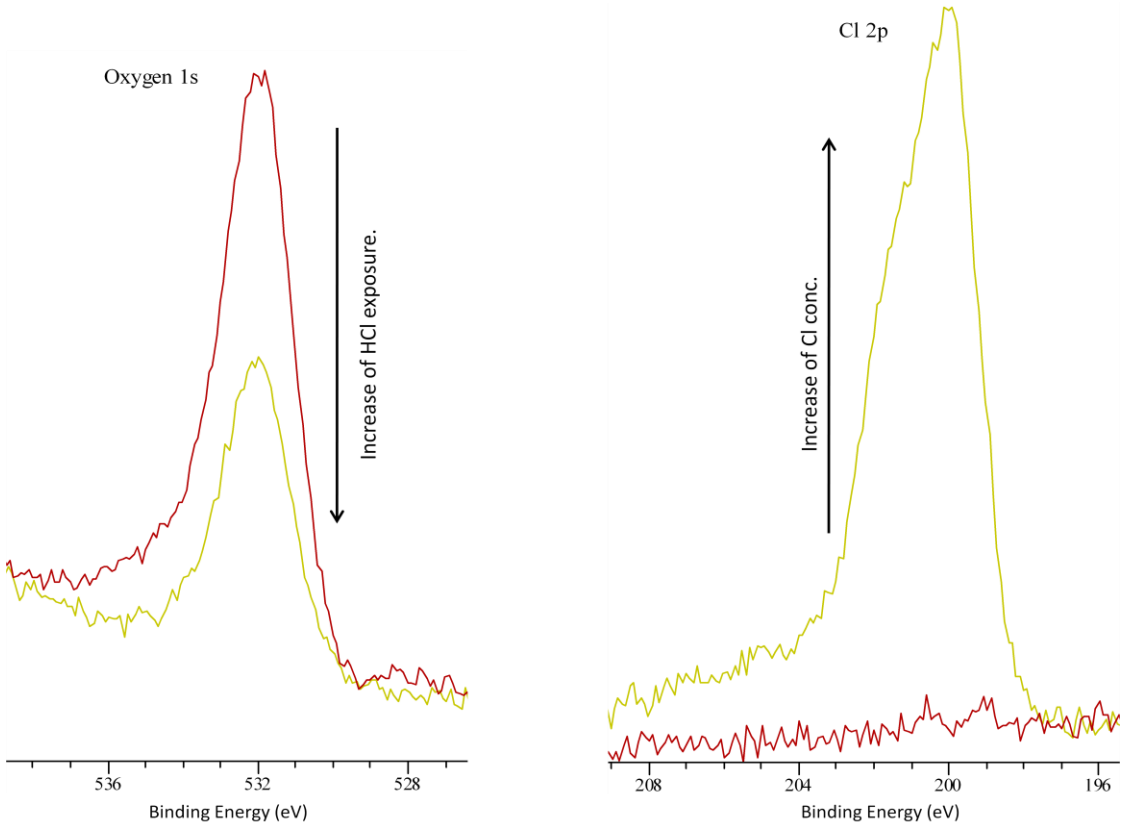

Figure 5.45: XP spectrum of oxygen 1s and Cl 2p shows the decreasing of oxygen concentration and increasing of Cl concentration.

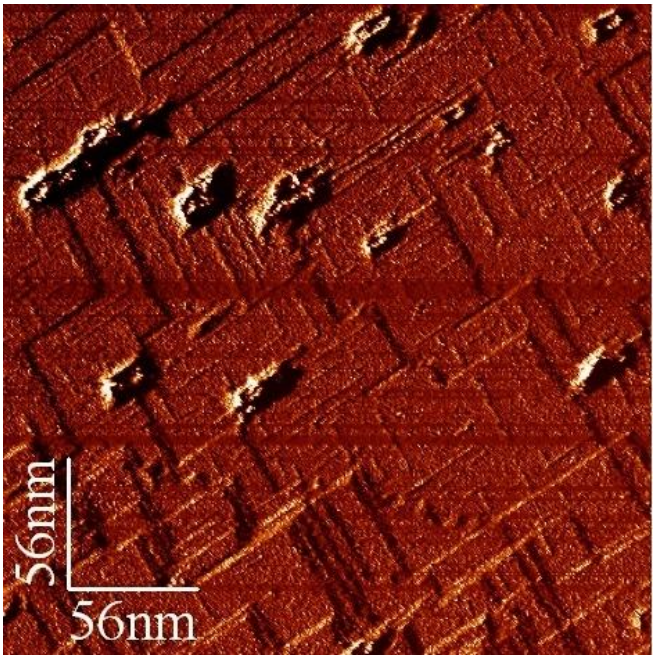

Figure 5.46: STM image of grooved oxygen after dosing HCl.

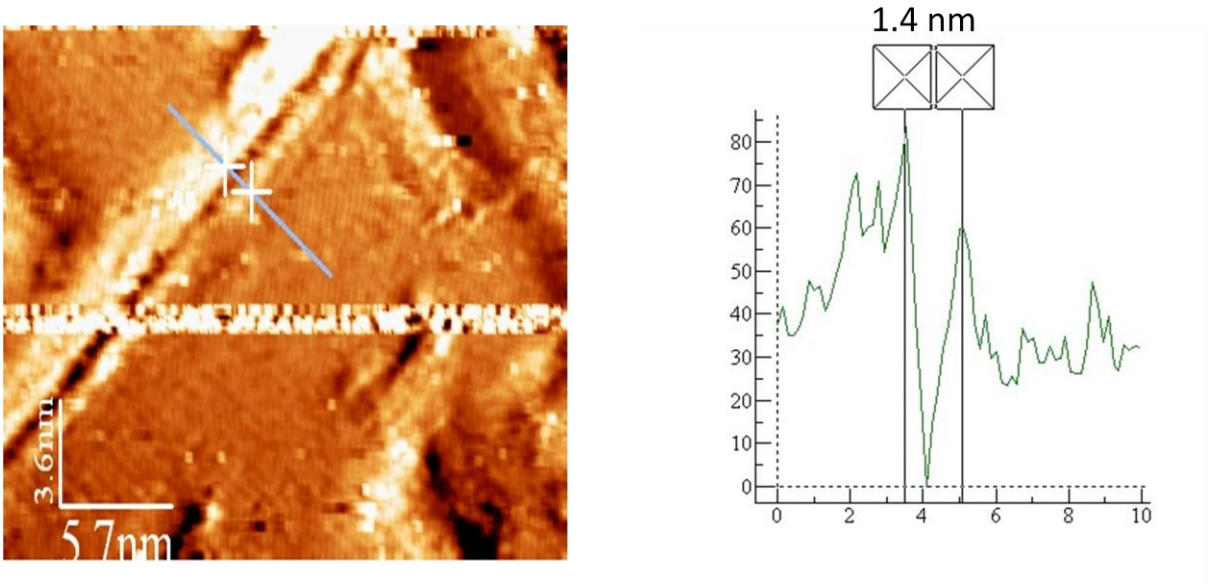

Figure 5.47: (a) STM image of grooved oxygen after dosing HCl. (b) line profile shows the wide of groove 1.4 nm.

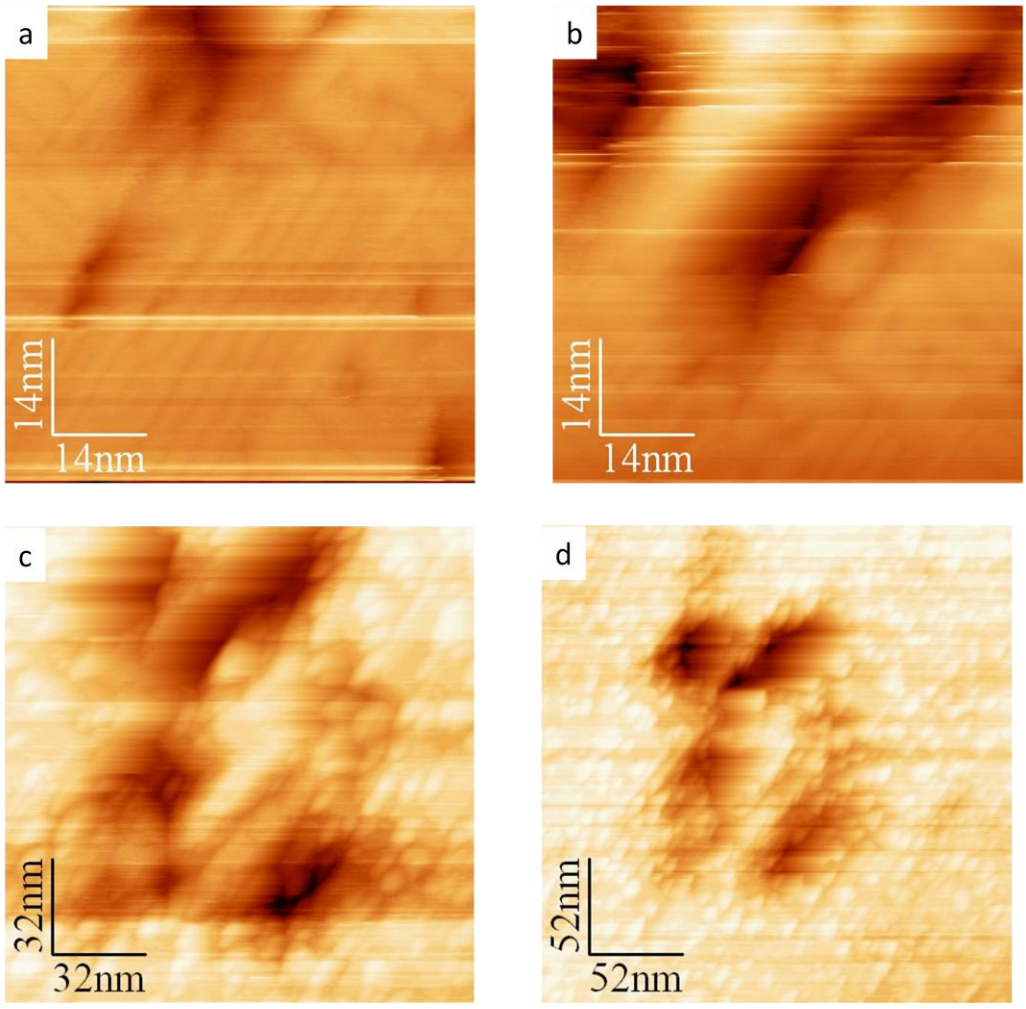

Figure 5.48: Series of STM images of Cu(100)/O after dosing HCl.

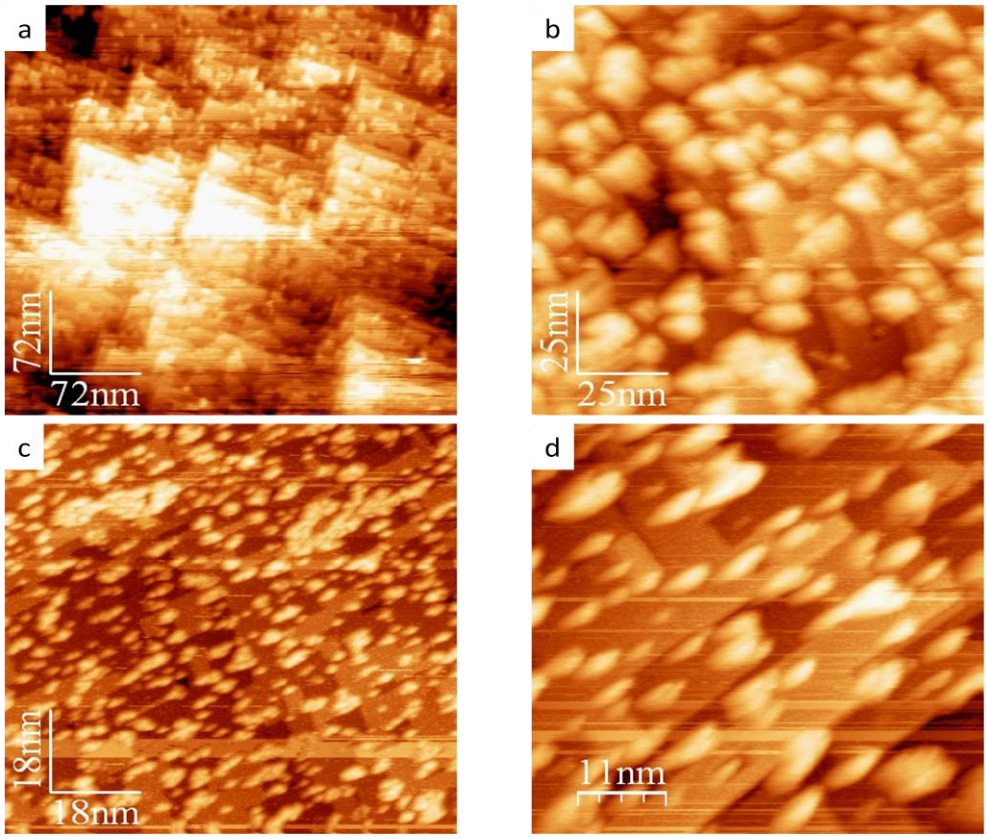

Figure 5.49: STM images shows the different size of Cu-Cl islands are sticking around step edge and on top of terraces

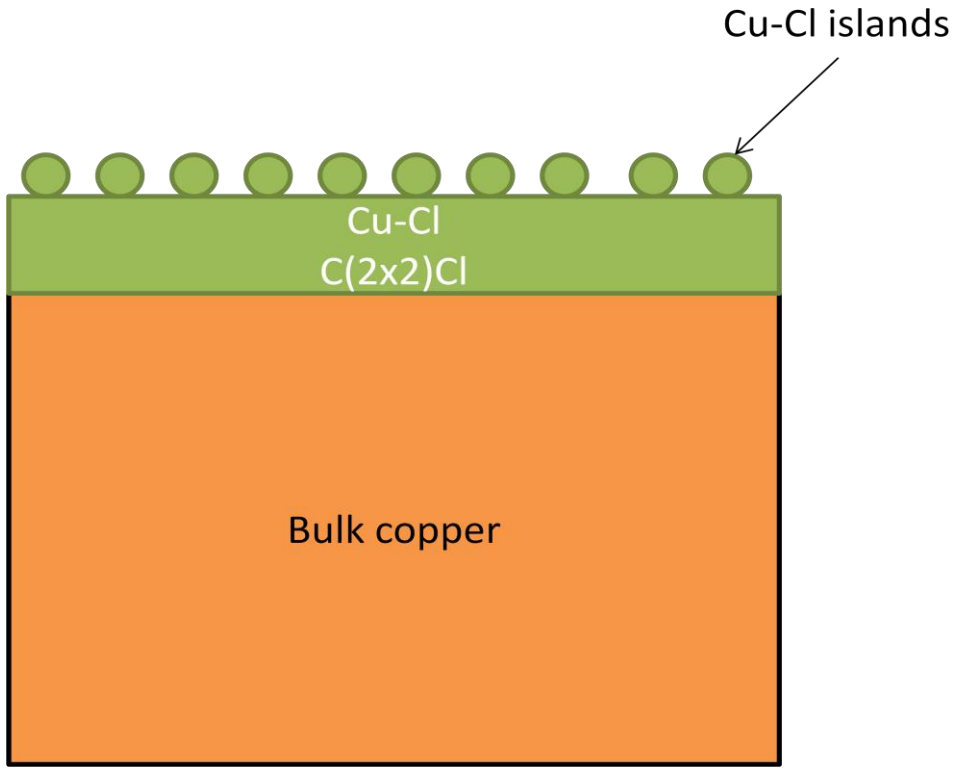

Figure 5.50: schematic diagram of Cu(100)/Cl and Cu-Cl islands.

5.4 Conclusions

A combination of the techniques of XPS and STM techniques at room temperature and under UHV condition has been used to investigate the interaction of HCl and oxygen on top of the Cu(100) sample.

The room temperature interaction of gaseous HCl with a clean Cu(100) sample has shown the dissociation of HCl molecules to give c(2x2)-Cl adlayer confirmed by both above techniques. The XPS data shows the chlorine concentration reaches a maximum $7.x10^{14}$ cm^{-2} which represents a half monolayer of chlorine atoms on the Cu(100) surface, and STM images give a space between the chlorine atoms of 5.1 Å. In the terms of STM atomic resolution of Cl atoms on top of Cu(100), the resolution was limited to about 90% of coverage up to saturation coverage as a result of atomic movement of Cl on the copper sample, and from the sample toward the STM tip in agreement with previous studies. STM images of the Cu(100) sample show a reduction in the image clarity at the copper step edges during exposure to HCl before saturation coverage is reached, this can be attributed to the extraction of copper atoms from the step edges by the HCl.

XPS, and STM of the clean Cu(100) exposed to oxygen at different temperatures were a part of study. The XPS of a series experiments of interaction of oxygen with Cu(100) for range between 30 to 1700 L at room temperature show an increase of oxygen concentration up to saturation coverage, and dosing more oxygen did not have any effect at this stage further oxygen adsorption is kinetically prohibited. STM images of the the Cu(100) surface correlate well with the XP data. Dosing 10 L of oxygen leads to the formation of holes in the surface, which is followed by groves at 80 L. Small islands have been seen at step edges, and terraces while the grooves disappear between 160 to 320 L. Exposing the sample to more oxygen up to 3800 L leads to the formation of large branched islands, these islands represent the c(2x2)-O, while the oxygen $(\sqrt{2}x2\sqrt{2})R45^{o}$ (missing row structure) was formed in the grooved area. These results confirm that, the two types of oxygen reconstruction are found at dosing oxygen at room temperature. To reduce the amount of c(2x2)-O reconstruction and increase the amount of $(\sqrt{2}x2\sqrt{2})R45^{o}$ reconstruction, a temperature of 100 ^{o}C was used for dosing oxygen up to 60 L. Under these conditions most of the surface is covered with $(\sqrt{2}x2\sqrt{2})R45^{o}$ with only small areas of c(2x2)-O remaining. The effect of ejection of copper atom during making of $(\sqrt{2}x2\sqrt{2})R45^{o}$ reconstruction was clear, the copper atoms being trapped at step

edges. By increasing the temperature up to 250 ^{o}C while exposing the Cu(100) sample to 5760 L oxygen, all the surface was covered with ($\sqrt{2}$x2$\sqrt{2}$)R45^{o} oxygen without any trace of c(2x2)-O.

Interaction of HCl with oxygen which was dosed at room temperature studied at two different coverages, first one was interaction of HCl at about one third of oxygen coverage of Cu(100) surface and showed the decrease of oxygen coverage and increase of chlorine coverage, and showed the limitation of reaction at certain pressure, but by increasing the pressure of dosing HCl all the oxygen was removed. When the surface is covered by a mixture of $Cl_{(ads)}$ and $O_{(ads)}$ the interaction of HCl with $O_{(ads)}$ is limited by the lack of clean sites. A kinetically slower reaction is now available that may involve more HCl molecules. Our model is that the reaction change from two separate steps:

(1) $HCl + O_{(ads)} \rightleftharpoons OH_{(ads)} + Cl_{(ads)}$ (Rate determining step)

(2) $HCl + OH_{(ads)} \rightarrow H_2O_{(gas)} + Cl_{(ads)}$

To an overall process:

$$2HCl + O_{(ads)} \rightarrow H_2O_{(gas)} + 2Cl_{(ads)}$$

STM data of the beginning of the reaction showed the change happen just on the area which we suggested to be c(2x2)-O while no change was recognised on the area of ($\sqrt{2}$x2$\sqrt{2}$)R45^{o} of oxygen reconstruction. STM imaging of the c(2x2)-Cl on the Cu(100) surface shows two features, the angle between them was 45^{o}. The space between the horizontal features was 1.2 nm, and 7.2 Å for the features which have 45^{o} angle with respect to the horizontal one. This difference in the spacing is suggested to be due to the STM tip showing the diagonal direction for the c(2x2)-Cl unit cell for the 7.2 Å, while it shows the space 1.2 nm for the space between the centred Cl atoms.

The interaction of HCl with saturated Cu(100)/O showed different behaviour of the two oxygen reconstructions. Replacement of oxygen with chlorine supposed to be done by ratio 2:1 which is explained as two molecules of HCl are replacing one atom of oxygen. The replacement process was fast at the beginning (at exposure to HCl from 1 to 13 L) of the reaction, but it is reduced after that (at exposure to HCl from 28 to 262 L). We attribute this behaviour to the rapid consumption of the c(2x2)-O reconstruction whereas reaction of HCl

with the ($\sqrt{2}$x2$\sqrt{2}$)R45^{o} reconstruction is much slower because of its greater stability Islands of Cu-Cl have been seen at step edges as a result of the interaction of mobile copper atoms produced from ejection of copper atoms in the operation of formation ($\sqrt{2}$x2$\sqrt{2}$)R45^{o} of oxygen reconstruction.

XPS data of the interaction of HCl with the oxidized Cu(100) surface formed by exposing the copper sample to 5700 L of oxygen at 250 ^{o}C shows that the decrease of oxygen and increase of chlorine concentration was 2:1, but not all the oxygen atoms left the surface, these remaining are not visible in the STM and there are may be formed subsurface oxygen. STM images show grooves formed on the oxide layer, suggested to be chlorine atoms sitting at the missing row structure before the replacement of all oxygen top layer with chlorine. Small Cu-Cl island were found at the step edges, suggested to be formed by interaction of copper atoms which are ejected in the processes of formation ($\sqrt{2}$x2$\sqrt{2}$)R45^{o} of oxygen with HCl. The XPS data of Cu-Cl islands show it is CuCl not $CuCl_2$.

5.5 References

1. Klier, K., *Methanol Synthesis*, in *Advances in Catalysis*, H.P. D.D. Eley and B.W. Paul, Editors. 1982, Academic Press. p. 243-313.
2. Szanyi, J. and D.W. Goodman, *CO oxidation on a model Cu/Rh(100) catalyst.* Catalysis Letters, 1992. **14**(1): p. 27-35.
3. Szanyi, J. and D. Wayne Goodman, *CO oxidation on a Cu(100) catalyst.* Catalysis Letters, 1993. **21**(1-2): p. 165-174.
4. Lloyd, L., *Handbook of Industrial Catalysts*. 2011, US: Springer Science and Business Media. 490.
5. Braithwaite, M.J., R.W. Joyner, and M.W. Roberts, *Interaction of oxygen with Cu (100) studied by low energy electron diffraction (LEED) and X-ray photoelectron spectroscopy (XPS).* Faraday Discussions of the Chemical Society, 1975. **60**: p. 89-101.
6. Kono, S., et al., *Chemisorption geometry of c(2×2) oxygen on Cu (001) from angle-resolved core-level x-ray photoemission.* Physical Review B, 1980. **22**(12): p. 6085-6103.
7. Ch. Woll, R.J.W., and S. Chiang, *Oxygen on Cu(100) surface structure studied by scanning tunneling microscopy and by low-energy-electron-difFraction multiple-scattering calculations.* Physical Review B, 1990. **42**(18).
8. Jensen, F., et al., *Dynamics of oxygen-induced reconstruction of Cu(100) studied by scanning tunneling microscopy.* Physical Review B, 1990. **42**(14).
9. Jensen, F., et al., *Dynamics of oxygen-induced reconstruction of Cu(100) studied by scanning tunneling microscopy.* Physical Review B, 1990. **42**(14): p. 9206-9209.
10. Sotto, M., *Oxygen induced reconstruction of (h11) and (100) faces of copper.* Surface Science, 1992. **260**(1–3): p. 235-244.
11. Leibsle, F.M., *STM studies of oxygen-induced structures and nitrogen coadsorption on the Cu(100)surface: evidence for a one-dimensional oxygen reconstruction and reconstructive.* Surface Science 1995. **337**: p. 51-66.
12. Fujita, T., et al., *Phase boundaries of nanometer scale c(2×2)-O domains on the Cu(100) surface.* Physical Review B, 1996. **54**(3): p. 2167-2174.
13. Tanaka, K.-i., et al., *Nano-scale patterning of metal surfaces by adsorption and reaction.* Applied Surface Science, 1998. **130–132**(0): p. 475-483.

14. Lampimaki, M., et al., *Nanoscale oxidation of Cu(100): Oxide morphology and surface reactivity.* The Journal of Chemical Physics, 2007. **126**(3): p. 034703.
15. Argile, C. and G.E. Rhead, *Calibration in Auger electron spectroscopy by means of coadsorption.* Surface Science, 1975. **53**(1): p. 659-674.
16. Hofmann, P., et al., *The adsorption and incorporation of oxygen on Cu(100) at T ≈ 300 K.* Surface Science, 1978. **72**(4): p. 635-644.
17. Habraken, F.H.P.M., C.M.A.M. Mesters, and G.A. Bootsma, *The adsorption and incorporation of oxygen on Cu(100) and its reaction with carbon monoxide; comparison with Cu(111) and Cu(110).* Surface Science, 1980. **97**(1): p. 264-282.
18. Lee, M. and A.J.H. McGaughey, *Energetics and kinetics of the c(2×2) to (√2x2√2)R45o transition during the early stages of Cu(100) oxidation.* PHYSICAL REVIEW B, 2011. **83**(16): p. 165447.
19. Leibsle, F.M., *STM studies of oxygen-induced structures and nitrogen coadsorption on the Cu(100) surface: evidence for a one-dimensional oxygen reconstruction and reconstructive interactions.* Surface Science, 1995. **337**(1–2): p. 51-66.
20. Mundenar, J.M., et al., *Oxygen chemisorption on copper (110).* Surface Science, 1987. **188**(1–2): p. 15-31.
21. Lahtonen, K., et al., *Instrumentation and analytical methods of an x-ray photoelectron spectroscopy--scanning tunneling microscopy surface analysis system for studying nanostructured materials.* Review of Scientific Instruments, 2006. **77**(8): p. 083901-9.
22. Nakakura, C.Y., G. Zheng, and E.I. Altman, *Atomic-scale mechanisms of the halogenation of Cu(100).* Surface Science, 1998. **401**(2): p. 173-184.
23. Altarawneh, S.A.S.a.M., *Electronic Structure of the CuCl2(100) Surface: A DFT First-Principle Study.* Journal of Nanomaterials 2012. **2012**: p. 7.
24. Suggs, D.W. and A.J. Bard, *Scanning Tunneling Microscopic Study with Atomic Resolution of the Dissolution of Cu(100) Electrodes in Aqueous Chloride Media.* The Journal of Physical Chemistry, 1995. **99**(20): p. 8349-8355.
25. Suleiman, I.A., et al., *Interaction of Chlorine and Oxygen with the Cu(100) Surface.* The Journal of Physical Chemistry C, 2010. **114**(44): p. 19048-19054.
26. Kiguchi, M., et al., *Coverage dependence of surface structure and vibration of Cl/Cu(100) compared to Cl/Ni(100).* Physical Review B 1997. **56**(3): p. 1561-1567.
27. Nakakura, C.Y., V.M. Phanse, and E.I. Altman, *Comparison of the interaction of Cl2 and Br2 with Cu(100).* Surface Science, 1997. **370**(1): p. L149-L157.

28. Nakakura, C.Y. and E.I. Altman, *Comparison of bromine etching of polycrystalline and single crystal Cu surfaces.* Journal of Vacuum Science and Technology A: Vacuum, Surfaces and Films, 1997. **15**(4): p. 2359-2368.
29. Nakakura, C.Y. and E.I. Altman, *Bromine adsorption, reaction, and etching of Cu(100).* Surface Science, 1997. **370**(1): p. 32-46.
30. Citrin, P.H., et al., *Geometry and Electronic Structure of Cl on the Cu {001} Surface.* Physical Review Letters, 1982. **49**(23): p. 1712-1715.
31. Galeotti, M., et al., *Chloride formation and photoreduction on the Cu(100) surface. A study by X-ray photoelectron spectroscopy and low energy ion scattering.* Journal of Electron Spectroscopy and Related Phenomena, 1995. **76**(0): p. 91-96.
32. Galeotti, M., et al., *Epitaxy and structure of the chloride phase formed by reaction of chlorine with Cu(100). A study by X-ray photoelectron diffraction.* Surface Science, 1996. **349**(3): p. L164-L168.
33. Citrin, P.H., et al., *Geometry and electronic structure of Cl on the Cu (001) surface.* Physical Review Letters, 1982. **49**(23): p. 1712-1715.
34. Eltsov, K.N., et al., *Surface atomic structure upon Cu(100) chlorination observed by scanning tunneling microscopy* JETP lett., 1995. **62**(5): p. 444.
35. Ehlers, C.B., I. Villegas, and J.L. Stickney, *The surface chemistry of Cu (100) in HCl solutions as a function of potential: a study by LEED, Auger spectroscopy and depth profiling.* Journal of Electroanalytical Chemistry and Interfacial Electrochemistry, 1990. **284**(2): p. 403-412.
36. Vogt, M.R., et al., *Adsorbate-induced step faceting of Cu(100) electrodes in HCl.* Surface Science, 1996. **367**(2): p. L33-L41.
37. Vogt, M.R., et al., *In-situ STM study of the initial stages of corrosion of Cu(100) electrodes in sulfuric and hydrochloric acid solution.* Surface Science, 1998. **399**(1): p. 49-69.
38. Suggs, D.W. and A.J. Bard, *Scanning tunneling microscopic study with atomic resolution of the dissolution of Cu(100) electrodes in aqueous chloride media.* Journal of Physical Chemistry, 1995. **99**(20): p. 8349-8355.
39. Abel, M., et al., *Scanning tunneling microscopy and x-ray photoelectron diffraction investigation of C_{60} films on Cu(100).* Physical Review B, 2003. **67**(24): p. 245407.
40. Tanaka, K.-i., T. Fujita, and Y. Okawa, *Oxygen induced order–disorder restructuring of a Cu(100) surface.* Surface Science, 1998. **401**(2): p. L407-L412.

41. Lahtonen, K., et al., *Instrumentation and analytical methods of an x-ray photoelectron spectroscopy-scanning tunneling microscopy surface analysis system for studying nanostructured materials.* Review of Scientific Instruments, 2006. **77**(8): p. 083901.
42. F. Carley, A., et al., *Flexibility of the Cu(110)-O structure in the presence of pyridine.* Chemical Communications, 1999. **0**(8): p. 687-688.
43. Moroney, L., S. Rassias, and M.W. Roberts, *Chemisorption of HCl and H2S by Cu(111)-O surfaces.* Surface Science, 1981. **105**(1): p. L249-L254.
44. Jia, L., Y. Wang, and K. Fan, *Theoretical Study of Atomic Oxygen Adsorption on the Chlorine-Modified Ag(111) Surface.* The Journal of Physical Chemistry B, 2003. **107**(16): p. 3813-3819.
45. Fujita, T., Y. Okawa, and K.-i. Tanaka, *STM study of preferential growth of one-dimensional nickel islands on a Cu(100)-(22×2)R45°-O surface.* Applied Surface Science, 1998. **130–132**(0): p. 491-496.
46. Carley, A.F., et al., *A low energy pathway to CuCl2 at Cu(110) surfaces.* Physical Chemistry Chemical Physics, 2009. **11**(46): p. 10899-10907.
47. Davies, P.R., D. Edwards, and D. Richards, *Possible Role for Cu(II) Compounds in the Oxidation of Malonyl Dichloride and HCl at Cu(110) Surfaces.* The Journal of Physical Chemistry C, 2009. **113**(24): p. 10333-10336.

Chapter 6 Interaction of HCl with Cu(111)

Contents

6.1 Introduction

6.1.1 Interaction of oxygen with Cu(111)

The structure and interaction mechanism of oxygen with Cu(111) have been studied for several years, but not as much as Cu(100), and Cu(110) because of the relatively low reactivity of the (111) surface [1]. Exposure of Cu(111) to less than 10^5 L of oxygen at room temperature leads to the formation of a disordered oxygen layer [2] with High-resolution electron energy loss spectroscopy (HREELS) suggesting that the oxygen atoms are chemisorbed at or below the top most Cu(111) layer. Cu_2O islands form after exposures of 10^6 L at about 180 ^oC by the transformation of chemisorbed oxygen atoms to bulk oxide in the defect site. By combined auger electron spectroscopy (AES), low energy ion scattering (LEIS), and low energy electron diffraction (LEED), Niehus [3] suggested that, the surface Cu(111)/oxygen is reconstructed by the lateral displacement of the top most layer of copper atoms by 0.3 Å and the formation of a rough and disordered oxygen over-layer, at room temperature. Surface extended X-ray absorption fine structure (SEXAFS), and surface extended electron energy loss fine structure (SEEELFS) used by Haase et al. and Luo et al. respectively, showed the oxygen atoms are chemisorbed at the threefold hollow site of the top most Cu(111) atoms, and partially penetrated to the second surface layer causing the lateral expansion [4, 5] causing roughening of the surface. Density functional theory (DFT) study of dissociation of oxygen on top of Cu(111) showed that, threefold hollow site is a favourable position of oxygen adsorbed on the surface [6]. Photoelectron diffraction (PhD) study suggested that, the oxygen atoms are adsorbed on the fourfold hollow site making a reconstruction to the top most layer of copper and making a contact to the unreconstructed under layer of copper(111), causing a disordered reconstruction like oxygen/Cu(100) [7]. STM investigation of the interaction of oxygen with Cu(111) showed that, the oxygen molecules are dissociated on the terraces to make isolated oxygen atoms sitting on threefold hollow sites of the unreconstructed terraces, while the two dimensional disordered oxygen layer formed as a result of the nucleation of the oxygen atoms at step edge. Consumption of the upper copper atoms in the terraces by oxygen leads to the formation of triangular islands [8]. At high temperatures, exposure of the Cu(111) to oxygen leads to formation of two ordered oxygen reconstructions ($\sqrt{13}$ R46.1^o x 7 R21.8^o), and ($\sqrt{73}$ R5.8 x $\sqrt{21}$ R-10.9^o) which they labelled ‘’29’’, and ‘’44’’ structure respectively [7, 9-11]. Exposing the Cu(111) sample to oxygen at room temperature, and then annealing the sample at 450 ^oC leads to the formation of the ‘’44’’ oxygen reconstruction, which can be transformed to ‘’29’’

reconstruction by annealing at 500 ^{o}C [9, 10]. A complex model of ‘’29’’ oxygen reconstruction suggested by Jensen et al. based on interaction of three oxygen atoms with two layers of copper, give the final structure a combination of Cu(1x1), and hexagonal substructure related with the (111) plane of Cu_2O as shown in Figure 6.1 [10]. A model of the ‘’44’’ reconstruction suggested by Matsumoto et al. [1] is shown in Figure 6.2. LEED, and STM studies, have reported the formation of ‘’44’’ at about 350 ^{o}C which is lower than previously suggested [9-11].

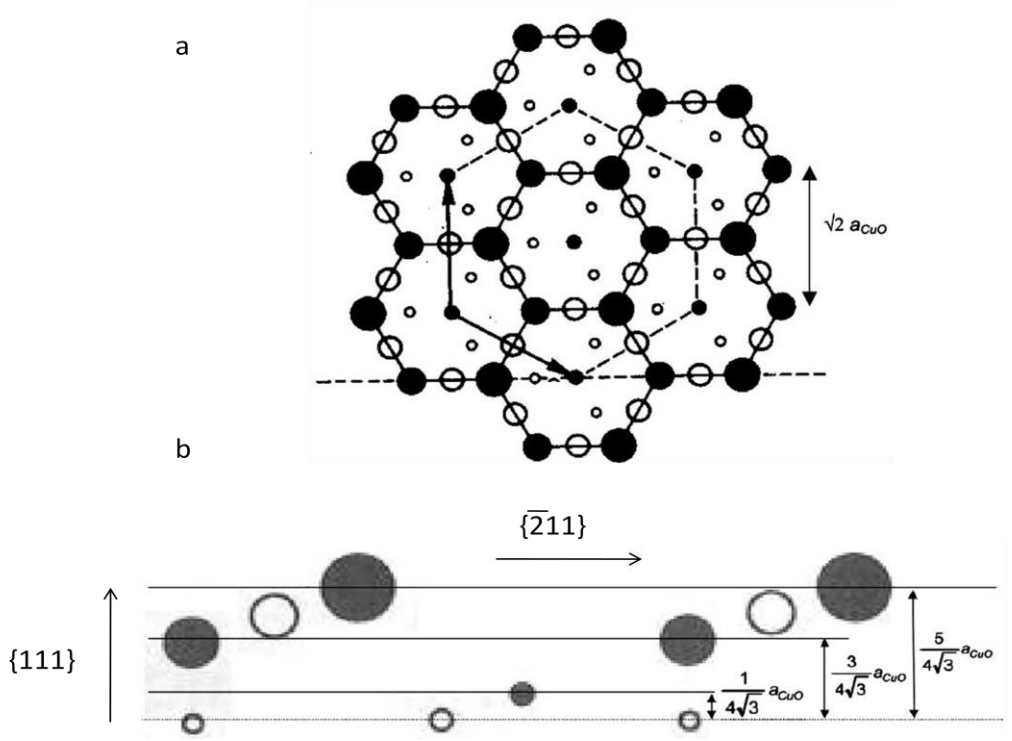

Figure 6.1: a model of ‘’29’’ structure of oxygen on top of Cu(111) surface, the black circles indicate oxygen atoms, while the white one are for copper. (a) top view, oxygen induced the reconstruction of the Cu(111) sample for the five layer, the top most three layer are indicated by solid line. (b) side view of Cu_2O layer [10].

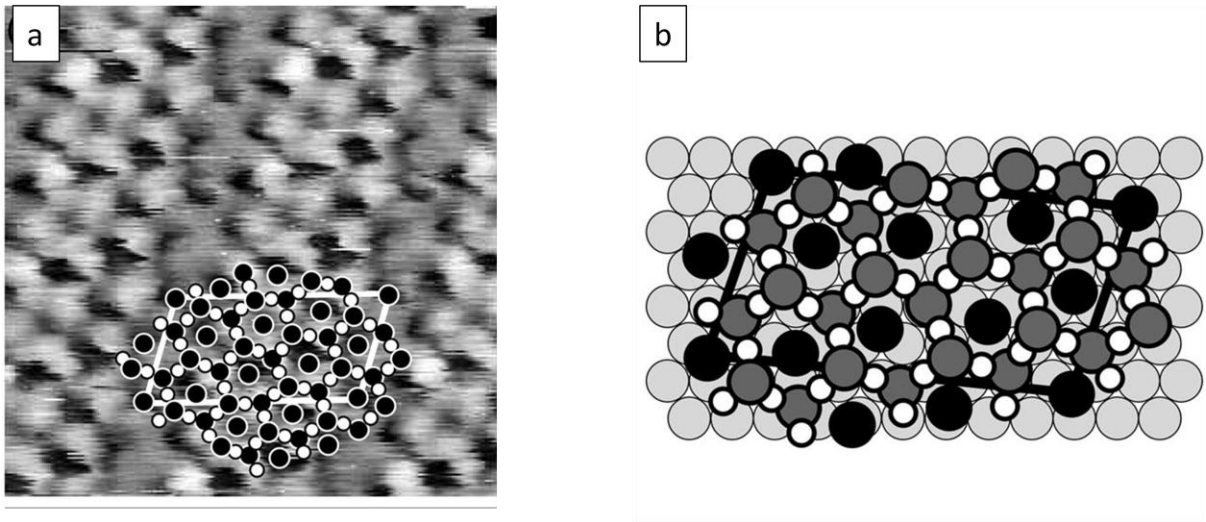

Figure 6.2: (a) STM image taken at room temperature of ’44’. (b) Model of ‘’44’’, the open and filled circles indicate the Cu and O atoms in the model, respectively [1].

XPS, STM, and DFT of interaction ‘’44’’of Cu_2O/Cu(111) with carbon monoxide [12, 13] have shown that, the reduction of Cu_2O/Cu(111) by carbon monoxide occurs via two stage, a slow, and fast reaction Figure 6.3. The slow reaction involves the “O-deficient Cu_2O” phase, which is produced by a transformation of the ‘’44’’ structure to a honeycomb structure by removing the central oxygen atoms. This leads to an increased reaction barrier for the removal of lattice oxygen in Cu_2O because of the low sticking coefficient of carbon monoxide on the well-ordered Cu_2O layer. Subsequently, a disordered Cu_2O layer (heptagon structure) is formed as a result of the reconstruction of the Cu_2O honeycomb. This provides a suitable place for the adsorption of the carbon monoxide molecule increasing the overall rate. The fast reaction is the interaction of carbon monoxide with the heptagon Cu_2O layer which has a low energy barrier for the removal of lattice oxygen from Cu_2O layer by carbon monoxide.

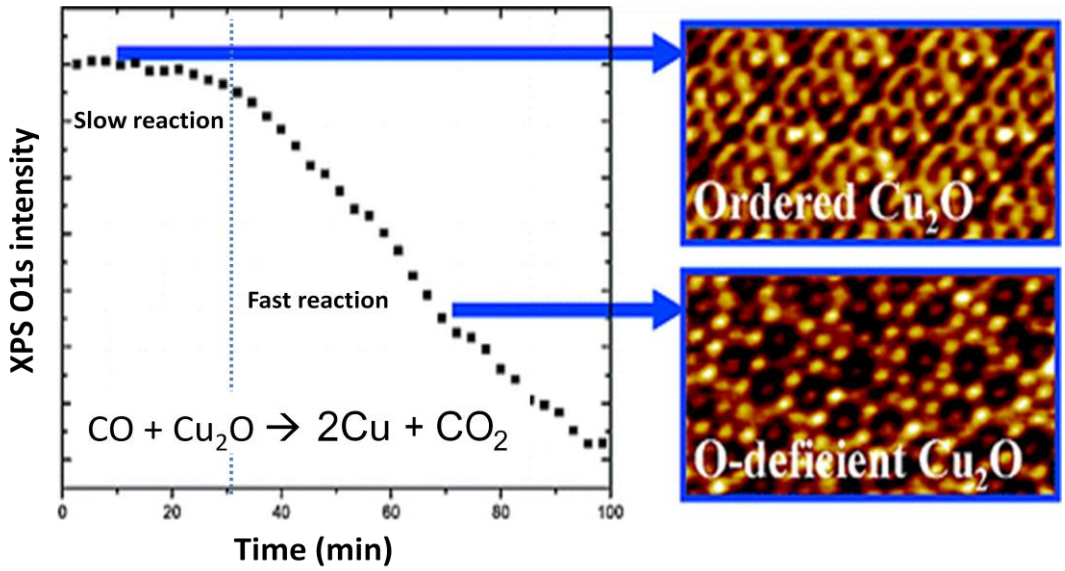

Figure 6.3: XPS of reduction of the "44" Cu_2O surface oxide by carbon monoxide at 6×10^{-8} Torr , and STM images of oxygen layer before and upon exposure to carbon monoxide [12, 13].

6.1.2 Interaction of Cu(111) with chlorine.

The first study of interaction of chlorine with Cu(111) has been done by Goddard and Lambert in 1977, using low energy electron diffraction (LEED), and Auger electron spectroscopy (AES). They found, at one third of chlorine coverage a long range ordered $(\sqrt{3}x\sqrt{3})R30^o$ reconstruction [14]. Surface extended X-ray absorption fine structure (SEXAFS), and Photoelectron diffraction (PhD) have been use to predict the distances between the chlorine and copper layer [15, 16]. The suggested adsorption sites were face centred cubic (fcc) hollow Figure 6.4, where the Cl atom sits on top of the copper atoms in the third layer, with distance 2.39 Å between Cu-Cl neighbours. The inter layer spacing between Cl and the bulk copper atoms has been shown to be 1.88 ± 0.05 Å by SEXAFS and normal incidence x-ray standing wave field absorption (NIXSW) [17, 18].A density functional theory study showed that the (fcc) hollow site was slightly preferred to the (hcp) hollow site[19]. STM of interaction of chlorine, and sulphur have been studied by Motai et al. and shown the effect of coverage and temperature on the reconstruction [20]. At room temperature and a coverage about one third monolayer confirmed by LEED and AES, the $(\sqrt{3}x\sqrt{3})R30^o$ reconstruction was formed, but by exposing the sample to chlorine at 100 ^oC two reconstructions were formed $(6\sqrt{3}x6\sqrt{3})R30^o$, and $(4\sqrt{7}x4\sqrt{7})R19.1^o$. Interaction of Cu(111) with dilute HCl was studied with in-situ STM, the adsorption structure of adsorbed Cl was $(\sqrt{3}x\sqrt{3})R30^o$ [21, 22]. XPS of the interaction of HCl with preoxidised Cu(111)

surface at 80 K have been studied by Roberts et al.[23] who identified three oxygen peaks, the first one at 529.8 eV which was assigned to the original oxygen peak. The second peak at 531.5 eV referred to surface hydroxyl species. The third one at 533eV was assigned to adsorbed H_2O. One broad oxygen peak at 533 eV was observed after exposing the sample to an additional 40 L of HCl. By warming the sample to 189 K all the oxygen peaks disappeared. The following equations illustrate the proposed mechanism [23].

$$HCl_{(g)} + O_{(a)} \xrightarrow{80\ K} OH_{(a)} + Cl_{(a)}$$

$$OH_{(a)} + OH_{(a)} \xrightarrow{80\ K} H_2O_{(a)} + O_{(a)}$$

$$H_2O_{(a)} \xrightarrow{189\ K} H_2O_{(g)}$$

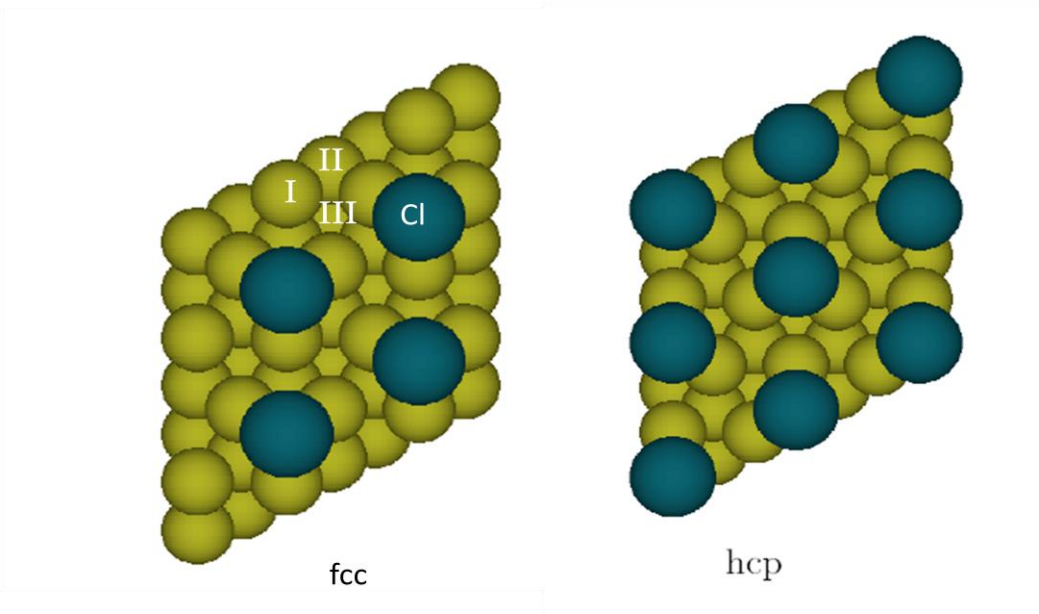

Figure 6.4: The $(\sqrt{3}x\sqrt{3})R30^o$ reconstruction of Cl atom sit at threefold hollow site, where I is first copper layer, II second copper layer, and III the third copper layer[19].

6.2 Experimental

The instrument used in these experiments is "UHV" which is described in chapter 3, together with the sample cleaning procedures. Oxygen and HCl gases were purchased from Argo international and, the purity was checked by using mass spectroscopy. In all of our STM images in this chapter, the height of the features is less than the actual height by about 0.6 Å, due to a technical problem in the STM calibration. So in all the line profile schemes the expected height is written but instead of the z axis values. The x, and y axis have already been calibrated which is consistent with the expected O-O distances on Cu(111) surface, so they represent the actual reading. This deviation of the Z axis value appears at measuring the

feature with highest greater than 1.0 Å while it disappears when measuring the smaller features. Step edge of Cu(111) with monatomic, two atomic, and three atomic layers showed the same deviation in the Z axis, while small oxygen ring with height about 40 pm, showed the right value.

6.3 Results and discussions

6.3.1 XPS and STM of clean Cu(111) surface

The Mg anode was used in the experiments described in this chapter. As a result the Auger peak appears shifted, as shown in the following wide scan Figure 6.5. The peaks observed in the spectra are (2s 1069 eV), ($2p_{1/2}$ 952 eV), ($2p_{3/2}$ 932.7 eV), (LMM d 489.2 eV), (LMM b 419.9 eV), (LMM c 411.7 eV), (LMM a 338.4 eV), (3s 120 eV), and ($3p_{1/2,3/2}$ 74 eV). The oxygen 1s and chlorine 2p peaks are calibrated to the $Cu2p_{3/2}$ peak, which is also used for the quantification of the spectra. The clean Cu(111) sample showed no oxygen, and carbon which are the most common contaminations of copper.

STM of freshly clean Cu(111) sample at room temperature show the clean surface without any traces of contaminations Figure 6.6. The height of mono atomic step is 2.0 Å in agreement with previous study [8]

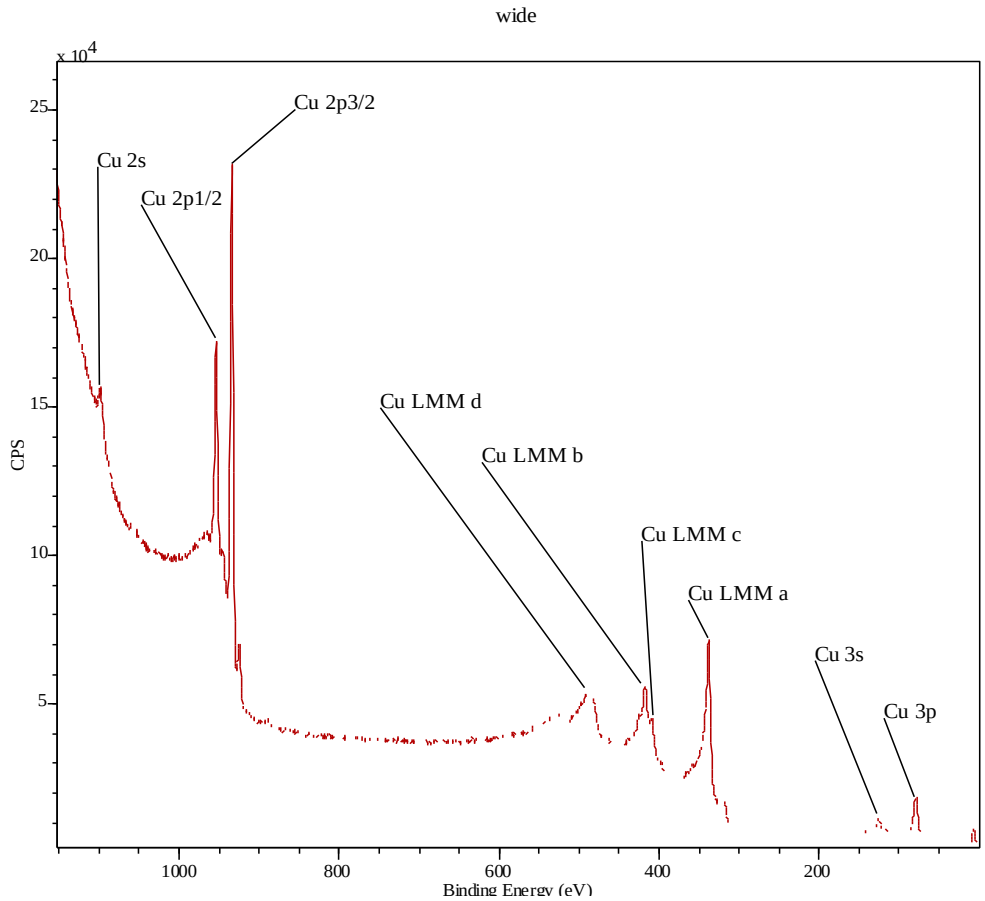

Figure 6.5: XP spectrum of wide scan of clean Cu(111) surface at room temperature excited by x-ray Mg Kα source.

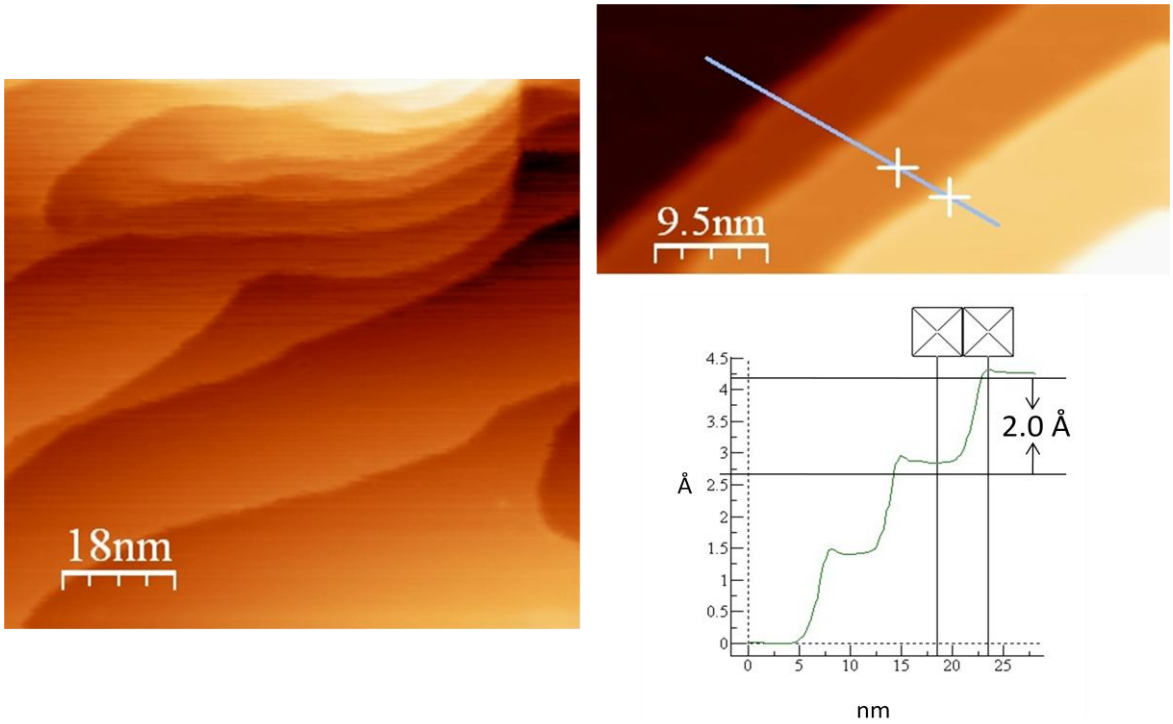

Figure 6.6: STM images of clean Cu(111) surface at room temperature. Tunnelling conditions: 1V, and 1nA. (a) A large scan image 90 nm x 90 nm size. (b, and c) Image of mono atomic step and the line profile.

6.3.2 Interaction of oxygen with clean Cu(111) at room temperature.

There was no evidence in XP spectrum of finding oxygen by exposing the clean Cu(111) sample to about 5 L of oxygen at room temperature, but STM image show traces of small rings with diameter about 1.8 nm, with depth about 0.4 Å appearing on the terraces and step edge, Figure 6.7. This result is in agreement with Wiame et al. of low coverage oxygen results [8] which they found small rings formed on the step edge and terraces, and the ring suggested to be one adatom of oxygen adsorbed on the threefold hollow site of Cu(111) surface. The oxygen peak was not observed in the XP spectrum because this coverage of oxygen is under the detection limit. STM after exposing the low coverage O/Cu(111) sample to about 150 L of oxygen at room temperature show that the oxygen atoms interact with Cu(111) surface by attack at the step edge and the defect site on the terraces as shown in the Figure 6.8. The feature indicated with arrows at the base of the step edge in Figure 6.8(c) is assigned to formation of chemisorbed oxygen adlayer. The sample was exposed to 1400 L of oxygen and studied with STM while no change was recognized in the terraces marked changes occur at the defect site as shown in the STM series images in Figure 6.9, making a triangle structure. The step edges become angular upon exposure to oxygen while the growths

of oxygen islands occurs at the defect site. The new surface formed between the terraces at the step edge joins these angular structures. The new surface is assigned to an oxide covered surface with a terrace to terrace step height of about 0.7 Å where the lower copper terrace was covered with oxygen layer while the top terraces was not, Figure 6.10 (a). Where both terraces are covered in oxygen the step height was measured to be 1.8 Å similar to the mono atomic copper step height Figure 6.10 (b).

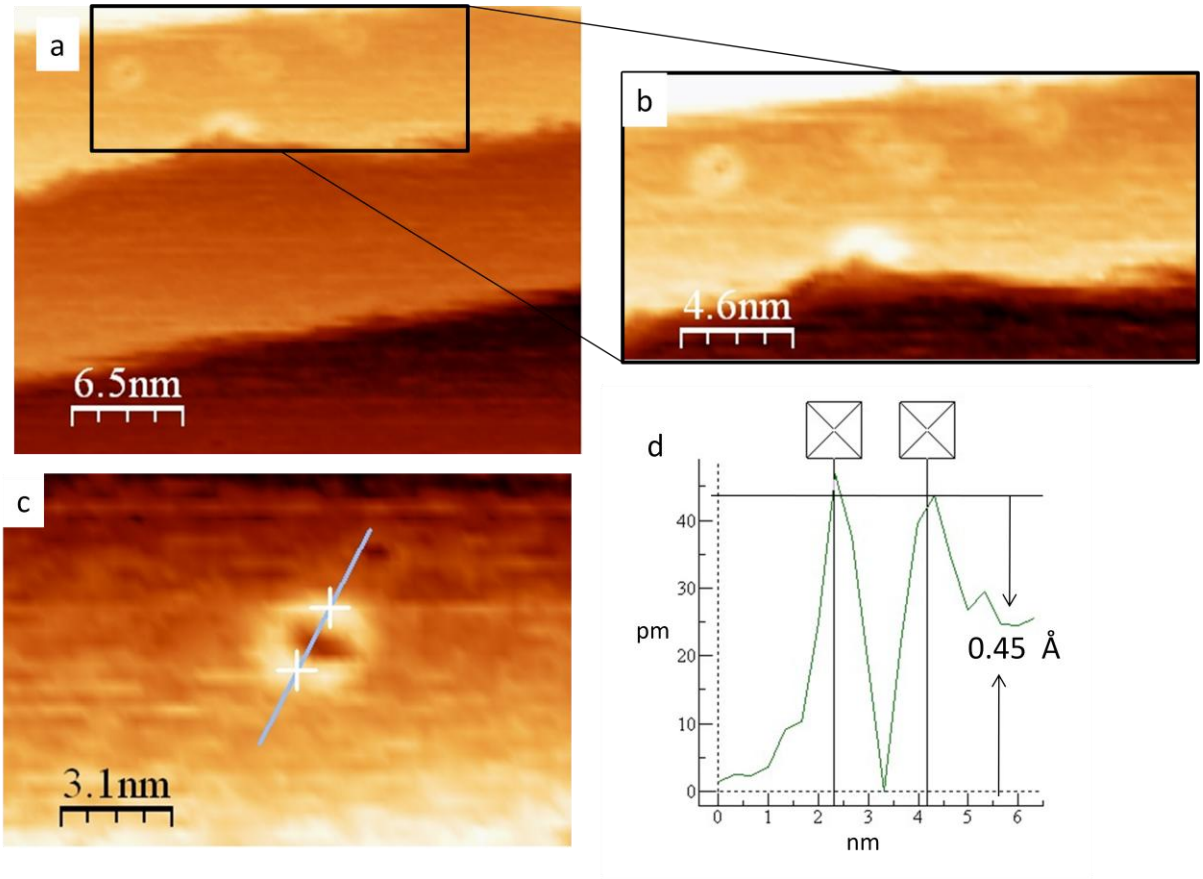

Figure 6.7: The STM images of low coverage oxygen after about 5 L at room temperature. Tunnelling conditions: 1V, and 1nA. (a, and b) oxygen rings shown on the terraces. (c, and d) line profile showing the diameter and depth of the ring.

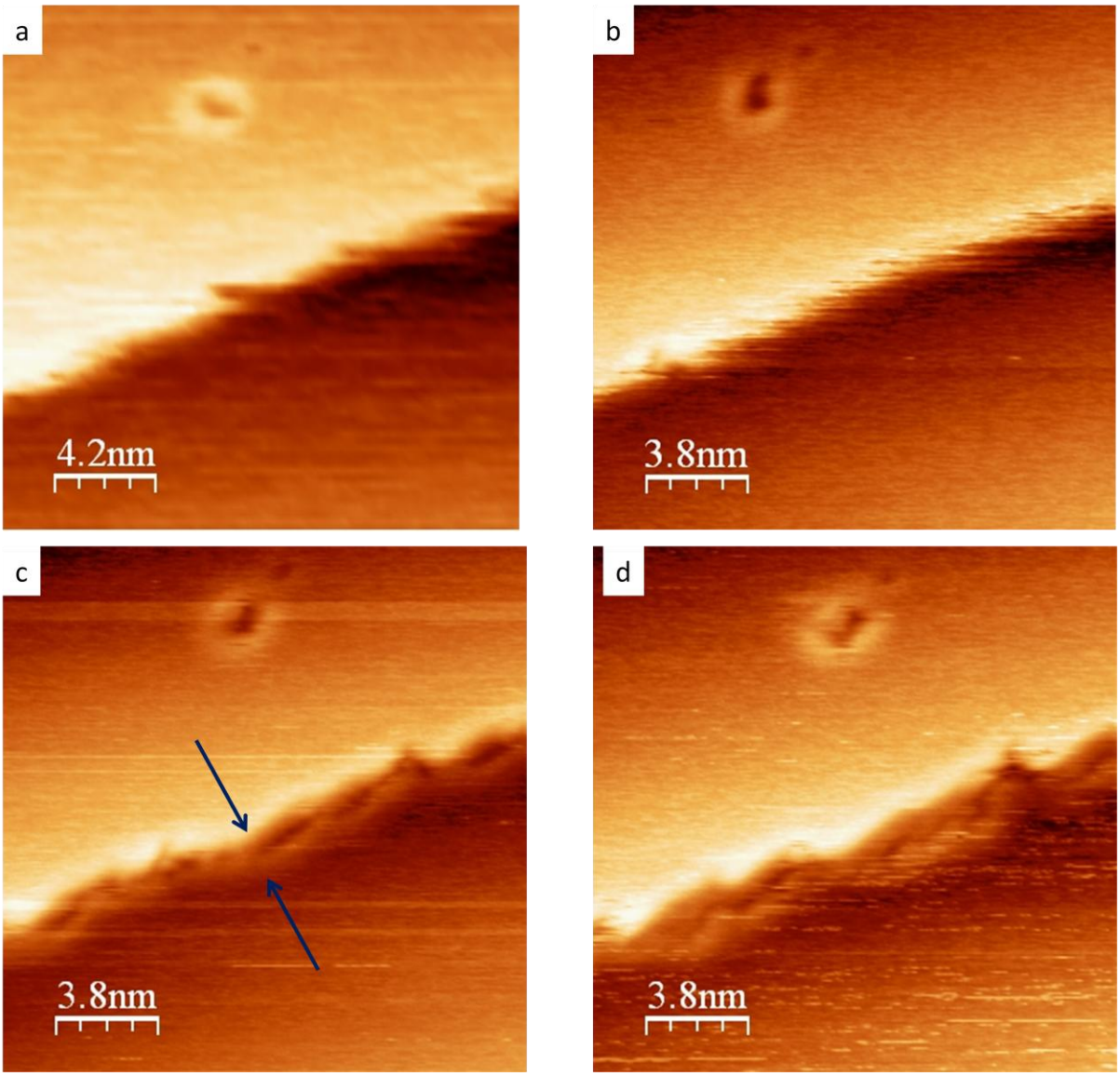

Figure 6.8: (a, b, c, and d) STM images of the effect of a dose of 150 L of oxygen on the O/Cu(111) formed at low coverage at room temperature. Tunnelling conditions: 1V, and 1nA.

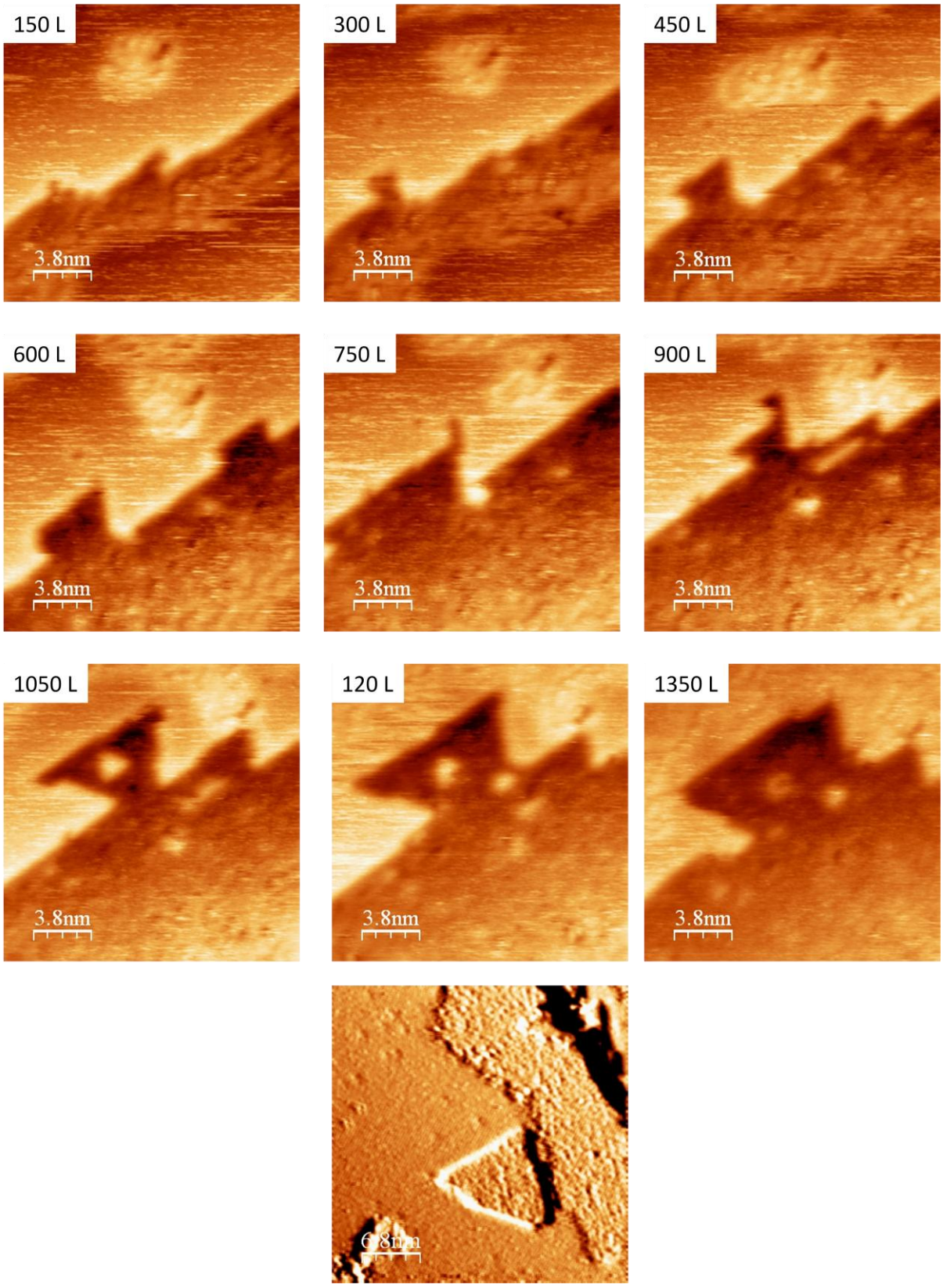

Figure 6.9: the sequence of STM images of exposing the Cu(111) sample to oxygen at room temperature. Tunnelling conditions: 1V, and 1nA.

STM images in Figure 6.11 show how the oxide layer forms at the step edge and then extends over the terraces. At the beginning the resolution was not good at the oxide layer but after a while atomic resolution can be reached as shown in Figure 6.12. A hexagonal arrangement of dots have been recognized inside the triangle structure and in the added oxygen at the top of the terraces with distance about 6.4 Å which is consistent with the $(\sqrt{3}x\sqrt{3})R30^{o}$. The add oxide is suggested to be the Cu_2O which make hexagonal structure, in agreement with previous result [1]. The saturation coverage of Cu(111) by oxygen was confirmed by XPS to be 8.1x 10^{14} cm^{-2} which is slightly more than the saturation coverage of Cu(111) when it covered by $(\sqrt{3}x\sqrt{3})R30^{o}$ reconstruction (one third monolayer) as shown in Figure 6.13 (the atomic density of Cu(111) is 1.772 x 10^{15} cm^{-2}).

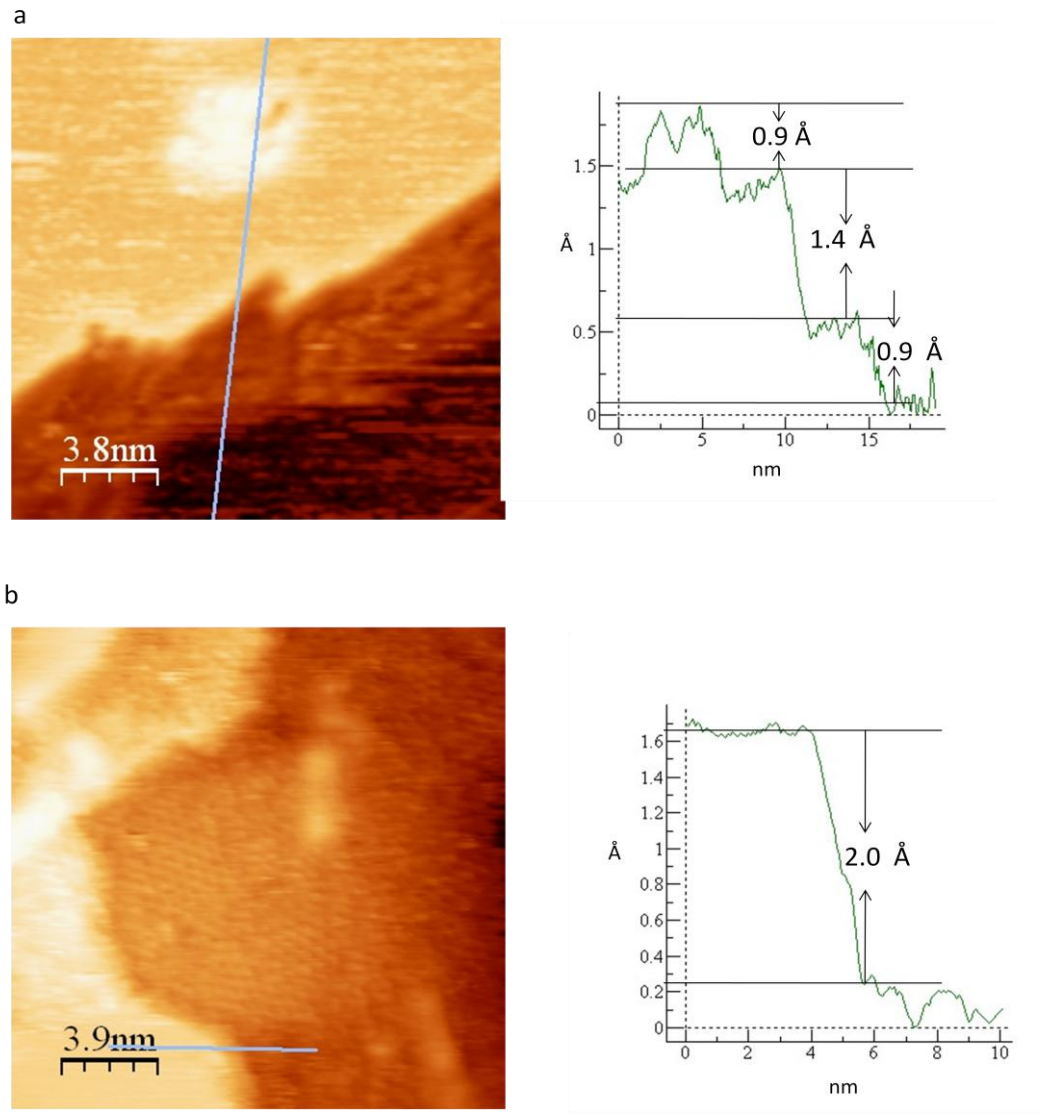

Figure 6.10: (a) STM image and line profile of the oxide step edge before the top and bottom terraces covered with oxygen. (b) STM image and line profile of the all terraces were covered with oxygen. Tunnelling conditions: 1V, and 1nA.

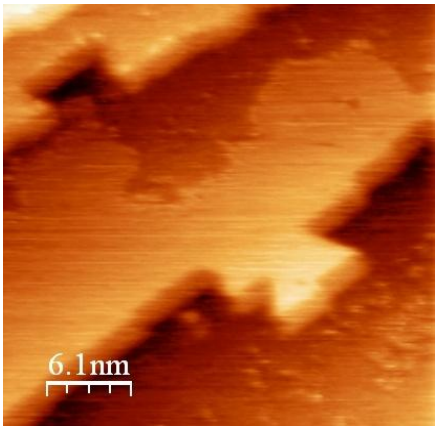

Figure 6.11: STM image shown the direction of extend the oxide layer over the terraces. Tunnelling conditions: 1V, and 1nA.

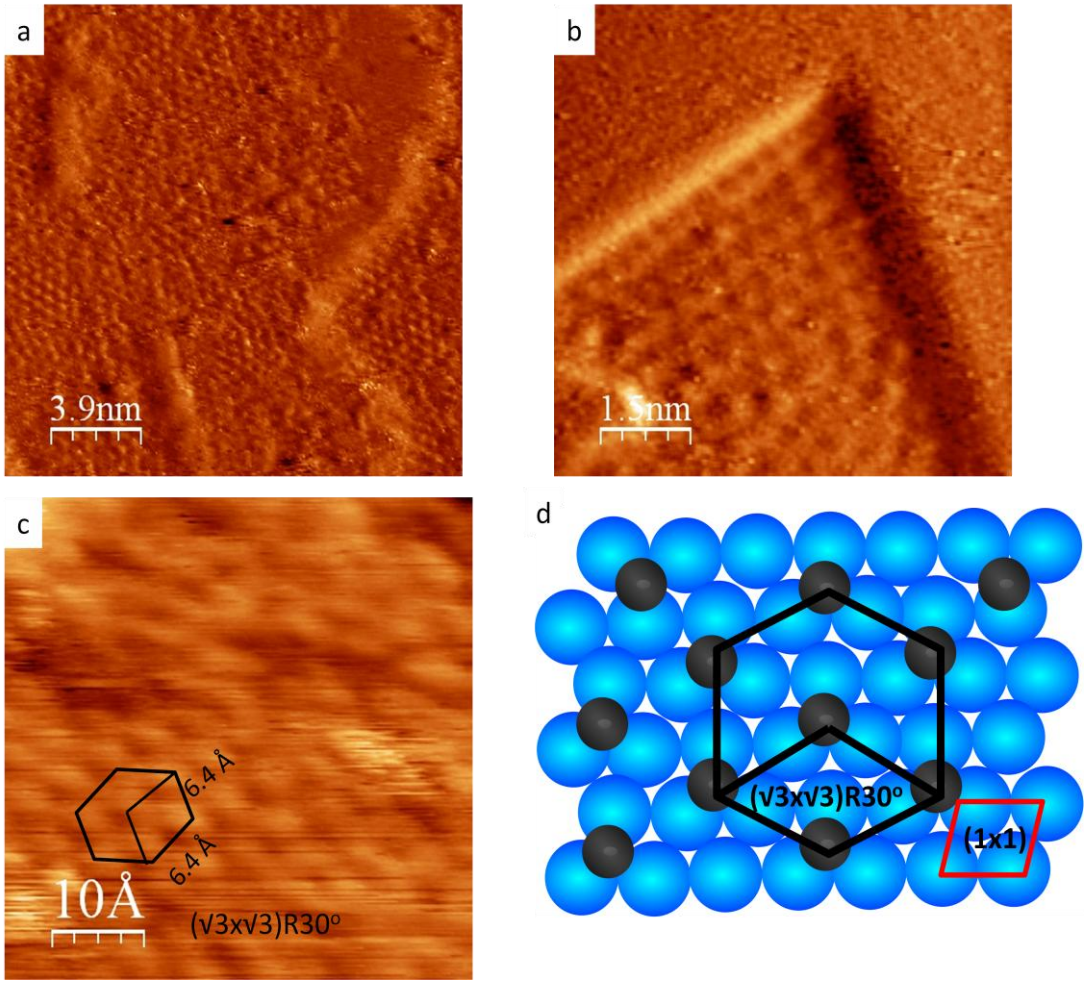

Figure 6.12: (a) STM image of the add oxide layer on top the terraces. (b) STM image of the oxide inside the triangle structure. (c, and d) STM image of with the atomic resolution and model of the oxide show the $(\sqrt{3}x\sqrt{3})R30^{o}$ reconstruction of the oxygen on top the Cu(111) surface oxygen represented as a black sphere while the blue one for copper. Tunnelling conditions: 1V, and 1nA.

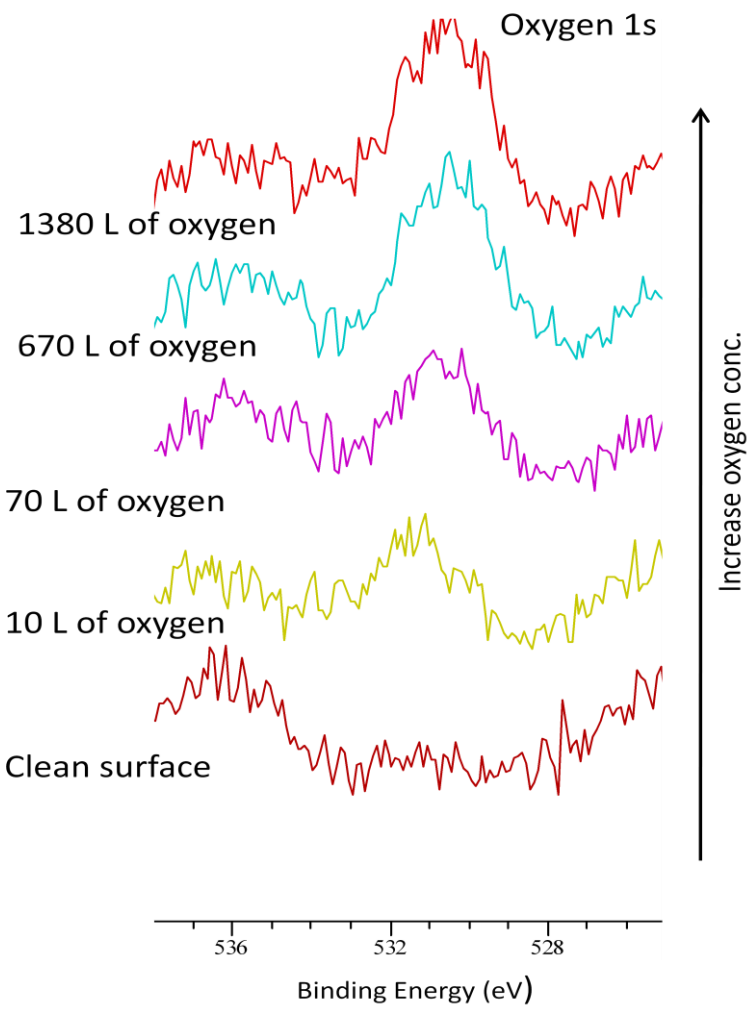

Exposure of oxygen/ L	Concentration of oxygen/ cm^{-2}
0	0
10	$4.1x10^{14}$
70	$4.7x10^{14}$
670	$8.0x10^{14}$
1380	$8.1x10^{14}$

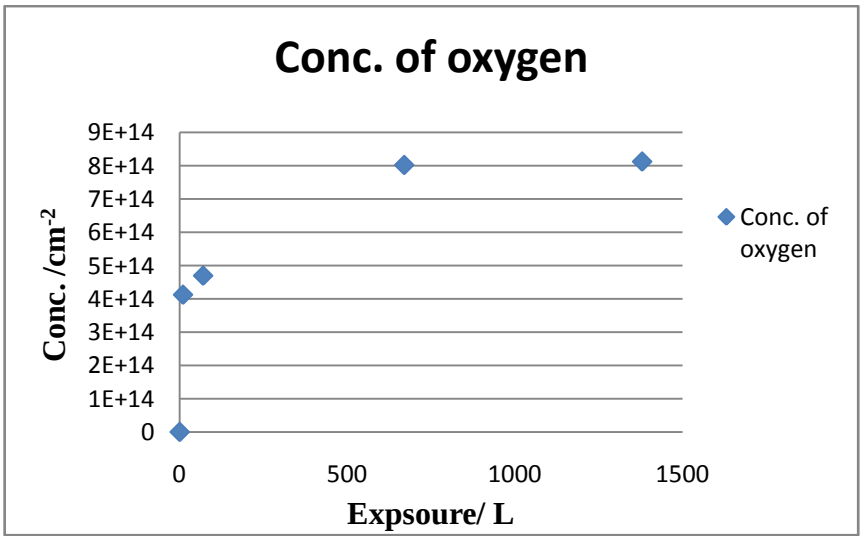

Figure 6.13: Quantified O1s XP spectra shows the increase of oxygen coverage with increasing O_2 exposure until saturated according to value in the table and graph.

6.3.3 Interaction of oxygen with Cu(111) sample at 380 ^{o}C

Exposing the clean Cu(111) sample to 600 L of oxygen at 380 ^{o}C leads to formation of sharp step edge in contrast to the angular and serrated step edge observed by exposing the Cu(111) sample to oxygen at room temperature. The absence of satellite features in the XPS of Cu(2p) rule out the presence of Cu^{2+} and hence CuO, so Cu_2O is suggested to be formed. Striped terraces covered with Cu_2O layer are shown in the wide area image of the surface 6.14 (a). This is assigned to an ordered Cu_2O layer with 44 time unit cell bigger than the unit cell (1x1) of the substrate called oxygen ‘’44’’ structure as shown in Figure 6.14. The height of the step edge between two terraces is equal to the height of step edge of clean Cu(111) surface indicating that, the Cu_2O was form on both terraces Figure 6.15. Some of these striped lines are in one direction, and some of them in different directions as shown in Figure 6.16 depending on the orientation of the step edge of Cu(111) surface. Atomic resolution of the Cu_2O area confirmed the ‘’44’’ structure which has unit cell with two factor (2.2 nm, and 1.18 nm) in agreement with previous works [1,8-10, 12,13] as shown in Figure 6.17.

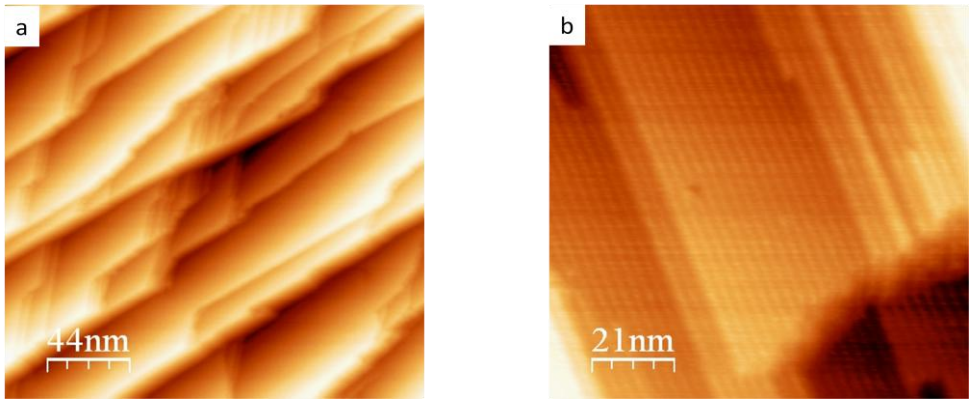

Figure 6.14: STM images at room temperature of Cu_2O layer on the Cu(111) surface. (a) STM images shown the sharp step edge. (b) Striped terraces covered with Cu_2O layer. Tunnelling conditions: 1V, and 1nA.

A disordered structure appears in a very rare percentage of some areas on the terraces with some ordered structure but with different domain Figure 6.18. A similar result has been found by Matsumoto et al by exposing the clean Cu(111) sample to oxygen at 100 ^{o}C and attributed to diffusion of copper atoms while heating the sample [1]. In our case the temperature is higher and all the surface was covered with ordered Cu_2O layer but this area could be result of non-complete transformation of disordered structure to the ordered one, or due the instability of the ‘44’’ structure which is shown in the following section. XP spectrum shown

in Figure 6.19 assigned to formation of Cu_2O at concentration $1.1x10^{15}$ cm^{-2}, while as the excess of the oxygen concentration it could be back to formation of subsurface oxygen due annealing temperature during exposed the sample to oxygen.

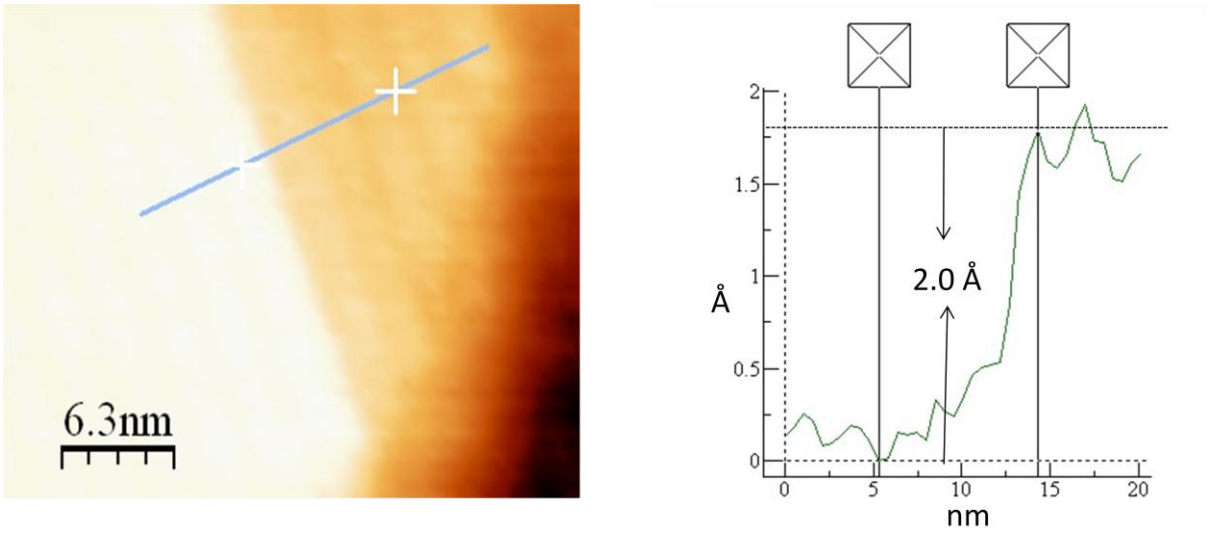

Figure 6.15: STM image and line profile showing the height of the step edge between two terraces covered by Cu_2O at room temperature. Tunnelling conditions: 1V, and 1nA.

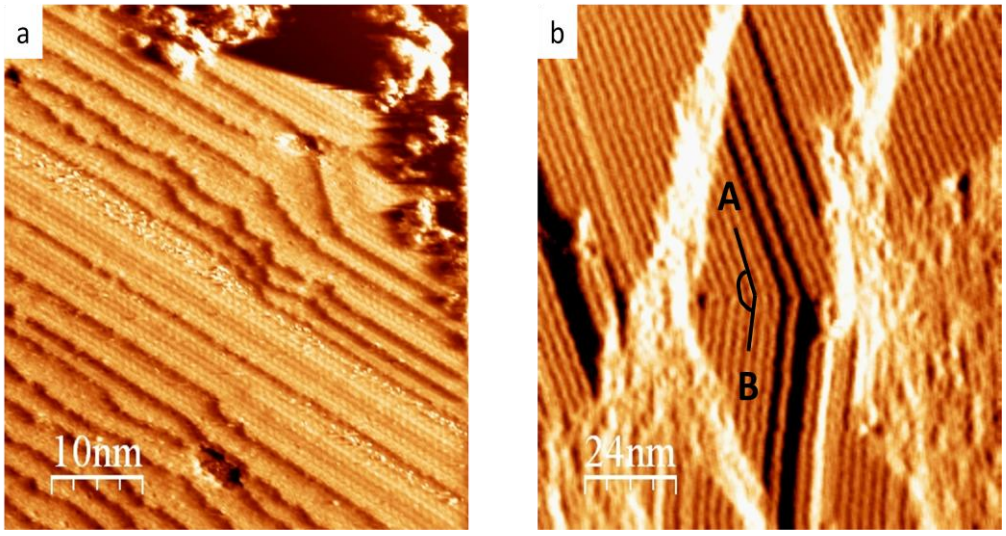

Figure 6.16: STM image of Cu_2O layer top Cu(111) at room temperature. (a) STM image show the striped lines are in one direction and taken the orientation of step edge. (b) STM image shows two directions of the striped lines in area A, and B with 154^o angle between them. Tunnelling conditions: 1V, and 1nA.

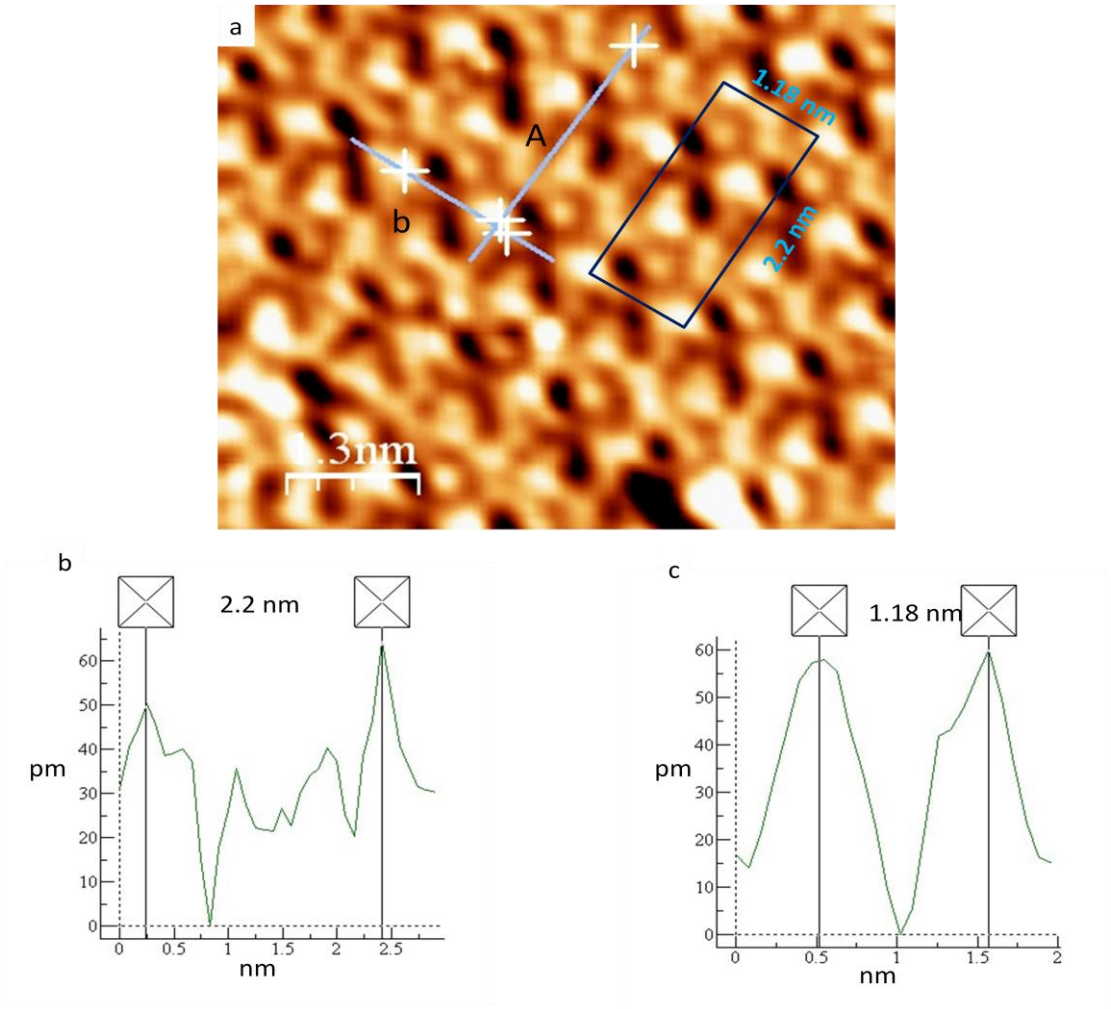

Figure 6.17: STM image showing the atomic resolution of the Cu_2O ‘’44’’ structure room temperature. Line profile (b, and c) show the unit cell vectors (2.2 nm, and 1.18 nm) of line A, and B respectively. Tunnelling conditions: 1V, and 1nA.

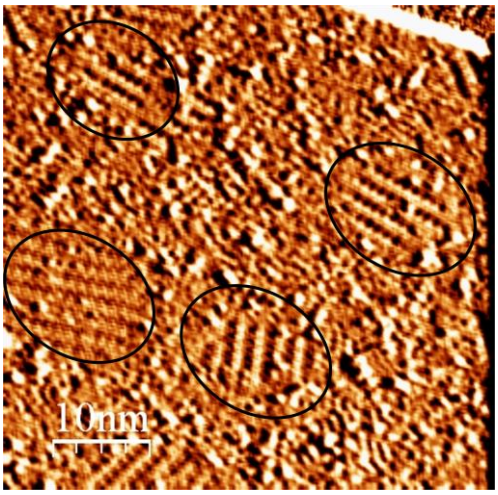

Figure 6.18 STM image of ordered and disordered Cu_2O on top of terraces of Cu(111) surface.

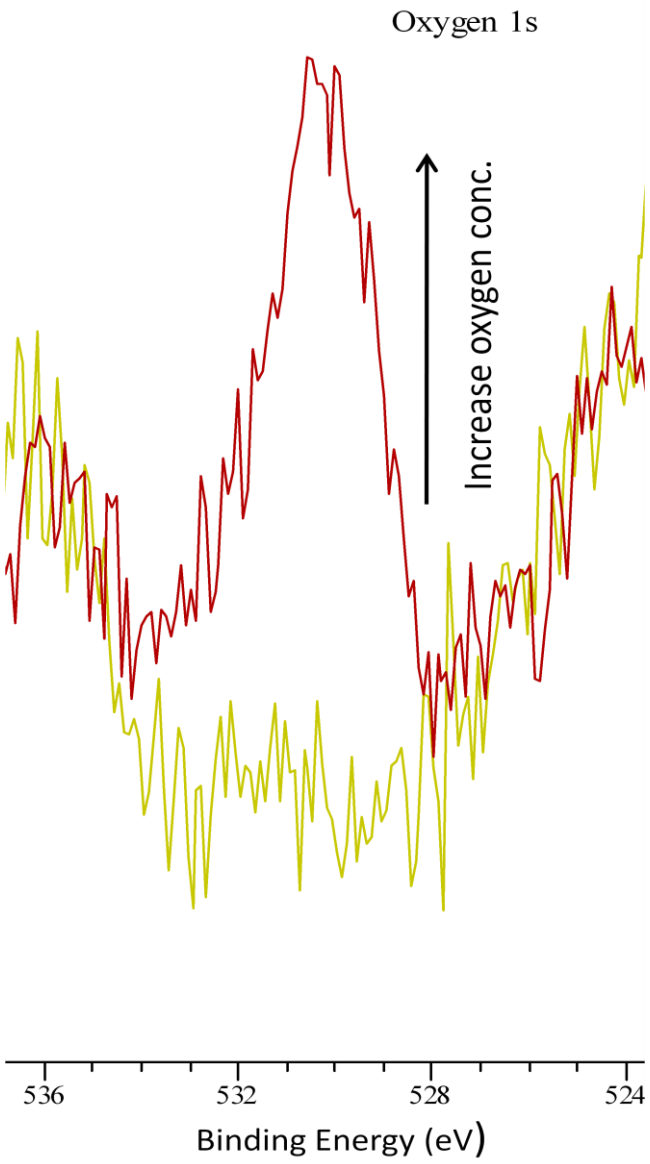

Figure 6.19: XP spectra of oxygen 1s after fresh formation of ‘’44’; oxygen structure top of Cu(111) surface. The oxygen concentration is 1.1×10^{15} cm^{-2}.

After leaving the sample overnight, wide scan images show the loss of some areas of ‘’44’’oxygen structure with the formation triangle holes on the terraces together with small changes at the step edge, as shown in Figure 6.20. By zooming in, three types of structure are observed on the surface, one as a protrusion, the second as a hole, and third an ordered structure as shown in Figure 6.21.

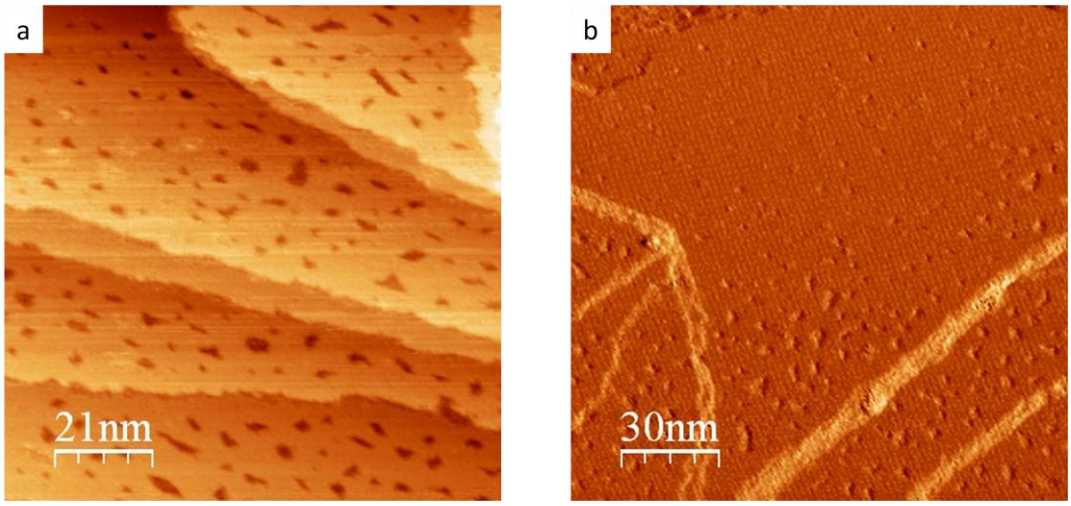

Figure 6.20: STM images of Cu(111) surface covered with ‘’44’’ after leave it overnight. (a) Wide scan image shown the holes formed at terraces. (b) Wide scan image shown the hole on the surface and ordered structure still on the terraces. Tunnelling conditions: 1V, and 1nA.

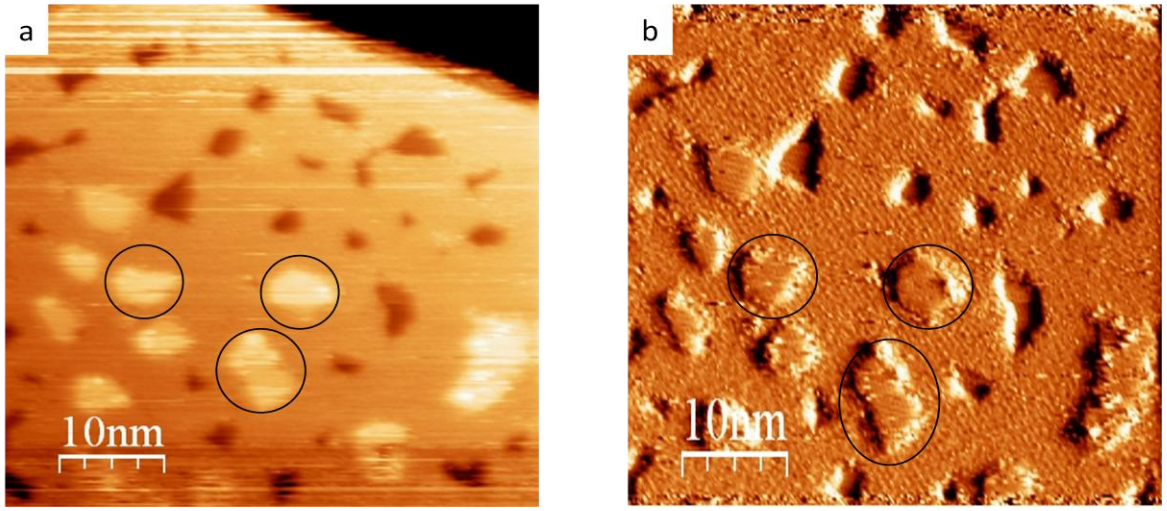

Figure 6.21: STM images of Cu(111) surface covered with ‘’44’’ after leave it overnight. (a, and b) STM image shows the two new (hole, and the add structure) formed on the Cu(111) surface. Tunnelling conditions: 1V, and 1nA.

The holes surrounding areas have ordered structure of the distorted honeycomb of ‘’44’’ suggested to form heptagonal rings as shown in Figure 6.22 (a, and b), while inside the holes a clearly $(\sqrt{3}x\sqrt{3})R30^{o}$ of oxygen reconstruction are observed Figure (c, and d) which is identical to the unit cell of oxygen $(\sqrt{3}x\sqrt{3})R30^{o}$ which was explained in section 6.3.2. The three structures found on ‘’44’’ oxygen/Cu(111) surface after leave the sample overnight could be explained as the ‘’44’’ oxygen structure broken back to the add oxide layer (Cu_2O-Like layer) on the terraces and oxide layer adsorbed on the Cu(111) surface. This is the

reverse of the formation of the ‘’44’’ oxygen structure which was suggested by Jensen et al and Matsumoto et al. to be formed by distorted (Cu_2O-like layer) [1, 9, 10]. Heptagonal rings have been suggested by Yang et al.[12] as a result of interaction carbon monoxide with ‘’44’’ oxygen structure on top of Cu(111) surface in which the central oxygen atom in the honeycomb of ‘’44’’ structure was the preferred attack site for CO molecules. In our case it could be that, the central oxygen atoms of the ‘’44’’ oxygen structure are the weakest link in the structure, and are ejected from the ring resulting to make the distortion in the honeycomb structure. The ejected oxygen reacts with step copper atoms to form Cu_2O-like layer on top of the ordered structure of Cu_2O (the islands are circled in Figure 6.21)

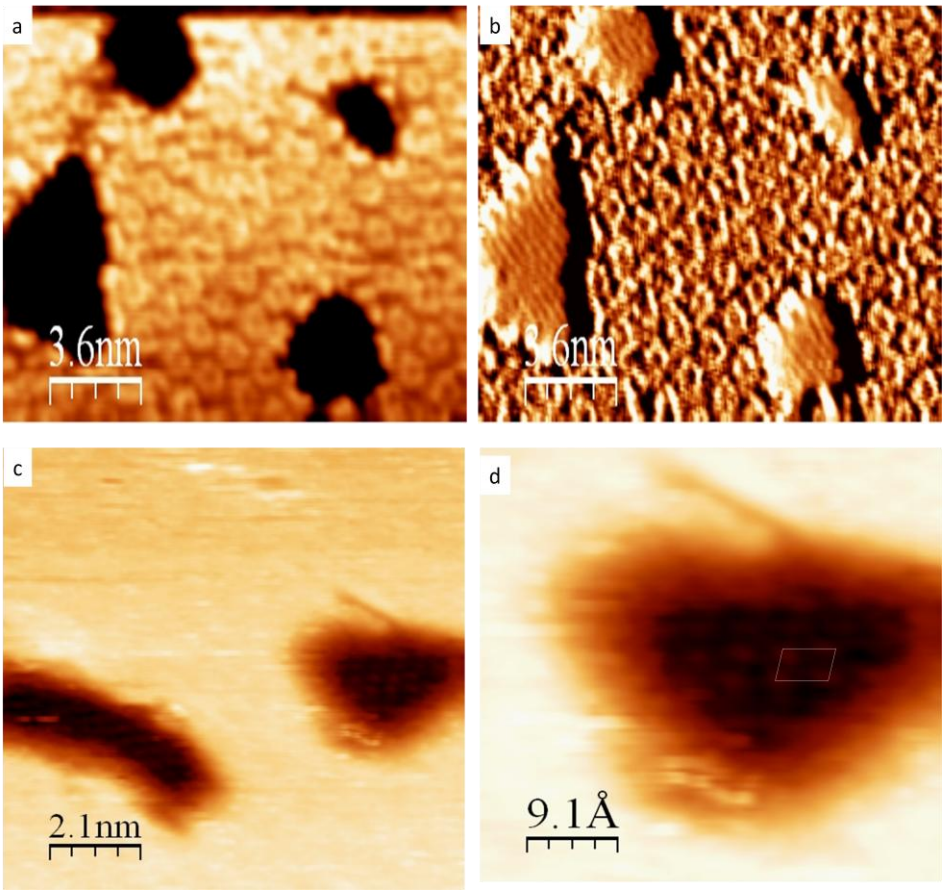

Figure 6.22: STM images of Cu(111) surface covered with ‘’44’’ structure after leave it overnight. (a, and b) STM images showed the ordered structure around holes. (c) The atomic resolution inside the hole, and (d) the atomic resolution and the unit cell of oxygen $(\sqrt{3}x\sqrt{3})R30^{o}$. Tunnelling conditions: 1V, and 1nA.

6.3.4 Interaction of oxygen with Cu(111) sample at 450 ^{o}C

The clean Cu(111) sample exposed to 1350 L of oxygen at 380 ^{o}C for 20 min, and then increase the annealing temperature to 450 ^{o}C for 10 min whilst in the presence of oxygen, leads to formation of ‘’29’’ oxygen structure with agreement with previous result [9, 10], while another study has shown that the ‘’29’’ structure possible to form at about 400 ^{o}C [1]. The oxygen concentration is $1.1x10^{15}$ cm^{-2}. STM images of the wide scan of the surface at room temperature shown again the striped line covering the terraces the height of step edge is 2.0 Å similar to the height of clean Cu(111) assigned to the two terraces were covered with oxygen Figure 6.23.

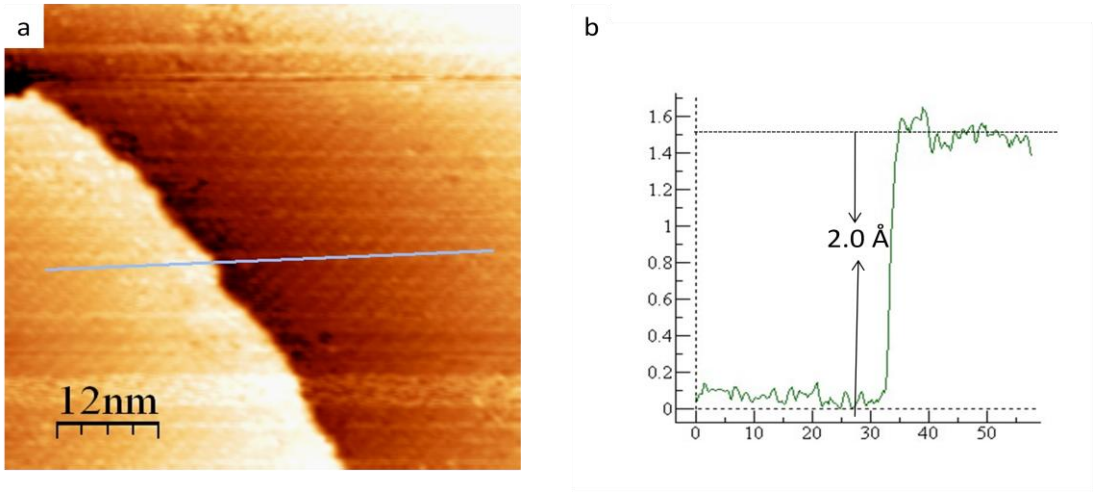

Figure 6.23: (a) STM image of ‘’29’’ oxygen structure top of Cu(111) surface. (b) Line profile shown the height of step edge. Tunnelling conditions: 1V, and 1nA.

Atomic resolution of the surface ‘’29’’ oxygen on top of Cu(111) surface shows a unit cell with vectors 1.7 nm, and 0.9 nm as shown in Figure 6.24, with agreement with previous result[1, 8-10]. Small difference between the total of atomic density in‘’29 oxygen (16/29 = 0.552, and ‘’44’’ oxygen structure (24/44 =0.545) [1] is assigned to little overall change in the structures when it transforms from the ‘’44’’ to ‘’29’’ which was suggested to be met by the annealing of the sample. Leaving the ‘’29’’ oxygen structure overnight no change observed which indicates higher stability of ‘’29’’ compared with the ‘’44’’ oxygen structure. The stability of ‘’29’’ oxygen structure it could be due to the arrangement of the centred atomic oxygen of the honeycomb structure. In ‘’29’’ structure all the centred atomic oxygen sit at threefold sites, while in the ‘’44’’ oxygen structure all centred atomic oxygen sit at threefold sites except one of them which sits at bridge-site [1]

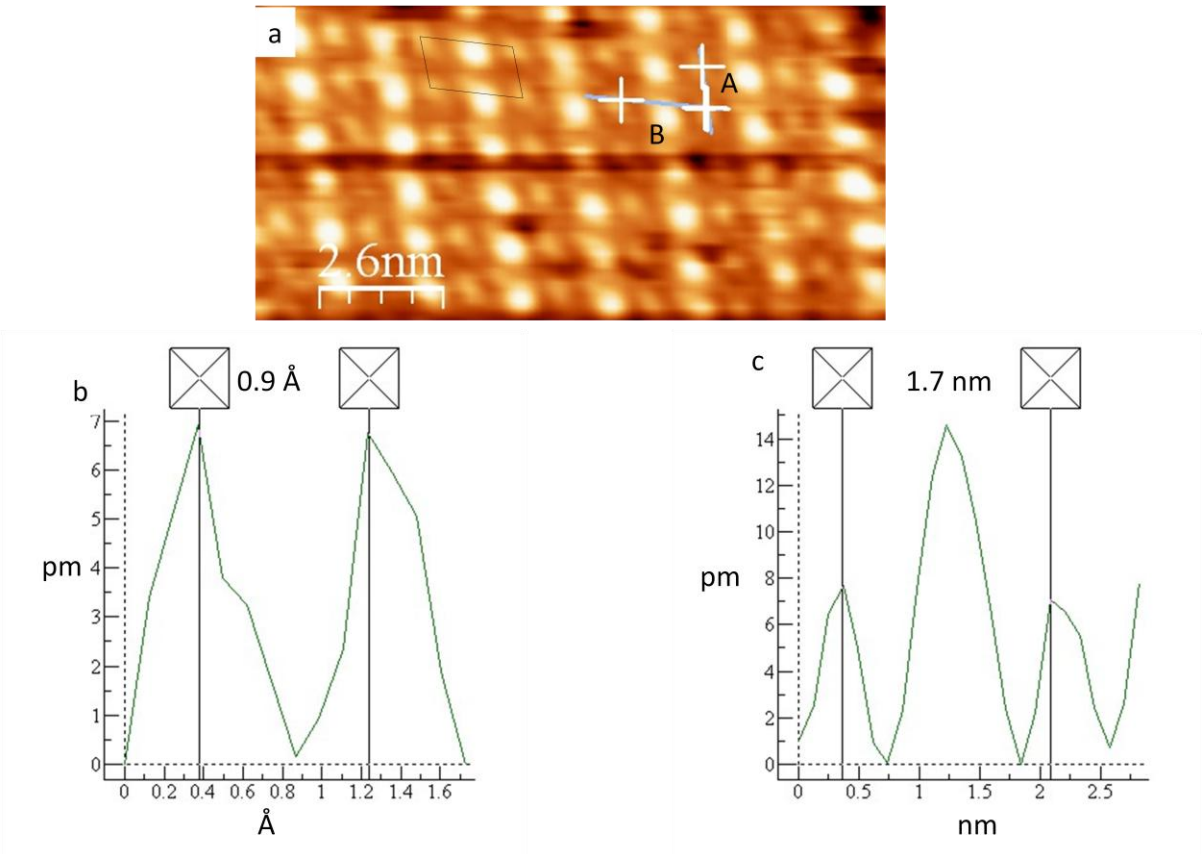

Figure 6.24: (a) STM images of atomic resolution of ‘’29’’ oxygen top of Cu(111) surface, and shown the unit cell. (b) Line profile of line A, and (c) line profile of line B. Tunnelling conditions: 1V, and 1nA.

6.3.5 Interaction of HCl with clean Cu(111) surface at room temperature

Exposure of the clean Cu(111) surface at room temperature to 180 L of HCl gas in UHV conditions leads to coverage of the copper surface by Cl as confirmed by XPS (the saturated concentration is 5.9×10^{14} cm^{-2} which is one third of the Cu(111) surface concentration 1.77×10^{15} cm^{-2}) as shown in Figure 6.25 in agreement with Motai et al. [20]. This concentration supports the suggestion of formation of $(\sqrt{3} \times \sqrt{3})R30^{o}$ of Cl structure. STM images after exposing the clean Cu(111) surface to HCl show similar behaviour as reported in section 5.3.2 in previous chapter for Cu(100). After exposure to 50 L HCl, the step edges of Cu(111) surface lose their sharpness indicating extraction of copper atoms from the step edge as shown in Figure 6.26, in agreement with previous result of work on Cu(100) [24].

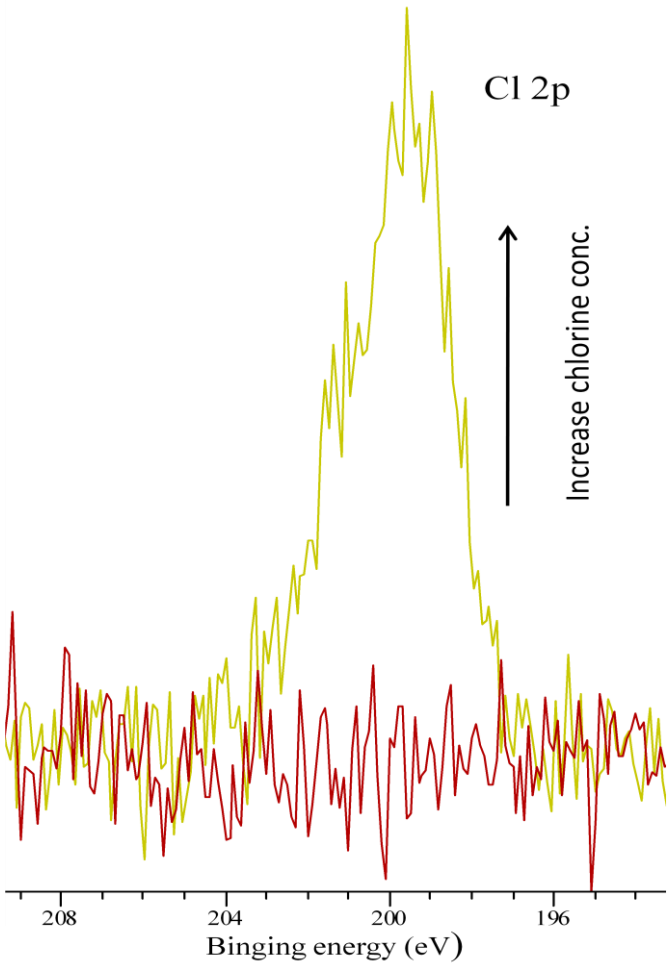

Figure 6.25: XP spectra of Cl 2p of Cu(111) surface saturated with Cl by exposing the clean Cu(111) surface to 180 L of HCl.

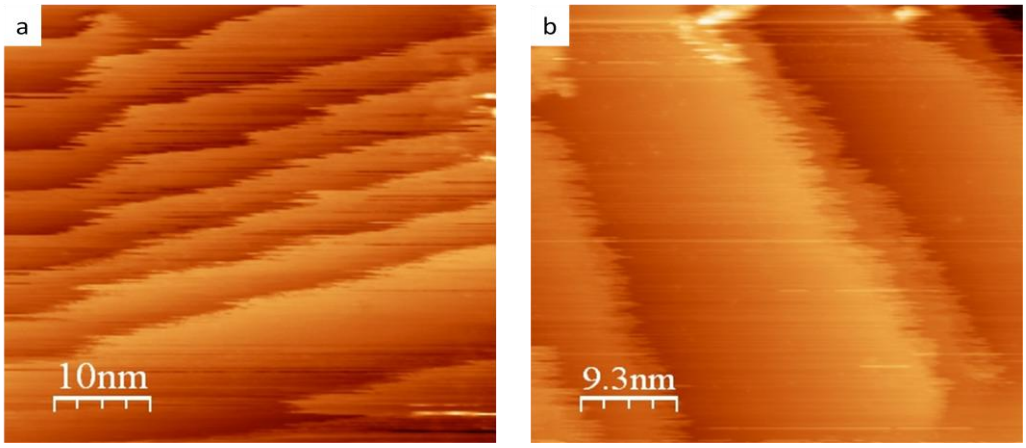

Figure 6.26: (a, and b) STM images of two different place at the Cu(111) surface showing the effect of exposing the sample to about 50 L of HCl on the step edges. Tunnelling conditions: 1V, and 1nA.

The extraction of copper atoms by reacting the Cu(111) surface with HCl can also be recognised in the effect HCl has on a hexagonal island shown in Figure 6.27. On the clean surface this island has the exact Cu(111) step edge properties (have the same height) except that, this island is open to interact with HCl from all directions. A sequence of STM images of this island exposed to 180 L of HCl are shown in Figure 6.28. At the beginning of the reaction after a dose about 25 of HCl no change recognised, but at 50 L small change happen to the copper island as a decrease in the island size indicate the extraction of copper atoms from the edge of it, and the same thing happens at the step edges. From 75 L to 125 there is a continuous decrease in copper island size. The increased noise in the image is probably due to the atomic movement of ejected copper atoms, and Cl atoms on the surface and tip due to mobility of the Cl atoms before saturation coverage is reached in agreement with previous result [25]. From 150 to 175 L of HCl the copper island disappears while the copper step edge is still not sharply resolved.

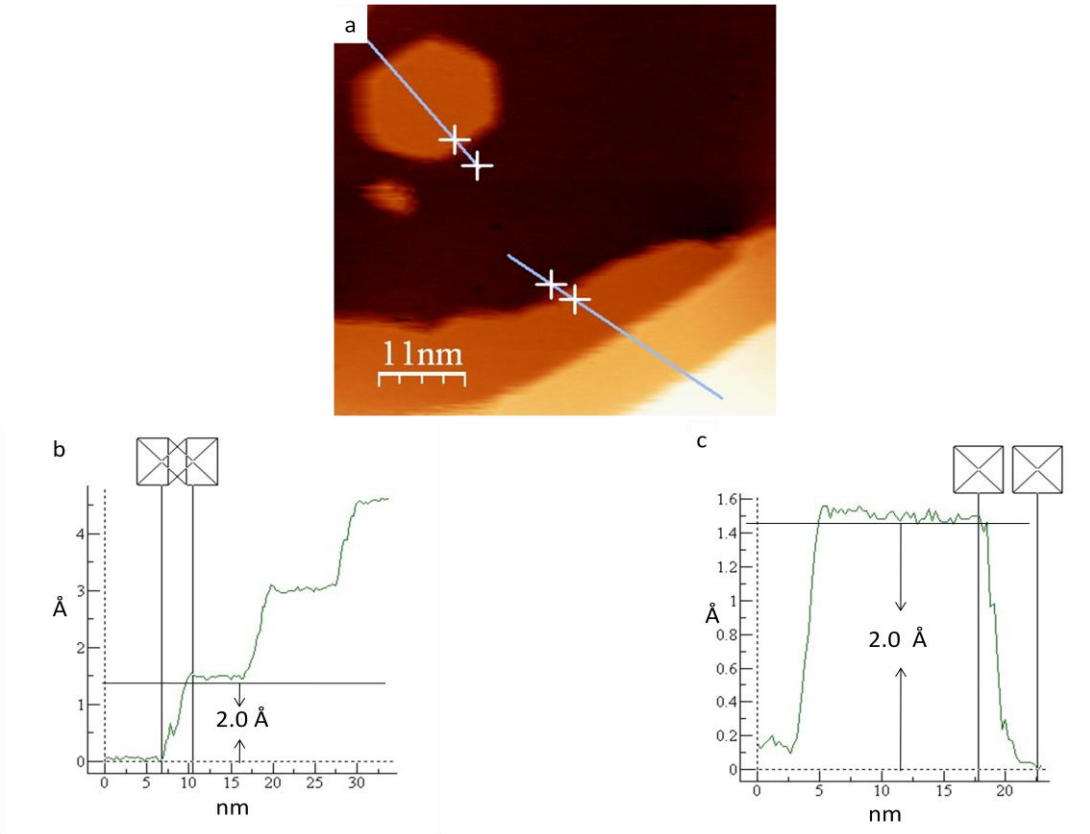

Figure 6.27: (a) STM image of Copper island top of Cu(111) surface. (b, and c) Line profile of copper island and Cu(111) step edge shown the same height. Tunnelling conditions: 1V, and 1nA.

The atomic resolution of Cl atoms on top of Cu(111) surface appeared at about 180 L of HCl as shown in Figure 6.29. The $(\sqrt{3}x\sqrt{3})R30^{o}$ structure of Cl was clearly recognised consistent with previous work suggesting that at one third coverage a long rang ordered $(\sqrt{3}x\sqrt{3})R30^{o}$ of Cl formed [14, 26] and no other reconstruction recognised in contrast to the Motai et al. work which reported $(6\sqrt{3}x6\sqrt{3})R30^{o}$, and $(4\sqrt{7}x4\sqrt{7})R19.1^{o}$ reconstruction by STM, and LEED at coverage about 7.96 x 10^{14} cm^{-2}. The step edge height of Cu(111) covered with $(\sqrt{3}x\sqrt{3})R30^{o}$ of Cl was similar to the height of the clean Cu(111) surface assigned to the chlorine atoms covered all the terraces.

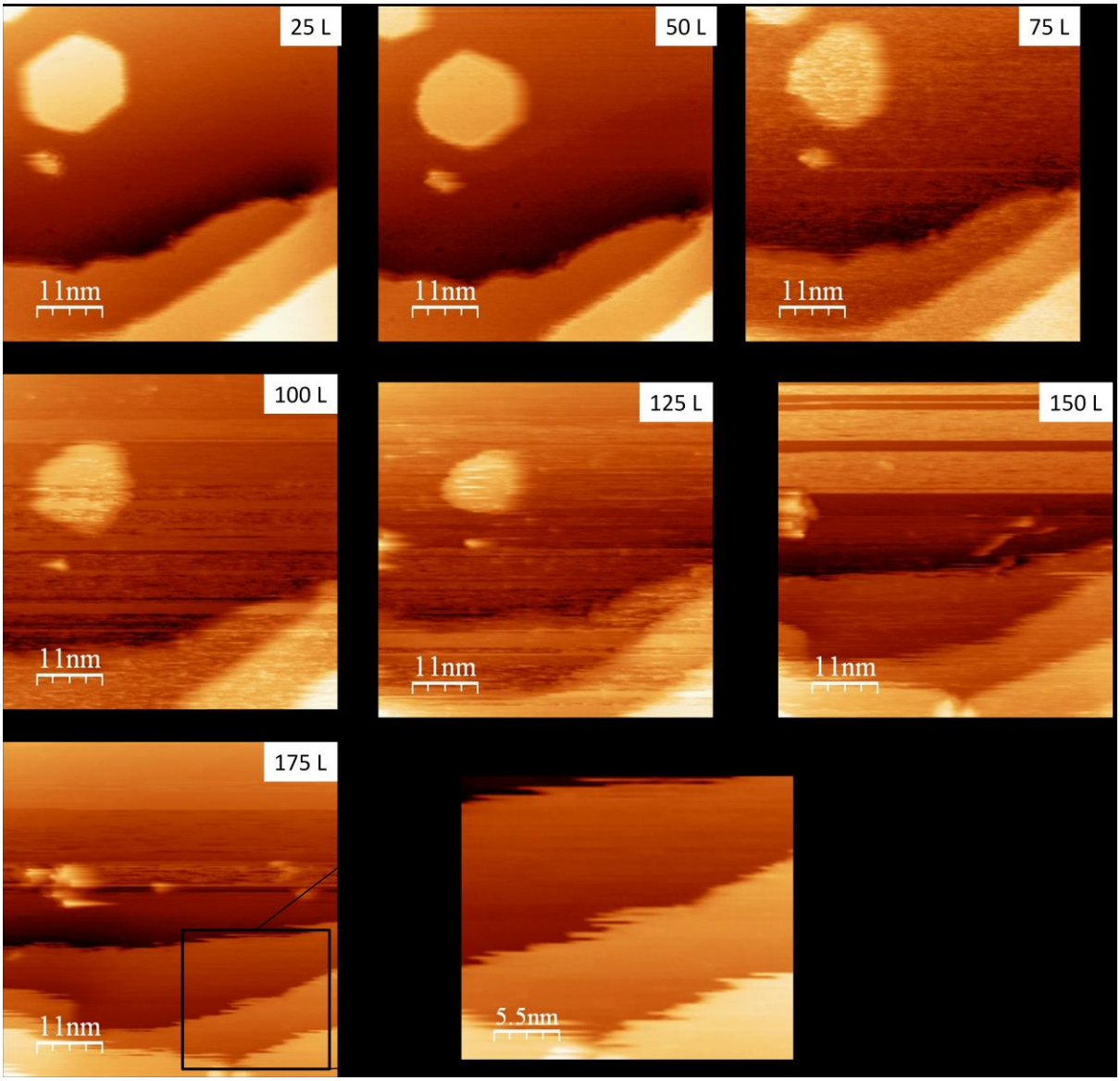

Figure 6.28: Sequence of STM images recorded during exposure of clean Cu(111) surface to 180 L of HCl. and showing the effect of HCl on the copper island. Tunnelling conditions: 1V, and 1nA.

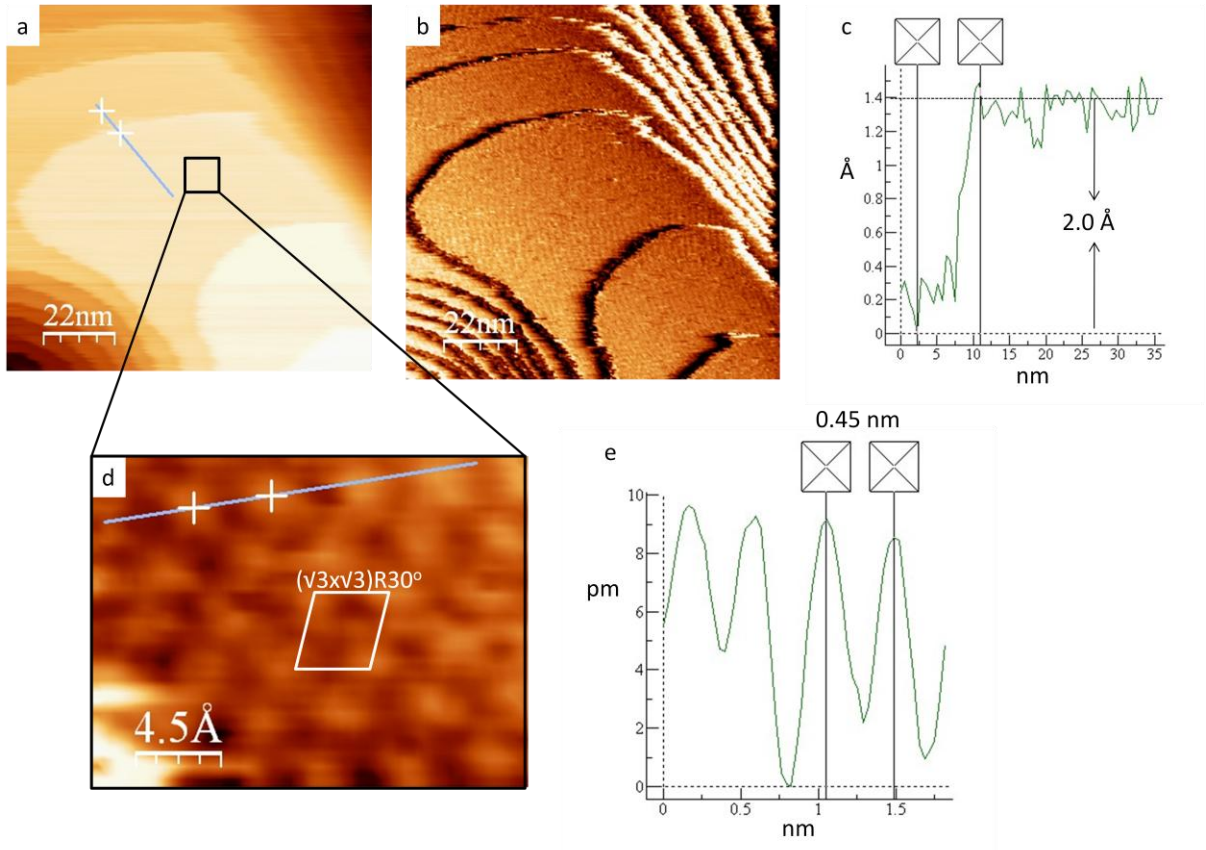

Figure 6.29: STM images of (√3x√3)R30° Cl structure covered Cu(111) surface. (a, and b) The wide terraces of Cu(111) surface show a long range of ordered structure of chlorine. (c) Line profile showing the height of step edge in (a). (d) Atomic resolution of (√3x√3)R30° structure of Cl. (e) Line profile showing the distance between two Cl atoms in (d).

6.3.6 Interaction of HCl with O/Cu(111) surface at room temperature

In this experiment the clean Cu(111) surface was exposed to 1500 L of oxygen at room temperature, then exposed to 200 L of HCl gas, and then an extra 50 L of HCl. The XP spectra showed the increase of the chlorine concentration to be 6.0×10^{14} cm^{-2} at 200 L and no big changed happened by adding an extra 50 L (6.1×10^{14} cm^{-2}) indicating the sample is saturated by chlorine, while all the oxygen was removed from the surface (the oxygen concentration before the reaction was 8.1×10^{14} cm^{-2}) as shown in Figure 6.30.

The STM experiments studying the interaction of the O/Cu(111) surface formed at room temperature with HCl is divided into two parts: the oxide islands layer formed at step edges and the triangle islands in the terraces. For interaction of HCl with step edge oxygen layer, the clean Cu(111) exposed to 550 L of oxygen was enough to form the step edge oxide layer. The sequence of STM images after exposing clean Cu(111) surface to 550 L of oxygen at

room temperature are shown in Figure 6.31. At 20 L the effect of exposing the sample to oxygen is evident in the STM images with the appearance of small angular structures at the step edges. The sizes of the angular structure increase as we increase the exposure. At 550 L the step edge oxide layer was clearly formed. The O/Cu(111) sample was then exposed to 115 L of HCl at room temperature. The sequence of STM images in Figure 6.32 show no change happened in the angular step edges and oxide layer by dosing HCl from 10 to 30 L. At 40 L the resolution of STM image is affected as a result of moving atoms on top of the copper surface. The oxide layer at angular step edge marked by black dotted line in some images (the non marked image was left to facilitate the monitoring and follow up the change in the terrace size). From 50 to 60 L shows a small change in the angular structures as they start losing sharpness, which is clearly noted by comparing the image of 60 L with the 10 L one. By exposing the sample to HCl from 70 to 100 L the decrease of oxide layer size was clearly noted, and combined by losing the angular structure at the step edges, until it disappeared at 110 L. Atomic resolution of chlorine atoms appeared at 115 L assigned to saturation coverage of the copper surface by chlorine was reached. The atomic resolution of chlorine atoms in Figure 6.33 showed consistent data with the data illustrated in section 6.3.4 of interaction HCl with clean Cu(111) sample with slightly different unit cell size (decrease by about 0.04 nm).

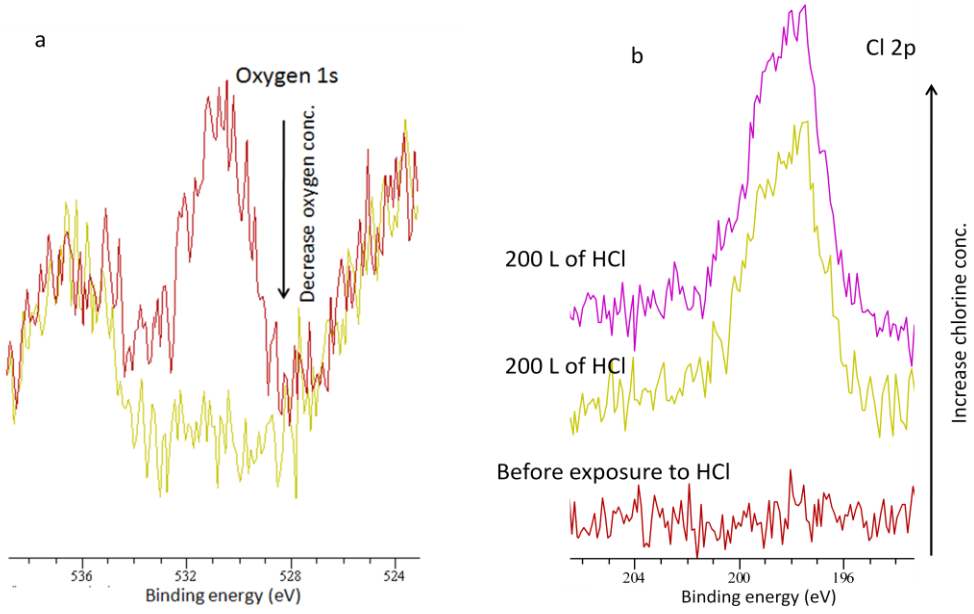

Figure 6.30: XP spectra showed the decrease of oxygen in (a), increase of chlorine concentration in (b). Oxygen concentration before the exposed to HCl was $8.1x10^{14}$ cm^{-2} while as the chlorine concentration after exposure to 250 L of HCl is $6.1x10^{14}$ cm^{-2}.

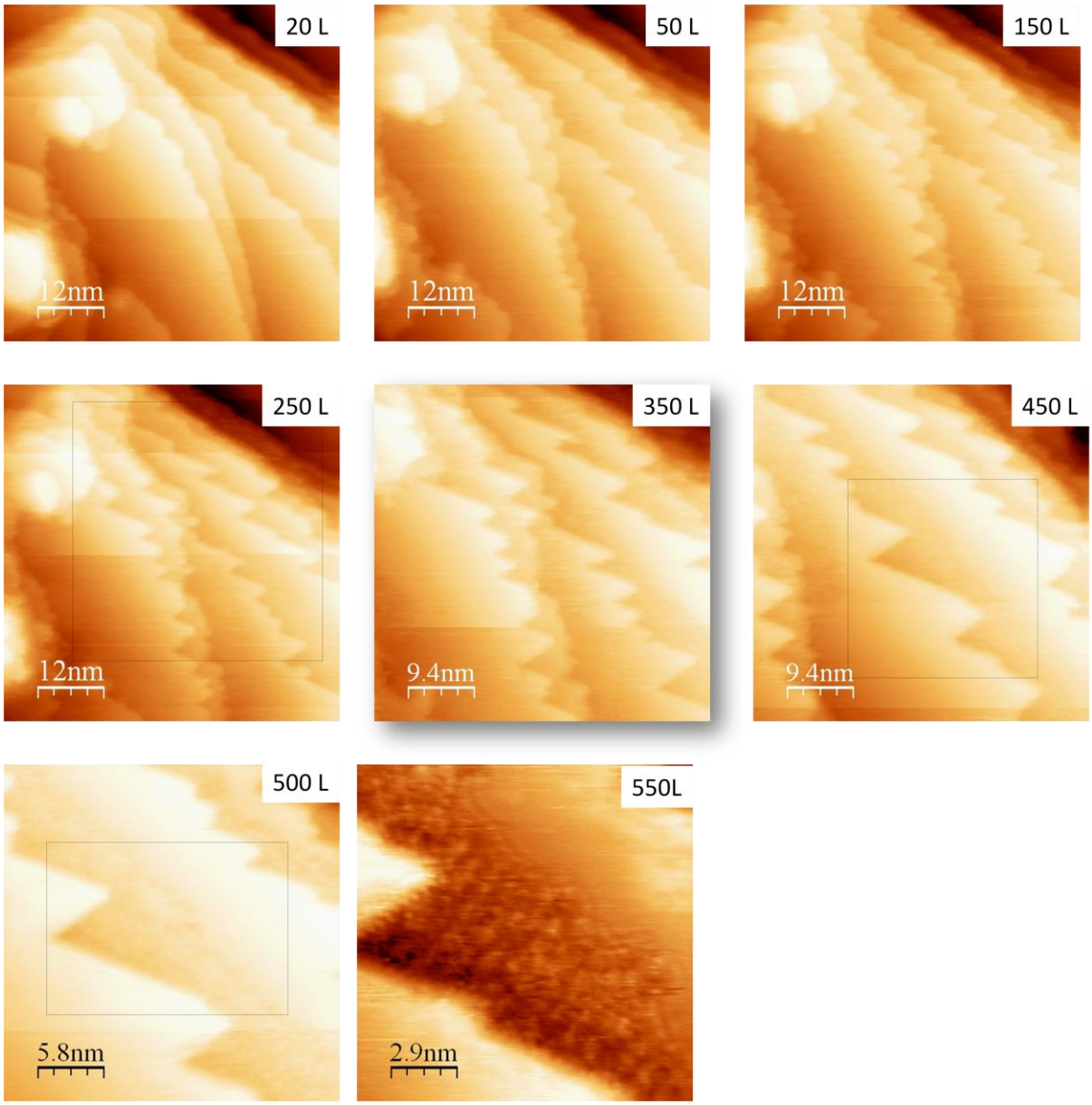

Figure 6.31: Sequence of STM images of clean Cu(111) surface exposed to 550 L of oxygen at room temperature to make the step edge oxide layer. The dotted square assigned to the zoomed in area. Tunnelling conditions: 1V, and 1nA.

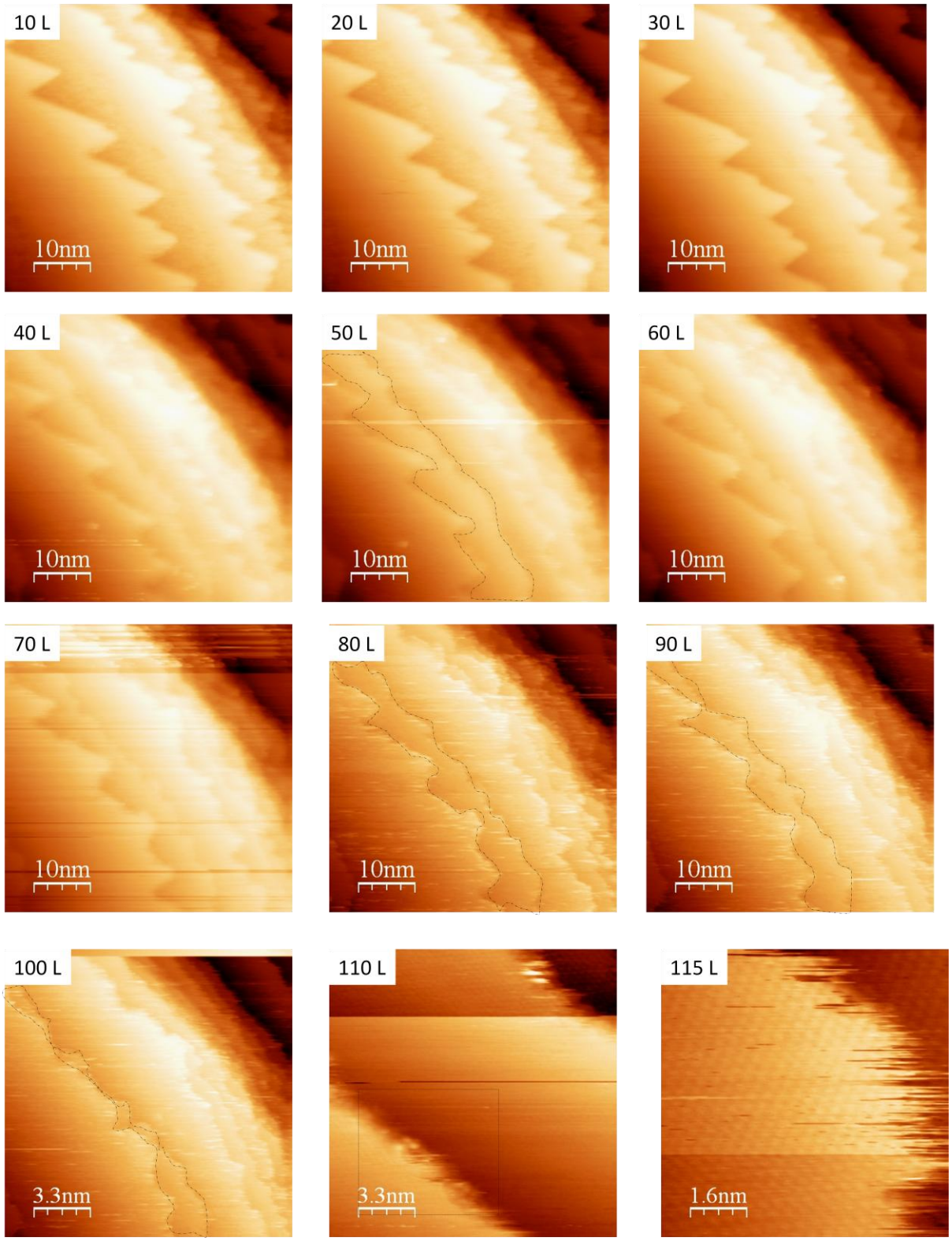

Figure 6.32: Sequence of STM images of O/Cu(111) surface exposed to 115 L of HCl at room temperature. Tunnelling conditions: 1V, and 1nA.

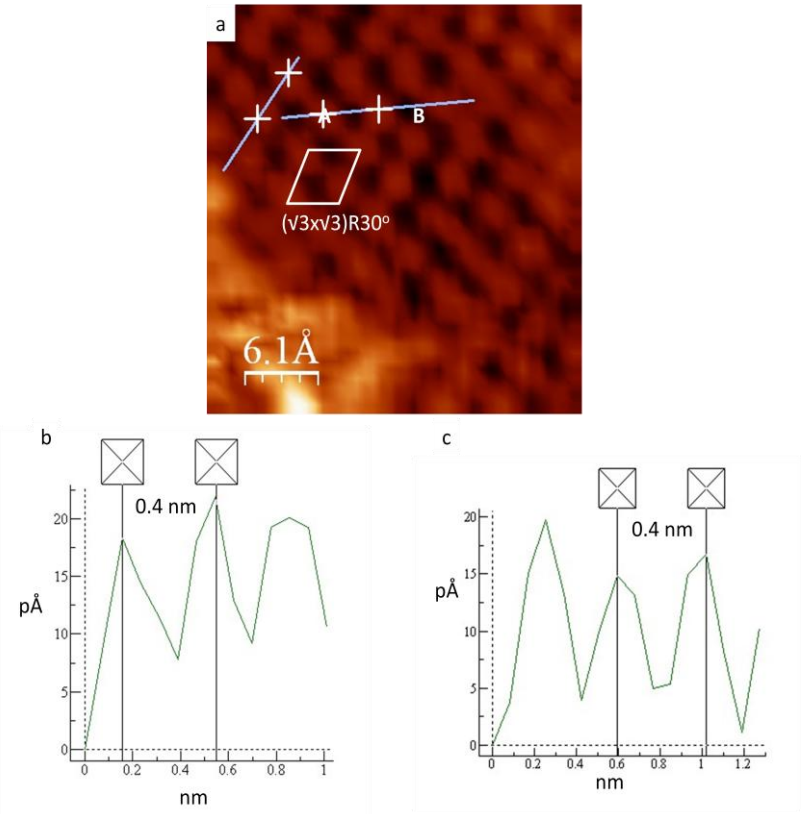

Figure 6.33: STM images of (√3x√3)R30° Cl structure covering the Cu(111) surface, (a) and (b) line profiles of line A, and B respectively. Tunnelling conditions: 1V, and 1nA.

To study the effect of interaction of HCl with triangular oxygen islands, the clean Cu(111) sample was exposed to 675 L of oxygen at room temperature. Again the consistent result obtained with above result. Figure 6.34 shows the angular step edges structure and the triangle oxygen islands formed at the terraces. The O/Cu(111) surface was then exposed to about 150 L of HCl at room temperature.

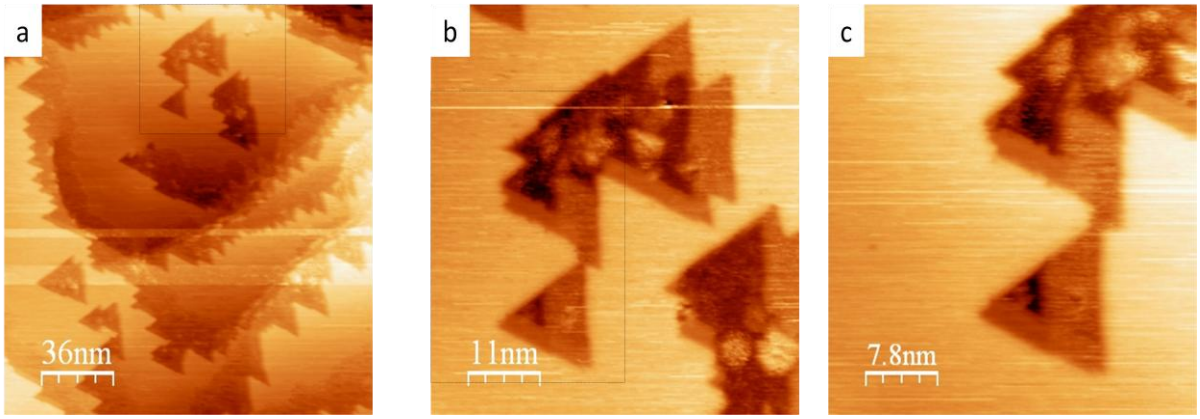

Figure 6.34: STM images of Cu(111) surface after exposure to 675 L of oxygen at room temperature showing the angular structure at the step edge and the triangle islands of oxygen. Tunnelling conditions: 1V, and 1nA.

The sequence of STM images in Figure 6.35 of the O/Cu(111) surface exposed to HCl show the effect of the dose of HCl on oxygen island. The island size decreased from outward to inward indicating that the chlorine atoms prefer to adsorb on top of the terraces rather than in the oxygen island. Atomic resolution of chlorine atoms is observed after removing all the oxygen atoms indicated to saturation coverage have been met.

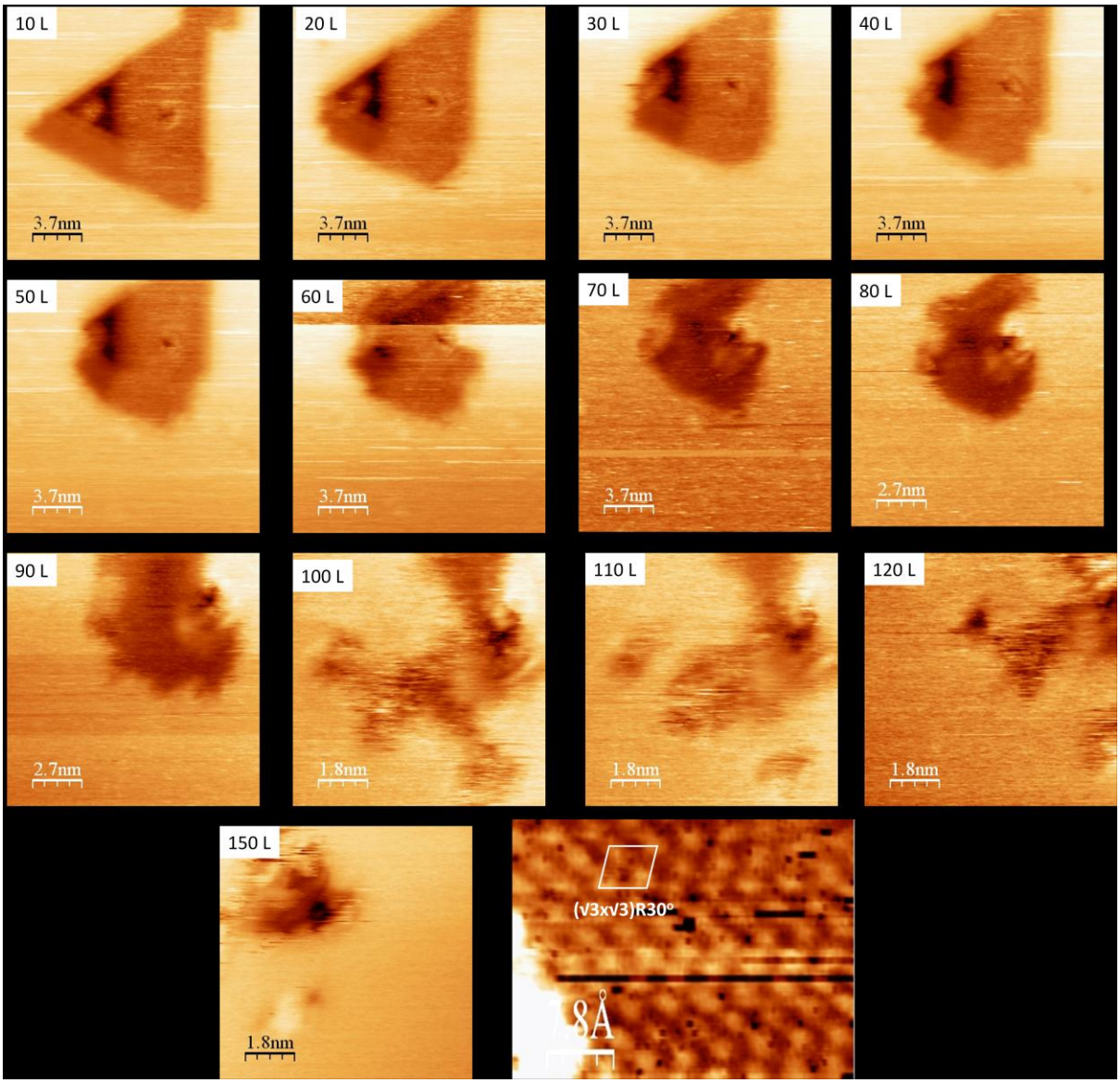

Figure 6.35: Sequence of STM images of O/Cu(111) surface exposed to 150 L of HCl at room temperature. Tunnelling conditions: 1V, and 1nA.

The third experiment is for studying the interaction of HCl with oxygen layer at the step edge, and the oxygen triangle island, after the preferred path of interaction of each of them separately with HCl are observed above. In this experiment the clean Cu(111) surface was

exposed to 1350 L of oxygen at room temperature to form the oxide layer at the step edge, and the oxide triangle layer as shown in Figure 6.36, then the O/Cu(111) surface was exposed to 170 L of HCl at room temperature. The triangle oxygen and the step edge oxide layer are attacked by HCl after the clean copper surface is covered with chlorine, but the triangle oxygen island are attacked by HCl faster than step edge of oxygen layer, that observed from image of dosing HCl from 100 to 140 L, which shows the decrease of triangle oxygen island size. The step edge oxygen layer is attacked by HCl from the terrace side rather than the step edge, as shown in the images of HCl exposure from 120 to 140 L. Consumption of triangle oxygen island is faster than the step edge oxygen layer due to multiple attack directions of HCl while as one direction was found for the step edge oxygen layer. At 160 L of HCl the atomic resolution of chlorine atoms appears referring to the saturation coverage shown in Figure 6.37.

Figure 6.36: STM image of Cu(111) surface after exposure to 800 L of oxygen, then a sequence STM images of O/Cu(111) surface exposed to 170 L of HCl at room temperature while the dotted square in the first image assigned to zoomed in area. Tunnelling conditions: 1V, and 1nA.

Figure 6.37: STM images of $(\sqrt{3}x\sqrt{3})R30^{o}$ Cl structure covering the Cu(111) surface. Tunnelling conditions: 1V, and 1nA.

6.3.7 Interaction of HCl with ‘’44’’ structure of oxygen at a Cu(111) surface at room temperature

Oxygen ‘’44’’ structure formed on top of Cu(111) surface as illustrated in section 6.3.2, leads to the formation of striped lines of Cu_2O covering all the surface. Exposure of ‘’44’’ structure to 210 L of HCl leads to decrease of oxygen coverage Figure 6.38(a) from $1.10x10^{15}$ cm^{-2} to $5.10x10^{14}$ cm^{-2} whereas the chlorine coverage increase to $1.15x10^{15}$ cm^{-2} Figure 6.38(b) which assigned to 2:1 ratio as shown in the following equation:

$$2HCl + O \rightarrow 2Cl + H_2O$$

The residual oxygen concentration could be due to the subsurface oxygen which formed as a result of annealing while exposing the sample to oxygen. These result have an agreement with work of interaction of HCl with oxygen on top of Cu(110) which they suggested the existence of oxygen top of Cu(110) surface is facilitating the formation of $CuCl_2$ [27]. The absence of satellite features in the XPS of Cu(2p) rule out the presence of Cu^{2+} and hence $CuCl_2$, so Cu-Cl island are suggested to be formed on top of chlorine layer as the result of interaction of HCl with the released copper atoms of the Cu_2O.

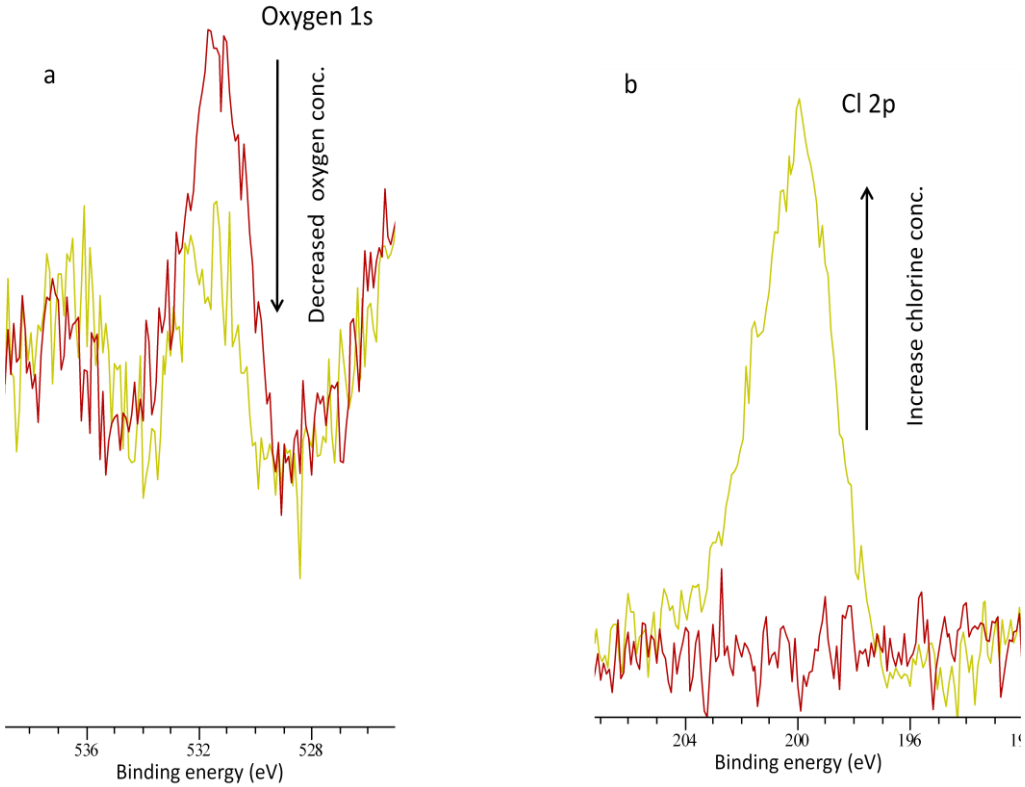

Figure 6.38: XP spectra showed the decrease of oxygen in (a), increase of chlorine concentration in (b). Oxygen coverage decreased from $1.10x10^{15}$ cm^{-2} to $5.10x10^{14}$ cm^{-2} while the chlorine coverage increased to $1.15x10^{15}$ cm^{-2}.

STM image of the ‘’44’’ structure of oxygen exposed to about 15 L of HCl leads to adsorbed species at the centred of honeycomb structure of oxygen as shown in Figure 6.39. The substitution of oxygen we suggest to be started by the centred oxygen atoms of honeycomb structure in agreement with previous result of interaction of carbon monoxide with ‘’44’’ structure [12, 13], then extend over the surface. After exposing the sample to about 25 L of HCl the imaging by STM was difficult, possibly because of the huge movement of atoms on surface until the exposure about 150 L STM image was back. The STM image of the surface after exposure to the 150 L of HCl is shown in Figure 6.40(a). All the Cu(111) surface is covered with disordered islands and with different size as shown in Figure 6.40(b, and c). Most of the small islands were trapped at the step edge whereas the large islands were dispersed over the terraces. These islands could be Cu-Cl over the Cl/Cu(111) surface which explain the excess of the chlorine concentration. Ease of imaging the surface at 15 L of HCl could be due to the slow reaction of HCl with centred atoms of honeycomb of ‘’44’’ structure and then the fast reaction, done after all the centred atoms were substituted, leading to large movement of the atoms causing the difficulty of imaging. Similar suggestion [12, 13] recognised the substitution of centred oxygen atoms as a slow step, and removing all the other oxygen atoms as fast step after all the centred place were covered by carbon monoxide.

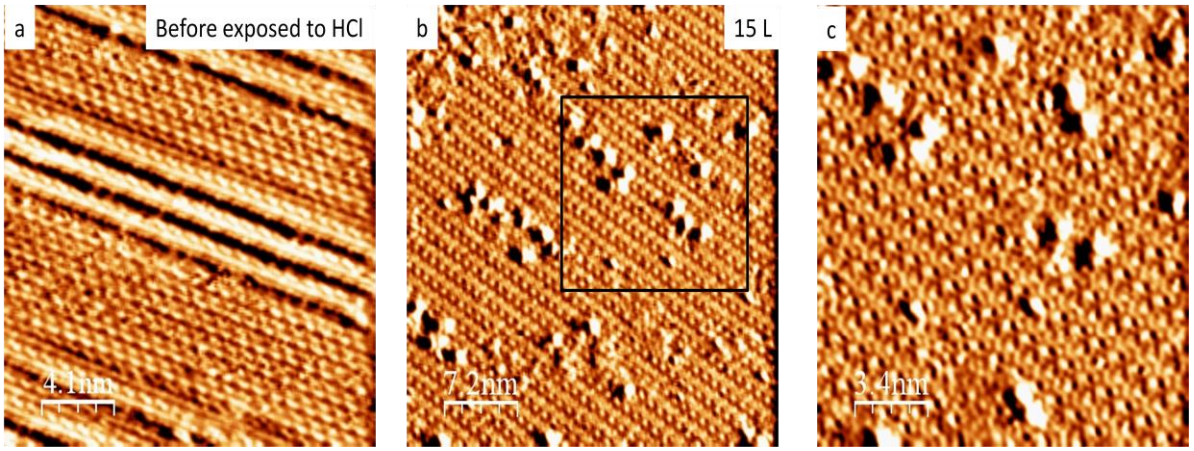

Figure 6.39: (a) STM images of ‘’44’’ oxygen structure exposed to 15 L of HCl at room temperature. (b) The magnified image of black square in (a) shows the adsorbate species at the centred of honeycomb structure of oxygen. Tunnelling conditions: 1V, and 1nA.

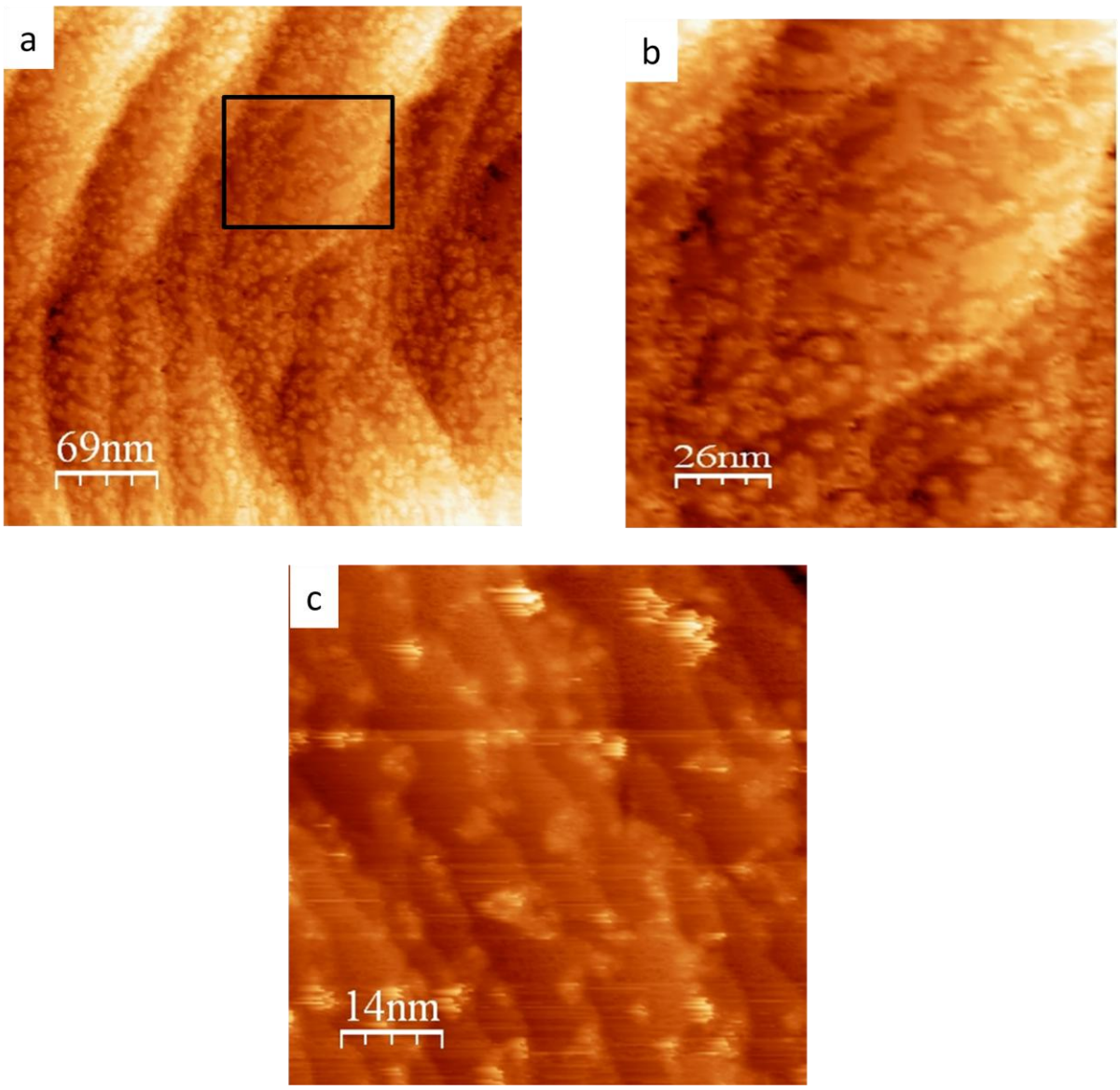

Figure 6.40: STM images of ‘’44’’ oxygen structure on top of Cu(111) after exposure to 150 L of HCl. (a, and b) showing the different size of Cu-Cl islands covering the surface. (c) STM image showing the small islands trapped at step edges. Tunnelling conditions: 1V, and 1nA.

6.3.8 Interaction of HCl with ‘’29’’ structure of oxygen on top of the Cu(111) surface at room temperature

Formation of ‘’29’’ oxygen structure on top of Cu(111) surface illustrated in previous section 6.3.4, as a transformation of ‘’44’’ structure to ‘’29’’ structure by increase of annealing temperature after the ‘’44’’ structure formed to 450 ^{o}C. After exposing the ‘’29’’ oxygen structure to 200 L of HCl, the oxygen concentration decreases from $1.1x10^{15}$ cm^{-2} to $4.8x10^{14}$ cm^{-2} while the chlorine concentration increases to $1.12x10^{15}$ cm^{-2} as shown in Figure 6.41 small amount of Cl adsorbed from the background). The ratio is about 2:1, consistent with previous result in section 6.3.7, which showed that two HCl molecules were required to eject one oxygen atom and leave the surface as H_2O.

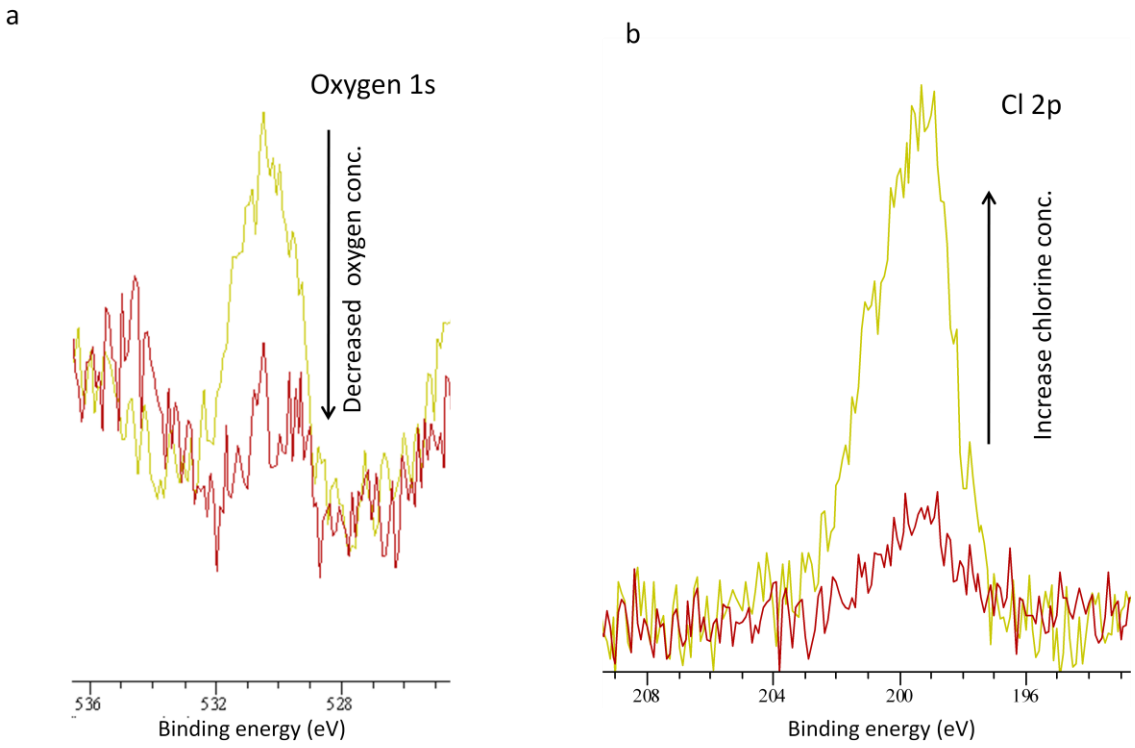

Figure 6.41: XP spectra showing the decrease of oxygen in (a), increase of chlorine concentration in (b). Oxygen concentration decreased from $1.1x10^{15}$ cm^{-2} to $4.8x10^{14}$ cm^{-2} while as the chlorine concentration increased to $1.12x10^{15}$ cm^{-2}.

The sequences of STM images of atomic resolution of ‘’29’’ structure after exposure to about 35 L of HCl are shown in Figure 6.42. As the exposure increases the small dot appeared on the surface which it could be HCl molecules adsorbed on the surface (at the centre of honeycomb structure). The oxygen unit cell size is not changed but the structure is slightly changed by comparison of the image of 15 L to the one of 20 L. The atomic resolution decreases until it disappears at 35 L suggesting that, the slow reaction was finished and the fast reaction started. Figure 6.43 shows the change in the structure of the unit cell unit between the image of 20 L of HCl and the image of ‘’29’’ structure before dosing HCl. The change could be because the HCl molecules are filling the honeycomb structure of oxygen or it could be because the change happened to the STM tip.

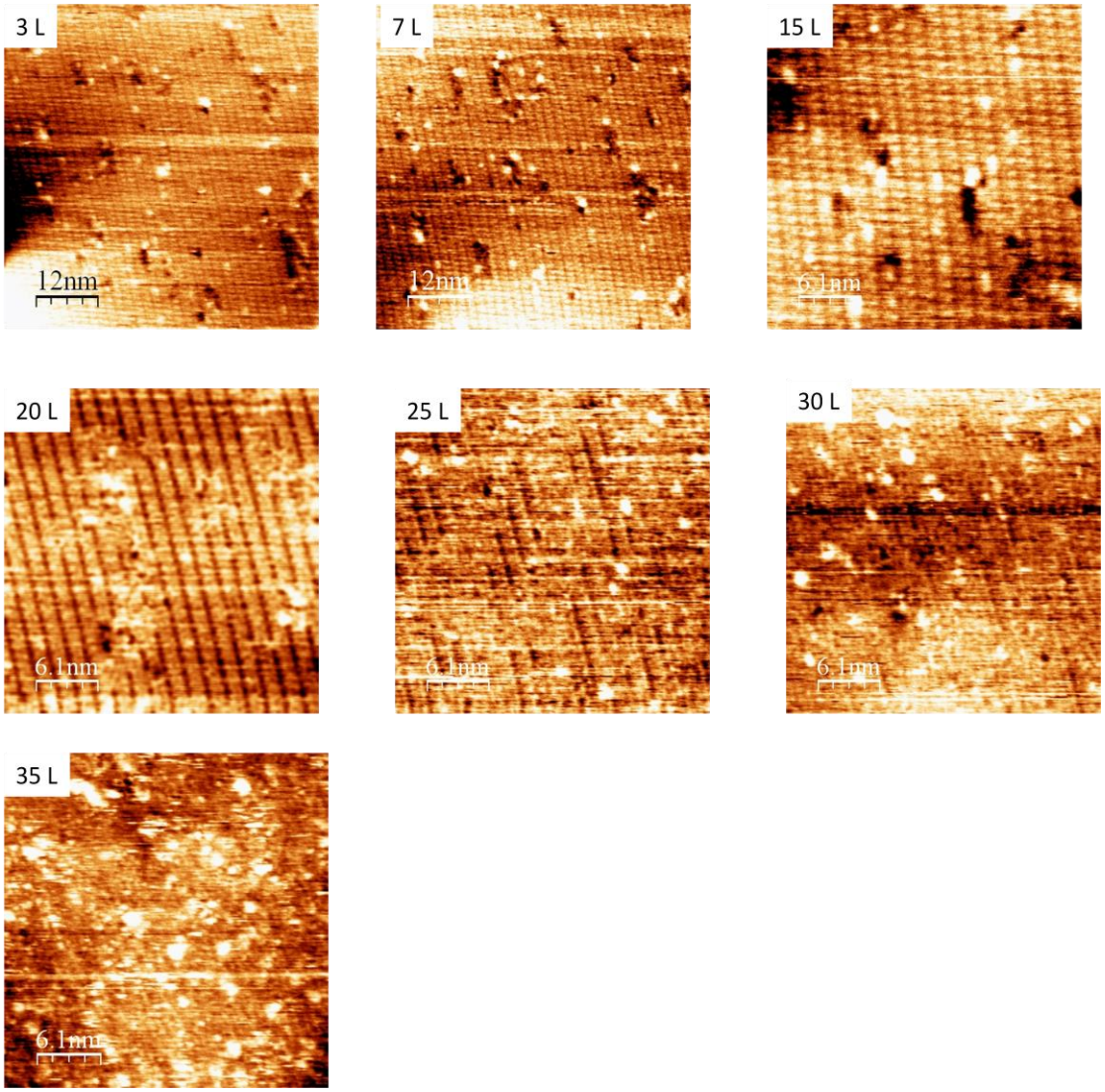

Figure 6.42: Sequence of STM images of atomic resolution of ‘’29’’ structure after exposure to 35 L of HCl. Tunnelling conditions: 1V, and 1nA.

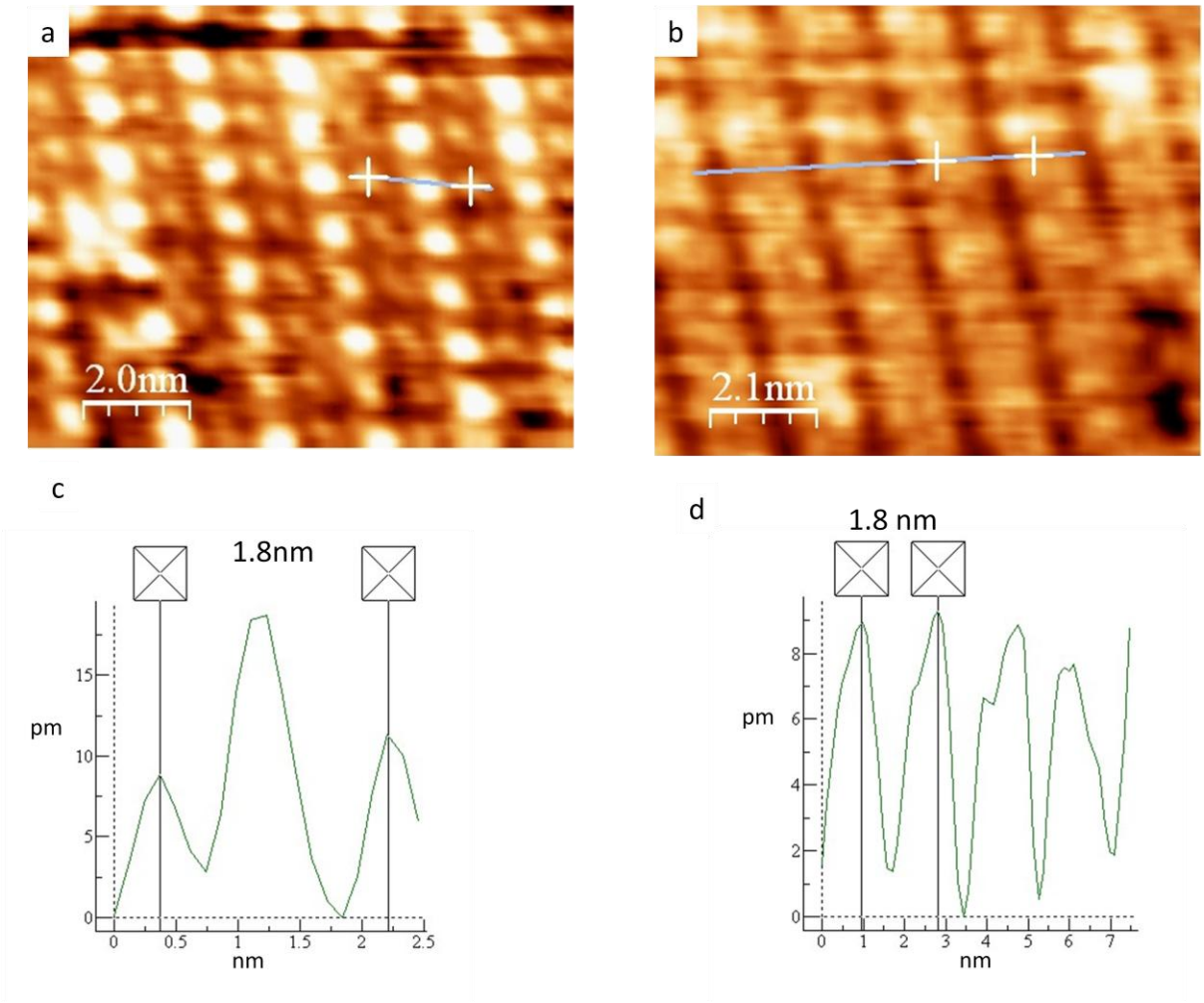

Figure 6.43: (a) STM image of the ‘’29’’ unit cell before exposure to HCl. (b) Change happened to ‘’29’’ unite cell after exposed to 20 L of HCl. (c, and d) are the line profile of image a, and b, showing no change happens to the unit cell size. Tunnelling conditions: 1V, and 1nA.

After leaving the sample to settle down and, by continued exposure of the sample to about 90 L HCl , the surface covered with small circle island concentrated in the step edge, similar to the island form after exposed the ‘’44’’ structure to HCl in section 6.3.7, which is suggested to be $CuCl_2$ islands as shown in Figure 6.44. The transformation of CuCl islands to a larger CuCl layer occurs after exposure of the sample to an extra 30 L of HCl as shown in Figure 6.45. Small islands are observed on top of the CuCl layer which may explain the excess in concentration of chlorine on the surface as shown in Figure 6.46.

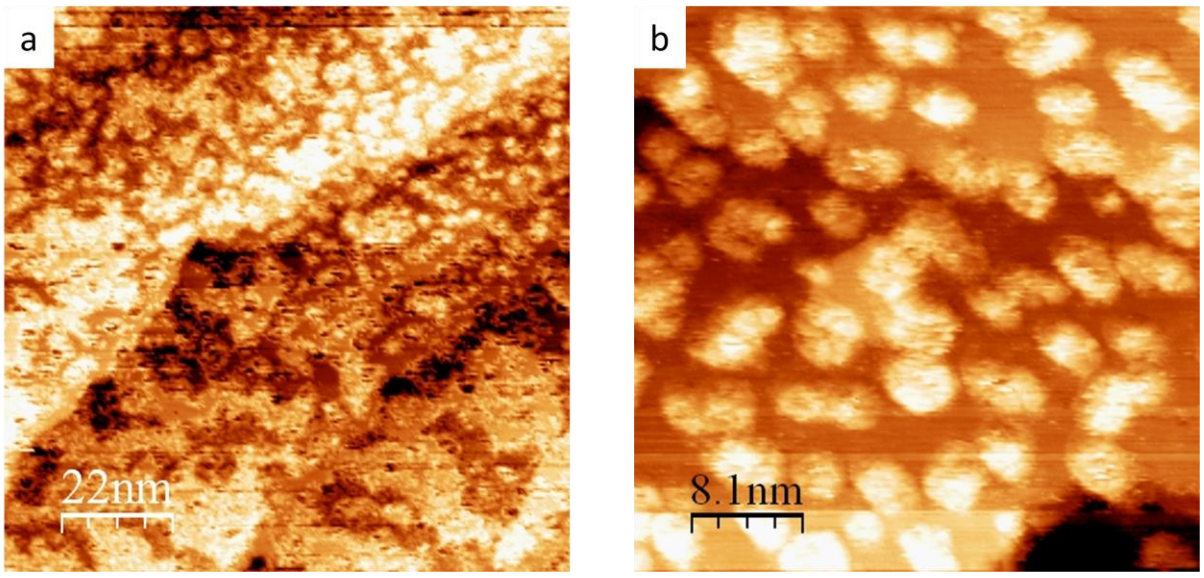

Figure 6.44: (a. and b) large and small scan respectively of STM image of small CuCl island concentrated at the step edges after exposure to 90 L of HCl. Tunnelling conditions: 1V, and 1nA.

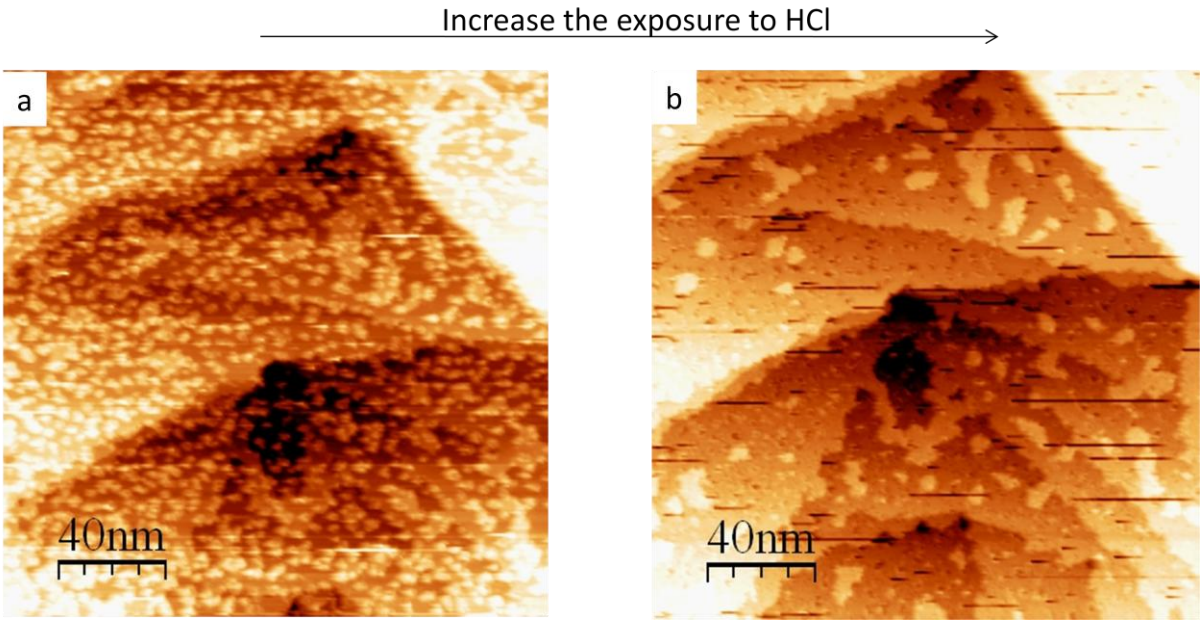

Figure 6.45: STM images showing the effect of exposing the sample to extra 30 L of HCl, leading to form CuCl layer in (b) from the small CuCl island in (a). Total exposures are 100, and 120 L in (a, and b) respectively. Tunnelling conditions: 1V, and 1nA.

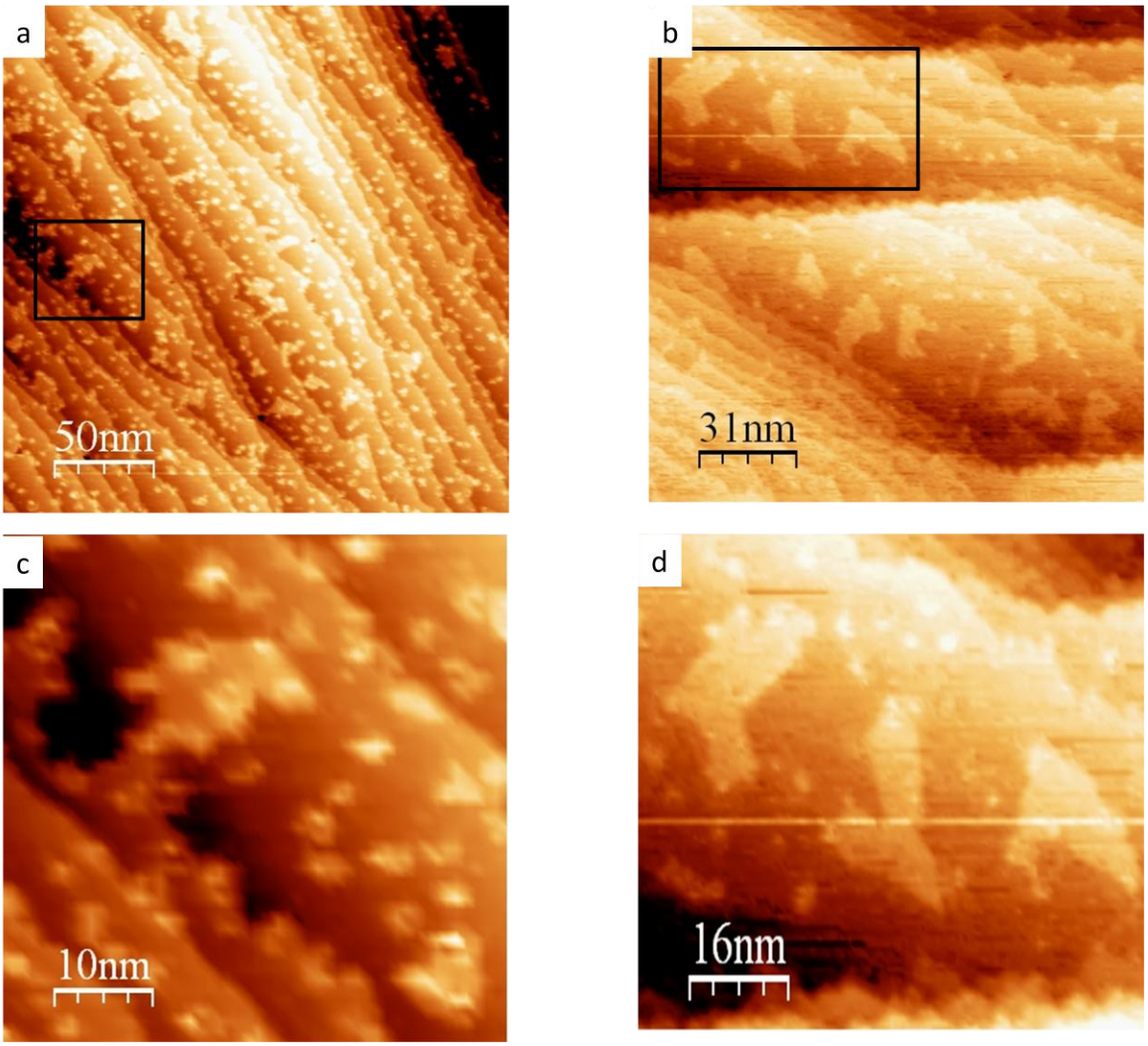

Figure 6.46: (a, and b) STM images shown the small islands are sitting at top of CuCl layer. (c, and d) are the magnified images of images a, and b respectively.

6.4 Conclusion

Room temperature interaction of HCl gas with clean and preoxidised Cu(111) at 25, 380, and 450 ^{o}C, have been studied in UHV system using STM and XPS techniques. XPS showed that interaction of HCl with clean Cu(111) surface at room temperature leads to a chlorine saturated surface by exposing the sample to about 180 L HCl. The saturated coverage was about $6.0x10^{14}$ cm^{-2}, which represents one third monolayer of copper in agreement with the observation of Motai et al. s' observations [20]. STM studied the interaction behaviour of HCl with clean Cu(111) surface and shows that, at low coverage the copper step edge lost its sharpness indicating the extraction of copper atoms from the step edges. At saturation coverage the atomic resolution of $(\sqrt{3}x\sqrt{3})R30^{o}$ of Cl structure is obtained at terraces. The poor resolution before saturation coverage is attributed to the movement and mobility of the chlorine atoms on the surface and from the surface toward the STM tip as well consistent with our previous observations of interaction of HCl with clean Cu(100) surface.

STM of interaction of oxygen with clean Cu(111) surface at room temperature showed that, the step edge is the preferred position of interaction of oxygen with copper leading to the formation of serrated step edges and oxide islands at terraces. The angular step edges refer to the extraction of copper atoms from the step edge while the oxide layer formed and extend over the lower terraces. The triangle oxygen islands indicated the atoms of oxygen were adsorbed on the threefold site consistent with previous results [1, 8]. XPS of interaction of clean Cu(111) with oxygen at room temperature showed the coverage about $8.1x10^{14}$ cm^{-2} by exposing the sample to about 1400 L which is more than saturated coverage (one third monolayer) indicates the formation of Cu_2O layer.

STM of HCl interaction with preoxidised Cu(111) surface of the step edge oxide layer and the triangle island showed that, the HCl prefers to interact and dissociated over the terraces rather than interact with the oxide island. After all the terraces were covered with chlorine the reaction of HCl with step edge adlayer area started by losing the angular step edge which is the distinct form of oxide layer at the step edge. The area of the oxide layer decreases indicating the attack of HCl was coming from the terraces until it disappeared. By comparing the behaviour of HCl with the oxide layer at the step edge and the oxide islands on the terraces we observe that, the oxide islands react faster than step edge oxide layer because the triangular oxide islands are open to the clean copper surface from three directions while the step edge oxide layer can only be attacked from the terrace. The atomic resolution of

chlorine atoms was achieved after the surface saturated with chlorine represented the ($\sqrt{3}x\sqrt{3}$)R30^{o} of Cl structure. XPS after exposure the sample to 200 L showed the surface was saturated by chlorine at ($6.1x10^{14}$ cm^{-2}).

Exposure of the clean Cu(111) sample to 600 L of oxygen at 380 ^{o}C leads to the formation of the ‘’44’’ oxygen structure, imaged as a series of striped lines covering the Cu(111) surface. STM atomic resolution image confirmed the ‘’44’’ oxygen structure from the unit cell dimension (2.2 nm, and 1.8 nm). Two different orientations of the ‘’44’’ oxygen structure were observed in same area depending on the step edge direction. A disordered oxide layer was observed in one area as well which may indicate some instability of the ‘’44’’ oxygen layer at room temperature. Leaving the ‘’44’’ oxygen structure overnight led to the formation of heptagonal rings surrounding the Cu_2O like layer confirmed by measuring the atomic distance. Matsumoto et al. suggested the ‘’44’’ oxygen structure formed as a result of distorted Cu_2O(111)-like structure. The instability of ‘’44’’ oxygen structure could be due to an equilibrium between the Cu_2O(111)-like structure and the ‘’44’’ oxygen structure.

By reacting the freshly formed ’’44’’ oxygen structure with HCl at room temperature, two reaction steps were observed. First, is slow step which represents a reaction of HCl with centred atomic oxygen of the honeycomb structure represented in STM as small dot adsorbed on the ‘’44’’ oxygen structure. Then the fast reaction substituted all the other oxygen atoms. Small Cu-Cl islands are trapped at the step edge over the Cl/Cu(111) surface which explain the excess of the chlorine concentration in XPS result. These result have an agreement with work of interaction of carbon monoxide with ‘’44’’ oxygen structure/Cu(111) at room temperature [12, 13].

The ‘’29’’ oxygen structure over the Cu(111) surface was formed by annealing the Cu(111) sample at 380 ^{o}C for 20 min while exposing to oxygen, then increase the temperature to 450 ^{o}C for 10 min while keep exposed to oxygen. The ‘’29’’ structure was confirmed by STM, which showed an atomic cell size of (1.7 nm, and 0.9 nm). XPS showed the excess of oxygen concentration which is explained as the result of formation of Cu_2O layer. The ‘’29’’ oxygen structure showed high stability compared with ‘’44’ oxygen, which could be because all the centred atomic oxygen in the honeycombed structure were adsorbed on the (fcc) site of the Cu(111) surface in contrast to the ‘’44’’ structure which has three centred oxygen atoms adsorbed at (fcc), and one at the bridge site.

The interaction of HCl with ‘’29’’ oxygen structure on the Cu(111) surface showed in STM similar behaviour to the interaction of HCl with the’’44’’ structure. Two reaction steps were found as well, slow and fast interaction. The slow interaction was due to the adsorbed HCl molecules on the centred atomic oxygen at honeycombed structure and the fast reaction done by substituting the other oxygen atoms. Small islands of Cu-Cl were found at the step edge, and by exposed to extra HCl , the small islands joined together to form the CuCl layer.

6.5 References

1. Matsumoto, T., et al., *Scanning tunneling microscopy studies of oxygen adsorption on Cu(111).* Surface Science, 2001. **471**(1–3): p. 225-245.
2. Dubois, L.H., *Oxygen chemisorption and cuprous oxide formation on Cu(111): A high resolution EELS study.* Surface Science, 1982. **119**(2–3): p. 399-410.
3. Niehus, H., *Surface reconstruction of Cu (111) upon oxygen adsorption.* Surface Science, 1983. **130**(1): p. 41-49.
4. Haase, J. and H.J. Kuhr, *Reconstruction and relaxation of the oxygen-covered Cu(111) surface: A sexafs study.* Surface Science, 1988. **203**(3): p. L695-L699.
5. Luo, B. and J. Urban, *Structure determination of oxygen adsorbates on Cu surfaces by means of the SEELFS technique.* Journal of Physics: Condensed Matter, 1991. **3**(17): p. 2873.
6. Xu, Y. and M. Mavrikakis, *Adsorption and dissociation of O2 on Cu(111): thermochemistry, reaction barrier and the effect of strain.* Surface Science, 2001. **494**(2): p. 131-144.
7. Toomes, R.L., et al., *Is PEXAFS really PhD* Surface Science, 2000. **445**(2–3): p. 300-308.
8. Wiame, F., V. Maurice, and P. Marcus, *Initial stages of oxidation of Cu(111).* Surface Science, 2007. **601**(5): p. 1193-1204.
9. Jensen, F., et al., *Oxidation of Cu(111): two new oxygen induced reconstructions.* Surface Science Letters, 1991. **259**(3): p. L774-L780.
10. Jensen, F., F. Besenbacher, and I. Stensgaard, *Two new oxygen induced reconstructions on Cu(111).* Surface Science, 1992. **269–270**(0): p. 400-404.
11. Besenbacher, F. and J.K. Norskov, *Oxygen chemisorption on metal surfaces: General trends for Cu, Ni and Ag.* Progress in Surface Science, 1993. **44**(1): p. 5-66.
12. Yang, F., et al., *Autocatalytic Reduction of a Cu2O/Cu(111) Surface by CO: STM, XPS, and DFT Studies.* The Journal of Physical Chemistry C, 2010. **114**(40): p. 17042-17050.
13. Yang, F., et al., *CO Oxidation on Inverse CeO_x/Cu(111) Catalysts: High Catalytic Activity and Ceria-Promoted Dissociation of O2.* Journal of the American Chemical Society, 2011. **133**(10): p. 3444-3451.
14. Goddard, P.J. and R.M. Lambert, *Adsorption-desorption properties and surface structural chemistry of chlorine on Cu(111) and Ag(111).* Surface Science, 1977. **67**(1): p. 180-194.

15. Crapper, M.D., et al., *Complete Adsorption Site Information for Cl on Cu(111) Using X-Ray Absorption Fine Structure and Photoelectron Diffraction.* EPL (Europhysics Letters), 1986. **2**(11): p. 857.
16. Crapper, M.D., et al., *Investigation of the Cu(111) (√3 × √3)R30°-Cl structure using sexafs and photoelectron diffraction.* Surface Science, 1987. **182**(1–2): p. 213-230.
17. Woodruff, D.P., et al., *A simple X-ray standing wave technique for surface structure determination - theory and an application.* Surface Science, 1988. **195**(1–2): p. 237-254.
18. Lüdecke, J., et al., *Structural study of Rb and Cl coadsorption on Cu(111): a case of overlayer compound formation.* Journal of Physics: Condensed Matter, 1997. **9**(22): p. 4593.
19. Doll, K. and N.M. Harrison, *Chlorine adsorption on the Cu(111) surface.* Chemical Physics Letters, 2000. **317**(3–5): p. 282-289.
20. Motai, K., et al., *STM of the Cu(111)1 × 1 surface and its exposure to chlorine and sulfur.* Applied Surface Science, 1993. **67**(1–4): p. 246-251.
21. Kruft, M., et al., *Chloride adsorption on Cu(111) electrodes in dilute HCl solutions.* Surface Science, 1997. **377–379**(0): p. 601-604.
22. Broekmann, P., et al., *In-situ STM investigation of specific anion adsorption on Cu(111).* Journal of Electroanalytical Chemistry, 1999. **467**(1–2): p. 307-324.
23. Moroney, L., S. Rassias, and M.W. Roberts, *Chemisorption of HCl and H2S by Cu(111)-O surfaces.* Surface Science, 1981. **105**(1): p. L249-L254.
24. Nakakura, C.Y., G. Zheng, and E.I. Altman, *Atomic-scale mechanisms of the halogenation of Cu(100).* Surface Science, 1998. **401**(2): p. 173-184.
25. Eltsov, K.N., et al., *Surface atomic structure upon Cu(100) chlorination observed by scanning tunneling microscopy* JETP lett., 1995. **62**(5): p. 444.
26. Walter, W.K., D.E. Manolopoulos, and R.G. Jones, *Chlorine adsorption and diffusion on Cu(111).* Surface Science, 1996. **348**(1–2): p. 115-132.
27. Carley, A.F., et al., *A low energy pathway to CuCl2 at Cu(110) surfaces.* Physical Chemistry Chemical Physics, 2009. **11**(46): p. 10899-10907.

Chapter 7 Interaction of HCl with Au/Cu(100) surface

Contents

7.1 Introduction

Alloying and intermixing of metals surfaces especially copper with transition metals plays an important role in many chemical reactions and understanding the new chemical and physical properties of the alloy surface is important as reported in chapter one. The interaction of gold with Cu(100) surface has received a great deal of interest in previous studies. At half a monolayer of gold deposited on clean Cu(100) surface at room temperature, low energy electron diffraction (LEED) showed an ordered structure is formed with a c(2x2) reconstruction referred to as a Cu_3Au alloy [1]. LEED of clean Cu(100) surface covered with two monolayers of gold deposited at room temperature (confirmed by Auger electron spectroscopy (AES)) shows a reconstruction attributed to a hexagonal gold layer on the c(2x2) structure [2]. A c(2x2) structure was also created by heating the sample with two monolayer of gold to 573 K, the excess gold diffusing into the copper [2]. The deposition of half monolayer of gold on top of clean Cu(100) at 233 K leads to formation of a close packed hexagonal layer of gold with out alloying with copper surface. A complete alloying c(2x2) surface was formed by warming this surface to room temperature with the first c(2x2) structure appearing in LEED at 248 K [1]. A hexagonal gold structure was formed as result of dealloying processes by increase the gold coverage from 0.6 to 1.2 ML have been observed by using LEED and Photoelectron diffraction (PhD) with a measurable gold concentration was detected in the second and third layer of copper as well [3]. Similar result have been seen by Shen et al. for depositing 1.2 ML of gold top of Cu(100) at room temperature which showed the top surface layer was totally covered with unmixed gold while finding no evidence for gold in the second or third layers of copper [4]. The ordered alloy surface of the deposition of half monolayer of gold, showed the gold atoms were extended outward from the surface by 0.1 Å forming a bend in the surface. The distance between the gold nearest atoms in pure gold was 2.88 Å while it was increase by 30% in case of c(2x2) surface alloy to be 3.75 Å, as well as the 4% increase found in the distances between the c(2x2) surface alloy to second layer of copper by compared with the clean Cu(100) surface [5]. STM study of the c(2x2) alloy of gold on top of Cu(100) have been studied by Chambliss et al. in 1992 [6], who showed that, at room temperature the ordered c(2x2) alloy reconstruction shows two peaks in the line profile with a difference in height of about 0.2 Å due to the difference in height between gold and copper atoms in the alloy surface. Most STM images of the Au/Cu(100) alloy surface show linear features with one atomic row wide with height about 0.5 Å, and distance between these features was about 21 ∓ 2 Å [7]. Islands of gold and copper atoms have been seen [6, 7] which have been suggested to be formed by alloying the

deposited gold atoms with the released copper atoms at the time of formation of the gold – copper alloy.

Growth of metal on the reconstructed Cu(100)-oxygen surface has been extensively studied by depositing metal on the Cu(100) covered with c(2x2)-O, or $(\sqrt{2}x2\sqrt{2})R45^{o}$ structure, individually or both together. Cu(100) covered with oxygen improves the 2D growth layer by layer of the depositing metal. For example, iron deposited on the Cu-O $(\sqrt{2}x2\sqrt{2})R45^{o}$ [8] gives 2D islands whereas depositing Fe on clean Cu(100) surface [9-13] shows the growth of 3D islands. That oxygen is working as a surfactant was proven by reflection high energy electron diffraction (RHEED) which showed the $(\sqrt{2}x2\sqrt{2})R45^{o}$ structure on Cu(100) floating above the Fe layer, even up to 45 monolayer [8]. Depositing copper on Cu(100) precovered with c(2x2)-O leads to the formation of rectangle islands which are of atomic height as shown in Figure 7.1(a) [14, 15], while, simultaneously the c(2x2)-O on Cu(100) surface moves to the top of the rectangular island and forms the $(\sqrt{2}x2\sqrt{2})R45^{o}$ structure as shown in Figure 7.1(b).

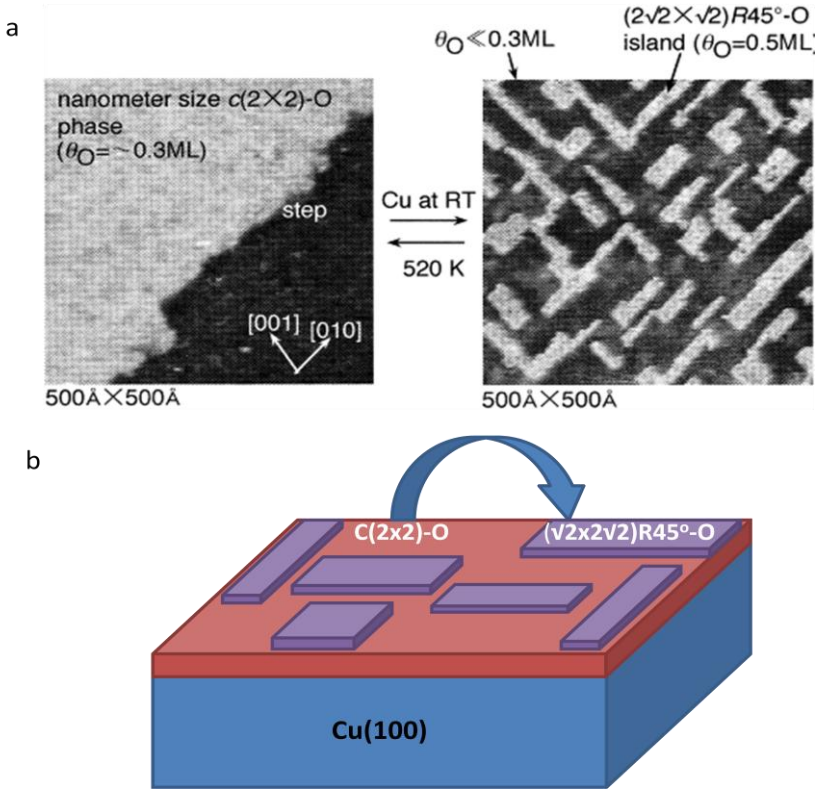

Figure 7.1: (a) STM image of $(\sqrt{2}x2\sqrt{2})R45^{o}$-O islands form on Cu(100)-c(2x2)-O after depositing Cu atoms at room temperature [14, 15]. (b) Schematic diagram illustrating the formation of $(\sqrt{2}x2\sqrt{2})R45^{o}$-O islands.

In contrast, depositing Ni on Cu(100) precovered with c(2x2)-O leads to the formation of atomic height islands with random structure as shown in Figure 7.2(a). The c(2x2)-O on surface moves to the top of the Ni islands to form this time c(2x2)-O structure Figure 7.2(b), confirmed by LEED [14, 15]. Depositing Ni on Cu(100) precovered with (√2x2√2)R45°-O leads to the formation of anisotropic Ni islands covered with c(2x2)-O. In this case the Ni atoms were found to adsorbs at the missing Cu row sites of the (√2x2√2)R45°-O reconstruction.

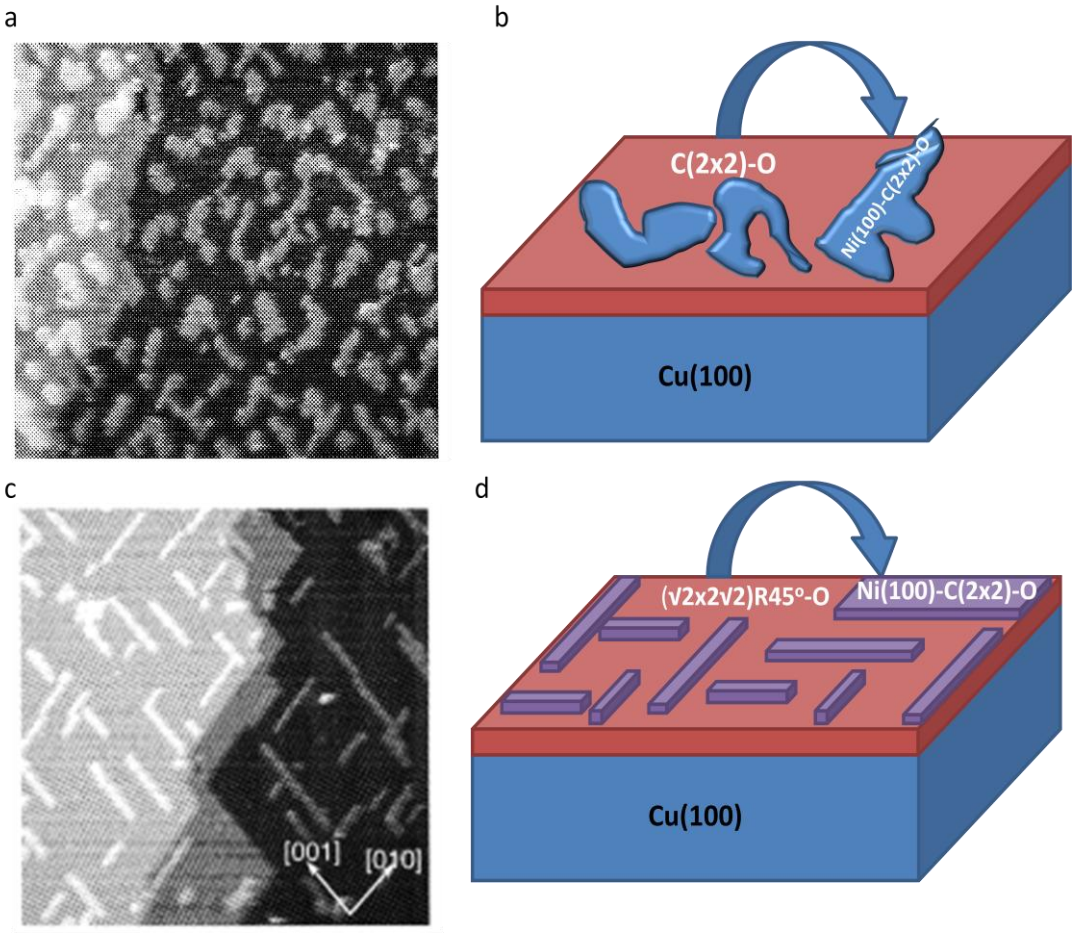

Figure 7.2: (a, and c) are the STM image of depositing Cu atoms to of C(100) precovered with c(2x2)-O reconstruction and (√2x2√2)R45°-O reconstruction respectively [14, 15]. (b, and d) schematic diagram illustrating the formation of Ni island in both state of precovered Cu(100) by oxygen.

Depositing 0.05 ML of Co on the Cu(100) precovered with the (√2x2√2)R45°-O reconstruction leads to the formation of two features on the surface, first one was an elongated island orientated in (100), and (010) directions, while the second feature was small dots scattered on the surface as shown in Figure 7.3(a) [16]. The elongated island was covered by (√2x2√2)R45°-O reconstruction as shown in Figure 7.3(b), which is characteristic of the reconstruction of oxygen on Cu(100) at high coverage, so the elongated island suggested to be copper while the scattered dots are due to the Co atoms confirmed by the immobility of dots with time. Since the formation of copper island requires the mobile of copper atoms to move on the surface and collect together, and then forming the island, the replacement of copper atoms by Co atoms was suggested [16].

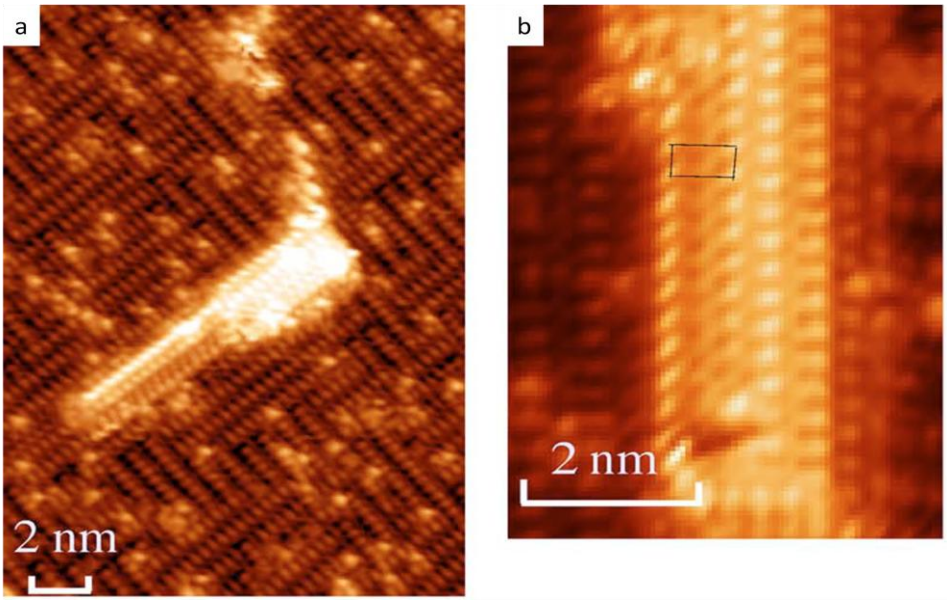

Figure 7.3: (a) STM image of depositing 0.05 ML of Co on the Cu(100) precovered with (√2x2√2)R45°-O reconstruction. (b) STM mage showed the (√2x2√2)R45°-O reconstruction on the elongated island [16].

Depositing Co, and Ni on the Cu(100)-c(2x2)-N surface show a different behaviour from depositing them on the Cu(100) precovered with oxygen [15, 17-20]. N leads to the formation of a square shaped structure on top of Cu(100) surface at room temperature as shown in Figure 7.4, the square lattice of the c(2x2)-N is resolved within the square structure [21]. Deposition of Ni on the Cu(100) precovered with c(2x2)-N leads selectively to the formation of Ni island at the crossing of the squarer structure of c(2x2) as shown in Figure 7.5(a) with the island size limited to the available area of the crossing area [15]. Similar behaviour was observed for the deposition of Co [18], and Fe [20].

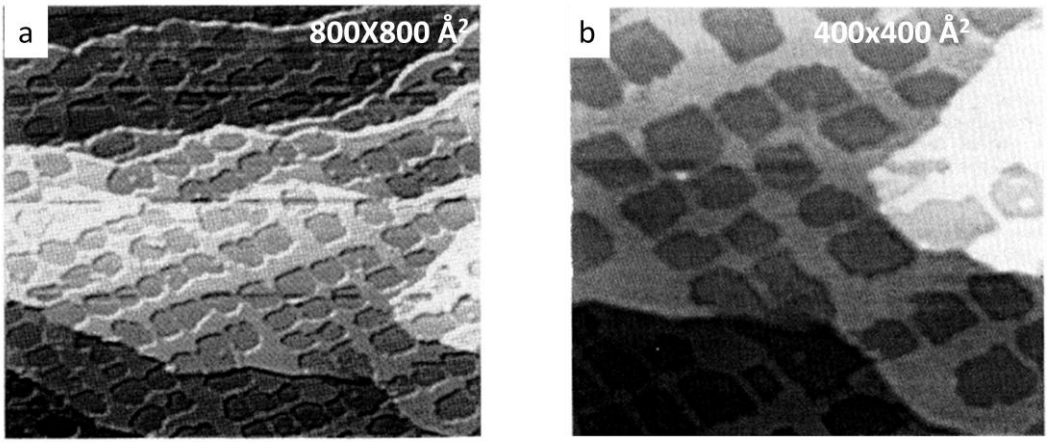

Figure 7.4: (a) STM image of Cu(100) covered with c(2x2)-N, (b) the magnified image [21].

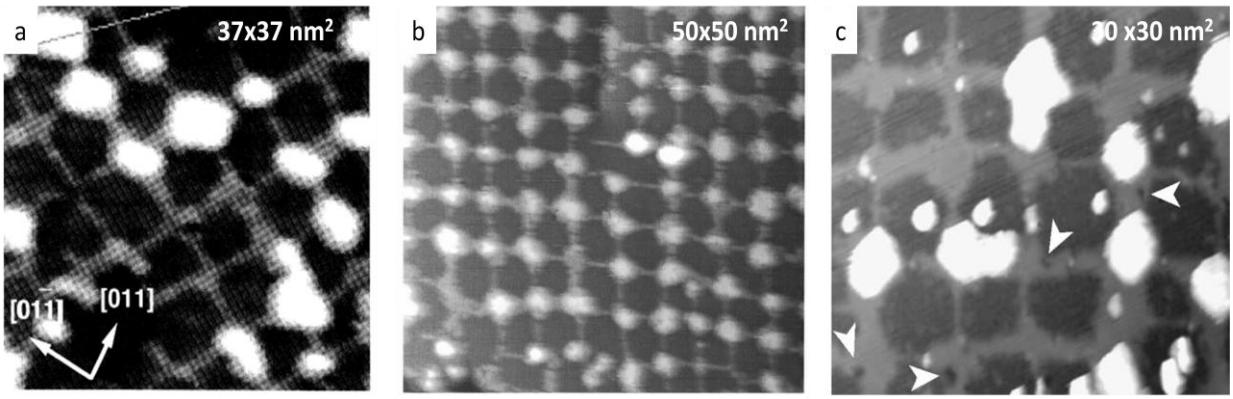

Figure 7.5: STM image of the deposition of (a) Ni [15], (b) Co [18], and (c) Fe [20], n the Cu(100) covered with c(2x2)-N at room temperature.

We can conclude from the above studies, that the deposition of metal on clean Cu(100) is different from those depositing when the Cu(100) was covered by oxygen or nitrogen. In case of Cu(100) surface covered with oxygen two different behaviour of growth of the metal have been found as well depending on the amount of oxygen coverage. So in this chapter we aim to shed light on the behaviour of depositing gold on clean Cu(100) and the oxygen pre-covered surface with oxygen. Then we have studied the interaction of HCl with Au/Cu(100), and Au/Cu(100)/oxygen surface

7.2 Experimental

The instrument used in these experiments is (UHV), was described in chapter 4, and sample cleaning procedures as well. Oxygen and HCl gases were purchased from Argo international and, the purity was checked by using mass spectroscopy. Gold evaporation by using tungsten filament is described in chapter 4. In all the gold/Cu(100) experiments in this chapter, the XP spectra of the Au ($4f_{7/2}$) peak are used to calculate the gold coverage, and all spectra are calibrated to $Cu2p_{3/2}$.

7.3 Results and discussion

7.3.1 Interaction of clean Cu(100) with gold low coverage to half monolayer)

Evaporated gold on the clean Cu(100) sample leads to the formation of Au/Cu(100) alloy. XP spectra in Figure 7.6(a) showed the $Au4f_{5/2,7/2}$ peak, the coverage was about $4.3x10^{14}$ cm^{-2} , while no change was observed in the $Cu2p_{3/2}$ Figure 7.6(b). This is consistent with the suggestion of the formation of a Cu_3Au alloy which has been suggested previously [1-7]. The small shift in the $Au4f_{5/2,7/2}$ and Cu3p peaks on gold adsorption may indicate a small change in the electron density of the copper.

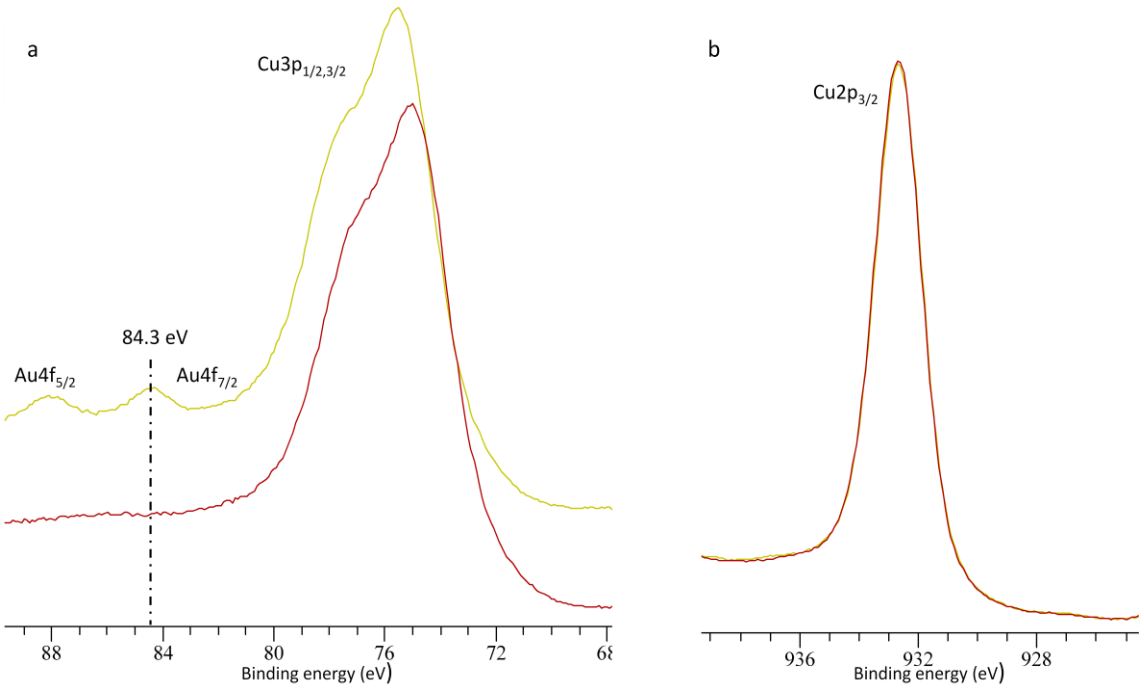

Figure 7.6: XP spectra of (a) $Au4f_{5/2,7/2}$,and (b) $Cu2p_{3/2}$ before and after evaporating gold on clean Cu(100) surface at room temperature. The gold coverage is about $4.3x10^{14}$ cm^{-2}.

STM images of the Cu(100) surface after gold deposition showed small features most of them are sticking in the step edge and some at the terraces as shown in Figure 7.7(a, and b). The height of the features on the terraces is about one atomic layer height of copper, while the features at the step edge have the same height as the step edge. In the following example the height of the features is 3.2 Å (about 2 atomic layer of copper) which is the same as the step edge shown in Figure 7.7(c). These features are assigned to the copper atoms which have been released at the time of the Au atoms landed on the surface to form the Au/Cu alloy. We suppose the released copper atoms moved on top of the alloy surface until they aggregated together forming clusters at the terraces and step edges. No similar features have been shown in the previous work [6, 7] of Au/Cu alloy at coverage about half of monolayer of gold. It could be because the adsorbed gold atoms prefer to adsorb in the terraces rather than making island with released copper atoms.

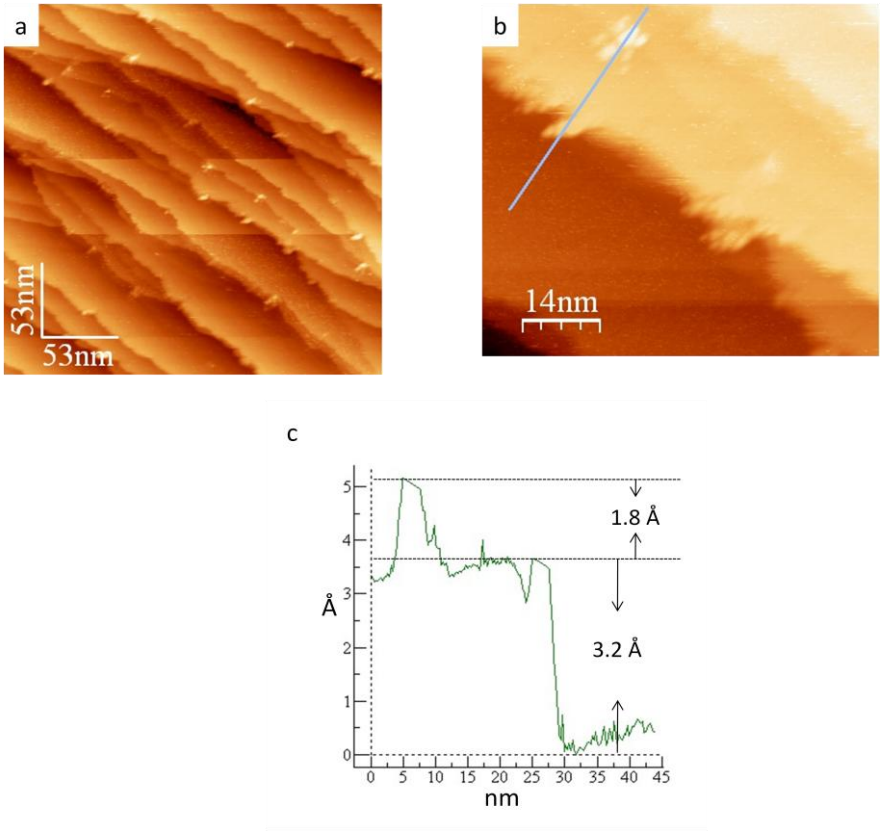

Figure7.7: STM images of the Cu(100) after depositing gold at coverage about 4.3×10^{14} cm^{-2} shown small features at step edges, and terraces in image (a, and b). (c) Line profile shown the height of two features in image (b). Tunnelling conditions: 1V, and 1nA.

Increase the gold coverage to about $5.9x10^{14}$ cm^{-2} by (less than half monolayer of Cu(100) surface which is $1.5x10^{15}$ cm^{-2}) evaporating more gold into the above Au/Cu(100) surface showed in XP spectra in Figure 7.8(a), and with out change in the height of the Cu($2p_{3/2}$) peak Figure 7.8(b) as well indicating the number of released copper atoms is equal to the adsorbed gold atoms. STM of this gold coverage shows the steps edges are decorated by copper atoms as shown in Figure 7.9. The increase of the copper clusters at the step edges of the Au/Cu(100) alloy surface backs the suggestion of the release of copper atoms on the adsorption of Au atoms on the surface. We believe these clusters are copper because a Au-Cu alloy should add to the step edge without making these clusters but the Cu atoms cannot go back into the surface they are remain on the surface until they are trapped at the step edges of the Cu-Au alloy. The height between two steps edge decorated by released copper atoms is 1.8 Å, which is the same in the clean Cu(100) surface.

A half monolayer of Au/Cu(100) alloy was formed by increasing the gold coverage to $7.8x10^{14}$ cm^{-2} (shown in XP spectra in Figure 7.8(a)). No change was observed in Cu$2p_{3/2}$ consistent with the previous results of gold coverage less than a mono layer (Figure 7.8(b).) STM images of the Au/Cu(100) alloy with half monolayer of gold showed step edges of Au/Cu(100) alloy and small islands scattered on top of the terraces as shown in Figure 7.9(d). On the other hand no clusters are observed at the step edges indicating of the formation of Au/Cu alloy island after saturation of the copper surface.

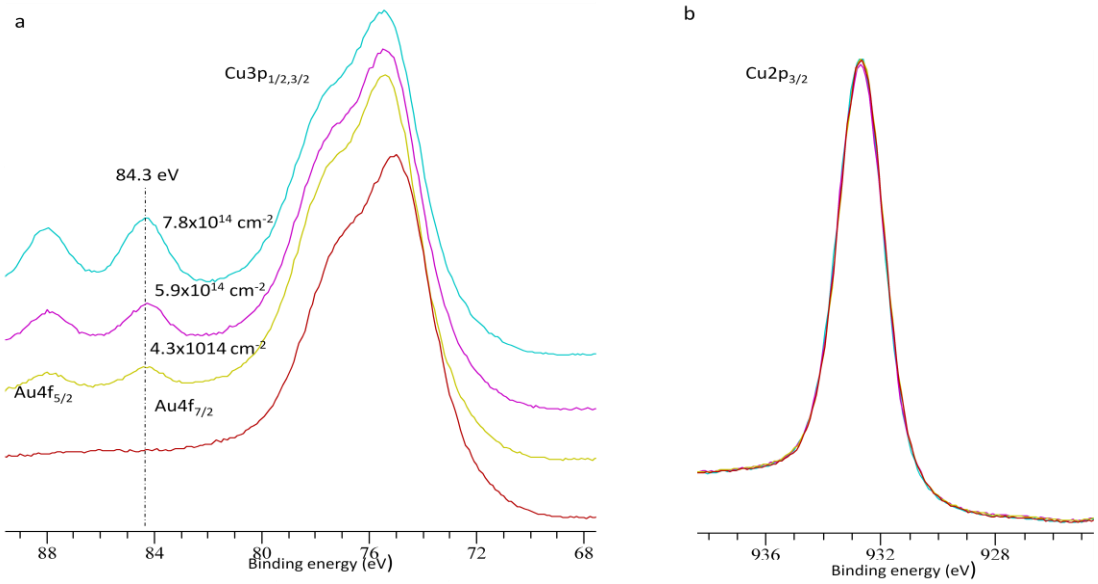

Figure 7.8: XP spectra of (a) Au$4f_{5/2,7/2}$,and (b) Cu$2p_{3/2}$ before and after evaporating gold on clean Cu(100) surface at room temperate.

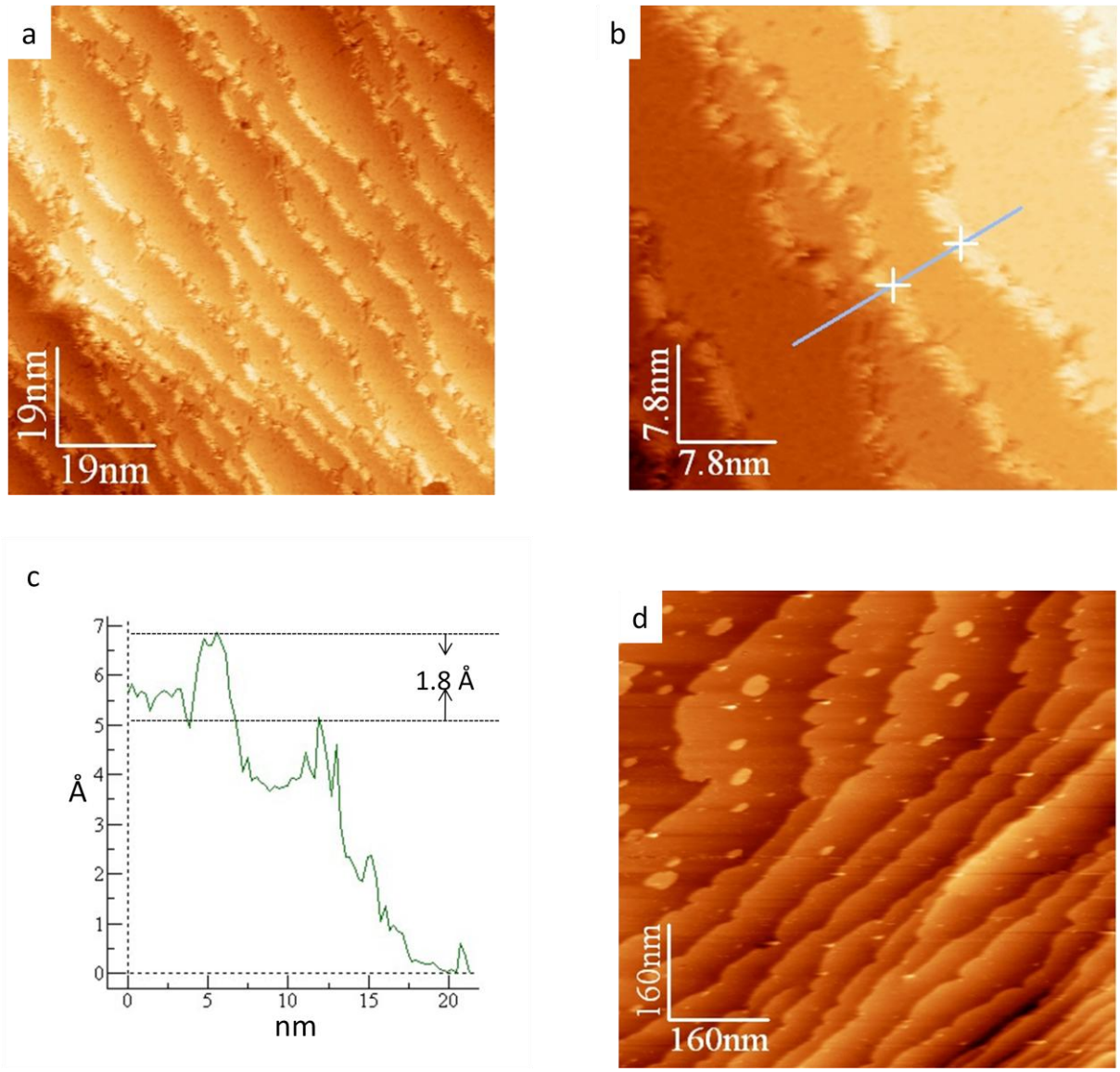

Figure7.9: STM images of the Cu(100) after depositing gold at coverage about $5.9x10^{14}$ cm^{-2} showing step edges decorated by released copper atoms (a, and b). (c) Line profile showing the height between two steps edge decorated by copper atoms in image (b). (d) STM image of Au/ Cu(100) alloy at half monolayer coverage. Tunnelling conditions: 1V, and 1nA.

7.3.2 Interaction of clean Cu(100) with gold at a coverage more than half monolayer

In this experiment gold evaporated onto the clean Cu(100) at room temperature leads to the formation of two monolayers of gold with $1.72x10^{15}$ cm^{-2} coverage shown by XPS, Figure 7.10(a). The Cu($2p_{3/2}$) peak in Figure 7.10(b) showed a decrease in copper (about 15% from the clean surface) indicating that, the copper signal is attenuated by formation of overlayer of gold in contrast to the above situation of formation of Au/Cu(100) alloy at half monolayer or less. Increase of gold coverage from more than half monolayer to one monolayer [3] or to

two monolayer [1, 2] have been shown that, the overlayer of gold has a close packed hexagonal structure (pure gold). This gold layer formed is by the adsorbed gold or from the evaporated and dealloyed gold atoms from the Cu_3Au lattice. A shift toward higher binding energy is observed in $Cu3p_{1/2,3/2}$, and $Au4f_{5/2,7/2}$ in agreement with previous work [22]. STM of this experiment showed a lot of islands scattered on the terraces with wide range of different sizes. The height of these islands and step edges are 1.9 Å which is higher than the clean Cu(100) step edge by about 0.1 Å as shown in Figure 7.11. Chambliss et al., using STM [6, 7], have been found islands on the terraces of the Au/Cu(100) alloy at half monolayer coverage with heights of 1.8 Å, which they suggested to have the same composition as the Au/Cu(100) alloy. In our case, we are unable to identify the composition of these islands and so in the following sections we try to deduce the composition of the islands from their of interaction with HCl.

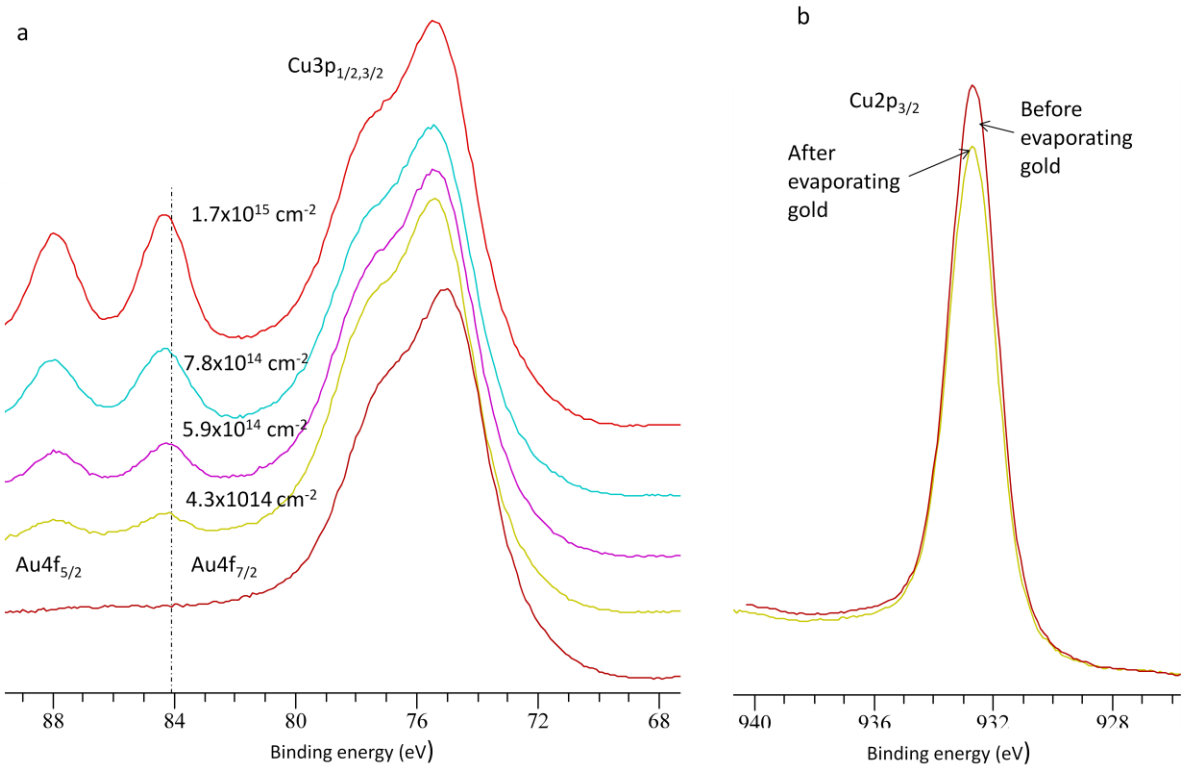

Figure 7.10: XP spectra of (a) $Au4f_{5/2,7/2}$,and (b) $Cu2p_{3/2}$ before and after evaporating gold on clean Cu(100) surface at room temperate.

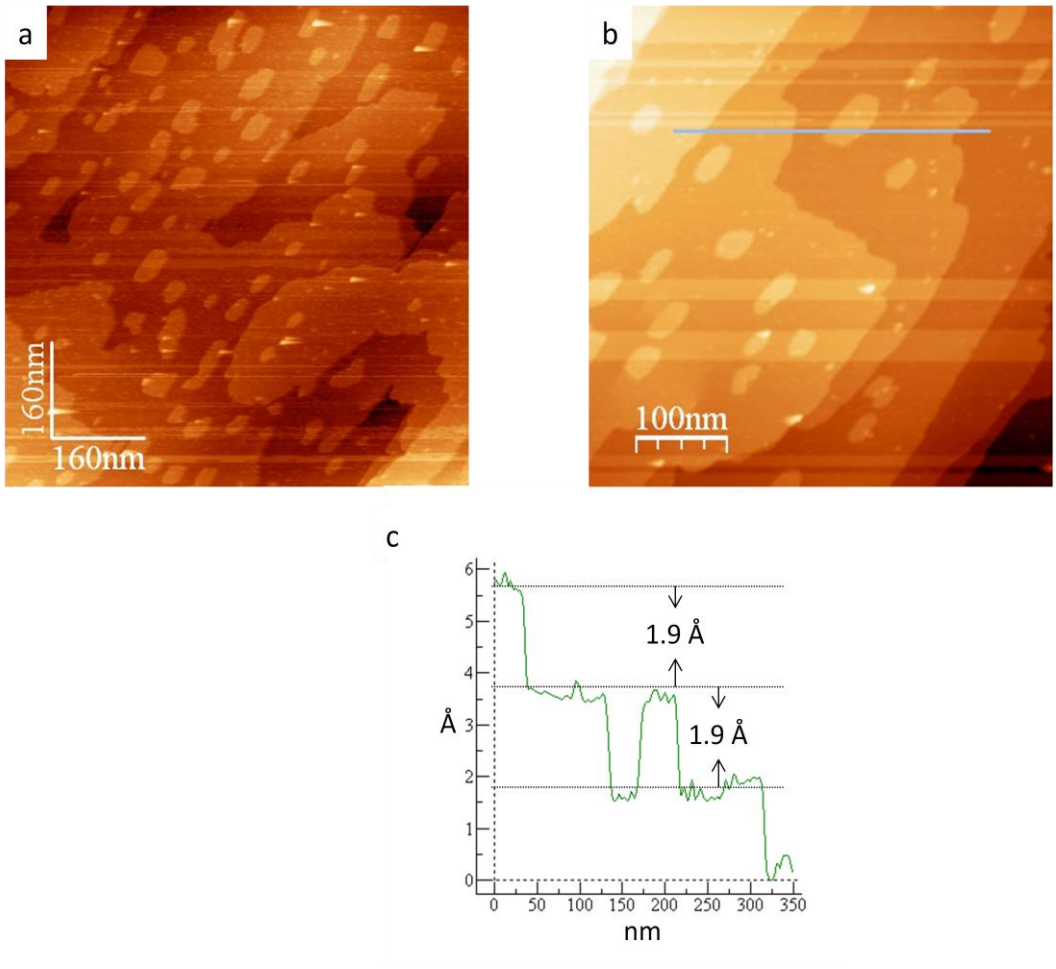

Figure 7.11: STM images of the Cu(100) after depositing gold at coverage about $1.7x10^{15}$ cm^{-2} the terraces are covered with a lot of island (a, and b). (c) Line profile shown the height between to steps edge and island in image (b). Tunnelling conditions: 1V, and 1nA.

7.3.3 Interaction of HCl with Au/Cu(100) alloy at half monolayer coverage of gold

Half monolayer of Au/Cu(100) alloy was formed by evaporating gold onto the clean Cu(100) sample at room temperature. The gold coverage calculated using XPS which showed the gold coverage is $7.8x10^{14}$ cm^{-2}, then the sample was moved to the STM chamber. STM images in Figure 7.12 show the Au/Cu(100) surface have a lot of islands which not different from those acquired before in case of depositing two monolayer of gold. Height of islands is 1.9 Å, consistent with previous results of depositing two monolayer of gold. A sequence of STM images recorded during the exposure of the Au/Cu(100) sample to 200 L is of HCl shown in Figure 7.13. Before exposure of the sample to HCl, three islands are present in Figure 7.13(a). After exposure of the sample to about 50 L of HCl, the island size started to decrease, and continued to do so for exposures up to 150 L of HCl as shown in Figure 7.13(b,

and c). The exposure to HCl was stopped at 200 L when no further change was observed in the islands size as shown in Figure 7.13(d). After leaving the sample to equilibrate, STM images of the terraces are shown in Figure 7.14. A lot of small adjacent islands, nearly forming one layer were found. The islands have a quite regular shape with spaces between the islands about 5.2 Å. STM atomic resolution of these islands was reached as shown in Figure 7.15, with clear c(2x2) structure while a unit cell dimension of 5.2 Å. XPS of these experiment showed a decrease in gold coverage to $5.2x10^{14}$ cm^{-2}. A shift toward higher binding energy is also observed in $Au4f_{5/2,7/2}$ peak from 84.3 eV before exposure to HCl to 85.3 eV after exposed to HCl, with clear broadening in the $Au4f_{5/2,7/2}$ peak as shown in Figure 7.15(a). The chlorine coverage after exposure to HCl was $7.4x10^{14}$ cm^{-2} with shift in the Cl(2p) of about 1 eV higher than from that observed on the clean Cu(100) sample, (chapter five) as shown in Figure 7.15(b). These islands are suggested to be nanometre size domains of c(2x2)-Cl top of the Au/Cu(100) alloy. The unit cell dimension are consistent with our previous result of exposing the clean Cu(100) to HCl which lead to formed c(2x2)-Cl over layer with half monolayer coverage at room temperature (half monolayer is $7.2x10^{14}$ cm^{-2}). The shift of $Au4f_{5/2,7/2}$ could be due to the interaction of extra gold atoms which reacted after exposure to HCl to form Au(I), or due to change in the charge of the Au/Cu(100) alloy.

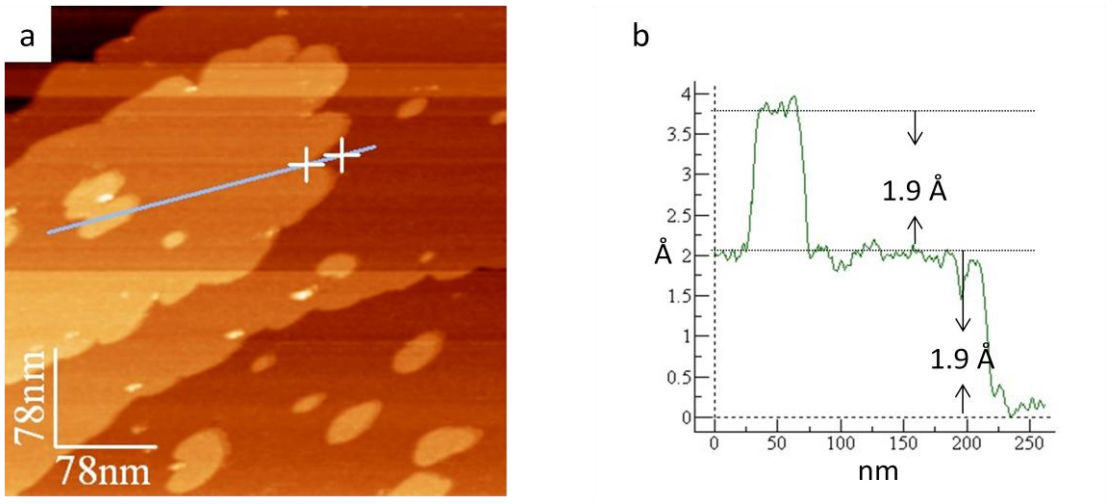

Figure 7.12: STM images of the Cu(100) after depositing gold at coverage about $7.8x10^{14}$ cm^{-2} the terraces were covered with a lot of island (a). (c) Line profile shown the height different between to steps edge and island in image (a). Tunnelling conditions: 1V, and 1nA.

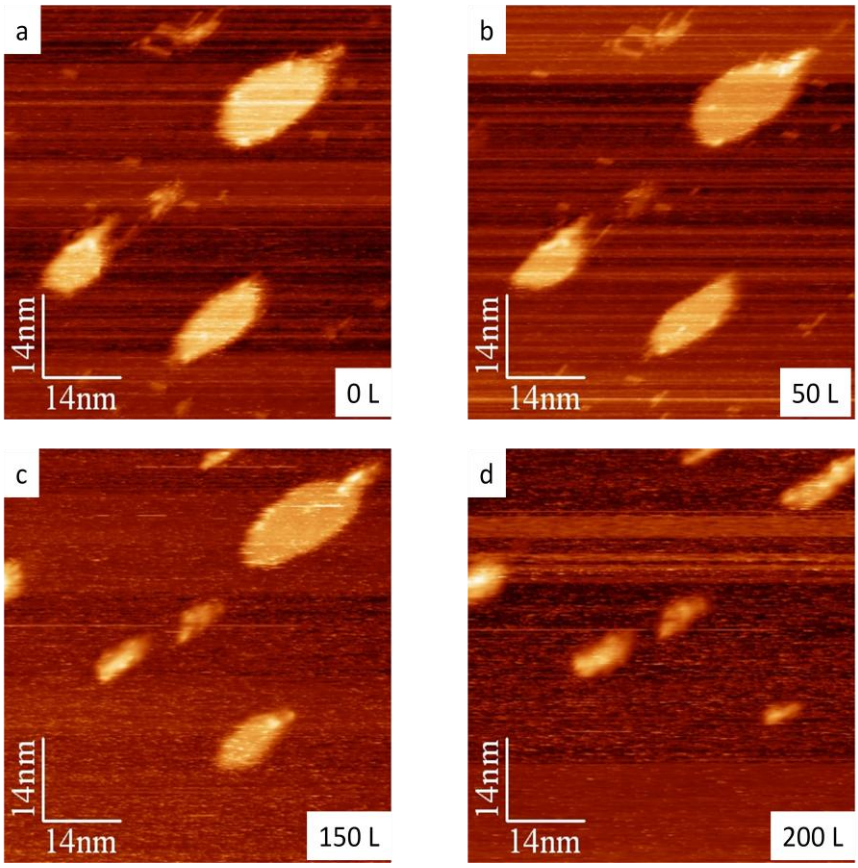

Figure 6.13: STM images of the Au/Cu(100) sample during exposure it to 200 L of HCl at room temperature. Tunnelling conditions: 1V, and 1nA.

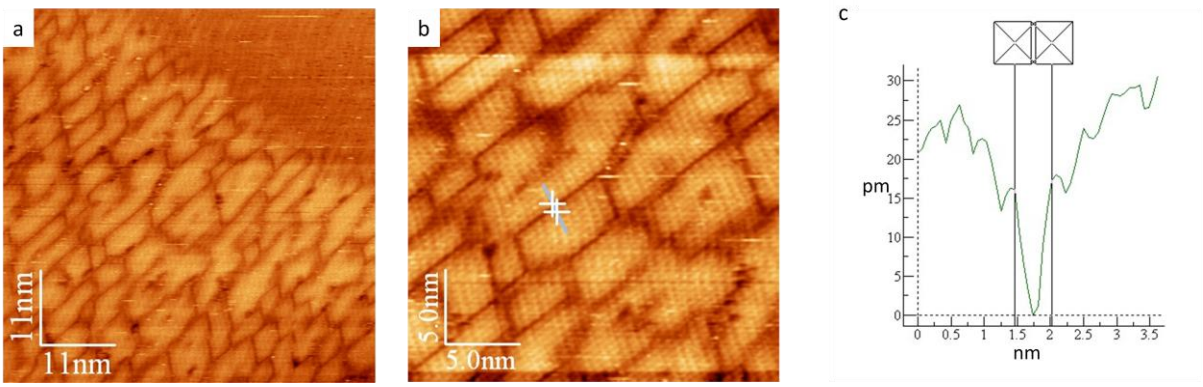

Figure 7.14: STM images of the Au/Cu(100) at half monolayer of gold coverage after exposure of the sample to 200 L of HCl at room temperature. (a, and b) shown a small nanometre size domain of c(2x2)-Cl. Tunnelling conditions: 1V, and 1nA.

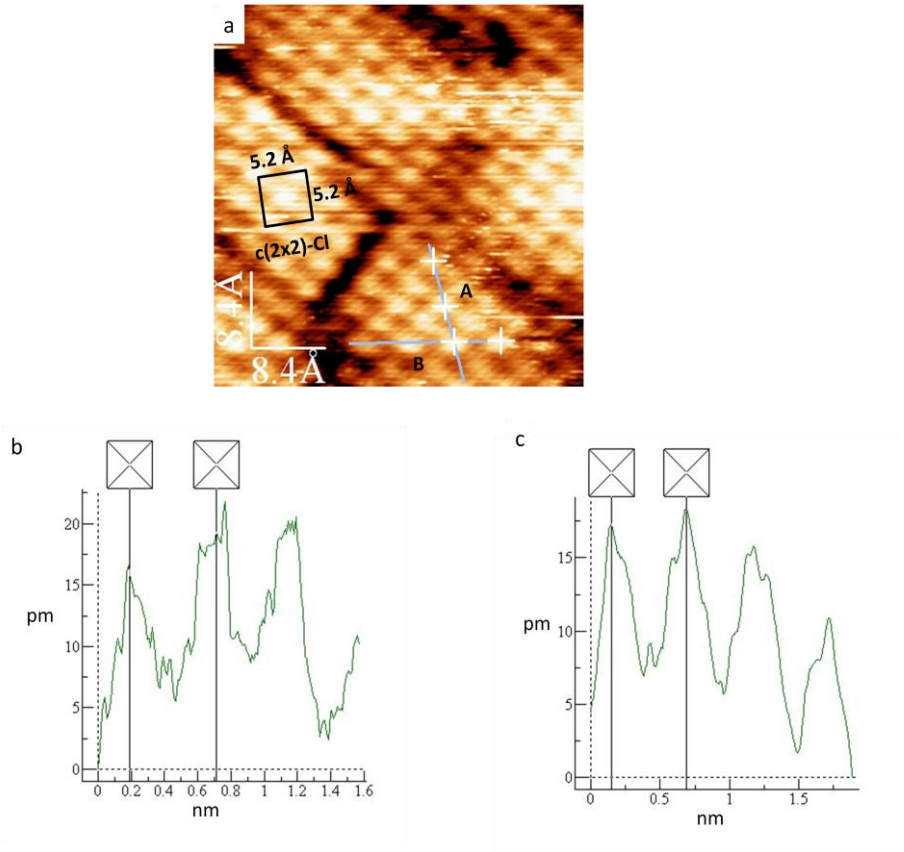

Figure 7.15: (a) STM image showed the atomic resolution of c(2x2)-Cl nano size domain, (b, and c) line profiles of line A, and B in image (a) respectively.

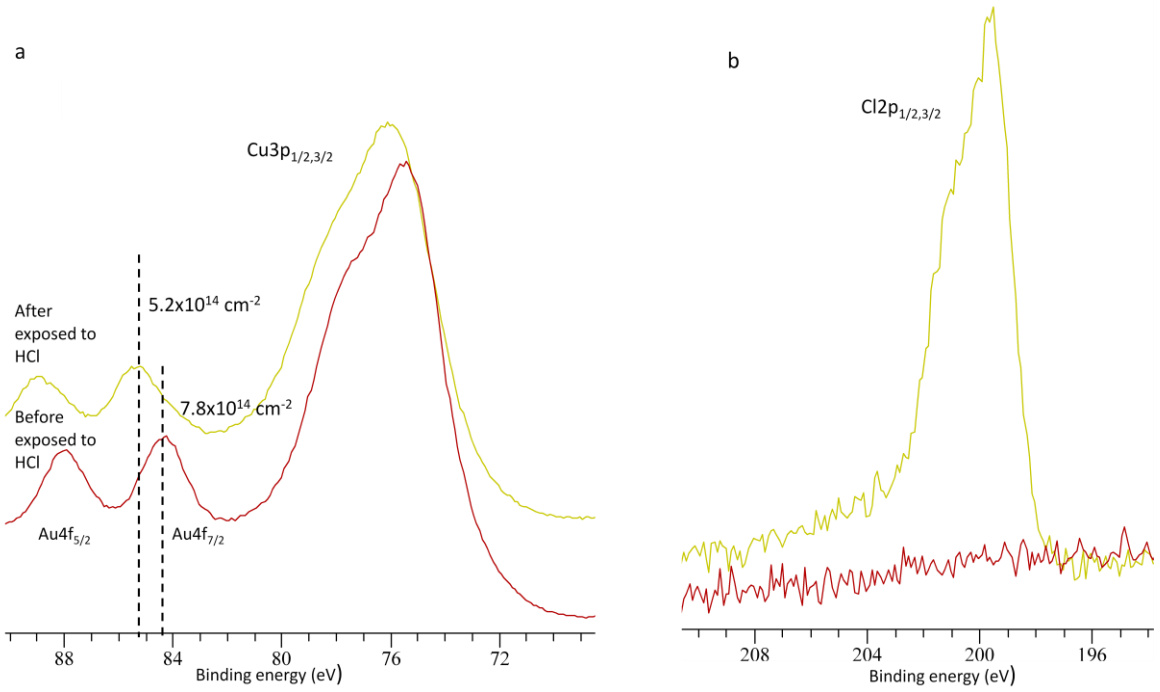

Figure 7.16: XP spectra of Au/Cu(100) alloy, (a) $Au4f_{5/2,7/2}$ before and after exposed to 200 L of HCl, (b) $Cl2p_{1/2,3/2}$ after exposed to HCl.

7.3.4 Interaction of HCl with Au/Cu(100) alloy at more than half monolayer coverage of gold

In this experiment Au/Cu(100) alloy with coverage of gold of $1.7x10^{15}$ cm^{-2} was exposed to 250 L of HCl at room temperature. The STM image sequence recorded during exposure of the sample to HCl is shown in Figure 7.17. Three islands and step edges have been found before exposure to HCl but no atomic structure could be observed in the surrounding area of the islands as shown in Figure 7.17(a). After exposing the sample to 30 L to 60 L of HCl, change was observed as a decrease in the island size and line features appearing as ridges or ditches in the area surrounding the islands as shown in Figure 7.17(b, and c). A current image of the line feature is shown in Figure 7.18 which shows them more clearly. The distance between these lines is about 5.8 nm, with height about 0.7±0.2 Å. These lines have been observed in the previous work of Chambliss et al.[6, 7] which they suggested was the result of the mismatch between the Au/Cu alloy layer and the underneath Cu(100) layer. In our case we suggest these lines appeared due to the exposure of the sample to HCl which assists the dealloying of the Au atoms from the surface, they areimaged very clearly at the start of the exposure to HCl but disappear with increasing exposure from 90 to 150 L as shown in Figure 7.17. The islands in the middle and step edge have features, new parts growing which are circled in Figure 7.17(e, and f). Compare it with the same area in Figure 7.17(d), these are due to the aggregation of the dealloying Au atoms from the Au/Cu alloy. Increase the exposure to HCl from 180 to 230 L leads to a decrease in the islands size by migrating the gold atoms from the island to step edge as shown in Figure 7.17(g, i, and h). The migration of Au atoms from the small feature to bigger one is due to the mobility of gold atoms on top of the Cl/Cu(100) layer after formation of c(2x2)-Cl structure. A large scan image of the Au/Cu alloy surface before and after exposure to HCl shown in Figure 7.19, the highlighted area is assigned to the same area in the two images. This image shows the aggregation of Au atoms to made a bigger pure gold island after the release of the Cu atoms from the Au/Cu island. The released copper atoms escaped back toward the step edge leading to an increase in the size of the terraces and then c(2x2)-Cl formed over it, this behaviour showed very clearly in Figure 7.19 by comparing the terrace size before and after exposed the sample to HCl. XPS result after exposed the sample to HCl in Figure 7.20 shows a small decreases in the gold coverage to be $1.2x10^{15}$ cm^{-2}, while the chlorine coverage was $1.2\ x10^{15}$ cm^{-2}. This excess of chlorine concentration could be due to the formation of CuCl underneath the gold layer. Previous work has suggested the layer of gold on top of Cu(100) hasthe hexagonal structure of Au(111) [1-3]. It is also known that the interaction of chlorine with Au(111) leads to the

formation of a $(\sqrt{3}x\sqrt{3})R30^{o}$ over layer of chlorine at a coverage of 0.33 ML [23]. However, here the STM atomic resolution images of the top most layer showed the unit cell of Au(111) layer with a 2.8 Å dimension after exposure to HCl, and no evidence in STM of finding chlorine on top of Au(111) in our case as shown in Figure 9.21

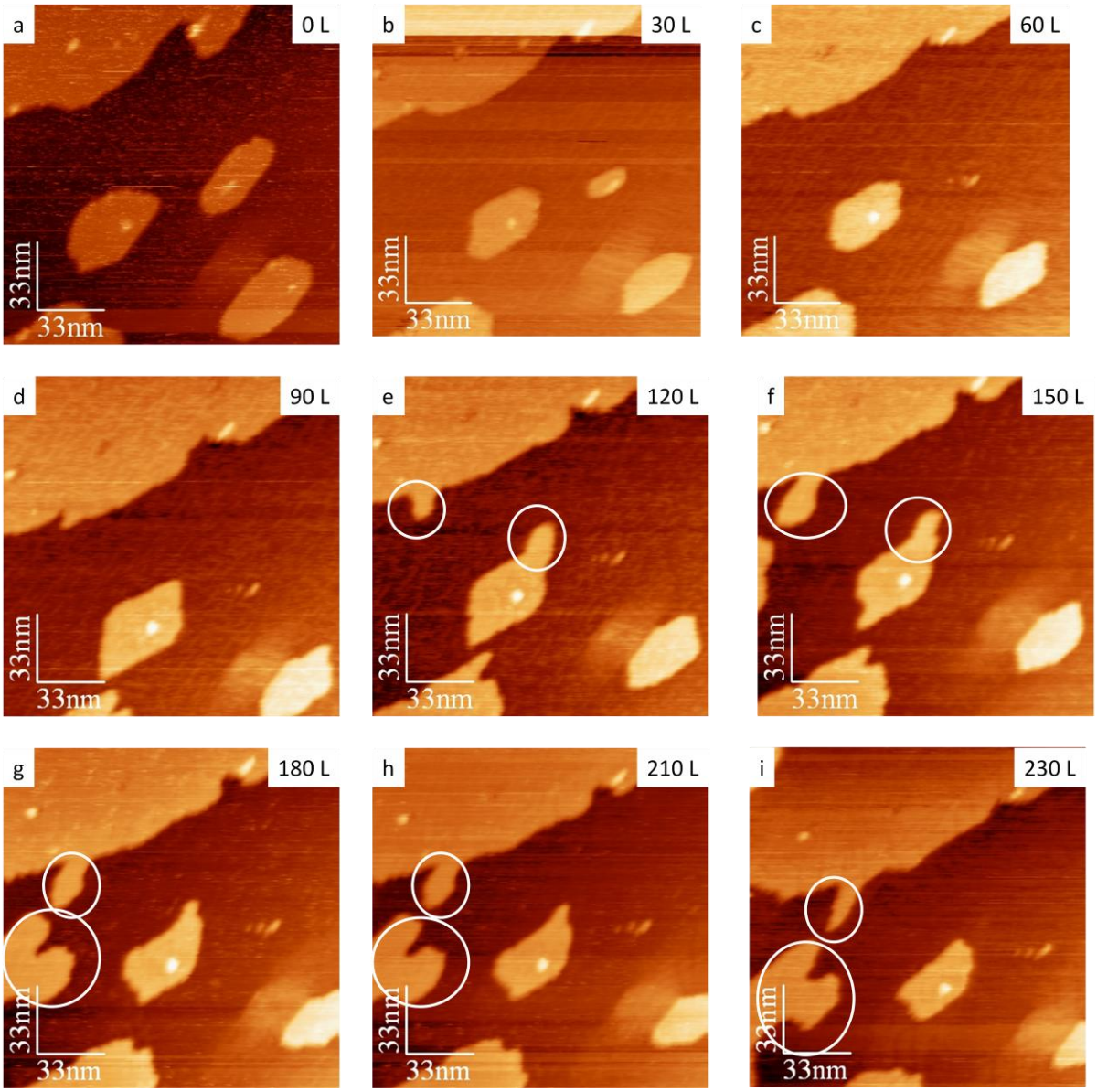

Figure 7.17: STM images of exposed the Au/Cu(100) alloy at coverage about $1.72x10^{15}$ cm^{-2} to 250 L of HCl at room temperature. Tunnelling conditions: 1V, and 1nA.

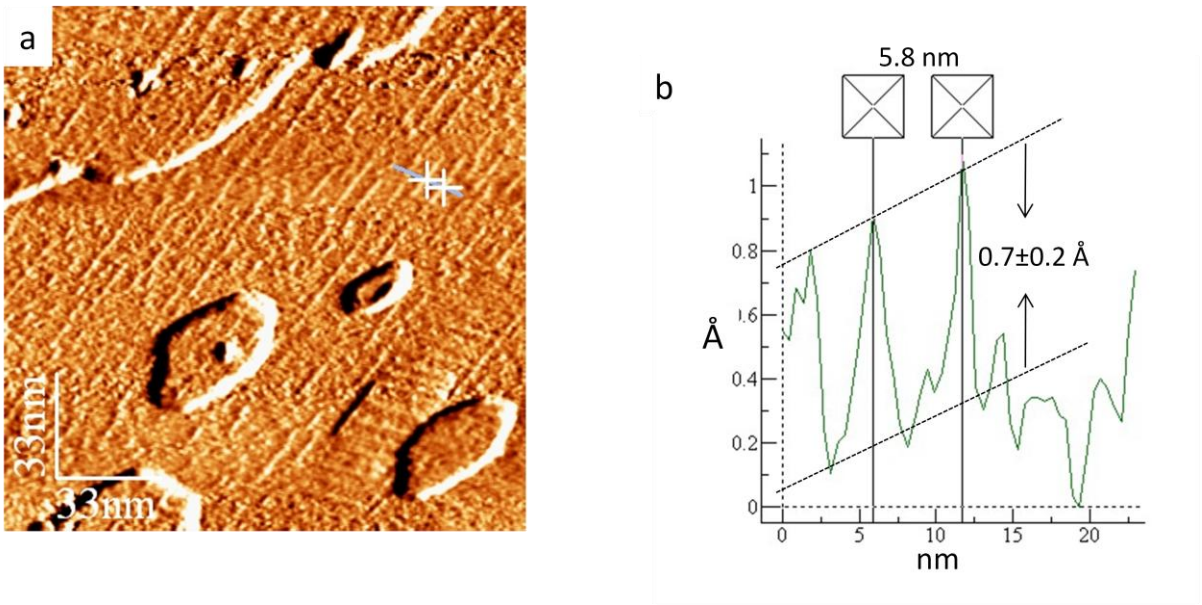

Figure 7.18: (a) STM current image of the line features which appear after exposure of the Au/Cu(100) alloy at coverage about 1.72×10^{15} cm^{-2} to 30 to 60 L of HCl at room temperature. (b) Line profile from the z image shown the distance of the line feature and its height.

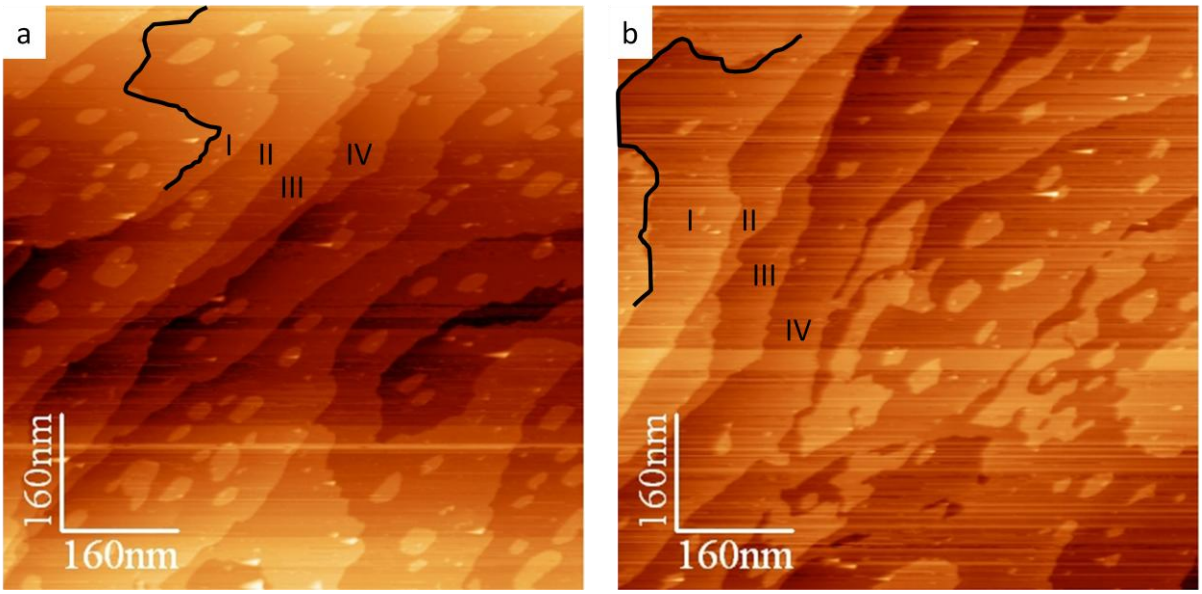

Figure 7.19: large size STM images of the Au/Cu alloy surface before (a), and after (b) exposed to 230 L of HCl at room temperature. The highlighted step edge and marks are assigned to the same area in the two images. Tunnelling conditions: 1V, and 1nA.

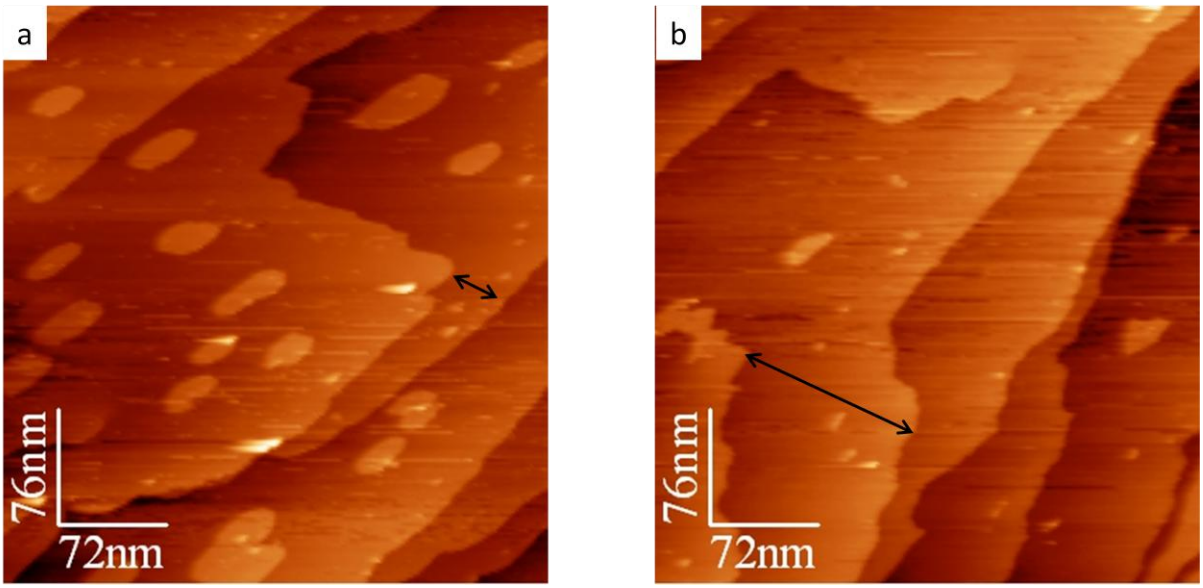

Figure 7.19: STM images of the Au/Cu alloy surface shown the increase of the terraces size after exposed the sample to HCl at room temperature. Tunnelling conditions: 1V, and 1nA.

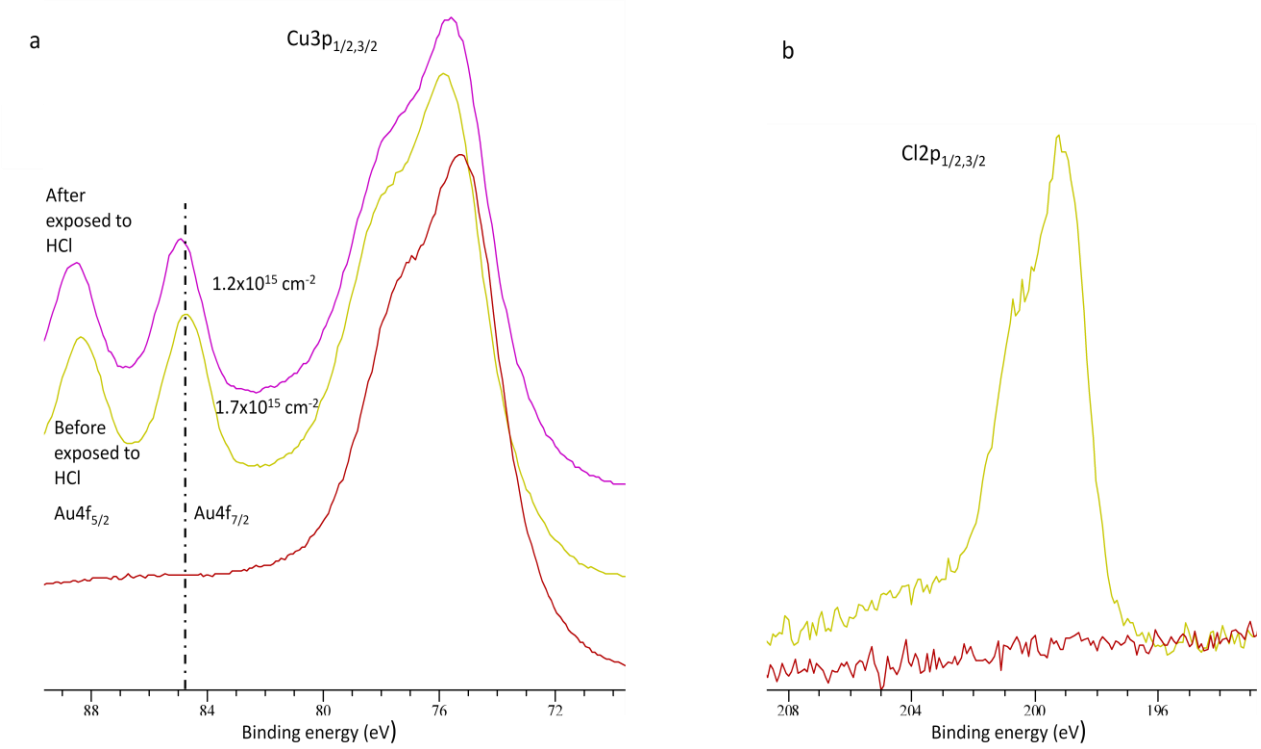

Figure 7.20: XP spectra of Au/Cu(100) alloy, (a) $Au4f_{5/2,7/2}$ before and after exposure to 230 L of HCl, (b) $Cl2p_{1/2,3/2}$ after exposed to HCl.

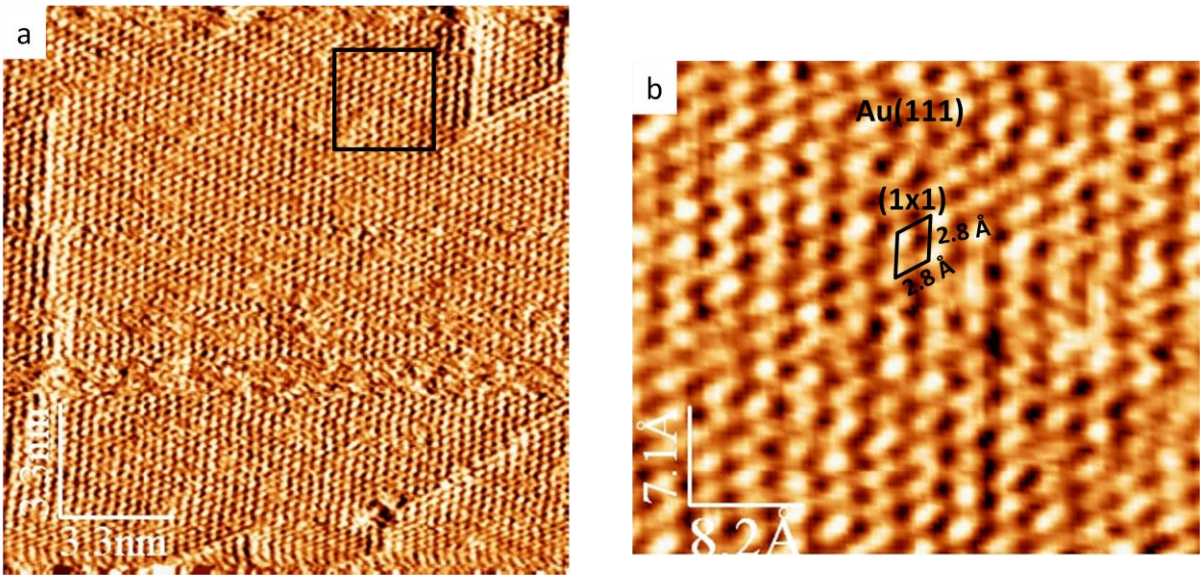

Figure 7.21: (a) Atomic resolution image of Au/Cu alloy surface after exposure to 230 L of HCl at room temperature. (b) Magnified image of the square area in (a) showing the (1x1) Au lattice. Tunnelling conditions: 1V, and 1nA.

7.3.5 Interaction of oxygen with Au/Cu(100) alloy at half monolayer coverage of gold

In this experiment the Au/Cu(100) alloy at half monolayer of gold coverage was exposed to 1800 L of oxygen at room temperature. XP spectra showed a small decrease in the gold coverage after exposure to oxygen from 6.75×10^{14} cm^{-2} to 5.30×10^{14} cm^{-2}. The oxygen coverage increase to 2.0×10^{14} cm^{-2}, (the sample also picked up some chlorine from the background giving a final chlorine coverage of about 1.0×10^{14} cm^{-2}.) A small shift in the gold position is observed as well from 84.3 to 84.6 eV as shown in Figure 7.22. A sequence of STM images recorded during the exposure of the Au/Cu(100) alloy to 150 L of oxygen are shown in Figure 7.23. Change happened to the terraces by grooving the surface similar to the behaviour of the clean Cu(100) to oxygen which is illustrated in chapter five. Continue exposure of the sample to oxygen leads to formation of oxygen top layer at 1800 L as shown in Figure 7.24. Striped features were observed in the surface but without direct evidence which oxygen structure were formed whether c(2x2)-O or $(\sqrt{2}x2\sqrt{2})R45^{o}$.

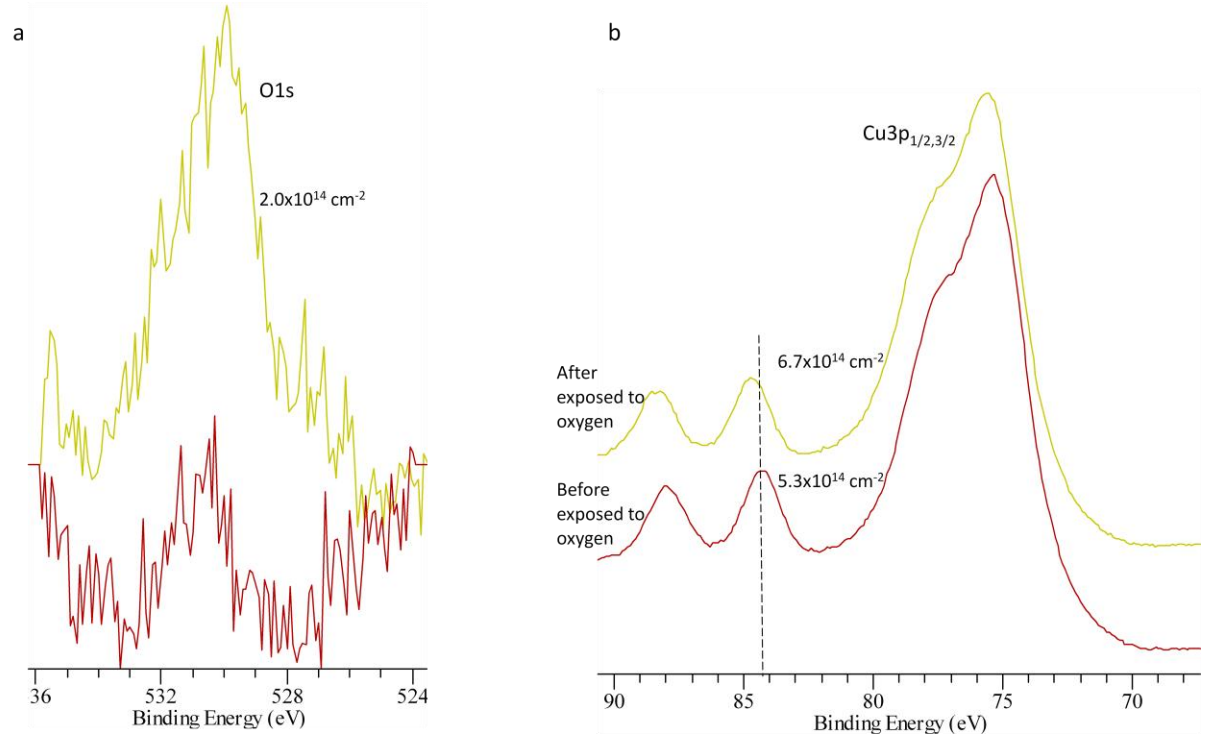

Figure 7.22: XP spectra of Au/Cu(100) alloy, (a) O(1s) before, and after exposed to oxygen, (b) $Au4f_{5/2,7/2}$ before and after exposed to 1800 L of Oxygen.

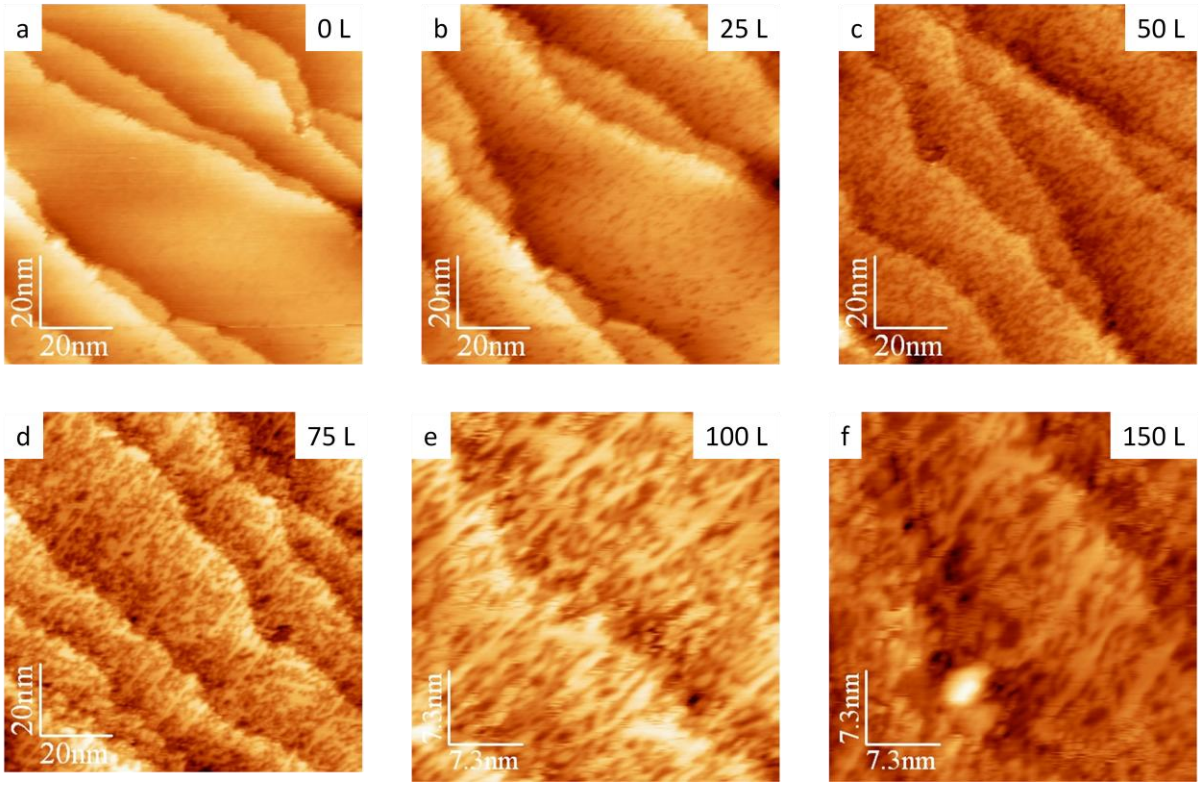

Figure 7.23: STM images of exposed the Au/Cu(100) alloy at coverage about $6.75x10^{14}$ cm^{-2} to 150 L of oxygen at room temperature. Tunnelling conditions: 1V, and 1nA.

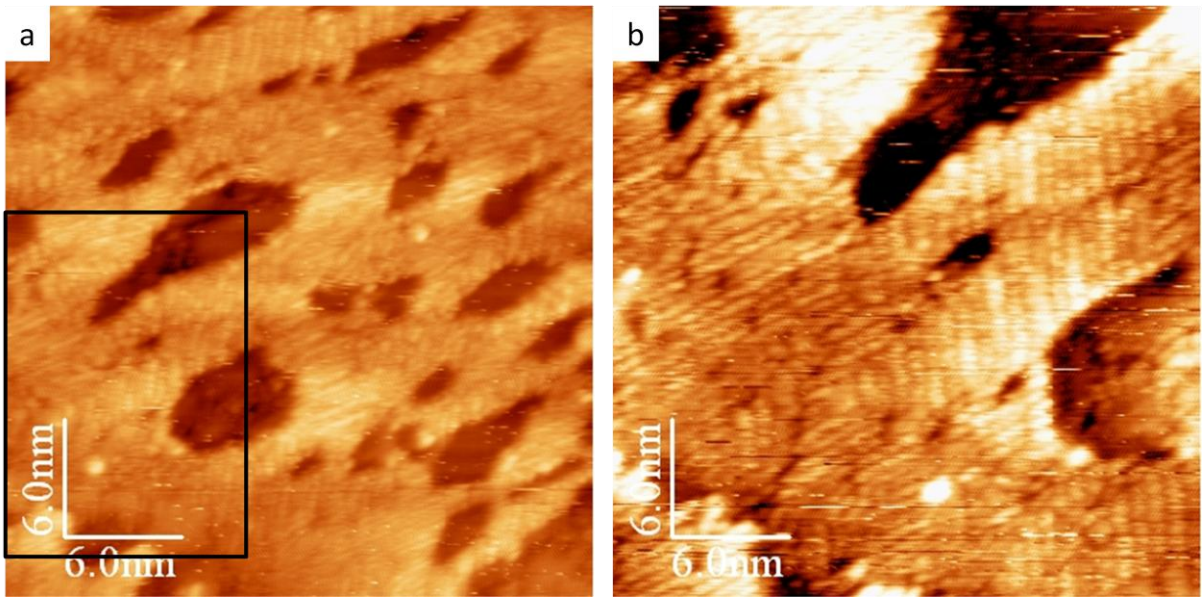

Figure 7.24: STM images of exposed the Au/Cu(100) alloy at coverage about $6.75x10^{14}$ cm^{-2} to 1800 L of oxygen at room temperature. Tunnelling conditions: 1V, and 1nA.

Exposing the Au/Cu(100) surface precovered with oxygen to 110 L of HCl leads to the removal of the oxygen from the surface very easily as shown in the XP spectra in Figure 7.25. No change is observed in the gold coverage after exposure to HCl. The chlorine coverage is $4.2x10^{14}$ cm^{-2} which is about double of the amount of removed oxygen. From these observations, the suggested mechanism are similar to what we suggested in chapter five as shown in the following equation:

$$O + 2HCl \rightarrow 2Cl + H_2O$$

The easy removal of oxygen could indicate that the removed oxygen had the c(2x2)-O structure which was more easily removed by HCl than the missing row reconstruction $(\sqrt{2}x2\sqrt{2})R45^{o}$. For this experiment no STM image could be taken after exposing the sample to HCl due to the poor resolution of the surface even after leaving the sample to settle down for a long time. This might be due to the surface not being completely saturated with Cl.

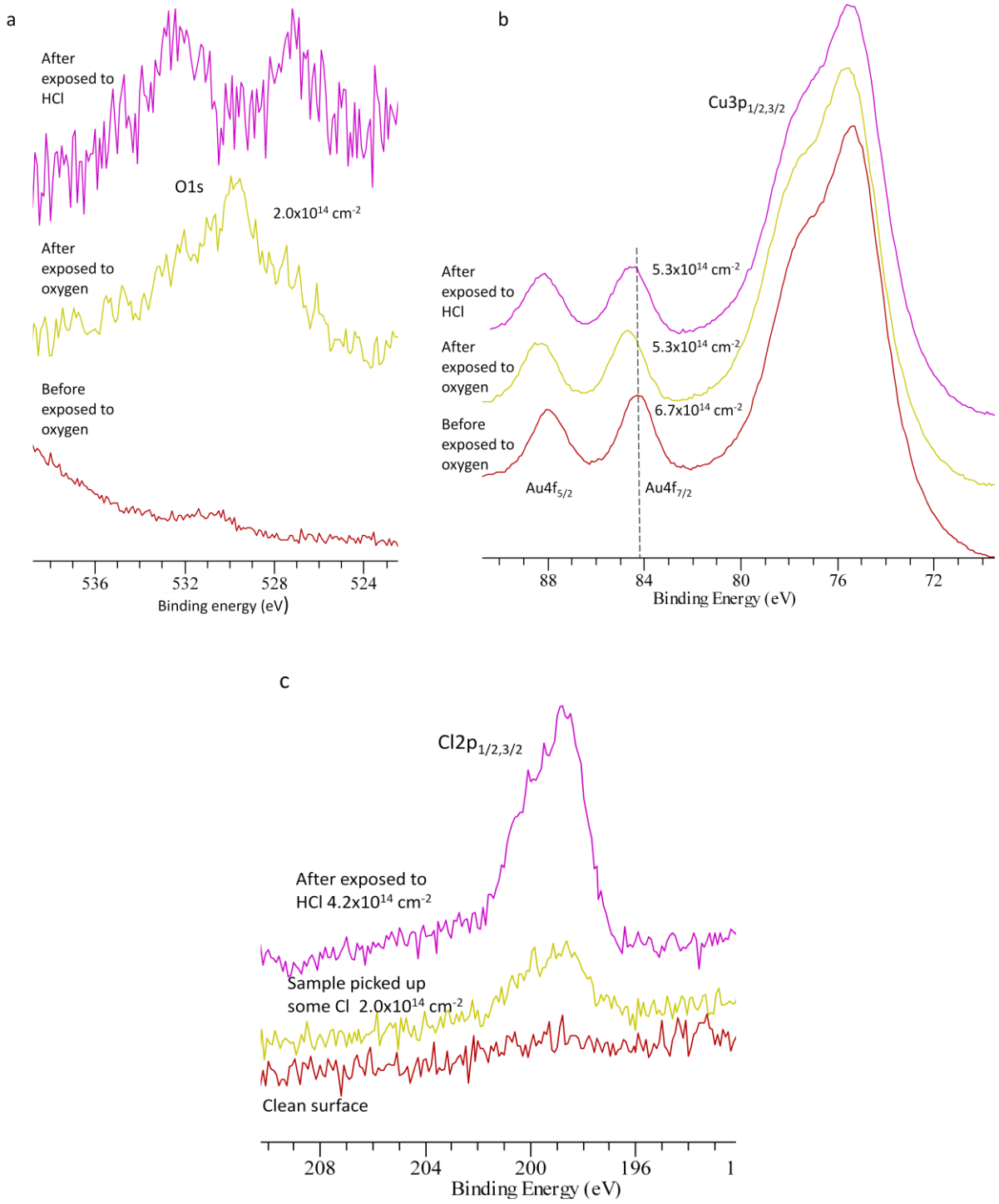

Figure 7.25: XP spectra of Au/Cu(100) alloy, (a) O(1s) before, and after exposed to 110 L of HCl, (b) $Au4f_{5/2,7/2}$ before and after exposed HCl, and (c) $Cl2p_{1/2,3/2}$ after exposed to HCl.

7.3.6 Interaction of gold with Cu(100) precovered with (√2x2√2)R45° of oxygen reconstruction

In this experiment the Cu(100) surface was oxidised by exposing the sample to 5760 L of oxygen at 250 °C. This makes a fully oxidized surface covered by missing row reconstruction (√2x2√2)R45° of oxygen with a coverage of about $1.2x10^{15}$ cm^{-2} [24]. The gold was then evaporated after the sample cool down to room temperature. The calculated gold and oxygen coverages from the XPS data are shown in Figure 7.26. The first evaporated gold dose on the precovered (√2x2√2)R45° of oxygen reconstruction sample showed an increase of gold coverage to $1.3x10^{14}$ cm^{-2} while the oxygen coverage had a small decrease to $1.1\ x10^{15}$ cm^{-2}. The increase of gold coverage and decrease of oxygen coverage continues until the gold coverage reaches $1.3\ x10^{15}$ cm^{-2} and the oxygen coverage $8.8\ x10^{14}$ cm^{-2}. The subsequent gold exposures did not have any effect on oxygen coverage which is stabilised at $8.8\ x10^{14}$ cm^{-2} even at about three monolayers of gold. STM images of the first dose of evaporated gold on the surface precovered with (√2x2√2)R45° O(a) show small dots scattered on top of the terraces as shown in Figure 7.27. Similar observation have been shown before for depositing Ni, and Co on top of Cu(100) surface precovered with (√2x2√2)R45° of oxygen reconstruction by Tanaka et al. [14, 15], and Xiangdong et al. [16]. No elongated islands are observed in our case at this coverage of gold. Increasing the gold coverage to $3.2x10^{14}$ cm^{-2} leads to the formation of elongated islands whereas the coverage of small dots decreased as shown in Figure 7.28(a, and b). The elongated islands have different size, but all of them have the same width which is about 5.2 nm as shown in Figure 7.28(c). The explanation of these islands have three possibilities; first one these islands being a pure gold nanowire resulted by one dimensional growth of gold through the missing row structure of Cu(100)-(√2x2√2)R45°-O, in agreement with previous studies [14, 15]. The second possibility is islands of Au/Cu alloy formed by aggregation of the adsorbed Au atoms with the ejected copper atoms which are produced as result of the formation of the missing row reconstruction of oxygen on top of the Cu(100) covered with oxygen. The third possibility is these islands are pure copper islands covered by (√2x2√2)R45°-O, produced by replacing the copper atoms with Au atoms in agreement with a previous study [16].

Heating the sample with a gold coverage $2.9x10^{15}$ cm^{-2} to 240 °C leads to a decrease in the gold, and oxygen coverage as a result of diffusing the gold atoms into a bulk. The oxygen maybe diffusing into the bulk or it could be desorbing as O_2. The desorption at low temperature maybe possible because the presence of Au weakening the Cu-O bond.

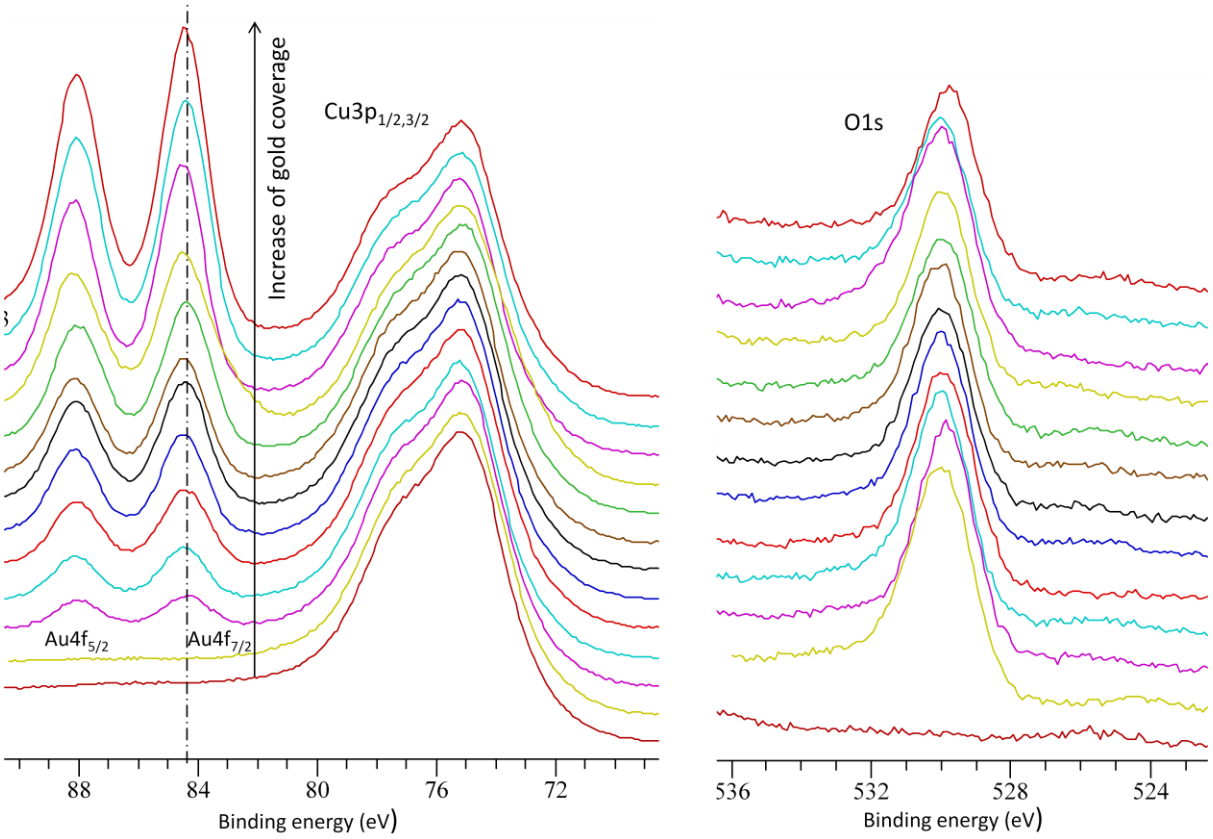

Time of evaporated gold in second	Gold Conc./cm^{-2}	Oxygen Conc./cm^{-2}
0	0	$1.2x10^{15}$
20	$1.3x10^{14}$	$1.1x10^{15}$
40	$3.2x10^{14}$	$1.1x10^{15}$
80	$5.3x10^{14}$	$1.0x10^{15}$
140	$7.9x10^{14}$	$9.9x10^{14}$
200	$1.1x10^{15}$	$9.0x10^{14}$
260	$1.3x10^{15}$	$8.8x10^{14}$
320	$1.7x10^{15}$	$8.8x10^{14}$
420	$1.9x10^{15}$	$8.8x10^{14}$
520	$2.3x10^{15}$	$8.8x10^{14}$
620	$2.9x10^{15}$	$8.6x10^{14}$

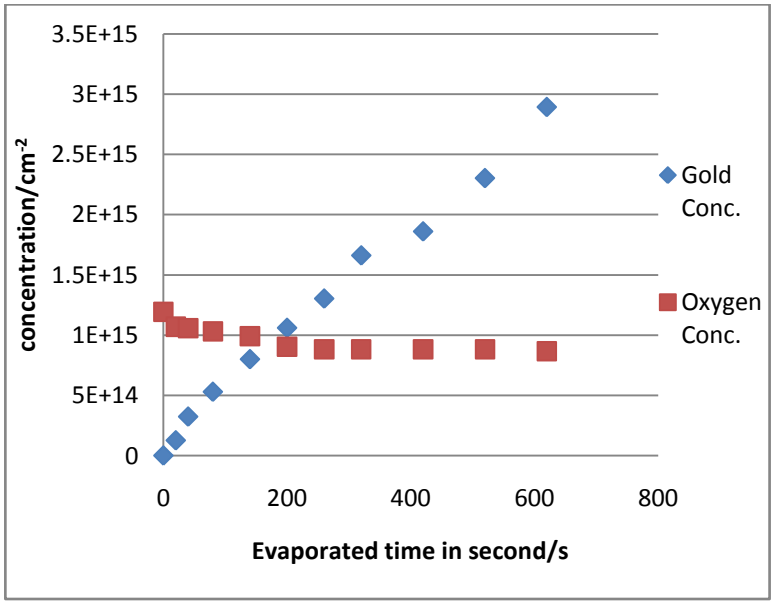

Figure7.26: (a) XP spectra of Au4f$_{5/2,7/2}$ for several coverage top of the Cu(100) precovered with ($\sqrt{2}x2\sqrt{2}$)R45^{o} of oxygen reconstruction, (a) XP spectra of O(1s) before, and after evaporated gold. Table and schematic diagram showed the concentration of gold and oxygen while evaporated gold.

The Au/Cu(100)-(√2x2√2)R45°-O sample with a gold coverage of $3.2x10^{14}$ cm^{-2} and oxygen coverage of $1.1x10^{15}$ cm^{-2} was exposed to 420 L of HCl and showed a decrease of gold and oxygen coverage to $2.7x10^{14}$ cm^{-2}, and $2.5x10^{14}$ cm^{-2} respectively while the chlorine coverage was $1.2x10^{15}$ cm^{-2} shown by XPS data as shown in Figure 7.28. The sequence of STM images shown in Figure 7.30 are for the exposure of the Au/Cu(100)-(√2x2√2)R45°-O sample with a gold coverage of $3.2x10^{14}$ cm^{-2} to 420 L of HCl. The elongated features showed a good stability toward interaction with HCl while the surrounding area, which is suggested to be covered by (√2x2√2)R45°-O shows a lot of grooves consistent with previous result in chapter five of the interaction of Cu(100)-(√2x2√2)R45°-O with HCl. The poor resolution in Figure 7.30(h to k) it could be due to the movement of atoms on the surface. STM images in Figure 7.31 show the difference between the Au/Cu(100)-(√2x2√2)R45°-O before and after exposure to the 420 L of HCl.

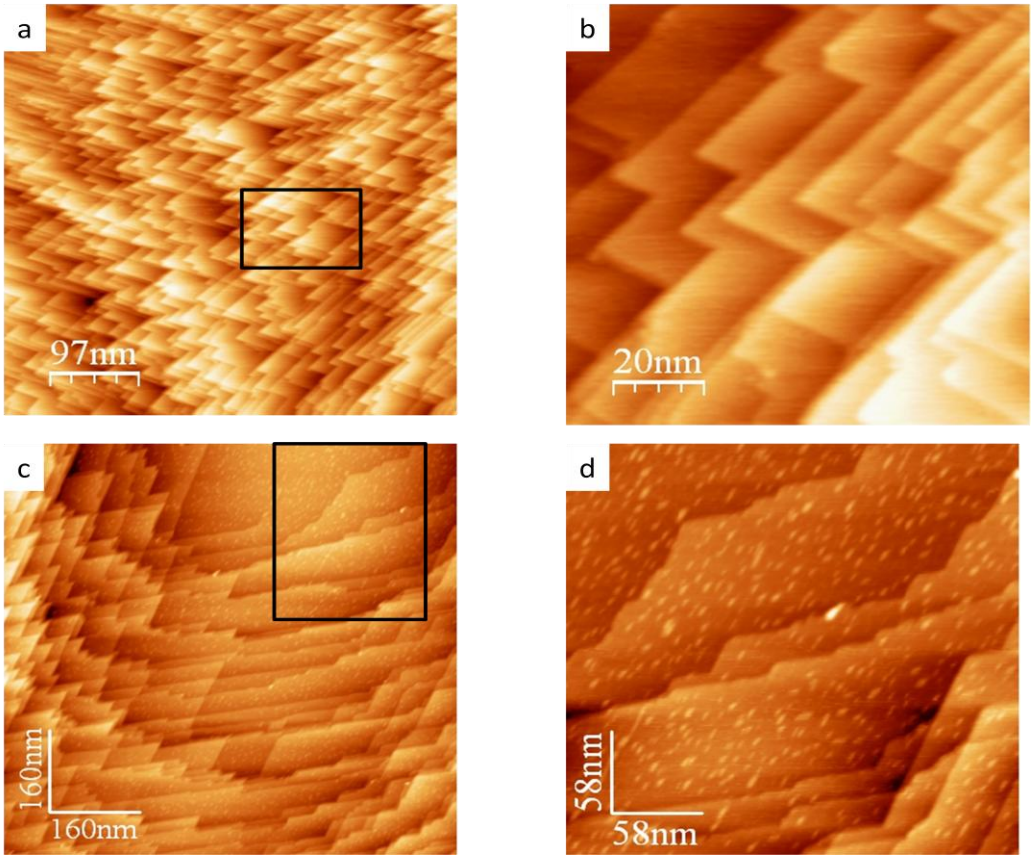

Figure7.27: STM images of the Cu(100) precovered with (√2x2√2)R45° of oxygen reconstruction (a, and b) before, and after (c, and d) evaporated gold with coverage $1.2x10^{14}$ cm^{-2}. The square areas assigned to the zoom in area. Tunnelling conditions: 1V, and 1nA.

From the above observation we can conclude that the elongated features are pure gold islands growing preferentially in the missing row structure of oxygen top of Cu(100) surface which

explained the small decrease of oxygen coverage. In contrast to the Ni, and Co situations [14-16] no oxygen appears on top of the gold islands. Furthermore, exposure of the Au/Cu(100)-($\sqrt{2}$x2$\sqrt{2}$)R45^{o}-O sample to HCl, results in reaction only with the Cu(100)-($\sqrt{2}$x2$\sqrt{2}$)R45^{o}-O; no change is observed with the elongated islands. If these islands were made up of a Au/Cu alloy we should expect to see the behaviour of sintering of gold atoms after exposure to HCl as a result of the dealloying process which was observed in the situation of exposing the Au/Cu(100) sample to HCl but this was not observed.

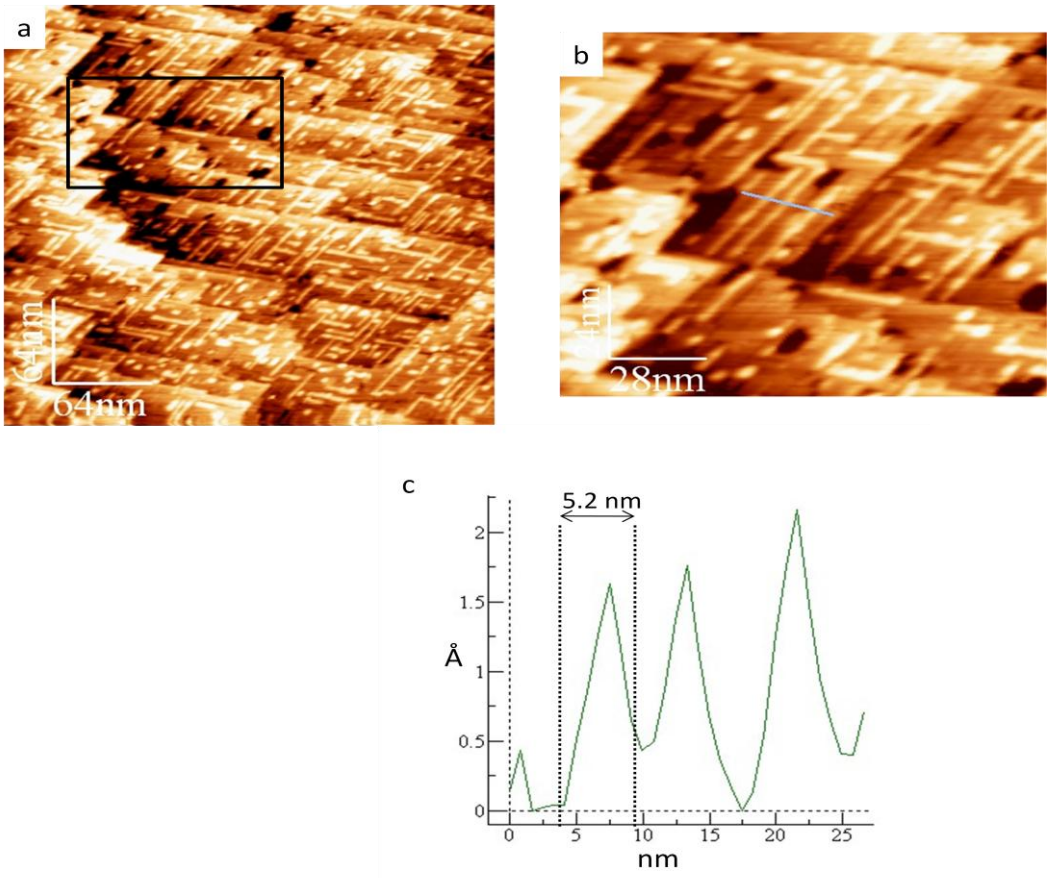

Figure7.28: (a) STM images Au/Cu(100)-($\sqrt{2}$x2$\sqrt{2}$)R45^{o}-O with gold coverage of 3.2x10^{14} cm^{-2}. (b) The magnified area of the square area in (a). (c) Line profile shown the width of the elongated feature in (b) Tunnelling conditions: 1V, and 1nA.

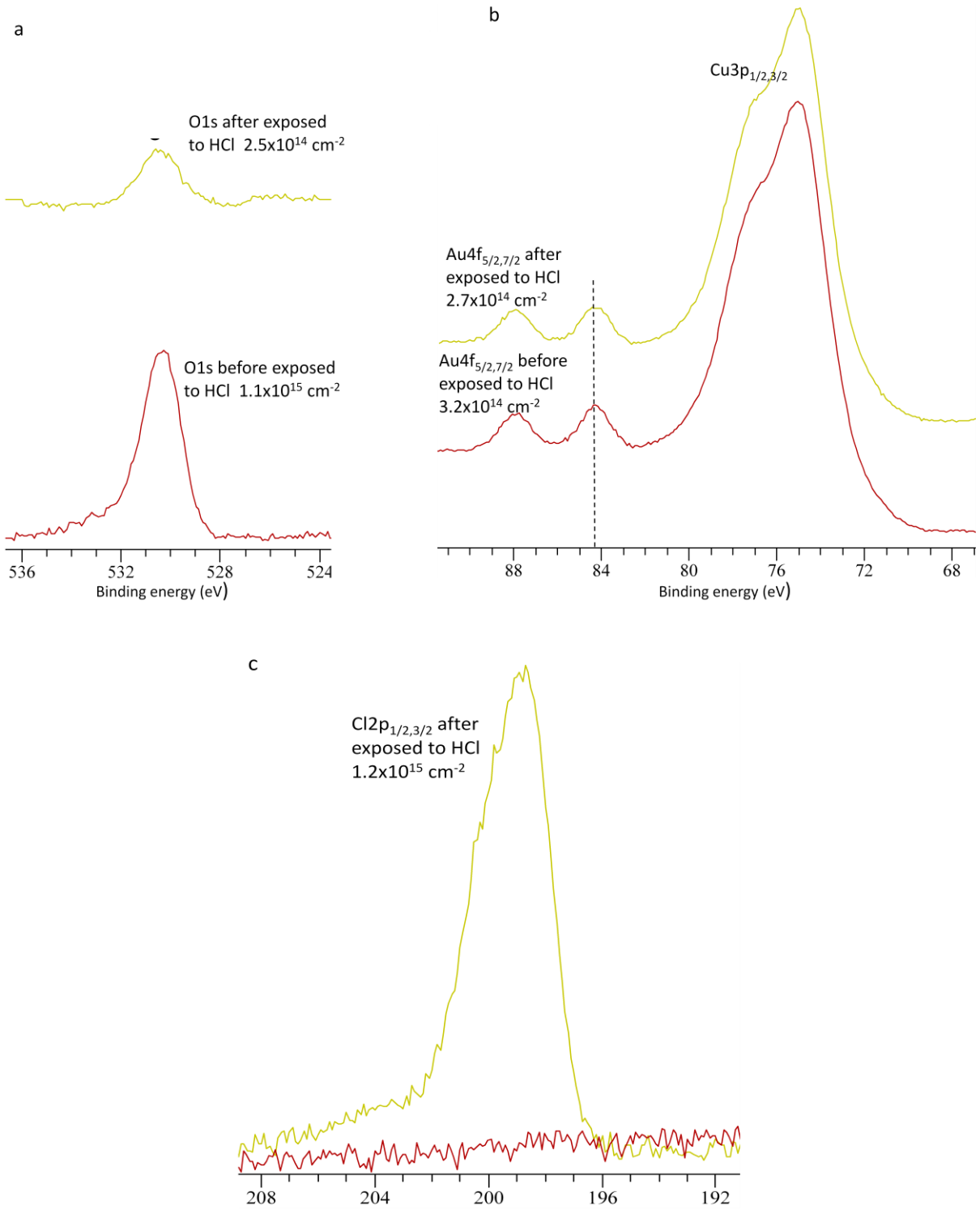

Figure 7.29: XP spectra of Au/Cu(100)-($\sqrt{2}$x2$\sqrt{2}$)R45°-O with coverage 3.2x10^{14} cm^{-2}, (a) O(1s) before, and after exposure to 420 L of HCl, (b) Au4f$_{5/2,7/2}$ before and after exposure to HCl, and (c) Cl2p$_{1/2,3/2}$ after exposure to 420 L of HCl.

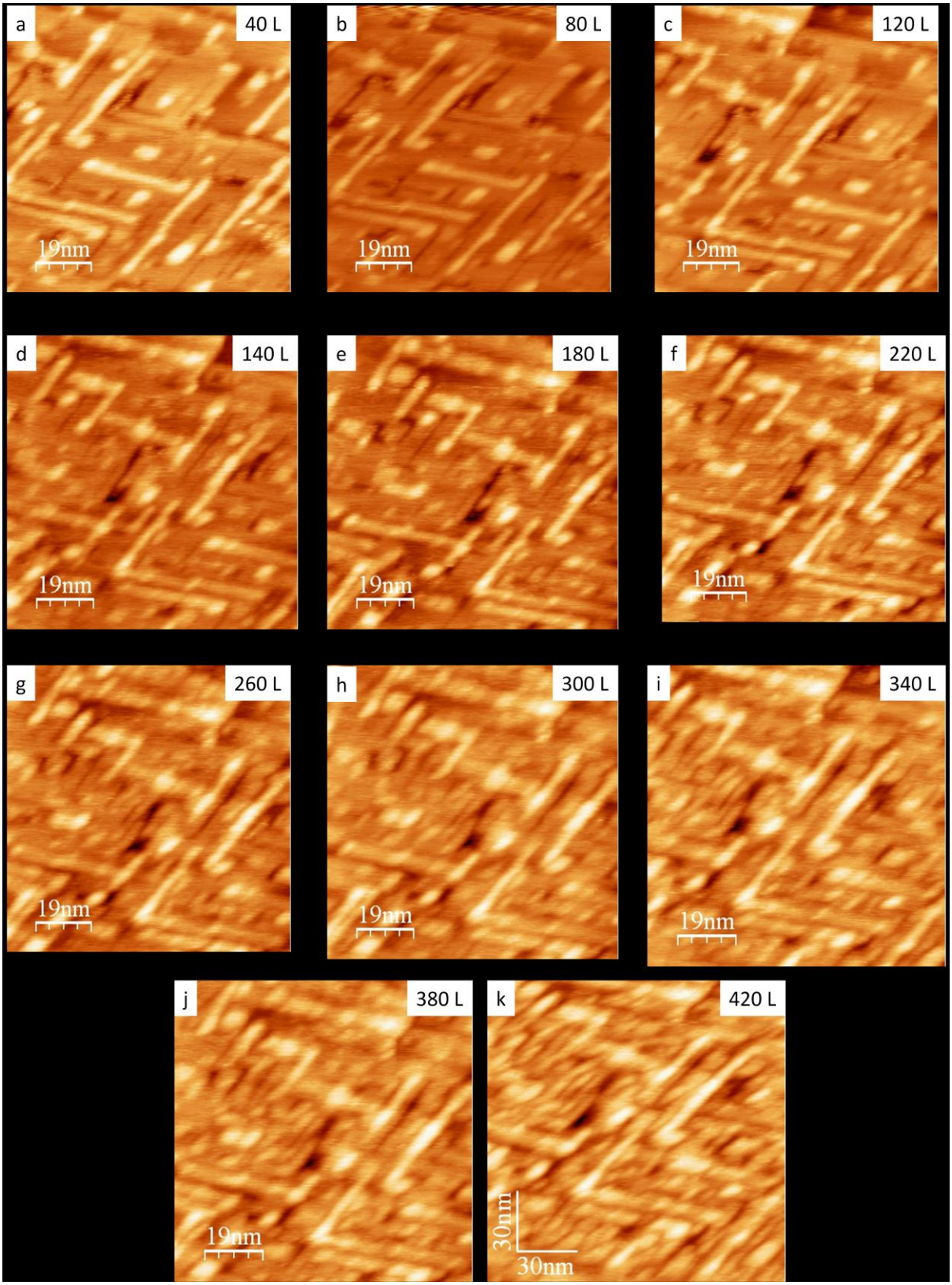

Figure 7.30: Sequences STM images of exposed the Au/Cu(100)-(√2x2√2)R45°-O sample with gold coverage $3.2x10^{14}$ cm^{-2} after exposed to 420 L of HCl. Tunnelling conditions: 1V, and 1nA.

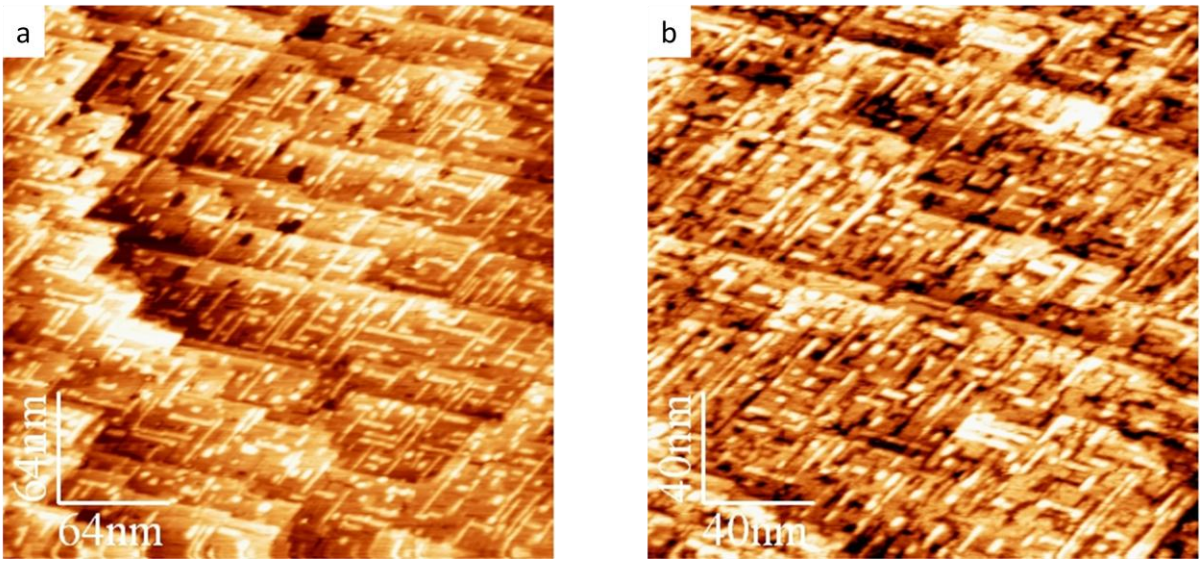

Figure 7.31: STM images of Au/Cu(100)-(√2x2√2)R45^{o}-O sample with gold coverage 3.2x10^{14} cm^{-2} (a) befor, and (b) after exposed to 420 L of HCl. Tunnelling conditions: 1V, and 1nA.

7.4 Conclusions

Evaporated gold on the clean Cu(100) sample leads to the formation of Au/Cu(100) alloy with a coverage or less a monolayer of gold in agreement with previous work [1, 2]. The islands which form on top of the Au/Cu(100) alloy have the same composition of alloy even at coverage more than half monolayer in contrast to the previous work [3] which suggested the gold island on Au/Cu(100) alloy formed by pure gold with hexagonal structure.

Interaction of HCl with Au/Cu(100) alloy at coverage about half monolayer leads to adsorbed chlorine on top of the alloy surface and made the c(2x2)-Cl reconstruction shown by STM and XPS. STM showed a lot of nano size domains of c(2x2)-Cl reconstruction with unit cell dimension 5.2 Å. XPS showed the chlorine coverage is 7.4x10^{14} cm^{-2} which is equal to a half monolayer coverage consistent with previous data of the interaction of HCl with clean Cu(100) in chapter five. The shift observed in XPS of Au(4f) and Cu(3p) could be assigned to a change in the charge movement between the Au and Cu of the alloy.

At high coverages of gold, exposure to HCl leads to the formation of a hexagonal, pure gold layer shown by STM with a unit cell dimension of 2.8 Å in agreement with the unit cell dimension of Au(111). The chlorine coverage is 1.2 x10^{15} cm^{-2}, this excess of chlorine concentration could be assigned to formation of CuCl underneath the gold layer as a result of interaction of Cl atoms with the released Cu atoms from the Au/Cu alloy in the topmost layer

and the alloy islands although there is no direct evidence of formation of Cu(100)-c(2x2)-Cl as shown in Figure 7.32. From this observation we assume the adsorbed gold at high coverage is disrupting the copper lattice like the oxygen does which allows the accommodation of more chlorine.

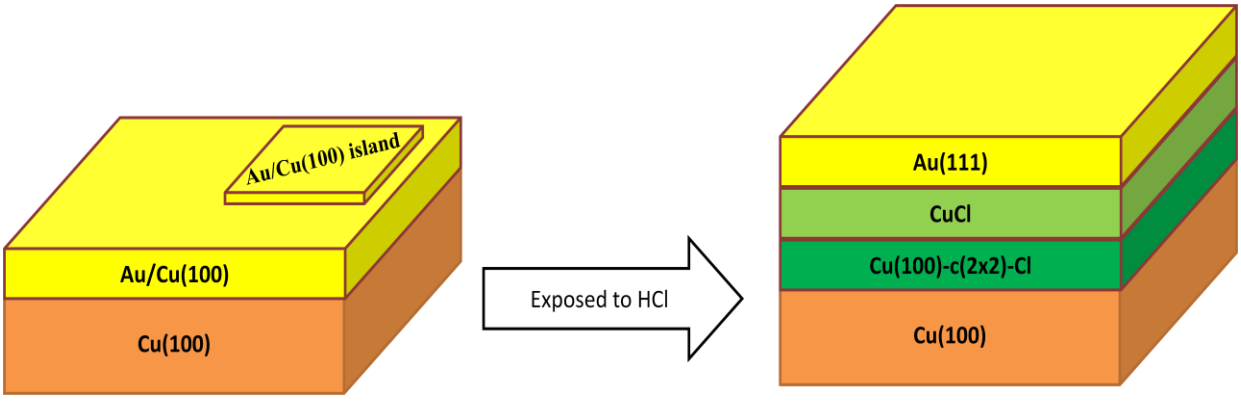

Figure 7.32: schematic diagram illustrating the formation of a Au(111) layer as result of dealloying and sintering of gold atoms after exposure of the Au/Cu(100) alloy with gold coverage more than half monolayer to HCl, while as the CuCl formed by reacting the released Cu atoms with HCl.

Exposing the Au/Cu(100) alloy surface with gold coverage of 6.75×10^{14} cm^{-2} to 1800 L of oxygen lead to a decrease in the gold coverage to 5.30×10^{14} cm^{-2}, while an oxygen coverage of 2.0×10^{14} cm^{-2} develops. This contrasts to the case of of a clean Cu(100) exposed to 1650 L of oxygen which resulted in a saturated Cu(100) surface with an oxygen coverage of 7.2×10^{14} cm^{-2} as shown in chapter five. The total coverages of gold and oxygen is equal to half monolayer, suggesting to the adsorbed gold is blocking the adsorption sites while as for gold adsorbed on Cu(111), the gold is adsorbed at step edges and prevents oxygen dissociation [25]. STM images of the Au/Cu(100) alloy surface after exposed to oxygen showed a similar behaviour to that of interaction of clean Cu(100) sample to oxygen which made a lot of grooved areas. Around these groove sort of striped structure which could be an oxygen but with out direct evidence of which type of oxygen reconstruction c(2x2) or $(\sqrt{2}x2\sqrt{2})R45^{o}$ was formed.

Evaporated gold on the preoxidised Cu(100)-$(\sqrt{2}x2\sqrt{2})R45^{o}$-O with oxygen coverage 1.1×10^{15} cm^{-2} formed by exposing the clean Cu(100) sample to 5760 L at 250 ^{o}C lead to the growth of a lot of small islands in STM images represented as a dots with gold coverage

$3.2x10^{14}$ cm^{-2}. These islands scatter randomly on top of the terraces without aggregation at the step edge. The immobility of these feature could be due to being trapped at the grain boundaries of the missing row structure in agreement with Xiangdong et al. who found immobile features after evaporating Co on the Cu(100)-($\sqrt{2}x2\sqrt{2}$)R45^{o}-O, assigned to Co atoms [16]. Increasing the gold coverage to $3.2x10^{14}$ cm^{-2} leads to the formation of elongated features, in the STM images with a decrease of amount of dots observed as well.

To explore the nature of these features the Au/Cu(100)-($\sqrt{2}x2\sqrt{2}$)R45^{o}-O was exposed to 420 L of HCl. The coverage estimate from XPS data for gold , oxygen , and chlorine were $2.7x10^{14}$ cm^{-2}, and $2.5x10^{14}$ cm^{-2}, and $1.2x10^{15}$ cm^{-2} respectively. STM images showed no changes in the elongated features during exposure to HCl, while a lot of grooves were developed in the surrounding area of the elongated features. From the above observation the nature of the elongated features is suggested to be a pure nanowire gold growth occurring preferentially at the grain boundaries of the oxygen missing row structure. The surrounding area of the elongated gold islands react with HCl in similar manner to the interaction of the Cu(100)-($\sqrt{2}x2\sqrt{2}$)R45^{o}-O which was described in chapter five. The excess chlorine coverage could be due to the interaction of copper atoms which are released as a result of the formation of the missing row structure with HCl to form of CuCl.

7.5 References

1. Palmberg, P.W. and T.N. Rhodin, *Atomic Arrangement of Au(100) and Related Metal Overlayer Surface Structures. I.* The Journal of Chemical Physics, 1968. **49**(1): p. 134-146.
2. Palmberg, P.W. and T.N. Rhodin, *Auger Electron Spectroscopy of fcc Metal Surfaces.* Journal of Applied Physics, 1968. **39**(5): p. 2425-2432.
3. Naumović, D., et al., *Submonolayer films of Au on Cu(001) studied by photoelectron diffraction.* Surface Science, 1992. **269–270**(0): p. 719-723.
4. Shen, Y.G., et al., *Au-segregated dealloying and Pd-induced clock reconstructing of Cu(001).* Journal of Physics: Condensed Matter, 1996. **8**(27): p. 4903.
5. Eberhardt, W., et al., *Core-level shifts and the electronic structure of Cu_{3}Au.* Physical Review B, 1985. **31**(12): p. 8285-8287.
6. Chambliss, D.D., R.J. Wilson, and S. Chiang. *Nucleation and growth of ultrathin Fe and Au films on Cu(100) studied by scanning tunneling microscopy*. 1992. Seattle, Washington (USA): AVS.
7. Chambliss, D.D. and S. Chiang, *Surface alloy formation studied by scanning tunneling microscopy: Cu(100) + Auc(2 × 2).* Surface Science, 1992. **264**(1–2): p. L187-L192.
8. Li, L., et al., *Surfactant effect of oxygen in epitaxial γ-Fe/Cu(001)–O(22×2)R45°.* Surface Science, 2001. **493**(1–3): p. 120-125.
9. K. E. Johnson, D.D.C., R. J. Wilson, and S. Chiang, *Growth and morphology of partial and multilayer Fe thin films on Cu(100) and the effect of adsorbed gases studied by scanning tunneling microscopy.* Jo Vac. Sci. Technol. A 1993. **11**(4): p. 1654.
10. Johnson, K.E., et al., *A structural model and mechanism for Fe epitaxy on Cu(100).* Surface Science, 1994. **313**(3): p. L811-L816.
11. Li, D., et al., *Magnetic and structural instabilities of ferromagnetic and antiferromagnetic Fe/Cu(100).* Journal of Applied Physics, 1994. **76**(10): p. 6425-6427.
12. Li, D., et al., *Magnetic phases of ultrathin Fe grown on Cu(100) as epitaxial wedges.* Physical Review Letters, 1994. **72**(19): p. 3112-3115.
13. Zharnikov, M., et al., *Magnetic Order-Disorder Transition Mediated by a Temperature-Driven Structural Transformation.* Physical Review Letters, 1996. **76**(24): p. 4620-4623.

14. Fujita, T., Y. Okawa, and K.-i. Tanaka, *STM study of preferential growth of one-dimensional nickel islands on a Cu(100)-(2√2×√2)R45°-O surface.* Applied Surface Science, 1998. **130–132**(0): p. 491-496.
15. Tanaka, K.-i., et al., *Nano-scale patterning of metal surfaces by adsorption and reaction.* Applied Surface Science, 1998. **130–132**(0): p. 475-483.
16. Xiangdong, L., et al., *Invasive growth of Co on (√2x2√)R45^o reconstructed O/Cu(001).* Applied Physics Letters, 2006. **88**(13): p. 133102.
17. Nakatsuji, K., et al., *Electron correlation effects in Co nanoscale islands on a nitrogen-covered Cu(001) surface.* Physical Review B, 2008. **77**(23): p. 235436.
18. Silva, S.L., et al., *Fabricating nanometer-scale Co dot and line arrays on Cu(100) surfaces.* Applied Physics Letters, 2000. **76**(9): p. 1128-1130.
19. Komori, F., et al., *Growth and magnetism of Co nanometer-scale dots squarely arranged on a Cu(001)-c(2×2)N surface.* Physical Review B, 2001. **63**(21): p. 214420.
20. Ohno, S., K. Nakatsuji, and F. Komori, *Growth mechanism of Fe nanoisland array on Cu(100)–c(2×2)N surfaces.* Surface Science, 2003. **523**(1–2): p. 189-198.
21. Leibsle, F.M., C.F.J. Flipse, and A.W. Robinson, *Structure of the Cu{100}-c(2×2)N surface: A scanning-tunneling-microscopy study.* Physical Review B, 1993. **47**(23): p. 15865-15868.
22. Kuhn, M. and T.K. Sham, *Charge redistribution and electronic behavior in a series of Au-Cu alloys.* Physical Review B, 1994. **49**(3): p. 1647-1661.
23. Gao, W., et al., *Chlorine Adsorption on Au(111): Chlorine Overlayer or Surface Chloride?* Journal of the American Chemical Society, 2008. **130**(11): p. 3560-3565.
24. C. L. H. Devlin, Y.S., and S. Chiang, *Morphology of the Cu2O surface oxide phase formed on Cu(100) at high temperature.* Journal of Aplied Physics 2009. **105**.
25. Altass, H., et al., *Interaction of HCl with Au/Cu(111) surface.* Will be published soon.

Chapter 8 Conclusion

Contents

8.1 Introduction

The aim of this thesis has been to investigate how modifying copper surfaces affects behaviour towards different reactants, HCl in particular using XPS and STM. We have looked at two modifiers in particular oxygen and gold, the former having the capability to become involved in the reaction, the latter expected to be inert.

8.2 Interaction of HCl with Cu(100) and (111)

Exposure of the Cu(100) and (111) samples to HCl under (UHV) at room temperature leads to the formation of a saturated copper surface by chlorine confirmed by XPS and STM. The saturation coverage of chlorine is dependent on the reconstruction of chlorine atoms which is corresponding to the copper surface. In the case of Cu(100) the saturated coverage was half monolayer corresponding to c(2x2)-Cl reconstruction (half monolayer is $7.25x10^{14}$ cm^{-2}). The saturation coverage of chlorine on Cu(111) which is less reactive than Cu(100) is one third monolayer consistent with the reconstruction of $(\sqrt{3}x\sqrt{3})R30^{o}$ (one third monolayer $5.9x10^{14}$ cm^{-2}). At the beginning of the interaction of HCl with both the copper surfaces, the sharpness of the step edges and the quality of the STM resolution are reduced observed due to the ejection of Cu atoms from the step edges and movement of the chlorine atoms on top of the copper surface and from the copper surface toward the STM tip as well. Atomic resolution of the two chlorine reconstruction c(2x2) and $(\sqrt{3}x\sqrt{3})R30^{o}$, are observed at the saturation coverage attributed to the limited movement of chlorine atoms at high coverage. The step edge height of the saturated Cl/Cu surface is identical to the height of the clean copper surface confirming to homogeneity of the surface. Exposure of the saturated Cl/Cu surface to extra HCl doesn't have any effect on the surface.

8.3Influence of oxygen on the interaction of Cu(100) and (111) with HCl

The interaction of HCl with Cu(100) and (111) precovered by oxygen show different behaviours from those exhibited by the clean copper surface depending on the way of interaction of oxygen with copper surface. In the case of the interaction of saturated Cu(111)-oxygen at room temperature with HCl, the concentration of chlorine was limited to a Cl monolayer. In contrast, the presence of oxygen on Cu(100) surface at saturation coverage or less leads to replacement by chlorine with a concentration more than the saturation coverage of the monolayer.

Oxidized Cu(100) and (111) surfaces at elevated temperature lead to the formation of multilayer of oxid. In the case of oxidising the Cu(111) surface, the structure of the oxide formed depends on the temperature of the copper surface at the time of interaction with of oxygen. Two oxide structure are observed which are referred to as ''44'' and ''29'' at 380 ^{o}C and 450 ^{o}C respectively. STM showed the ''44'' structure has less stability than the ''29''. Exposure of these two oxide surfaces to HCl leads to the formation of Cu-Cl surface with excess in chlorine concentration. STM showed small islands are scattered and trapped at step edges of the Cu(111) surface which are probably the site of the excess in chlorine concentration. No difference was observed for the manner of reaction of HCl with the two oxide surface.

Cu(100) oxidized at 250 ^{o}C leads to the formation of multi layer of oxide of ($\sqrt{2}$x2$\sqrt{2}$)R45^{o} reconstruction which is the major reconstruction found at saturated Cu(100)-oxygen at room temperature as well. Interaction of this surface with HCl leads to formation of Cu-Cl surface and Cu-Cl islands trapped at the step edges which account for the excess of chlorine concentration.

8.4 Influence of gold on the interaction of Cu(100) with HCl

Interaction of HCl with Au/Cu(100) showed two different behaviours depending on the gold coverage. An Au/Cu(100) alloy formed at half monolayer of gold coverage, forming c(2x2) structure. Exposing the Au/Cu(100) alloy at half monolayer of gold coverage to HCl leads to the formation of c(2x2)-Cl structure with a saturation coverage of half monolayer in similar manner of interaction of HCl with the clean Cu(100) surface.

Interaction of HCl with Au/Cu(100) surface at gold coverage more than half monolayer leads to dealloying of the gold from the copper surface and forming an overlayer Au(111) surface. Cu-Cl formed underneath the Au(111) surface shows an excess of chlorine concentration. There is no evidence in STM about the chlorine structure underneath the Au(111) surface and no chlorine atoms are observed on top of the gold surface.

Exposing the Cu(100) alloy to oxygen at gold coverages of less than half monolayer leads to the adsorption of oxygen at the pure copper surface only indicating, the gold is blocking the adsorption site. Interaction of HCl with Au/Cu(100)-O leads to the remove of all the oxygen from the surface. The surface chlorine concentration was found to be double the concentration of the removed oxygen atoms.

Depositing gold onto the Cu(100) surface oxidized at 250 ^{o}C leads to the formation of elongated islands of gold at the grain boundaries of the ($\sqrt{2}$x2$\sqrt{2}$)R45^{o} reconstruction. Interaction of HCl with Au/Cu(100)-($\sqrt{2}$x2$\sqrt{2}$)R45^{o}-O leads to the reaction with Cu(100)-($\sqrt{2}$x2$\sqrt{2}$)R45^{o}-O without any change observed in gold island. The increase in concentration of chlorine atoms was double the amount of removed oxygen in agreement with similar behaviour of HCl with the Cu(100) surface oxidized at 250 ^{o}C without gold. However, no islands of Cu-Cl are observed in presence of gold.

8.5 Summary

From this work we can identify a number of common factors: Firstly where the copper surface is reconstructed by oxygen the surface showed a higher reactivity toward HCl and leads to the accommodation of more chlorine than the clean copper surface. On the other hand two examples of where surface is nonreconstructed give flat chlorides. One of the most interesting observations is the way in which the multilayer of gold also enables the formation of multilayer of chloride.

8.6 Future work

The implications of these observations are important for understanding reactivity and rate of chlorination. The result should be explored using similar reactants to HCl such as HBr, and also Ag/O/HCl and Ni/O/HCl. More structural information would be very important for determine exact nature of chlorine such as LEED, EXAFS, ISS, and photoelectron diffraction.